Study of Standard Model processes with leptons of high transverse momentum with the ATLAS detector

Andreas Petridis

Department of Physics

Aristotle University of Thessaloniki

A thesis submitted for the degree of

Doctor of Philosophy, PhD

June 2012

1. Reviewer: Professor Chara Petridou
2. Reviewer: Professor Theodoros Alexopoulos
3. Reviewer: Professor Panos A. Razis
4. Reviewer: Associate Professor Nikolas Vlachos
5. Reviewer: Associate Professor Fotios Ptohos
6. Reviewer: Assistant Professor Dimitrios Sampsonidis
7. Reviewer: Lecturer Konstantinos Kordas

Day of the defense: 22/06/2012

Signature from head of PhD committee:

Abstract

This PhD thesis has taken up various aspects in experimental particle physics by analyzing the first data of the ATLAS detector. The main subject of the thesis is the production cross section measurement of the ZZ process at $\sqrt{s} = 7$ TeV of proton-proton collisions. In order to study this, the author has contributed to various topics, such as detector related issues, the study of standard candle processes and Monte Carlo studies.

In specific, this thesis presents a detailed study for the improvement of the hit position and peaking time resolution of the CSCs with 0.6% and 0.4% relative errors respectively.

This thesis has also contributed to the first Z inclusive cross section measurement at $\sqrt{s} = 7$ TeV, by analyzing the first 316 nb^{-1} of data recorded by the ATLAS detector. The $Z \to \ell\ell$ cross section measurement is used as a standard candle for detector performance assessment as well as for the tuning of theoretical predictions at the new energy regime. The fiducial and total cross sections have been found to be:

$$\sigma^{\text{fid}}_{Z\to ee} = 0.33 \pm 0.04(\text{stat}) \pm 0.03\ (\text{syst})\ \pm 0.04\ (\text{lumi})\ \text{nb}$$
$$\sigma^{\text{tot}}_{Z} = 0.75 \pm 0.09\ (\text{stat})\ \pm 0.08\ (\text{syst})\ \pm 0.08\ (\text{lumi})\ \text{nb}.$$

and are in agreement with the Standard Model NNLO predictions of 0.96±0.05 nb.

This thesis studies the $ZZ \to 4\ell$ process and completes the analysis with the first 1 fb^{-1}. The fiducial and total cross section were determined to be:

$$\begin{aligned}\sigma^{\text{fid}}_{ZZ\to\ell^+\ell^-\ell^+\ell^-} &= 19.4^{+6.3}_{-5.2}\ \text{(stat)}^{+0.9}_{-0.7}\ \text{(syst)}\ ^{+0.9}_{-0.6}\ \text{(lumi) fb} \\ \sigma^{\text{tot}}_{ZZ} &= 8.5^{+2.7}_{-2.3}\ \text{(stat)}\ ^{+0.4}_{-0.3}\ \text{(syst)}\ \pm 0.3\ \text{(lumi) pb.}\end{aligned}$$

and are statistically consistent with the SM NLO total cross section of $6.5^{+0.3}_{-0.2}$ pb.

Finally, the current thesis seacrhes for doubly charged Higgs bosons and the Randal-Sundrum Graviton in the same final states as in the $ZZ \to 4\ell$ analysis. In the former, an upper limit on the fiducial cross section of four lepton production has been set at 4.7 fb and in the graviton case, an upper limit on the production cross section of ZZ pairs from high mass resonances was established, within the fiducial region, at 0.92 pb. The observed and expected 95% C.L. lower limit on the mass of the graviton is $M_G > 575$ GeV.

Περίληψη

Το κυρίως θέμα του διδακτορικού αυτού είναι η μέτρηση της ενεργού διατομής της παραγωγής ζεύγους μποζονίων Z σε ενέργεια κέντρου μάζας $\sqrt{s} = 7$ TeV, αναλύοντας τα πρώτα δεδομένα του ATLAS. Για να επιτευχθεί αυτός ο στόχος, ο συγγραφέας έχει καταπιαστεί με διάφορα θέματα της πειραματικής φυσικής υψηλών ενεργειών. Πιο συγκεκριμένα, έχει ασχοληθεί με τεχνικά θέματα που αφορούν τον ίδιο τον ανιχνευτή, έχει μελετήσει τη διαδικασία του Καθιερωμένου Προτύπου που αποτελεί κλειδί στις μετέπειτα διερευνήσεις του και μελέτησε εξονυχιστικά Monte Carlo δείγματα για την κατανόηση τόσο της διαδικασίας που τον απασχολεί όσο και του υποβάθρου που την συνοδεύει.

Ο συγγραφέας συμμετείχε ενεργά στην ομάδα που είναι υπεύθυνη για την λειτουργία και απόδοση του ανιχνευτή 'Καθοδικοί Θαλάμοι Μικρολωρίδων', όπου και δούλεψε για τη βελτίωση της μέτρησης της θέσης των μιονίων και του χρόνου ολίσθησης των ηλεκτρονίων αναλύοντας δεδομένα από τον LHC.

Ως ενεργό μέλος της ομάδας του ATLAS που μελετά τις διαδικασίες του Καθιερωμένου Προτύπου συμμετείχε σε διάφορες αναλύσεις. Μια από τις πιο κύριες ήταν η μέτρηση της ενεργού διατομής της παραγωγής Z μποζονίων αναλύοντας τα πρώτα δεδομένα που είχαν καταγραφεί από το πείραμα ATLAS, μέτρηση η οποία πραγματοποιόταν για πρώτη φορά σε $\sqrt{s} = 7$ TeV. Η μελέτη της διαδικασίας αυτής αποτελούσε καίριο σημείο για τις μελέτες που θα έπονταν για τη μέτρηση της ενεργού διατομής ζεύγους Z μποζονίων.

Ο συγγραφέας κατά τη διάρκεια του διδακτορικού του συμμετείχε σε όλες τις φάσεις της μελέτης του ζεύγους Z μποζονίων, ξεκινώντας από μελέτες σε Monte Carlo μέχρι και την τελευταία δημοσίευση. Κατα τη διάρκεια των μελετών σε Monte Carlo επίπεδο, ανέπτυξε αλγόριθμο για την ανίχνευση ZZ μποζονίων διαμέσου των διασπάσεων τους σε τέσσερα λεπτόνια, $ZZ \to \ell\ell\ell'\ell'$,

και βελτιστοποίησε τα κριτήρια επιλογής για την καλύτερη ανάδειξη της διαδικασίας αυτής. Με την καταγραφή του 1 fb^{-1} δεδομένων από τον Ατλας, ήταν πλέον δυνατή η μελέτη της διαδικασίας αυτης σε επίπεδο πραγματικών δεδομένων. Στις μελέτες αυτές διαδραμάτησε σημαντικό ρόλο όπου και έφερε εις πέρας τις ακόλουθες υποχρεώσεις: Βελτιστοποίησε τα κριτήρια επιλογής της ανάλυσης, μελέτησε και εξήγησε τις διαφορές που παρατηρούνταν μεταξύ δεδομένων και Monte Carlo στις κατανομές της αναλλοίωτης μάζας των διαδικασιών $Z \to ee/\mu\mu$, μελέτησε τα συστηματικά σφάλματα που επηρεάζουν τη μέτρηση της ενεργού διατομής, μελέτησε το υπόβαθρο της διαδικασίας και τέλος μέτρησε την ενεργό διατομή. Αρκετά από τα κομμάτια του διδακτορικού αυτού είναι καίριας σημασίας για την ανάλυση που ακολούθησε στο ZZ κανάλι χρησιμοποιώντας όλη τη διαθέσιμη στατιστική του 2011, όπως επίσης κάποια άλλα κομμάτια θα μπορούσαν να χρησιμοποιηθούν σε τελικές καταστάσεις με τέσσερα λεπτόνια γενικότερα.

Επιπρόσθετα, ο συγγραφέας συμμετείχε στις έρευνες για γκραβιτόνιο και διπλά φορτισμένα μποζόνια Higgs μέσω των διασπάσεων τους σε τέσσερα λεπτόνια. Οι μελέτες αυτές βασίστηκαν στην ανάλυση της διαδικασίας $ZZ \to 4\ell$, καθώς μοιράζονται τις ίδιες τελικές καταστάσεις. Τα αποτελέσματα αυτών των ερευνών συζητούνται επίσης στο διδακτορικό αυτό.

στην αγαπημένη μου γυναίκα, Μόνικα
στην κόρη μας, Οριάνα

Acknowledgements

There are so many people to whom I owe a great thank you!

Dear Professor Chara Petridou! I still remember our first appointment four years ago, entering the seminar room and getting prepared for the usual presentation-interview, in order to join the PhD program offered by the Physics department. That was the moment I first observed the intimacy towards your students as well as your unique way of approaching them. Your friendliness and gentle character helped me quickly adapt in the AUTh group. You were always willing to provide answers to my numerous questions and spend hours explaining physics aspects to me. Your excellent guidance played a crucial part towards my incorporation in the Standard Model Working Group of ATLAS. Your strongly driven personality and fearless attitude towards work along with your active participation in the ongoing searces for new discoveries in your field constitute an endless source of inspiration for the students and the people around you. I will never forget how much you supported and encouraged me in the Summer of 2011, working day and night in your office at CERN for the publication of the first ZZ paper of the ATLAS experiment. You will always be my mentor! Thank you for everything.

Assistant Professor Dimos Sapmsonidis. I would like to thank you for showing trust in me during my start up as a PhD student. Working with you, I learned to be patient and calm. Your attitude towards life taught me how to be a real gentleman. The beautiful moments spent with your family will always have their place in my heart.

Lecturer Kostas Kordas. Two years working with you were more than enough to understand how much trustworthy and hard working person you are. Your advices during those years were invaluable. I was lucky to have your support in the tough years of my PhD. Always keeping good spirits, your sense of humour made the office atmosphere a lot more pleasant, giving us more strength and courage. I have never met a more cheerful person.

Dr Ven Polychronakos for the time devoted to me explaining me the Cathod Strip Chambers (CSCs) of the ATLAS detector and also for the fruitful discussions we had during group meetings. For sure I have learned a lot of interesting and important detector issues.

Dr Kostas Nikolopoulos for his willingness to help me in my first steps working for the CSCs. Of course, I will never forget the productive discussions in building 40 and your invitation to the Higgs Workshop held in Athens to present the results of the ZZ paper. Apart from work, I will keep the beautiful discussions during the coffee breaks at building 54 and the nights out. I am sure that I made a real friend whom I can count on.

Dr. Ilektra Christidi for all the help and support provided to me in the first year of my PhD. Sharing your knowledge on Particle Physics and $C++$ programming language topics provided me with the necessary information and tools needed in the upcoming years. I recall our outbreaks when sharing the office at building 54.

The people from the ZZ group and especially Dr Shih-Chieh Hsu for his leadership and guidance as well as for the effective discussions providing me with smart ideas and solutions for physics and programming.

Dr Daniel Whiteson for his invitation to join the Exotics paper.

Dr Dinos Bachas and Dr Christos Anastopoulos for their input in the start up of my PhD, especially concerning programming language issues.

Dr. Mohamed Acharouche for the constructive discussions during my participation in the Z inclusive publication.

My colleagues from University Yianni Nomidi (the cool), Dimitri Iliadi (the open-minded) and Vasiliki Kouskoura (the saint woman). Johnny thank you very much for your hospitality, our cohabitation was really enjoyable. I will always call to mind the beautiful discussions and the spontaneous music breaks, you really have a talent. Dimitris for the discussions on any hot topic during coffee breaks. Vaso for volunteering to work on any subject and helping the people around her.

Dr Zinonas Zinonos, my classmate during our Master studies, and his wife Louiza Zinonos for their great friendship and hospitality, the beautiful picnics and nights out.

My previous supervisor Professor Panos Razis for his recommendations to Professor Chara Petridou as well as Associate Professor Fotis Ptochos for his ability to trigger the young minds.

My parents George and Niove Petridis for their unconditional love and encouragement especially during hard times. Thank you very much for the economic support and trust in me during my studies. Ευχαριστώ πατέρα που με έσπρωξες να ξεκινήσω το διδακτορικό. Yiannoula Diomidous, my beloved grandmother, for her endless love and her economic support during the last year of my PhD! My sister Yiannoula Tziambazi and her husband Christos Tziambazis for the beautiful nights out at unique restaurants. Their five year old son Giorgos for taking me back to my childhood.

My friends outside CERN for their pure friendship: Dr Aris Kleanthous and Maria Kleanthous, Dimitris Christofidis and Eleni Andreou, Dr George Panayi and Vicky Panayi, Dr Yiannis Pantziaras and Dr Louiza Pantziara, Stefanos Sofroniou and Guste Sofroniou, and Stella Paphitou . You really are my closest friends and the people I can count on for life! Apologies if I sometimes exceeded the limits by talking too much about physics.

Finally, I would like to say a very big thank you to my beautiful wife Monika Petridou! I owe to you so many thanks, for your love, your encouragement, your caring, your forbearance listening to me talking about physics and your endurance these four years! You have been my private teacher, reading and correcting my PhD. Thank you once again for giving birth to our newborn child, the most excting time in my lifetime. Being with you makes me stronger. This PhD thesis is dedicated to you and to our newborn child!

Contents

List of Figures

List of Tables

Glossary

ALEPH	Apparatus for Lep Physics
ALICE	A Large Ion Collider Experiment
ASM	Amplifier Shaper Module
ATLAS	A Toroidal LHC Apparatus
CDF	Collider Detector at Fermilab
CERN	European Organization for Nuclear Research
CM	Center of Mass
CMS	Compact Muon Solenoid
CSC	Cathod Strip Chambers
DAQ	Data Acquisition
DELPHI	DEtector with Lepton, Photon and Hadron Identification
EM	ElectroMagnetic
FCal	Forward Calorimeter
HCAL	Hadronic Calorimeter
HLT	High Level Trigger
ID	Inner Detector
IP	Interaction Point
LArEM	Liquid Argon Electromagnetic Calorimeter
LEP	Large Electron Positron
LHC	Large Hadron Collider
LHCb	Large Hadron Collider beauty
LHCf	Large Hadron Collider forward
LO	Leading Order
L3	LEP Experiment
MC	Monte Carlo
MCFM	Monte Carlo for FeMtobarn processes
MDT	Muon Drift Chambers
MS	Muon Spectrometer
MWPC	MultiWire Proportional Chambers
NLO	Next to Leading Order
NNLO	Next to Next to Leading Order
OF	Opposite Flavor
OPAL	Omni-Purpose Apparatus for LEP
OS	Opposite Sign
pdf	Probability density function
PDF	Parton Distribution Function
PS	Proton Synchotron
QCD	Quantum ChromoDynamics
RFQ	Radio Frequency Quadrapole
ROB	Read Out Buffers
ROD	Read Out Drives
RoI	Region of Interest
RPC	Resistive Plate Chambers
RS Graviton	Randal-Sundrum Graviton
SCT	Semiconductor Tracker
SF	Same Flavor
SM	Standard Model
SPS	Super Proton Synchotron
SS	Same Sign
SUSY	SuperSymmetry
TGC	Thin Gap Chambers
TGCs	Triple Gauge Coupling
T&P	Tag and Probe
TOTEM	TOTal Elastic and diffractive cross section Measurement
TRT	Transition Radiation Tracker

..By opening Pandora's box you will see the word "Hope" written on the bottom ...

Chapter 1

Introduction

Particle physics came into prominence in the middle of the 20^{th} century with the successful construction of the Standard Model (SM) by Sheldon Glashow, Steven Weinberg and Abdus Salam. The SM is a relativistic quantum field theory providing the theoretical framework to describe the fundamental interactions of nature i.e the strong, the weak and the electromagnetic interactions. In 1960 Sheldon Glashow combined the electromagnetic and weak interactions into one (the electroweak interaction) and a few years later in 1967 Steven Weinberg and Abdus Salam incorporated the Higgs mechanism into Glashow's electroweak theory, in order to explain the spontaneous electroweak symmetry breaking and how the particles interact with the Higgs field acquiring their masses. The theory of the strong interactions, described by the Quantum Chromodynamics (QCD), has been built by various physicists and acquired its modern form around 1973-74, after the experiments confirmed that the hadrons were composed of quarks.

Through time, various experiments at LEP and TEVATRON performed extensive studies at different energy scales and precise measurements of the SM observables at the level of 0.1% have been achieved. The only puzzle piece still missing from this elegant theory is the Higgs particle. However, extensive searches carried out from the previous and current experiments provided strict boundaries regarding the Higgs mass.

Despite its many advantages, the SM also carries some disadvantages, making it an incomplete theory. Among others, SM does not describe gravity, it doesn't provide a unification of the three interactions as well as an answer to the hierarchy problem and it doesn't explain dark matter and the small mass of the neutrinos. Probable answers to these mysteries may be given by different models beyond the SM, like the grand unified theories (GUT), supersymmetry (SUSY), left-right symmetric models (LRSM), little higgses, extra dimensions e.t.c.

Nowadays, with the successful construction of the Large Hadron Collider (LHC) at the European Organization for Nuclear Physics (CERN), we physicists have the opportunity to perform even more accurate measurements of the SM (like the W boson mass and width, M_W and Γ_W, through the W boson decay distributions, the top quark mass, M_t, and $\sin^2\theta_{\rm W}$ via the Z forward backward asymmetry) and test its validity in the TeV region by measuring the production cross sections of the electroweak processes (W, Z etc.). Moreover, we can search for the "ghost" Higgs particle in the full mass range as well as for other new physics phenomena and particles predicted by a variety of physics models built through time.

The LHC is the world's largest circular hadron accelerator with the highest center of mass energy, located at the borders of Switzerland and France near Geneva. It has been designed to operate at $\sqrt{s} = 14$ TeV by accelerating two proton beams at the energy of 7 TeV each. The proton beams are programmed to collide at four different points across the ring, where the four big experiments ATLAS, CMS, LHC b and ALICE are installed. The first two experiments are general purpose detectors constructed to scrutinize a wide range of particle physics theories, while LHC b is dedicated to B physics measurements, the physics processes involving the $b-$ quark. LHC is also designed to accelerate heavy ion beams, $Pb - Pb$, and the ALICE detector is specialized to detect the products of these collisions.

Getting prepared for new discoveries at the LHC, the first goal of the experiments is the deep understanding of the detector and the validation of the electroweak sector by measuring the cross sections of different standard candle processes (like the Z inclusive production cross section), at the TeV energy scale. The current PhD thesis has studied detector performance issues, SM production cross sections with main emphasis on the ZZ process and contributed to the topic of exotic physics. A short description of the contributions of this thesis in the ATLAS experiment and particle physics in general, is presented below.

On detector aspects

This thesis reports the work done for the Cathode Strip Chambers (CSCs) of the ATLAS detector, a detection system dedicated to the muon identification and the precise measurement of their position and momenta in the forward region of the ATLAS detector. The CSCs are of great importance especially in the case of multilepton final states, like in the $ZZ \to 4\ell$ process, where at least one of the muons falls outside of the Innder Detector's (ID) acceptance and has a track in the Muon Spectrometer (MS). It has been shown that with the inclusion of these events in the $ZZ \to 4\mu$ studies a 10% increase in the signal yield can be achieved. In order to reduce background contribution because of high track activity in the forward region of the detector, the muon track position should be known with high accuracy (several tens of μm). A detailed study for improvement in the hit position and peaking time resolution for the CSCs is carried out in this thesis, with the resulting algorithm included in the ATLAS software.

On standard candle studies

This thesis contributed to the first production cross section measurement of the Z inclusive channel. The high rates expected in the proton-proton collisions allowed already with the first few hundreds nb^{-1} integrated luminosity to perform the first test of the SM at the TeV energy scale. The methodology towards a cross section measurement is presented. The systematic uncertainties affecting the cross section measurement and the data driven technique utilized to estimate the QCD background are discussed. In addition, this measurement as well as the lepton identification studies, paved the way to the next and main topic of this thesis, which is the cross section measurement of the ZZ production.

Studies on the $ZZ \to \ell\ell\ell'\ell'$ channel

The main part of this thesis is concentrated on the studies of the $ZZ \to 4\ell$ channel. The production of the ZZ dibosons is predicted by the electroweak sector and its production cross section measurement can provide an additional test of the SM in the new energy regime. Beyond this, the study of the $ZZ \to 4\ell$ channel is of great interest in the searches of the Higgs boson via the "golden" decay channel $H \to ZZ \to 4\ell$, since it is the irreducible background surrounding the Higgs candidate events. Thus, the measurement of the production cross section of the ZZ channel plays a crucial role in the background subtraction for the emergence of the Higgs boson. Monte Carlo studies using fully simulated ZZ candidates were originally analysed along the plans of ATLAS for Computing System Commissioning (CSC). The work on the reconstruction and identification efficiencies of leptons is presented and the expected signal kinematic distributions using different trigger chains and selection criteria are shown. Moreover, a detailed description on the procedure followed for the production cross section measurement of the $ZZ \to \ell\ell\ell'\ell'$ (where $\ell = e, \mu$) process at $\sqrt{s} = 7$ TeV is presented. The data-driven techinque used to estimate the background from data is also discussed.

Searches for New Physics

Through the four lepton final states the present thesis searched for heavy resonances like the Randal-Sundrum Graviton through the channel $G^* \to ZZ \to 4\ell$ and for doubly charged Higgs bosons via the decaying channel $H^{++}H^{--} \to \ell^+\ell^+\ell^-\ell^-$. Based on the selection criteria built for the ZZ analysis, the studies on these heavy resonances are presented as well as a full description of the methodology followed with the limit extraction in the production cross sections of these processes.

The structure of this thesis is as follows: Chapter 2 discusses the motivation behind the physics processes studied in this thesis. Chapter 3 introduces the accelerator complex at CERN and the basic parameters of the LHC are discussed. Chapter 4 introduces the ATLAS experiment, where the different sub-detectors and the magnet systems are discussed, while Chapter 5 is devoted to the improvements on resolution of the CSCs detector of the Muon Spectrometer. Chapter 6 reports the studies on the production cross section measurement of the Z inclusive channel with the first ATLAS data, while Chapter 7 provides the complete analysis for the ZZ cross section measurement at $\sqrt{s} = 7$ TeV. Chapter 8 examines the same final states with the previous one and has as its main subject the search for RS Graviton and doubly charged Higgs bosons. The summary of the thesis is given in Chapter 9.

..Do not forget the past...

Chapter 2

Motivation

This chapter discusses the motivation behind the physics processes studied in this thesis, including a brief theoretical overview of each process as well as the current state of the art, with results from previous experiments.

2.1 Z inclusive production

The measurement of the Z inclusive production cross section at hadron colliders constitutes an important test of the SM. The high rate in the production of Z bosons at the LHC [1], allows precise measurement of its cross section in a previously unexplored kinematic domain as well as studies in great detail of the kinematic properties of the leptons resulting from its decays. Therefore, the well known topologies of the Z leptonic decays helps us to understand the leptonic decays of the LHC collision data and the detector response to leptons. Different techniques can be employed for the calculation of the reconstruction and identification efficiencies of leptons or to perform in-situ calibrations for the detector energy and momentum scale.

On the cross section site, the theoretical calculations involve parton distribution functions (PDF). They are affected by significant higher-order QCD corrections. Calculations of the Z inclusive production cross section have been performed at next-to-leading order (NLO) [2; 3; 4] and next-to-next-to leading order (NNLO) in perturbation theory [5; 6; 7] by employing the programs FEWZ [7] and ZWPROD [6; 8] with the MSTW 08 NNLO [9] structure functions. This is found to be 0.99±0.05 nb.

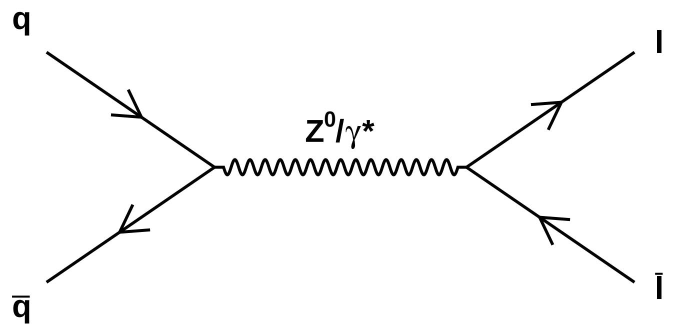

Figure 2.1: The leading order Z production mechanism.

The production mechanism of the Z boson proceeds via the $q\bar{q}$ annihilation, as shown in Figure 2.1.

The study of the Z leptonic decays was one of the first milestones in the ATLAS physics program for early LHC data [10]. Previous experiments at hadron colliders had also measured the Z production cross section at different center of mass energies, in specific UA1 [11] and UA2 [12] experiments at $\sqrt{s} = 0.63$ TeV at the CERN $Sp\bar{p}S$, followed by the CDF [13; 14; 15] and DØ [16; 17] experiments at $\sqrt{s} = 1.8$ TeV and $\sqrt{s} = 1.96$ TeV at the Fermilab TEVATRON proton-antiproton collider.

2.2 ZZ diboson production

The production of Z boson pairs at the LHC is of great interest, since it allows us to test the predictions of the electroweak sector at the TeV energy scale. Moreover, taking into account that a heavy Higgs boson ($>$ 130 GeV) will decay through the diboson channels WW and ZZ [18] (the WW decaying channel is the dominant one but the ZZ provides a cleaner signature via the four lepton channel) makes the study of these channels even more interesting, since they constitute the irreducible background in the discovery of the Higgs boson.

The ZZ production also provides a probe of new physics through the existence of neutral Triple Gauge Couplings (TGCs) [19]. According to the SM only the charged TGCs, such as WWZ and $WW\gamma$ are allowed at tree level, while the existence of neutral TGCs such as ZZZ and $ZZ\gamma$ is forbidden. Many models of physics beyond the SM predict values of nTGCs at the level of 10^{-4} to 10^{-3} [20]. The signature of non-zero

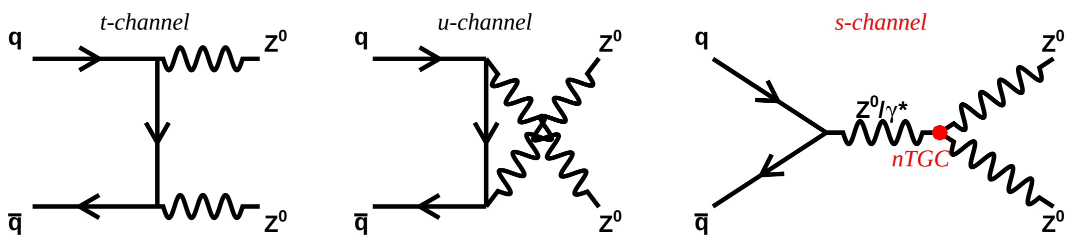

Figure 2.2: The SM tree-level Feynman diagrams for ZZ production through the $q\bar{q}$ initial state in hadron colliders. The s-channel diagram, on the right, contains the ZZZ neutral TGC vertex not existing in the SM.

nTGCs is an increase of the ZZ cross section at high ZZ invariant mass and high transverse momentum (see Section 4.1) of the Z bosons [21]. Another direct probe to new physics through the ZZ production channel is the search of a spin-0 radion [22] and excited states of a spin-2 Randal-Sundrum (RS) Graviton (G^*) [23; 24] resonances or ZZ production in supersymmetry [27]. In addition, other common signatures with four charged leptons in the final states, are the non SM doubly charged Higgses $H^{++}H^{--}$ [28; 29] predicted by the Left-Right Symmetric Model (LRSM) [30], or signatures produced from extra bosons (W', Z') [31], leptoquarks [32; 33] or technicolor particles [34]. Therefore, the detailed study and deep understanding of the ZZ production, especially in the first phase of LHC data-taking, is needed before any new discovery can be made.

At the LHC, the dominant ZZ production mechanism is from quark-antiquark ($q\bar{q}$) initial states, where the ZZ production proceeds at LO via $t-$channel and $u-$channel as shown in the left and middle Feynman diagrams of Figure 2.2. The diagram on the right corresponds to the s-channel and it is SM forbidden. Such kind of production mechanisms can exist only in the case of nTGCs.

The lowest order significant diagram for $pp \to Z/\gamma^* Z/\gamma^* \to \ell^+\ell^-\ell'^+\ell'^-$ in the SM, is shown in Figure 2.3 and corresponds to the experimentally cleanest ZZ signature, since it is the only SM process with four leptons in the final state.

The contribution from gluon-gluon (gg) fusion corresponds to NNLO corrections and proceeds via the quark box diagrams shown in Figure 2.4. Their impact to the ZZ production cross section at $\sqrt{s} = 7$ TeV ($\sqrt{s} = 14$ TeV) for $m_{4\ell} < 2M_Z$ is at the few percent level while for $m_{4\ell} > 2M_Z$ the contribution increases to $\sim$7% ($\sim$10%) [35; 36].

At $\sqrt{s} = 7$ TeV ($\sqrt{s} = 10$ TeV) the production cross section of $pp \to ZZ$ has been

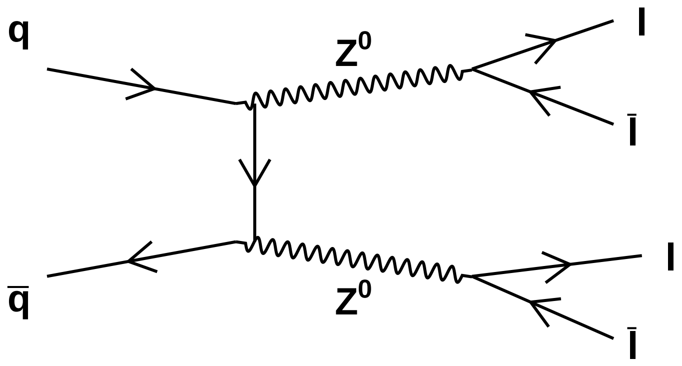

Figure 2.3: The SM tree-level Feynman diagrams for ZZ decaying to 4ℓ through the $q\bar{q}$ initial state in hadron colliders.

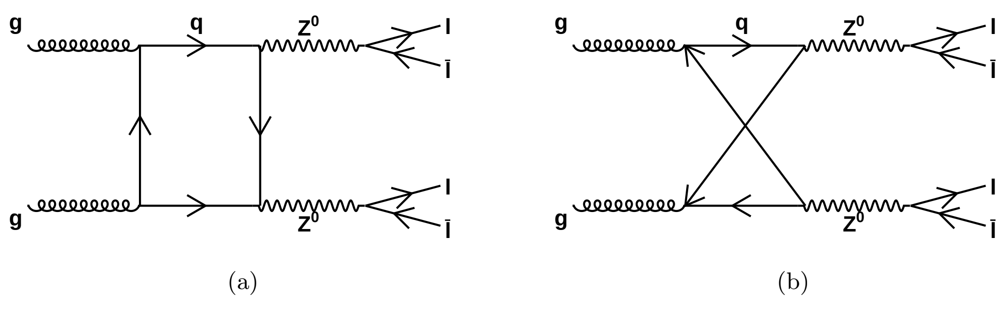

Figure 2.4: The next-to-next to leading order ZZ production mechanisms.

calculated at NLO with the MCFM [37] program to be $6.46^{+0.30}_{-0.21}$ pb [35] ($11.03^{+0.45}_{-0.32}$ pb [35]) using the MSTW2008 PDF [9]. Taking into account the branching fraction of Z decaying leptonically, $BR(Z \to \ell\ell) = 0.036$ [38], one can calculate the predicted cross section for $pp \to ZZ \to \ell^+\ell^-\ell'^+\ell'^-$ to be 7.29 fb for the $eeee$ and $\mu\mu\mu\mu$ channels, and 14.58 fb for the $ee\mu\mu$ channel. That is a total of 29.16 fb (45.88 fb) for all three channels, so approximately 29 (46) events in total are expected to be produced with an integrated luminosity of 1.0 fb^{-1}. However, because of limited geometric and kinematic acceptance, as well as lepton selection criteria, far fewer events are expected to be detected.

Z boson pair production was studied at Lep by the L3 [39], Opal [40], Aleph [41] and Delphi [42] collaborations in multiple final states, including $e^+e^- \to \ell\ell\ell\ell$. Lep experiments have also set limits on anomalous ZZZ and $ZZ\gamma$ couplings [43].

The Tevatron experiments have also looked for the pair production of Z bosons. The DØ analysis of $ZZ \to \ell^+\ell^-\ell'^+\ell'^-$ and $ZZ \to \ell^+\ell^-\nu\nu$ lepton production with 1.9 fb^{-1} of data has yielded a measurement of 1.60 ± 0.63 (stat.)$^{+0.16}_{-0.17}$ (sys.) pb on the ZZ production cross-section [44]. A more recent paper submitted for publication, using 6.4 fb^{-1} of data, has yielded a measurement of $1.40^{+0.43}_{-0.37}$ (stat.) $\pm$ 0.14 (sys.) pb [45]. Additionally, limits on anomalous ZZZ and $ZZ\gamma^*$ couplings have also been derived [46]. The Cdf experiment has used 1.9 fb^{-1} of data to look for Z pair production. The observed significance in combined $\ell^+\ell^-\ell'^+\ell'^-$ and $\ell^+\ell^-\nu\nu$ channels is 4.4σ, and the measured cross section is $\sigma_{ZZ} = 1.4^{+0.7}_{-0.6}$ (stat. + sys.) pb [47].

2.3 New physics searches with four leptons in the final state

The excelent performance of Lhc opened a new era in experimental particle physics and we physicists have the opportunity to study extensively various models beyond the SM. One common signature of phenomena beyond the SM is an enhanced production of events with many leptons which can be produced in a variety of new physics models, noted in Section 2.2. Such kind of processes could be the production of doubly charged Higgses [28; 29] or the production of a heavy ZZ diboson resonance.

Doubly charged Higgs appears in the LRSM [30], Higgs triplet models [48; 49] and little Higgs models [50]. Depending on the model, the doubly charged Higgs can be a

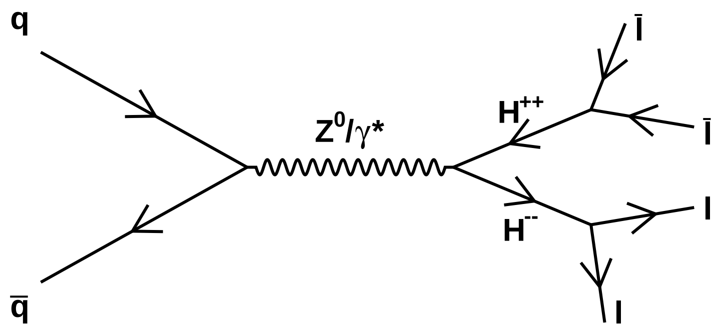

Figure 2.5: Feynman diagrams for pair production of doubly-charged Higgs bosons decaying to same-sign same-flavor lepton pairs, $H^{++}H^{--} \to \ell^{+}\ell^{+}\ell^{-}\ell^{-}$

member of a singlet, doublet or triplet symmetry group [29], each one corresponding to a different production cross section. The dominant production mechanism for $H^{\pm\pm}$ is Drell-Yan pair production through an $s-$channel by exchanging a photon or a Z boson. The corresponding Feynman diagram can be seen in Figure 2.5. $H^{\pm\pm}$ can be searched in final states with four or more isolated leptons that have same-sign (SS) same-flavor (SF) or opposite flavor (OF) pairs [28] falling inside the Z mass window $66 < M_{\ell\ell} < 116$ GeV. According to the SM expectations, the contribution of $ZZ \to 4\ell$ candidates outside that mass region is very small, so such observations could be a direct indication of new physics.

CDF experiment searched for doubly charged Higgs bosons decaying to dileptons by analyzing 240 pb^{-1} of data and they didn't observe any evidence for $H^{\pm\pm}H^{\pm\pm}$

Direct searches from the experiments at LEP have excluded doubly charged Higgs bosons below masses 100 GeV/c^2 [51], assuming exclusive $H^{\pm\pm}$ decay to a given dilepton channel. DØ experiment at TEVATRON also searched for $H^{\pm\pm}H^{\pm\pm}$, by assuming 100% branching in the dacaying of $\mu^{+}\mu^{+}\mu^{-}\mu^{-}$, and excluded a $H_L^{\pm\pm}$ below a mass of 118 GeV/c^2 [52]. Moreover, CDF collaboration has further searched final states including also ee and $e\mu$ final states and excluded a $H_L^{\pm\pm}$ with mass smaller than 133 GeV/c^2 [53].

The existence of heavy ZZ diboson resonances are predicted from many SM extension models, for example warped extra dimensions [25; 26]. In the analysis appearing in this thesis, the ZZ resonance is modelled assuming a spin-2 RS G* [23; 24] with coupling $k/\bar{M}_{Pl} = 0.1$ (where k is the curvature scale of the extra dimension and

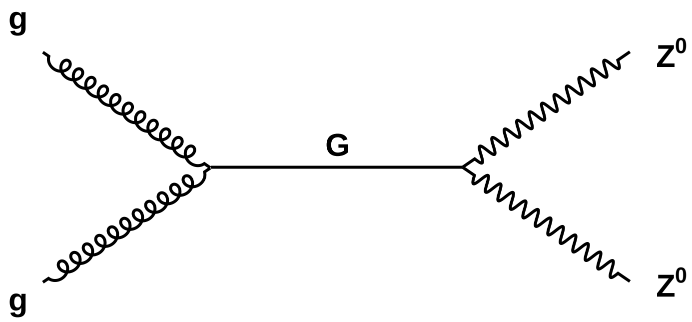

Figure 2.6: Feynman diagram for a Randal-Sundrum Graviton production decaying to opposite-sign same-flavor lepton pairs $ZZ \to \ell^+\ell^-\ell'^+\ell'^-$

$\bar{M}_{Pl} = M_{pl}/\sqrt{8\pi}$ is the reduced Planck scale) which is produced through gluon-gluon fusion. The leading order Feynman diagram is shown in Figure 2.6. The CDF experiment at TEVATRON searched for ZZ resonances using four lepton events and excluded such a resonance with mass less than 491 GeV [54] in data corresponding to $\mathcal{L}$ = 2.5-2.9 fb^{-1}. Recent studies at CDF reported an excess of four lepton events at 327 GeV by analyzing data corresponding to $\mathcal{L}$ = 6 fb^{-1}. This excess though, has not been confirmed in the $\ell\ell jj$ and $\ell\ell\nu\nu$ final states [55].

Bibliography

[1] L. Evans and P. Bryant, “LHC Machine”, JINST 3 (2008) S08001. 5

[2] J. Kubar and F. E. Paige, “Gluon Corrections to the Drell-Yan Model”, Phys. Rev. D19 (1979) 221. 5

[3] G. Altarelli, R. K. Ellis, and G. Martinelli, “Large Perturbative Corrections to the Drell-Yan Process in QCD”, Nucl. Phys. B157 (1979) 461. 5

[4] J. Kubar, M. Le Bellac, J. L. Meunier, and G. Plaut, “QCD Corrections to the Drell-Yan Mechanism and the Pion Structure Function”, Nucl. Phys. B175 (1980) 251. 5

[5] P. J. Rijken and W. L. van Neerven, “Order a_s^2 contributions to the Drell-Yan cross-section at fixed target energies”, Phys. Rev. D51 (1995) 44. 5

[6] R. Hamberg, W. L. van Neerven, and T. Matsuura, “A complete calculation of the order a_s^2 correction to the Drell-Yan K factor”, Nucl. Phys. B359 (1991) 343; Erratum-ibid. B644 (2002) 403. 5

[7] C. Anastasiou, L. J. Dixon, K. Melnikov, and F. Petriello, “High precision QCD at hadron colliders: Electroweak gauge boson rapidity distributions at NNLO”, Phys. Rev. D69 (2004) 094008. 5

[8] W. L. van Neerven, and E. B. Zijlstra, “The $O\ (a_s^2)$ corrected Drell-Yan K factor in the DIS and MS scheme”, Nucl. Phys. B382 (1992) 11; Erratum-ibid. B680 (2004) 513. 5

[9] A.D. Martin, W.J. Stirling, R.S. Thorne, G. Watt, “Parton distributions for the LHC”, Eur.Phys.J.C63:189-285,2009. 5, 9

[10] The ATLAS Collaboration,"Measurement of the $W \to \ell\nu$ and $Z\gamma^* \to \ell\ell$ production cross sections in proton-proton collsions at $\sqrt{s} = 7$ TeV with the ATLAS detector", JHEP 1012 (2010) 060. 6

[11] The UA1 Collaboration, C. Albajar et al., "Intermediate Vector Boson Cross-sections at the CERN Super Proton Synchrotron Collider and the Number of Neutrino Types", Phys. Lett. B198 (1987) 271. 6

[12] The UA2 Collaboration, J. Alitti et al., "A Measurement of the W and Z Production Cross-sections and a Determination of Γ_W at the CERN $\bar{p}p$ collider", Phys. Lett. B276 (1992) 365. 6

[13] CDF Collaboration, F. Abe et al., "Measurement of $\sigma \cdot B(W \to e\nu)$ and $\sigma \cdot B(Z^0 \to e^+e^-)$ in $p\bar{p}$ collisions at $\sqrt{s} = 1.8$ TeV", Phys. Rev. Lett. 76 (1996) 3070. 6

[14] CDF Collaboration, F. Abe et al., "Measurement of Z^0 and Drell-Yan production cross section using dimuons in $p\bar{p}$ collisions at $\sqrt{s} = 1.8$ TeV", Phys. Rev. D59 (1999) 052002. 6

[15] CDF Collaboration, A. Abulencia et al., "Measurements of Inclusive W and Z Cross-sections in $p\bar{p}$ collisions at $\sqrt{s} = 1.96$ TeV", J. Phys. G34 (2007) 2457. 6

[16] The D0 Collaboration, B. Abbott et al., "Extraction of the width of the W boson from measurements of $\sigma(p\bar{p} \to W + X) \times B(W \to e\nu)$ and $\sigma(p\bar{p} \to Z + X) \times B(Z \to ee)$ and their ratio", Phys. Rev. D61 (2000) 072001. 6

[17] The D0 Collaboration, D0 conference notes: 4403-CONF, 4750-CONF. 6

[18] Julien Baglio, Abdelhak Djouadi, "Higgs production at the LHC", JHEP 1103:055,2011. 6

[19] G. J. Gounaris, J. Layssac, and F. M. Renard, "New and standard physics contributions to anomalous Z and γ self-couplings", Phys. Rev. D 62, 073013 (2000). 6

[20] J. Ellison and J. Wudka, "Study of trilinear gauge-boson couplings at the Tevatron collider", Annu. Rev. Nucl. Part. Sci. 48, 33 (1998). 6

[21] U. Baur and D. L. Rainwater, "Probing neutral gauge boson self-interactions in ZZ production at hadron colliders", Phys. Rev. D 62, 113011 (2000). 7

[22] , P. K. Das, "Neutral Z boson pair production due to radion resonance in the Randal-Sundrum model: prospects at the CERN LHC", Phys.Rev. D72 (2005) 055009. 7

[23] L. Randall and R. Sundrum, "Large Mass Hierarchy from a Small Extra Dimension", Phys. Rev. Lett. 83 (1999) 3370. 7, 10

[24] L. Randall and R. Sundrum, "An Alternative to Compactification", Phys. Rev. Lett. 83 (1999) 4690. 7, 10

[25] P. Osland, A. A. Pankov, A. V. Tsytrinov, N. Paver, "Signals of Warped Extra Dimensions at the LHC", AIP Conf.Proc.1317:201-208,2011. 10

[26] H. Davoudiasl, J.L. Hewett, T.G. Rizzo, "Experimental Probes of Localized Gravity: On and Off the Wall", Phys.Rev.D63:075004,2001. 10

[27] S. Martin, "A supersymmetry primer", arXiv:hep-ph/9709356v6. 7

[28] T. Rizzo, "Doubly charged Higgs bosons and lepton-number-violating processes", Phys. Rev. D25 (1982) 1355; addendum ibid 27 (1983) 657. 7, 9, 10

[29] V. Rentala, W. Shepherd and S. Su, "A Simplified Model Approach to Same-sign Dilepton Resonances", Phys. Rev. D85 (2011) 35004. 7, 9, 10

[30] J. C. Pati and A. Salam, Phys. Rev D 10, 275 (1974); R. N. Mohapatra and J. C. Pati, Phys. Rev. D 11, 566, 2558 (1975); G. Senjanovich and R. N. Mohapatra, Phys. Rev. D 12, 1502 (1975); R. N. Mohapatra and R. E. Marshak, Phys. Lett. B 91, 202 (1980); R. N. Mohapatra and D. Sidhu, Phys. Rev. Lett. 38, 667 (1977); K. Huitu and J. Maalampi, Phys. Lett. B 344, 217 (1995) 217-224. 7, 9

[31] P. Langacker, "The physics of heavy Z' gauge bosons", Rev. Mod. Phys. 81 (2009) 1199. 7

[32] H. Harari, "A schematic model of quarks and leptons", Phys. Lett. B86 (1979) 83. 7

[33] B. Schrempp and F. Schrempp, “Light leptoquarks”, Phys. Lett. B153 (1985) 101. 7

[34] E. Eichten and K. Lane, “Dynamical breaking of weak interaction symmetries”, Phys. Lett. B90 (1980) 125. 7

[35] J. Campbell, K. Ellis, and C. Williams, “Vector Boson Pair Production at the LHC”, JHEP 1107:018,2011. 7, 9

[36] S. Dawson et all., “Higgs Working Group Summary Report”, arXiv:0803.1154v1 [hep-ph]. 7

[37] J. M. Campbell, R. K. Ellis, “MCFM for the Tavatron and the LHC”, Nucl.Phys.Proc.Suppl.205-206:10-15, 2010. 9

[38] K. Nakamura et al. (Particle Data Group), “Review of particle physics”, J. Phys. G 37, 075021 (2010). 9

[39] L3 Collaboration, M. Acciarri et al., “Study of Z Boson Pair Production in e^+e^- collisions at LEP at $S^{(1/2)}$ = 189-GeV”, Phys.Lett.B465:363-375,1999. 9

[40] OPAL Collaboration, G. Abbiendi et al., “Study of Z pair production and anomalous couplings in e+ e- collisions at s**(1/2) between 190-GeV and 209-GeV”, Eur.Phys.J.C32:303-322,2003. 9

[41] ALEPH Collaboration, R. Barate et al., “Measurement of the e+ e- $\rightarrow$ Z Z production cross section at centre-of-mass energies of 183-GeV and 189-GeV”, Phys.Lett.B469:287-302,1999. 9

[42] DELPHI Collaboration, J. Abdallah et al., “ZZ production in e+ e- interactions at $\sqrt{s}$ = 183 GeV to 209 GeV”, Eur.Phys.J.C30:447-466,2003. 9

[43] P. Spagnolo, “Boson Gauge Couplings at LEP”, arXiv:hep-ex/0506048v1. 9

[44] D0 Collaboration, V. Abazov et al., “Observation of ZZ production in $p\bar{p}$ collisions at $\sqrt{s}$ = 1.96 TeV”, Phys.Rev.Lett.101:171803,2008. 9

[45] D0 Collaboration, V. M. Abazov et al., “Measurement of the ZZ production cross section in $p\bar{b}$ collisions at $\sqrt{s}$=1.96 TeV”, Phys.Rev.D84:011103,2011. 9

[46] D0 Collaboration, V. M. Abazov et al., “Search for ZZ and $Z\gamma^*$ production in $p\bar{p}$ collisions at $\sqrt{s} = 1.96$ TeV and limits on anomalous ZZZ and $ZZ\gamma^*$ couplings”, Phys.Rev.Lett.100:131801,2008. 9

[47] CDF Collaboration, T. Aaltonen et al., “First Measurement of ZZ Production in $p\bar{p}$ collisions at $\sqrt{s}$=1.96 TeV”, Phys.Rev.Lett.100:201801,2008. 9

[48] T. Han, H. E. Logan, B. Mukhopadhyaya and R. Srikanth, “Neutrino masses and lepton-number violation in the Littlest Higgs scenario”, Phys. Rev. D 72, 053007 (2005). 9

[49] J. Y. Lee, “Neutrino Masses in the Composite Little Higgs Model”, JHEP 0506, 060 (2005). 9

[50] N. Arkani-Hamed, A. G. Cohen and H. Georgi, “Electroweak symmetry breaking from dimensional deconstruction”, Phys. Lett. B 513, 232 (2001). 9

[51] DELPHI Collaboration, J. Abdallah et al., Phys. Lett. B552, 127 (2003); OPAL Collaboration, G. Abbiendi et al., Phys. Lett. B526, 221 (2002); L3 Collaboration, P. Achard el al., Phys. Lett. B576, 18 (2003). 10

[52] D0 Collaboration, V.M.Abazov, et al, “Search for Doubly-charged Higgs Boson Pair Production in the Decay to $\mu^+\mu^+\mu^-mu^-$ in $p\bar{p}$ Collisions”, Phys.Rev.Lett.93:141801,2004. 10

[53] CDF Collaboration, D. Acosta, et al, “Search for Doubly-Charged Higgs Bosons Decaying to Dileptons in $p\bar{p}$ Collisions at $\sqrt{s}$=1.96 TeV”, Phys.Rev.Lett.93:221802,2004. 10

[54] CDF Collaboration, T. Aaltonen et al., “Search for new heavy particles decaying to $ZZ \to \ell\ell\ell\ell, \ell\ell jj$ in $p\bar{p}$ collissions at $\sqrt{s} = 1.96$ TeV”, Phys. Rev. D83 (2011) 112008. 11

[55] CDF Collaboration, “Search for high-mass ZZ resonances”, CDF/PUB/EXOTICS/PUBLIC/10603 (2011). 11

..To approach the time of the Big Bang one needs tools
... big tools ..

Chapter 3

The Large Hadron Collider

3.1 Introduction

The Large Hadron Collider (LHC) [1] is the new circular accelerator, constructed by the European Organization for Nuclear Research (CERN) and installed in LEP's[1] existing tunnel. The LHC is the world's largest and highest-energy particle accelerator, designed to operate at $\sqrt{s} = 14$ TeV and with peak luminosity $\mathcal{L} = 10^{34}$ cm$^{-2}\cdot$ s^{-1}. The LHC circumference is ∼27 km and the tunnel where is settled is buried around 50 m to 175 m under the ground surface, located at the Franco-Swiss boarders near Geneva.

The discovery of new phenomena, presupposes the usage of wavelengths, λ, smaller than the size r of the object that one is searching for. In the case of the SM, the distance scale is defined from the Higgs boson mass limit $u > 114$ GeV set by the experiments at LEP [2]. In natural units, the corresponding distance is of the order of $d = \hbar c/u \sim 10^{-19}$ m $= 0.0001$ fm. Thus, the LHC operates in the TeV energy regime where the transformed distance is of that order.

3.2 Protons' journey and LHC designed parameters

Protons are extracted from a bottle of hydrogen gas and are then accelerated to 90 keV by a radio frequency quadrapole (RFQ[2]) which acts as an accelerator and proton

[1] Large Electron Positron collider (LEP), as the name suggests was colliding electron and positron beams at a $\sqrt{s} \approx 90$ GeV in the initial phase and 209 GeV in the last data taking period. It was the main accelerator at CERN from 1989 - 2000.

[2] Radio frequency quadrapole is a linear accelerator component used to accelerate (∼50 keV to ∼3 MeV) and focus particle beams.

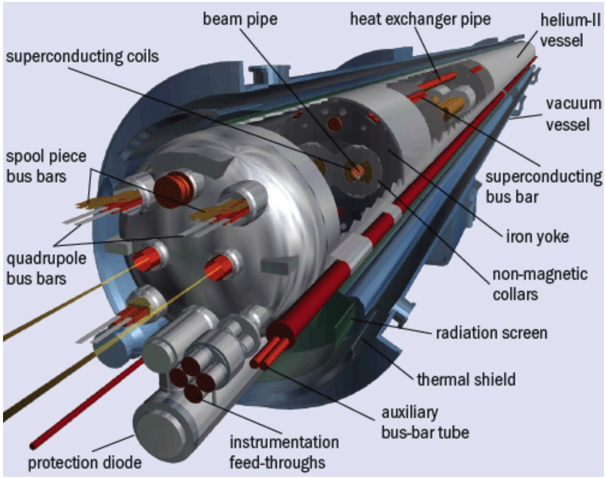

Figure 3.1: A superconducting dipole magnet of the LHC.

concentrator. The protons are then sent to a linear accelerator, called LINAC2, where they speed up to 50 MeV. Next, protons are injected to the Proton Synchotron Booster, which boosts them to 1.4 GeV. Afterwards, the protons are inserted in another circular accelerator, called Proton Synchotron (PS) , where they reach the energy of 25 GeV. The beam is then sent to the Super Proton Synchotron (SPS) where it is accelerated up to 450 GeV. In the last stage, the proton bunches are fed to the LHC where they are accelerated for 20 minutes until they can reach in the future phase of LHC the nominal beam energy of 7 TeV.

In specific, LHC has two storage rings where it accelerates two independent beams, one moving clockwise and one anticlockwise. Each beam is made up of 2808 bunches with $1.15{\times}10^{11}$ protons each. The bunches travel at almost the speed of light, with frequency equal to $f = 11.245$ kHz, so the period is $T = 1/f \approx 9{\cdot}10^{-5}$ s. The distance between two consecutive bunches is 7.5 m, so keeping in mind that protons travel at almost the speed of light, one can easily calculate that the collisions will happen every 24.95 ns. Besides the proton - proton collisions, LHC is scheduled to also accelerate heavy ion (Pb-208) beams at an energy of 575 TeV, which corresponds to 2.76 TeV per nucleon.

Another important and challenging characteristic of the LHC are the magnet dipoles (see Figure 3.1) which require opposite fields in order to collide two beams of equally charged particles. Thus the LHC is designed with separate magnet fields and vacuum

Parameter	Value
Circumference	26659 m
Energy	7 TeV
Dipole's temperature	1.9 K
Dipole field B	8.33 T
Bunch spacing s	25 ns
Number of bunches per beam	2808
Bunch radius $\sigma_x = \sigma_y$	16 μm
Bunch length σ_s	75 mm
Bunch population N	1.15×10^{11} protons
Collision time interval	24.95 ns

Table 3.1: LHC parameters.

chambers in the main arcs and common sections, in average 130 m long, in the interaction regions (IR) where the four exepriments are located [1]. To avoid parasitic collision points inside the common beam pipe, the two beams have been designed to collide with a sufficiently large crossing angle (θ_c) which negatively affects the achievement of the peak luminosity (see Section 3.3). In specific, the LHC uses twin bore magnets consisting of two sets of coils and beam channels within the same mechanical structure and cryostat. The superconducting dipole magnets are 1232 in total and are cooled down to 1.9 K, under the influence of liquid helium, where they operate reliably at a nominal magnetic field of 8.33 T. Moreover, LHC utilizes another 858 quadrapole magnets mandatory for beam focusing, so that the beams are constrained in the vacuum chambers and the greatest possible number of collisions occurs. A list with the basic parameters of the LHC can be found in Table 3.1.

3.3 LHC luminosity

Apart from the center of mass energy, another important parameter of the LHC is the luninosity, $\mathcal{L}$, which by assuming equal beam parameters for both circulating beams is given by the equation:

$$\mathcal{L} = \frac{N_b^2 n_b f_{rev} \gamma_r}{4\pi \varepsilon_n \beta^*} F \tag{3.1}$$

where N_b is the proton population in each bunch and it is equal to $N_b = 1.15 \times 10^{11}$. n_b represents the number of bunches per beam and its design value in the high luminosity environment will be equal to 2808. f_{rev} is the revolution frequency, which alternatively is the rate of collisions and is equal to $1/24.95 \approx 40$ MHz and γ_r is the relativistic gamma factor.

The beam size is demonstrated as a function of the normalized transverse beam emittance, ε_n, and the amplitude function at the collision point, β^*. The emittance, ε, is defined as the volume occupied by the beam in the trace space, whereas the transverse emittance refers to the occupied area in the $x - y$ plane. It has units of length and is determined by the initial conditions during the injection (bunch preparation) from SPS to LHC. As the momentum of protons increases during acceleration, their longitudinal momentum is increased and their transverse momentum remains the same, hence the beam divergence decreases, maximizing the number of collisions per bunch crossing. Therefore, by accelerating the beam leads to a reduction of the occupied area in phase space which is proportional to the increase of the relativistic gamma. Based on this correlation, it is convenient to define the normalised transverse emittance which is the transverse emittance multiplied by the relativistic γ factor ($\varepsilon_n = \gamma\varepsilon_T$) and it is constant under acceleration.

The amplitude function, β, is determined by the focusing of the quadrupole magnets of the accelerator and its value varies along the accelerator. It can be expressed in terms of the cross sectional size of the bunch, $\sigma^2 = \sigma_x\sigma_y$, and the normalized transverse emittance, $\beta = \pi\sigma^2/\varepsilon$. The smaller the β value the narrower the beam is. At the peak luminosity of the LHC, the corresponding values of β^* and ε_n are 0.55m and 3.75μm respectively. The value given for the β^* parameter corresponds to the distance between the interaction point (focus point) and the point where the beam width is twice as wide as the focus point.

F is the geometric luminosity reduction factor due to the crossing angle at the IP and it is given by the equation:

$$F = \frac{1}{\sqrt{1 + (\frac{\theta_c\sigma_z}{2\sigma^*})^2}} \tag{3.2}$$

where θ_c is the full crossing angle at the IP, σ_z the RMS bunch length and σ^* the transverse RMS beam size at the IP.

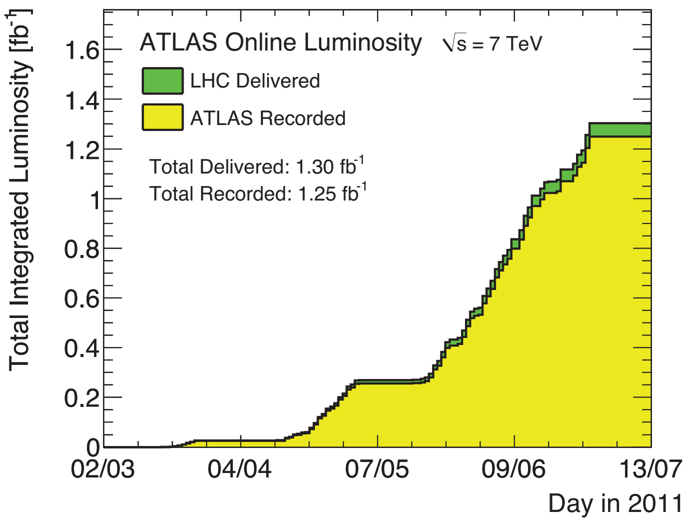

Figure 3.2: Cumulative luminosity versus day delivered to (green), and recorded by ATLAS (yellow) during stable beams and for pp collisions at $\sqrt{s}$ =7 TeV until July 2011.

The above values correspond to the design luminosity of the LHC, $\mathcal{L} \approx 10^{34}$ cm^{-2}s^{-1}. However, in the first two years of its operation, the luminosity has been set to one order of magnitude smaller than the designated one $\mathcal{L} \approx 10^{33}$ cm^{-2}s^{-1}, the so called "low luminosity period", whereas the center of mass energy has been fixed to $\sqrt{s} = 7$ TeV. The total delivered luminosity from LHC and the recorded one from the ATLAS experiment is shown in Figure 3.2.

Following a two-year pause for upgrades commencing in 2013, the LHC will start operating at its designated values, the so called "high luminosity period".

The number of produced events for a given process, N, is proportional to the integrated luminosity and the cross section characterizing the specific process and it is given by the equation:

$$N = \mathcal{L}\sigma \tag{3.3}$$

It implies that the higher the luminosity, the easier it is to observe rare decays which are characterized by small cross sections. Figure 3.3 shows the cross sections of various physics processes as a function of the center of mass energy.

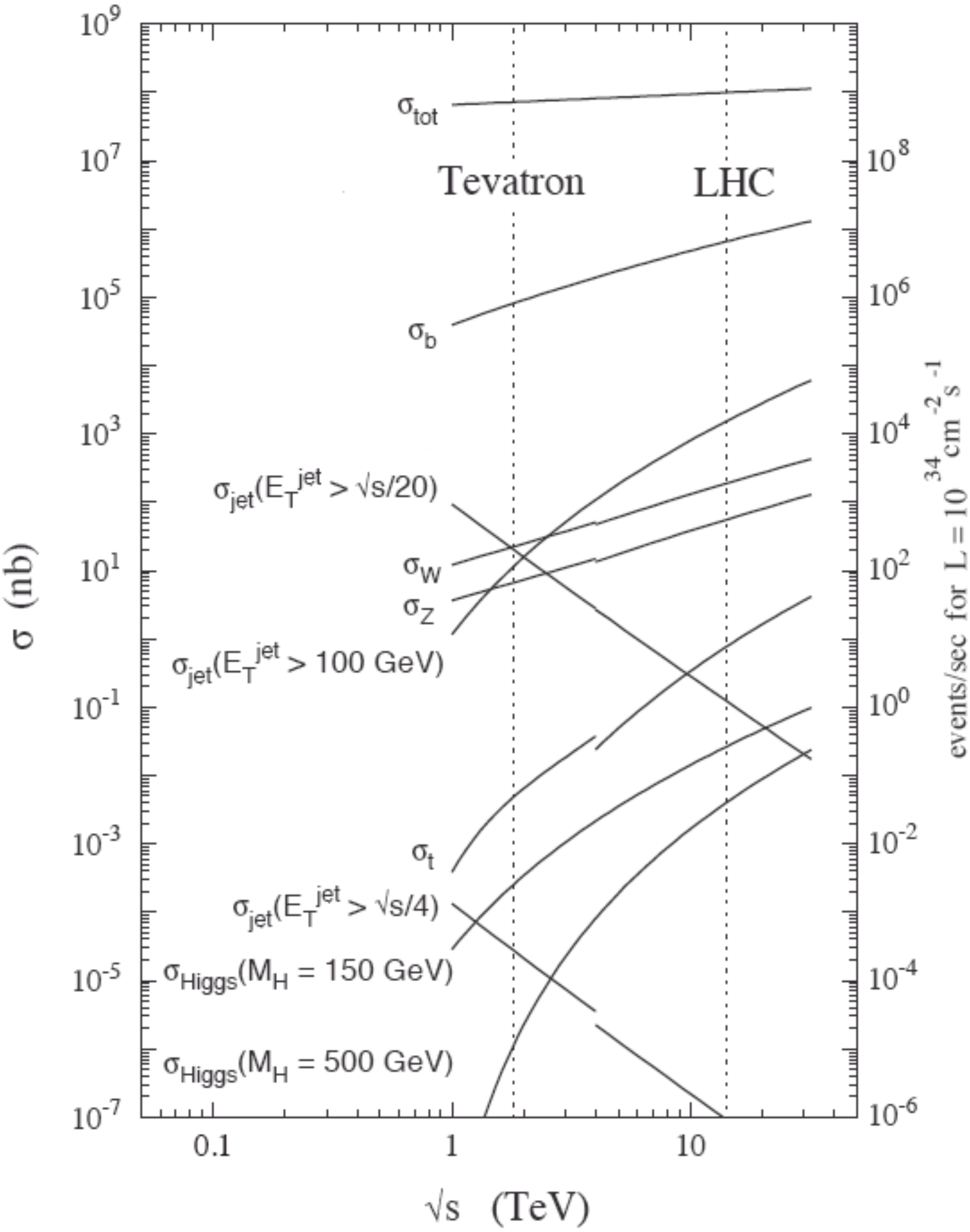

Figure 3.3: Cross sections for various physics processes. The dotted lines show the center of mass energy for Tevatron (at 1.96 TeV) and LHC (at 14 TeV).

3.3.1 Performance limitations

In order to achieve the desirable luminosity at the LHC, scientists must prevent the following effects limiting the performance of the machine:

- **Beam-Beam limit**: The protons' density per bunch is limited by the nonlinear beam-beam interaction when the beams collide in the interaction regions. The beam-beam interaction is quantified by the linear tune shift $\xi = \frac{N_{bunch} r_p}{4\pi\varepsilon_n}$, with r_p being the proton radius. The total linear tune shift must be confined to less than 0.005 in each experiment.

- **Pile-up effect**: Each time two bunches of protons collide, a different number of interactions between protons occurs, depending on the intensity of the bunches. For physics analysis only the most energetic vertex is considered and is called "primary vertex". An example of an event with twenty reconstructed vertices is shown in Figure 3.4.

- **Mechanical aperture**: According to the maximum acceptable transverse beam emittance, which is determined from the beam screen size[1], and the limit on the linear beam-beam tune shift, the mechanical aperture of the LHC limits the maximum bunch intensity to $N_{bunch} = 1.15 \times 10^{11}$ protons. Moreover, the quadrupole magnets limit the minimum attainable β^* value at the IP and the maximum attainable crossing angle orbit bump in the experimental interaction regions, resulting in limitation on the peak luminosity at the LHC.

- **Maximum dipole field and Magnet quench limits**: Beam losses due to the non-homogeneous heat load and temperature margins inside the cryo-magnets.

- **Energy stored in the circulating beams and in the magnetic fields**: The energy stored by the circulating beams and the magnet system must be absorbed safely at the end of each run or in the case of an emergency, but the imperfections of the beam dumping system and the magnet system provide additional limits in the maximum attainable beam energies and intensities.

[1]The horizontal and vertical apertures are 44.04 mm and 34.28 mm, respectively.

- **Heat load**: The heat load to the cryogenic system from the synchotron radiation and the heat deposition induced from luminosity losses limit the maximum attainable beam intensities.
- **Field quality and dynamic aperture**: Beam losses can also be produced due to field quality errors which spoil the protons' stability in the storage ring.
- **Collective beam instabilities**: The electromagnetic interactions of the charged particles in each beam as well as their interactions with the conducting boundaries of the vacuum system have as a result the instability of the beam.

3.3.2 Luminosity lifetime

Another important aspect of the luminosity which is worth mentioning, is the beam lifetime. Each run at the LHC consitsts of a number of luminosity blocks corresponding to different values of instantaneous luminosity due to the degradation in the intensities and emittances of the circulating beams after the collisions. The initial decay time of the bunch intensity is given by the equation:

$$\tau_{nuclear} = \frac{N_{tot,0}}{\mathcal{L}\sigma_{tot}k} \tag{3.4}$$

with $N_{tot,0}$ being the initial beam intensity, $\mathcal{L}$ the initial luminosity, σ_{tot} the total cross section ($\sigma_{tot} = 10^{-25}\text{cm}^2$) and k the number of interaction points. Assuming a high luminosity environment with two high luminosity experiments (ATLAS and CMS), the initial decay time is calculated to be $\tau = 44.85$ h.

The decay of the beam intensity and luminosity can then be expressed as a function of time:

$$N_{tot}(t) = \frac{N_{tot,0}}{1 + t/\tau_{nuclear}} \tag{3.5}$$

$$\mathcal{L}(t) = \frac{\mathcal{L}_0}{(1 + t/\tau_{nuclear})^2} \tag{3.6}$$

The time needed for luminosity to be decreased at $1/e$ of its initial value is given by:

$$t_{1/e} = (\sqrt{e} - 1)\tau \tag{3.7}$$

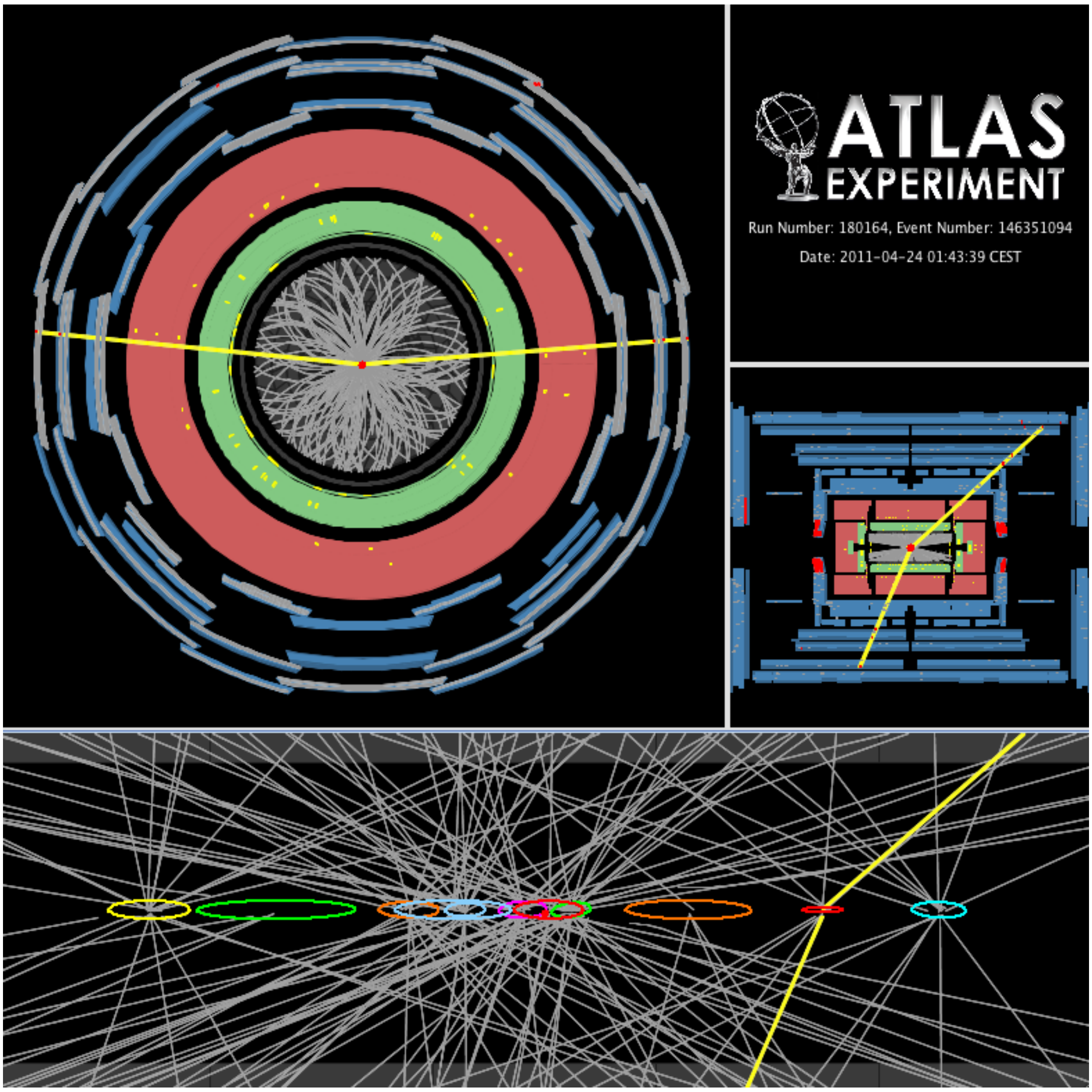

Figure 3.4: A candidate Z boson event in the dimuon decay with 11 reconstructed vertices. This event was recorded on April 24th and is typical for the 2011 environment with high pileup. For this display the track p_T threshold is 0.4 GeV and all tracks are required to have at least 2 Pixel and 7 SCT hits. The vertices shown are reconstructed using tracks with p_T greater than 0.4 GeV. The smallest separation between any two of them is 3.2±0.2 mm. The invariant mass of the two muons is 93.4 GeV.

yielding a luminosity decay time of $\tau_{nuclear,1/e} = 29$ h.

The net luminosity lifetime can be calculated by taking into account the main sources contributing to beam losses like the intra-beam scattering (IBS) effects, Toucheck scattering and the nonlinear force of the beam-beam interaction, all having as a result the irreversible growth of emittance. Taking also into account the vacuum beam lifetime, the net luminosity is reduced to ∼15 h [1].

3.4 The LHC experiments

Six experiments frame the LHC ring and are all run by international collaborations, having all great performance in their first two years (2010 & 2011) of operation. The six experiments in alphabetic order are:

- ALICE (A Large Ion Collider Experiment) [3] is devoted to the search and study of quark-gluon plasma by analyzing the heavy ion collisions. The quark-gluon plasma is a state of matter where quarks and gluons behave as free particles. It is believed that this state of matter existed just after the Bing Bang, when the Universe was still extremely hot. The size of the detector is 26 m long, 16 m high and 16 m wide.

- ATLAS (A Toroidal LHC ApparatuS) [4] is a general purpose detector with enriched physics program. Topics like Higgs boson, SUSY particles and CP violation measurements will be studied. The detector has a cylinder form with 44 m long, 22 m diameter and a total weight of 7000 t.

- CMS (Compact Muon Solenoid) [5] objectives are similar to the ones of ATLAS. It is a multipurpose detector and is the second biggest experiment in the LHC ring. It has a total length of 21 m, 15 m wide, 15 m high and it weights 12500 tonnes, almost twice the ATLAS weight. It is located at Point 5 of the LHC ring.

- LHC *b* (Large Hadron Collider beauty) [6] experiment is exploring why our Universe is composed from matter but no antimatter. In order to understand why that occured in the early Universe one must study the *b*-quark physics and CP violation. Detector's size is 21 m long, 10 m high and 13 m wide.installed at Point 8.

The other two experiments are significantly smaller than the previous ones and are named TOTEM (TOTal Elastic and diffractive cross section Measurement) [7] and LHC **f** (Large Hadron Collider forward) [8]. The former studies forward particles and its main purpose is to measure the size of the proton as well as to accurately monitor the LHC's luminosity. The latter studies forward produced particles as a source to simulate cosmic rays in laboratory conditions.

Bibliography

[1] O. Bruning et al., "Lhc design report. v1: the Lhc main ring", CERN-2004-003-V-1, 2004. 17, 19, 26

[2] G. Abbiendi, et al. (the ALEPH Collaboration, the DELPHI Collaboration, the L3 Collaboration and the OPAL Collaboration, The LEP Working Group for Higgs Boson Searches), "Search for the Standard Model Higgs Boson at LEP", Phys.Lett.B565:61-75, 2003. 17

[3] Alice Collaboration, "Alice Technical Proposal for a Large Ion Collider Experiment at the CERN LHC", CERN / LHCC / 95-71 LHCC / P3, December 1995. 26

[4] Atlas Collaboration, "Detector and Physics Performance Technical Design Report", CERN/LHCC/99-14, ATLAS TDR 14, May 1999. 26

[5] Cms Collaboration, "Cms Physics Technical Design Report, Volume II: Physics Performance", J. Phys. G: Nucl. Part. Phys., 34:995-1579, 2007. 26

[6] LHCb Collaboration, "LHCb technical proposal", CERN-LHCC-98-4, 1998. 26

[7] Totem Collaboration, "Totem technical design report", CERN-LHCC-2004-002, 2004. 27

[8] LHCf Collaboration, "Technical design report of the LHCf experiment. Measurement of photons and neutral pions in the very forward region of Lhc", CERN-LHCC-2006-004.

27

...Photographs capture beauty, especially when they reveal the components of the early universe...

Chapter 4

The ATLAS detector

The ATLAS collaboration [1] proposed to build a general-purpose pp detector, designed to exploit the full discovery potential of the LHC. The ATLAS [2] detector is the biggest detector installed in the 27 km LHC tunnel. Its design and construction involves roughly 2000 scientists and engineers from 165 institutions around the world. ATLAS has a cylinder shape with total length 44 m, diameter equal to 25 m and weights about 7000 tonnes. A sketch of the ATLAS detector can be seen in Figure 4.2. It is a multipurpose detector with which one can test the SM at the TeV energy scale, search for the SM Higgs boson, which is the only missing block of the SM, as well as to search for massive particles beyond the SM, which have not yet been observed. In general, as in other high energy physics experiments, the ATLAS detector incorporates the following detector subsystems:

- **Inner detector (ID)**: It is responsible for the momentum measurement of the charged particles;
- **Electromagnetic calorimeter (LArEM)**: It is in charge of the detection of electron and photon objects;
- **Hadronic calorimeter (HCAL)**: It is liable for the identificaction and energy measurement of jets produced from the hadronization process of partons (gluons and quarks);
- **Muon spectrometer (MS)**: It is used for the identification and momentum measurement of muons;

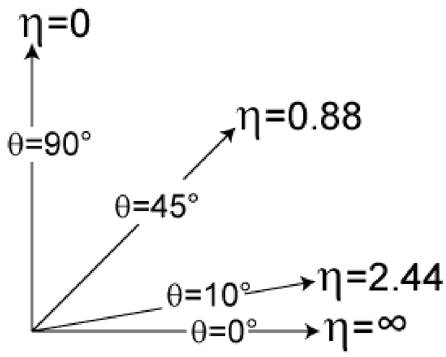

Figure 4.1: Pseudorapidity values of different polar angles.

- **Magnet system**: A high strength magnetic field is required to bend the trajectories of charged particles and therefore to measure charged particles momenta.

In the following subsections a brief description of the coordinate system as well as each subdetector is discussed.

4.1 The coordinate system

The coordinate system of the ATLAS detector is right handed, with its origin located in the middle of the detector at the interaction point. The $z-$ axis is defined from the beam direction, and the $x-y$ plane is the plane transverse to the beam direction. The side A of the detector is defined as the side with positive z, and the side C is the side with $z < 0$. The positive $x-$ axis points from the interaction point to the centre of the LHC ring, and the positive $y-$ axis is pointing upwards.
The azimuthal angle, ϕ, is measured around the beam axis and the polar angle, θ, is measured from the beam axis. The pseudorapidity, η, is defined from the equation

$$\eta = -\ln\left[\tan\left(\frac{\theta}{2}\right)\right] \tag{4.1}$$

where θ is the polar angle. Figure 4.1 shows the corresponding pseudorapidity values of different polar angles. The transverse momentum, p_T, and transverse energy, E_T, are defined in the $x-y$ plane and are given by the equations:

$$p_T = P \cdot \sin\theta,\ E_T = Esin\theta \tag{4.2}$$

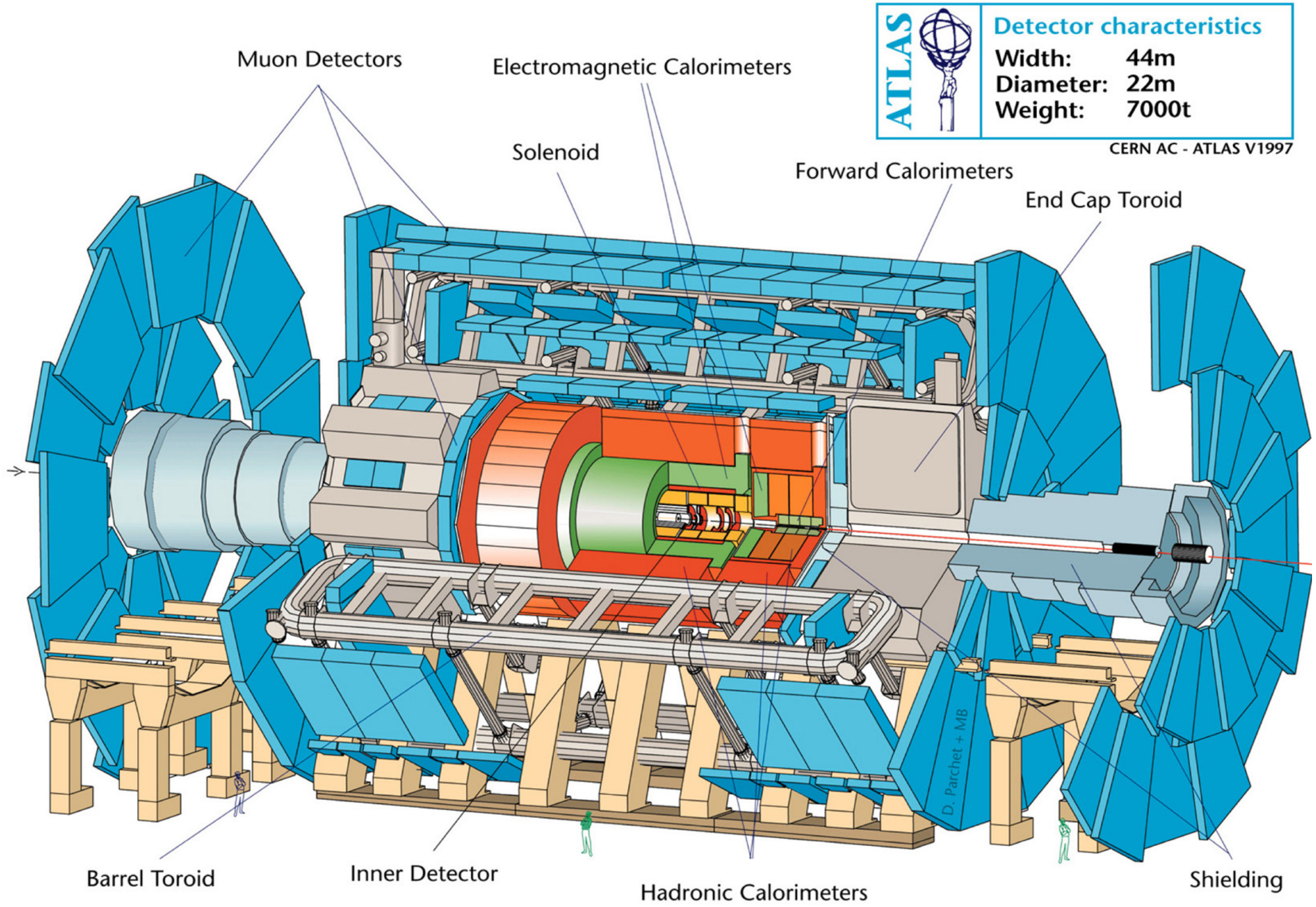

Figure 4.2: A layout of the ATLAS detector.

Another important variable used in particle physics experiments is the distance ΔR, which in the pseudorapidity-azimuthal angle phase space is given by the equation:

$$\Delta R = \sqrt{\Delta\eta^2 + \Delta\phi^2} \tag{4.3}$$

The parameters used for the description of the trajectories of charged particles are:

- q/p_T: Inverse transverse momentum (where q is particle's charge);
- ϕ: Azimuthal angle, where $\tan\phi = p_y/p_x$
- d_0: Transverse impact parameter, defined as the transverse distance to the beam axis at the point of closest approach;
- $\cot\theta$: Cotangent of the polar angle, where $\cot\theta = p_Z/p_T$;
- z_0: Longitudinal impact parameter, defined as the z distance of the track at the point of closest approach.

The first three parameters are defined in the $x-y$ plane, while the last two are defined in the $R-z$ plane.

4.2 Atlas sub-detectors

4.2.1 The Inner Detector

The innermost part of the Atlas detector consists of the Inner Detector (ID) [3]. The system has a cylinder form with 7 m length and radius 1.15 m, with a full ϕ-coverage and $\eta \leq 2.5$. The ID consists from three independent detectors, the Pixel Detector, the SemiConductor Tracker and the Transition Radiation Tracker. The whole system is immersed inside a 2 T magnetic field formed by the central solenoid (see Section 4.2.4.1). The three subsystems function independently in order to have precise measurements of the charged particles trajectories, including impact parameter measurements and vertexing. A schematic representation of the ID and its three sub-systems is shown in Figure 4.3.

The transverse momentum resolution in the $x-y$ plane is given by the equation [4]:

$$\frac{\Delta p_T}{p_T} \sim 0.00036 \times p_T[\text{GeV}] \oplus \frac{0.013}{\sqrt{\sin\theta}} \tag{4.4}$$

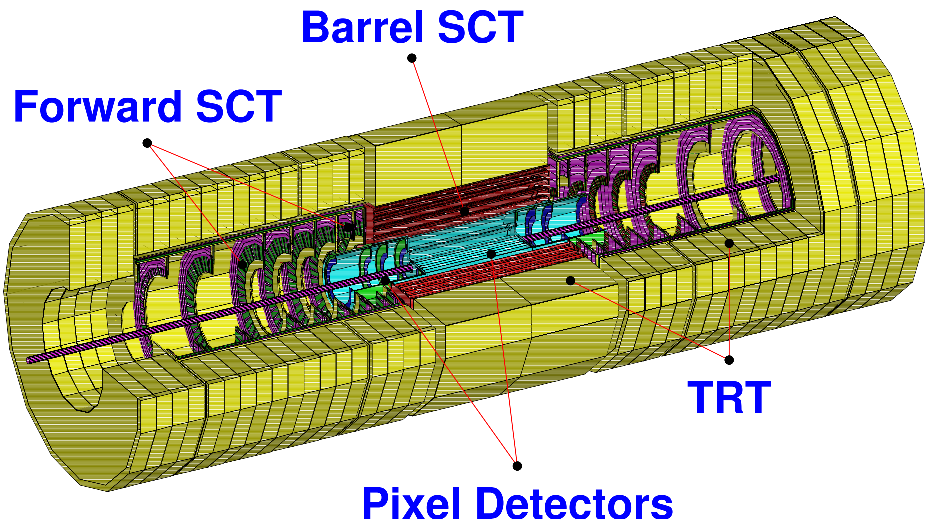

Figure 4.3: The Inner Detector of the ATLAS experiment. Starting form inside and going outwards one can see the Pixel Detector, the SemiConductor Tracker and the Transition Radiation Tracker.

The first term is the intrinsic resolution and the second one refers to the multiple scattering effects. As can bee seen, this term is η dependent, since the additional material in the forward regions increases the scattering effects.

4.2.1.1 Pixel Detector

The pixel detector is located in the innermost region and has been designed to provide a very high granularity and high precision set of measurements. In total, it provides three precision measurements and determines the impact parameter resolution. The barrel region consists of three concentric cylindrical layers placed around the beam axis in radii of 5.05 cm, 8.85 cm and 12.25 cm. The endcaps constist of three disks on each side (perpendicular to the beam axis), between radii 11 and 20 cm. There are 1744 silicon pixel modules. Each module covers an active area of 16.4×60.8 mm^2 and contains 47232 pixels, each with 50 μm in the Rϕ direction and 400 μm in z. The Pixel Detector has a total of 80.4 million read-out channels.

4.2.1.2 Semiconductor Tracker

The next building block of the ID is the Semiconductor Tracker (SCT). It contributes to the determination of the $z-$ position of the vertex, the momentum resolution as well

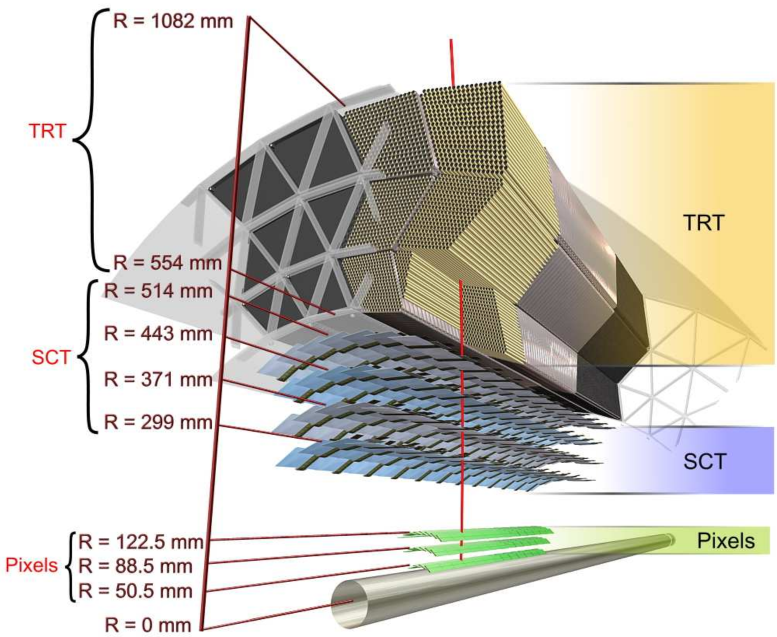

Figure 4.4: Position of the structural elements of the ID. The red line indicates a track passing the barrel region.

as the pattern recognition of the reconstruction algorithms. It covers the radial region from ∼30 cm to ∼60 cm. As in the case of the Pixel detector, the SCT uses silicon as active material and consists of 4088 modules arranged in four concentric cylinders in the barrel region and nine disks in each end-cap. Each module is made up of four layers. On each side of the module, two layers are wire-bonded together, which are then glued back to back with another pair of such layers. Each silicon detector is 6.36×6.30 cm^2, with 768 readout strips each, with 80 μm pitch. In the barrel region, there are 2112 modules which are approximately parallel to the beam pipe, while in the end-caps there are 1976 modules positioned in the radial direction. It provides eight precise measurements (four space points) and the designed resolution in the $R-\phi$ plane is 22 μm and 580 μm in the $z-$ coordinate.

4.2.1.3 Transition Radiation Tracker

The TRT is the outermost part of the ID and its technology is based on the use of straw detectors. It covers the radial range from 56 to 107 cm. Each straw has a diameter of 4 mm and is 144 cm long in the barrel region and 37 cm long in the end-caps. The straw tubes are filled with a gas mixture of 70% Xe, 27% CO_2 and 3% O_2. The anode wires of a diameter 31 μm are located in the middle of the straw and are made up of gold-plated tungsten. There are approximately 351000 TRT read-out channels.

The TRT system can provide 36 hits per track with an intrinsic precision of 130 μm per tube covering the range $\eta < 2.0$. In the barrel region ($|\eta| < 1.0$), the tubes are placed parallel to the beam axis, while in the end-cap regions ($0.8 < |\eta| < 2.0$) they are arranged radially on wheels. The principle of operation is similar to the drift tubes used in the MS. The straws are surrounded with polypropylene fibers which help distinguish electrons from pions, since the charged particles traversing this material emit transition radiation (TR) photons proportional to the Lorentz factor $\gamma = E/mc^2$. Typically, for electrons the factor γ is greater than for other charged particles.

4.2.2 Calorimeters

The ATLAS Calorimeter System is situated between the solenoid and the MS and is responsible for the identification of photons, electrons and hadrons (jets) with energies up to 1 TeV. In addition, the calorimeter also provides information on the missing transverse energy (E_T^{miss}), which requires very good hermiticity. In specific, the calorimetry consists of an Electromagnetic (EM) calorimeter covering the range $|\eta| < 3.2$, a barrel hadronic calorimeter covering $|\eta| < 1.7$, a hadronic end-cap calorimeter covering $1.5 < |\eta| < 3.2$ and forward calorimeters covering $3.1 < |\eta| < 4.9$. Figure 4.5 shows a cut-away view of the ATLAS calorimeter system.

Another important property of the calorimeters is the limitation of particles' rate escaping to the muon system and this is realized from the calorimeter depth in the barrel region which is greater than 22 radiation lengths[1] (X_0) and over 24 X_0 in the end-caps. The energy and position are measured by sampling the energy deposit in the calorimeter.

4.2.2.1 The electromagnetic calorimeter

The electromagnetic calorimeter [5] [6] is a lead-Liquid-Argon (LAr) detector with accordion shape (see Figure 4.6) absorbers (Pb). The active medium is LAr. Two important actions are taking place when the electrons and photons enter the EM calorimeter.

[1] The radiation length (X_0) of a material is the mean length to reduce the energy of an electron by the factor 1/e.

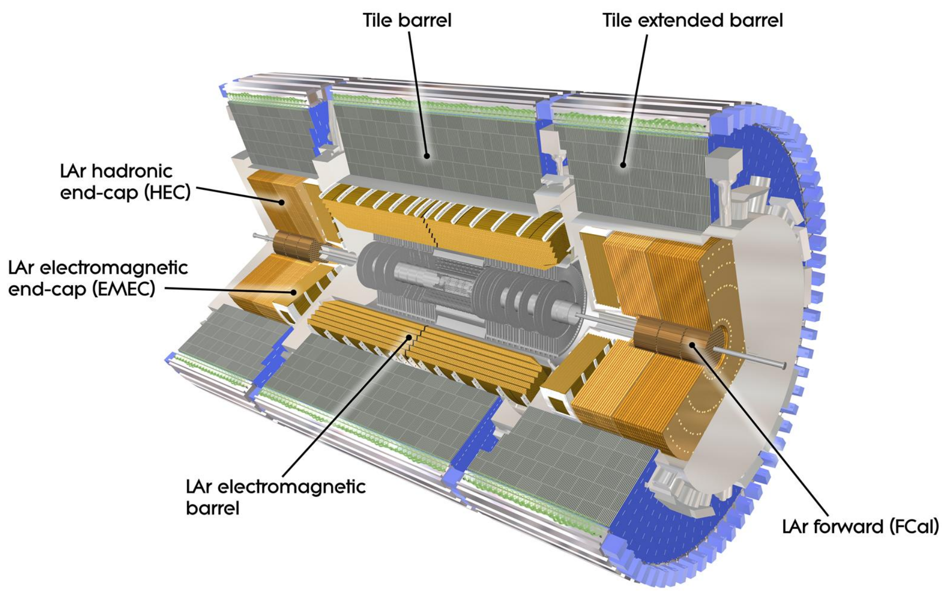

Figure 4.5: Cut-away view of the ATLAS calorimeter system; Electromagnetic and hadronic.

The first one is the bremsstrahlung radiation of electrons when they interact with matter, leading to the production of an additional photon and the second one is the pair production of electron-positron. These two actions are repeated until all or the biggest part of the initial energy of the particle is absorbed by the material. The result of these actions is a cascade of electrons and photons.

The electromagnetic calorimeter (LArEM) is divided in two parts. The barrel which covers the range $|\eta| < 1.4575$ and the end-caps which extend the LArEM up to 1.375 $< |\eta| < 3.2$. Figure 4.6 illustrates a LArEM module. The region which is also covered from the ID ($|\eta| < 2.5$) consists of three compartments. Each compartment is segmented in cells of different sizes. The first sampling comprises of strip cells with a pitch of $\sim$4 mm in the η direction. This compartment acts as a "preshower"detector, enhancing particle identification ($\gamma/\pi^0, e/\pi$ seperation) and it also provides a precise position measurement in η. The second sampling is segmented into square towers of size $\Delta\eta\times\Delta\phi$ $= 0.025 \times 0.025$ and here the biggest energy deposition of the shower takes place, thus is the thickest of the three compartments (16 X_0). The third sampling has a quite larger granularity in η, $\Delta\eta \times \Delta\phi = 0.05 \times 0.025$ and the depth (in radiation length) varies

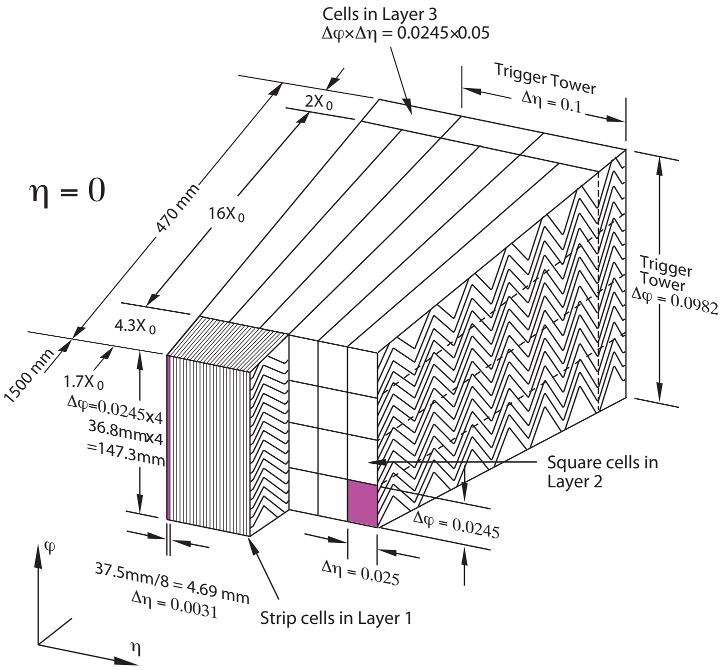

Figure 4.6: Sketch of a barrel module of the electromagnetic calorimeter.

between 2 X_0 and 12 X_0 depending on η. In the region $|\eta| > 2.5$ the calorimeter consists from only two samplings with a coarser granularity satisfying the physics requirements for the jet reconstruction and the E_T^{miss} measurement. There are in total ∼190000 channels.

The energy resolution can be parametrized by [4; 6]:

$$\frac{\sigma_E}{E} = \frac{11\%}{\sqrt{E[GeV]}} \oplus 0.4\% \tag{4.5}$$

where the first term stands for the statistical fluctuations of the sampling method and the second term includes the systematic uncertainties, which arise from inhomogeneities in the response of the calorimeter.

4.2.2.2 The Hadronic calorimeter

The hadronic calorimeter (TileCal - see Figure 4.7a) [7; 8] of the Atlas detector is located behind the LArEM, covering the pseudorapitidy range up to $|\eta| < 4.9$. It is responsible for the jet identification and reconstruction, which result from the hadronization of partons (quarks and gluons) as well as for the measurement of the missing tran-

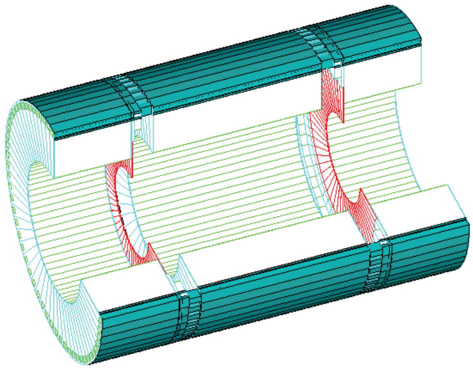

(a)

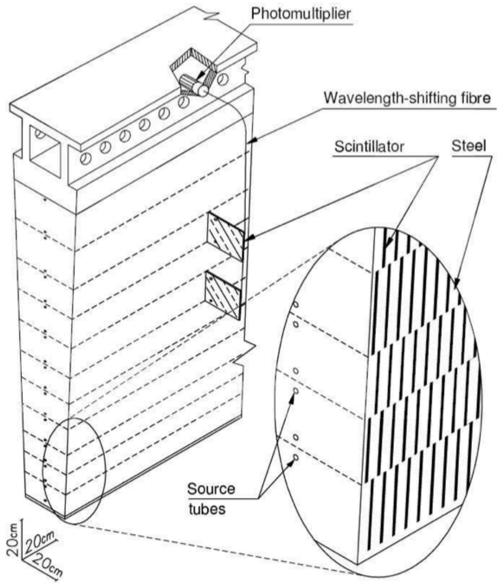

(b)

Figure 4.7: (a) Layout of the Tile Calorimeter barrel and extended barrels. (b) A module of the tile calorimeter.

verse energy (E_T^{miss}) of the event. The latter plays an important role in the searches for new physics, especially in supersymmetry (SUSY) theory where the lightest supersymmetric particle (LSP) escapes from the detector. The hadronic calorimeter must be thick enough in order to provide good containment for hadronic showers and also reduce punch-through for the muon system.

In order to fulfill the requirements of the experiment, different techinques and devices have been empoyed in the different η regions. The TileCal is divided in one barrel and two extended barrel parts. It has a cylindrical structure with inner radius 2.28 m, outer radius 4.23 m and total length 5.64 m. The barrel covers the region $|\eta| < 1.0$ and the extended barrels extend the pseudorapidity coverage to $0.8 < |\eta| < 1.7$. As in the case of the LArEM, the TileCal is a sampling calorimeter using iron as the absorber material and plastic scintillating tiles as active medium. The tiles are 3 mm thick and are positioned perpendicular to the beam axis. The total thickness of the iron plates in one period is 14 mm. The read-out of the scintilation light is achieved with optical fibers situated at the edges of the tile. Longitudinally, the TileCal is divided in three compartments at 1.5, 4.1 and 1.8 interaction lengths (λ) and 1.5, 2.6 and 3.3 λ in the extended barrel. In the first two layers the granularity is $\Delta\eta \times \Delta\phi = 0.1 \times 0.1$ and in the third one is 0.2×0.1. TileCal also offers a full azimuthal coverage by installing 64 modules around the beam pipe. A single TileCal module can be seen in Figure 4.7b.

Due to electronic technicalities (cables, electronics and services) resulting from the innermost detectors (ID, LArEM), an empty space of 60 cm between the barrel and the extended barrel has been left. In order to have an hermetic calorimeter, an Intermediate Tile Calorimeter (ITC) has been employed in that region covering partially the empty space.

Moving from the barrel to the end-caps ($1.5 < |\eta| < 3.2$), the detector requirements change due to the higher radiation doses. The HEC in the end-caps uses copper (Cu) plates as absorber material and LAr as ionization material. The granularity till $|\eta| = 2.5$ is the same as in the first two layers of the barrel and for $|\eta| > 2.5$ has double size. The designed energy resolution in region $\eta < 3$ is given by [7; 8]:

$$\frac{\Delta E}{E} = \frac{50\%}{\sqrt{E}} \oplus 3\% \tag{4.6}$$

4.2.2.3 Forward Calorimeter

The forward calorimeter (FCal) covers the region $3.1 < |\eta| < 4.9$ and uses as active material LAr. Its worth noticing here that the expected radiation doses in this region are extremely high, so the radiation tolerance of the detector plays a crucial role. For that reason the liquid argon gaps are very small. The absorber is Cu in the first compartment and tungsten in the other two compartments. The resulting thickness is $\sim$10 interaction lengths. The forward calorimeter is not used for precise measurements but its usage is important in the calculation of the E_T^{miss} and in the determination and reconstruction of the forward jets. The designed energy resolution is [9]:

$$\frac{\sigma_E}{E} = \frac{100\%}{\sqrt{E}} \oplus 10\% \tag{4.7}$$

where the first term is the stochastic term and the second one is the constant term, taking care of the local non-uniformities in the response of the calorimeter.

4.2.3 The Muon spectrometer

The Muon Spectrometer (MS) [10; 11; 12] of the ATLAS detector has been designed to provide a standalone identification and reconstruction of muons up to $|\eta| < 2.7$ with full azimuthal coverage. Additionally, it is also used for trigger in $|\eta| < 2.4$. The MS can also operate in a combined mode with the other sub-detectors, especially with the ID for the track reconstruction of muons. The momentum resolution of the MS is of the order of ∼3% for muons with $p_T = 50$ GeV and around 10% for muons with $p_T = 1$ TeV.

For that reason, four independent systems have been employed and are located in the outermost part of the ATLAS detector (see Figure 4.8). The four systems are:

- **Monitor Drift Tube Chambers (MDT)**: They cover 99.5% of the area and are used for precision measurements up to $|\eta| < 2.7$, except from the innermost end-cap layer which stops at $|\eta| < 2.0$;

- **Cathode Strip Chambers (CSC)**: They are located on the innermost wheel of the endcap covering the region $2.0 < |\eta| < 2.7$ and they provide the same objectives as the MDTs. They can also be used for trigger.

- **Resistive Plate Chambers (RPC)**: They are utilized for triggering in the barrel region;

- **Thin Gap Chambers (TGC)**: They are the trigger elements in the end-cap regions.

The track reconstruction is achieved by the hit measurements from three homocentric cylindrical layers in the barrel at radii of 5 m, 7.5 m, and 10 m, the so called "inner", "middle" and "outer" stations. In the end-caps, the muon chambers are arranged on four homocentric wheels at distances of $|z| = 7.4$ m, 10.4 m, 14 m and 21.5 m. Apart from the second wheel which corresponds to special chambers covering the transition region between the barrel and the end-caps, one can refer to the other three with the same nomenclature as in the barrel. The barrel chambers are placed between and on the eigth coils of the toroid magnet following their ϕ symmetry. This results in the symmetric structure of eight octants. Each octant is subdivided in the azimuthal direction in two sectors, called "Small" and "Large". The name given to them declares

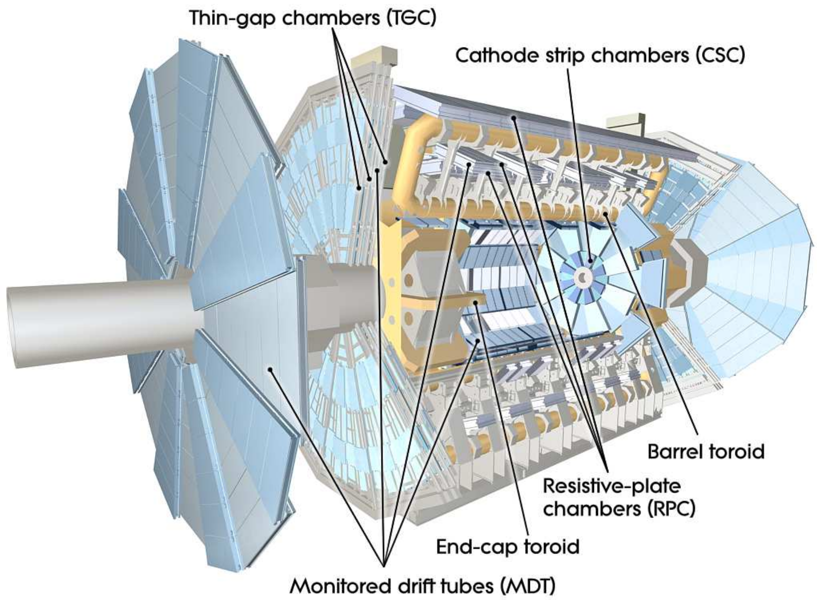

Figure 4.8: Cut-away view of the ATLAS muon spectrometer. The four systems employed for the muon identification, reconstruction and triggering are shown.

their lateral length. This structure results in an overlapping between the chambers which minimises gaps in the detector coverage. Deliberately, a small gap at $\eta \approx 0$ has been left open for maintenance of the calorimeter, the solenoid and the inner detector.

In the first ring, ATLAS incorporated the Cathode Strip Chambers which withstand the demanding rate and background conditions.

4.2.3.1 Monitor drift tube chambers

The basic component of the MDTs are the aluminium tubes of ~30 mm diameter and 400 μm thickness. In the middle of each tube there is a tungsten-rhenium (W-Re) wire of 50 μm diameter which plays the role of the anode; The cathode is the tube wall. The potential difference between the anode and the cathode is 3080 V. The tubes are filled with gas mixture Ar:CO_2/93:7% at 3 bar absolute pressure. The chamber is formed by eight (2×4 monolayers for the inner station) and six (2×3 monolayers for the middle and outer stations) drift tube layers. Each layer consists of several tubes in consecutive order. After the installation of each chamber in its permanent position in the spectrometer, mechanical deformations are monitored by an optical alignment

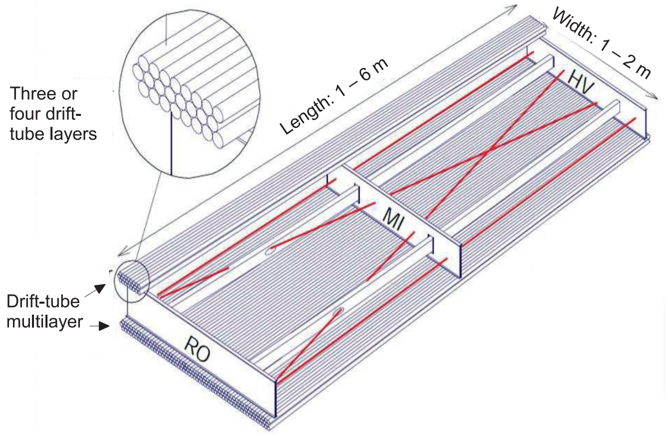

Figure 4.9: Sketch of a MDT chamber. The alignment rays, shown in red, allow for the monitoring of chamber deformations.

system, thus they are called "monitor drift tubes". A sketch of an MDT chamber is illustrated in Figure 4.9.

When a muon passes through the tube, it ionizes the gas. As a consequence, the resulting free electrons under the influence of the electric field, start drifting towards the wire, while the positive ions drift towards the tube's wall. Once the primary electrons reach some critical energy, they ionize further gas molecules creating an avalanche near the wire. The induced signal on the wire is then propagated at the end of the tube where further reprocessing is followed. The drift time can be translated into distance by using the space-time relation.

4.2.3.2 Cathode Strip Chambers

The Cathode Strip Chambers are described in great detail in Chapter 5. They are multiwire proportional chambers without separating walls. They have better response than the MDTs fulfilling the appopriate requirements in the forward region where the expected particle fluxes are increased dramatically.

4.2.3.3 Resistive Plate Chambers

The Resistive Plate Chambers (RPCs) are the muon trigger systems in the barrel region. They are located on three concentric cylindrical layers around the beam pipe (see Figure 4.10). In specific, RPCs are gaseous detectors which are made of two parallel resistive

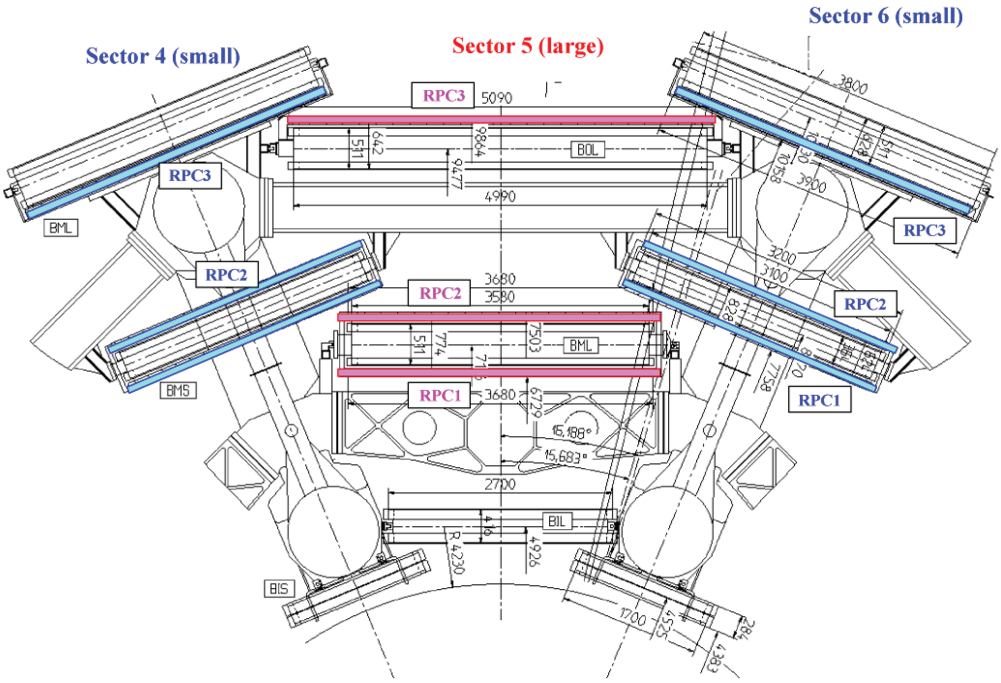

Figure 4.10: Cross-section through the upper part of the barrel with the RPC's marked in blue and pink colour. RPC1 and RPC2 are located below and above the middle station chambers, while the RPC3 are positioned below (above) the small (large) outer station chambers.

electrode-plates of phenolic-melaminic plastic laminate, seperated by insulating spacers. The resulting gap of 2 mm is filled with a gas mixture of $C_2H_2F_4$ (tetrafluorethane). The charged particles traverse the narrow gap, ionizing gas molecules. The uniform electric field of 4.5 kV/mm between the two plates accelerates the primary electrons, which in turn further ionize the gas molecules creating an avalanche. The two plates are covered with read-out strips, mounted on their outer sides, providing the η (strips are parallel to the MDT wires) and ϕ (strips are perpendicular to the MDT wires) coordinates of the hit. A schematic representation of an RPC layer can be seen in Figure 4.11. The spatial and time resolution is 1 cm and 2 ns respectively. The inner stations provide the low p_T trigger between 6 - 9 GeV muons, while the two external chambers (middle and outer) are used to select high momenum tracks ($p_T > 9$ GeV).

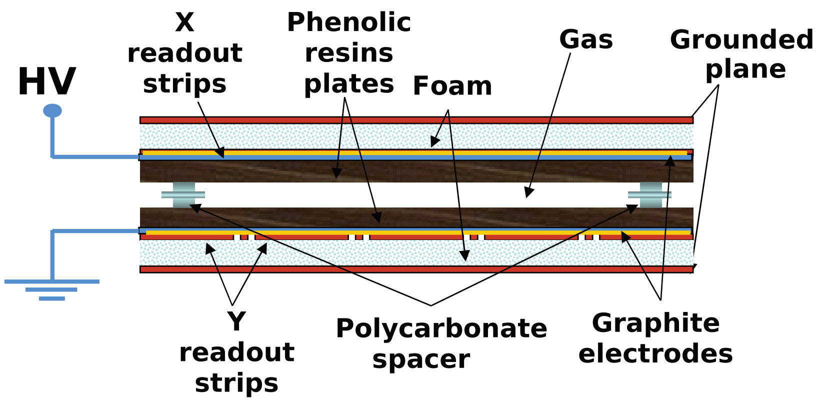

Figure 4.11: Sketch of an RPC layer.

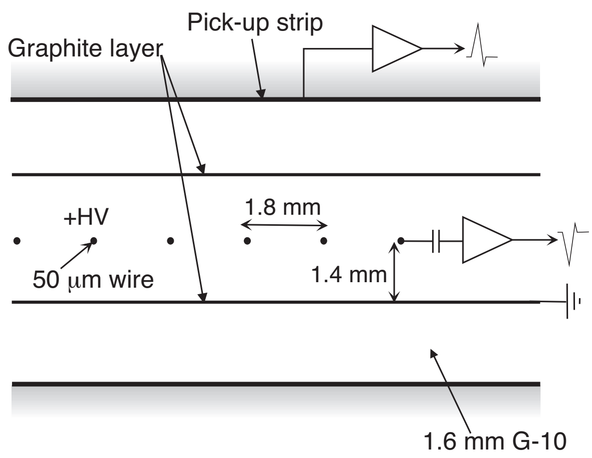

Figure 4.12: Sketch of a TGC layer.

4.2.3.4 Thin Gap Chambers

The Thin Gap Chambers (TGC) are the trigger elements in the end-caps. Similar to the CSC system, TGCs are multiwire proportional chambers (see Section 5.2). The wire to cathode distance is 1.4 mm and the wire to wire distance is 1.8 mm (see Figure 4.12). The gap between the two cathodes is filled with a mixture of CO_2:n-C_5H_{12} (n-pentane) (55:45). The anode wires have 50 μm diameter and are surrounded by a strong electric field (operation voltage 2.9 kV). The radial coordinate is measured from the anode wires, while the azimuthal coordinate is measured from the pick-up strips which are radially oriented (perpendicular to the anode wires). Each chamber consists of two or three layers.

4.2.4 The Magnet System

The magnet system [13] of the Atlas experiment is responsible for the trajectories bending of charged perticles and therefore for the momentum measurement in both the ID and MS. It is separated in one superconducting solenoid magnet, which provides an axial magnetic field surrounding the ID and three toroidal magnets, one in the barrel region and one in each end-cap. In general, the magnetic system is 22 m in diameter and 26 m in length, with a stored energy of 1.6 GJ. The operation temperature is 4.5 K.

4.2.4.1 Central solenoid

The central solenoid, shown in Figure 4.13a, has been designed to provide a 2 T magnetic field at the center and 0.5 T at the edges, parallel to the beam axis. It has been optimized to minimize the radiative thickness in front of the electromagnetic calorimeter (contribution of ∼0.66 radiation lengths), therefore the solenoid windings and the LAr calorimeter share the same cryogenic system. The solenoid is a single layer coil wounded on the inside of a cylinder with an inner radious of 1.23 m and outer radious of 1.28 m. Its length is 5.8 m while the stored energy is 40 MJ. The flux is returned from the hadronic calorimeter's steel.

4.2.4.2 Air core toroid

The toroid magnet system provides the nessecary magnetic field for the MS. The barrel toroid consists of eight superconducting coils circularly positioned around the beam axis, while in the end-cap regions two extra toroids (one in each end-cap) have been empoyed (see Figure 4.13b). The magnetic field lines follow the azimuthal direction ($\vec{B} = B\hat{\phi}$) and are perpendicular to the solenoid's field lines. The size of the magnet system in the barrel region is 25.3 m in length, with inner and outer diameters of 9.4 m and 20.1 m respectively. The resulting strength of the magnetic field is 0.5 T in the central region and 1 T in the end-caps. In order to achieve the appropriate operational temperature the toroids are cooled by a liquid helium cooling system.

(a)

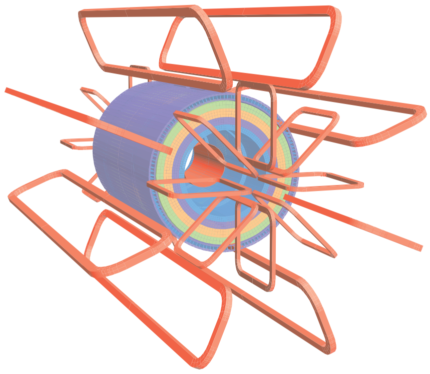

(b)

Figure 4.13: (a) The central solenoid of the ATLAS detecto after completion of the coil winding. (b) Geometry of the barrel and the end-caps air core toroid magnets.

4.2.5 The trigger system

As it has been noted in Chapter 3, the LHC has been designed to operate at 40 MHz bunch crossing. Considering that each colliding event corresponds to ∼1 MB space one would need 40 TB free disc space per each second in order to store the events. Unfortunately, current technology does not allow this enormous amount of data to be captured. So, the ATLAS experiment developed a series of procceses, called the trigger system (see Figure 4.14), in order to creatively handle all this information.

The first action taking place is the so called Level-1 (L1) trigger. The L1 trigger is hardware based and receives data from the calorimeters and the muon system (RPCs and TGCs). Its target is to reduce the initial rate (40 MHz) to 75 kHz. L1 defines the regions of interest (RoIs) of each event, where high activity has been detected, e.g. muon (electron) with $p_T > 20$ GeV ($E_T > 20$ GeV). The time necessary for L1 to decide whether to reject or keep the event is 2.5 μs.

The events selected by the L1 trigger are subjected to further processing from the High-Level trigger (HLT) which compises from the Level-2 (L2) trigger and the event filter (EF), both software based. In specific, the RoIs of the detector are passed to the L2 trigger which uses the available information provided by the RoIs (location of the detector $\eta - \phi$, energy, type of signature e.t.c) in order to reduce the event rate below 3.5 kHz. Approximately, the L2 event processing lasts 40 ms.

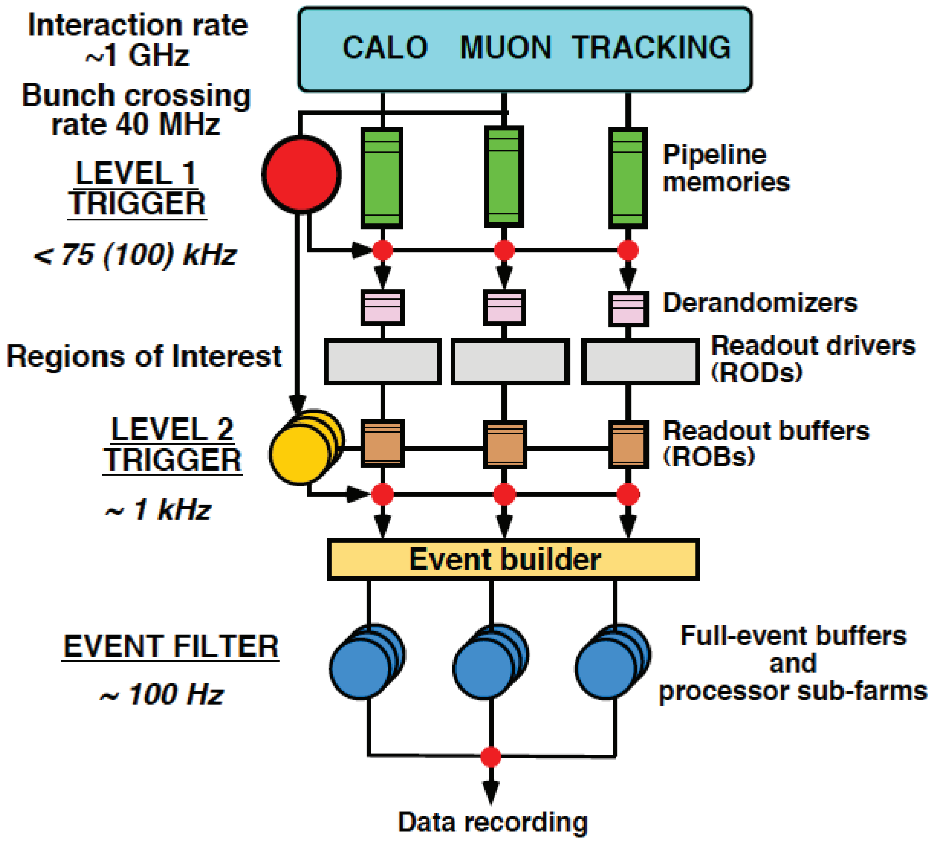

Figure 4.14: Overview of the ATLAS trigger system.

The events fulfilling the L2 trigger requirements pass through an extensive reprocessing for the final decision. For that reason, the Event Builder collects all the data from the Read Out Buffers (ROBs) of the detector and feeds them to the EF which uses more sophisticated algorithms in order to record the event or not. EF's target is to reduce the recorded rate to 100 Hz.

It is of great importance to note here that even this rate is extremely high since the storage space needed by the ATLAS experiment per year is of the order of 1 PB[1]. Therefore the ATLAS collaboration has built a very powerful computing environment for storage and reprocessing of the data. In addition to this, another noteworthy development is the GRID, a form of distributed computing. GRID is developed by scientists around the world in order to quickly reprocess and analyze large amounts

[1] 1 PB (petabyte) = 10^{15} bytes

of data within a secure environment. ATLAS and CERN in general contribute to this cutting edge technology by developing it, using it and providing feedback for further improvements.

Bibliography

[1] Atlas Collaboration,"Technical Proposal for a General-Purpose *pp* Experiment at the Large Hadron Collider at CERN", LHCC/94-43;LHCC/P2, December 1994. 29

[2] Atlas Collaboration, "The Atlas experiment at the CERN Large Hadron Collider", 2008 JINST 3 S08003. 29

[3] Atlas Collaboration, "Atlas Inner Detector technical design report", LHCC/97-16;LHCC/97-17, 1997. 32

[4] M. Schott, "Lecture Notes: Standard Model of Particle Physics. Experiments, Measurements and Interpretations", Wintersemester 2011/12. 32, 37

[5] Atlas Collaboration, "Atlas liquid argon calorimeter technical design report", LHCC/96-41, 1996. 35

[6] Atlas Collaboration, "Readiness of the Atlas liquid argon calorimeter for Lhc collisions", Eur.Phys.J.C70:723-753, 2010. 35, 37

[7] Atlas Collaboration, "Atlas tile calorimeter technical design report", LHCC/96-42, 1996. 37, 39

[8] Atlas Collaboration, "Readiness of Atlas tile calorimeter for Lhc collisions", Eur.Phys.J.C70:1193-1236, 2010. 37, 39

[9] P. Krieger, "Performance of the Atlas Liquid Argon forward calorimeter in beam tests", Astroparticle, particle and space physics, detectors and medical physics applications, (p 341-345). 39

[10] Atlas Collaboration, "Atlas muon spectrometer technical design report", LHCC/97-22, 1997. 40

[11] M. J. Woudstra, “Precision of the Atlas muon spectrometer”, PhD thesis, 2002. 40

[12] Van Eldik, N., “The Atlas muon spectrometer : calibration and pattern recognition”, PhD thesis, 2007. 40

[13] Atlas Collaboration, “Atlas magnet system technical design report”, CERN-LHCC-97-18, 1997. 45

..Reliable and pioneering results require deep understanding and highly operative machines...

Chapter 5

The Cathode Strip Chambers of the ATLAS experiment

The present chapter introduces the CSCs and describes the studies performed to improve the spatial resolution of muons and the measured drift time of electrons. The resulting algorithm of these studies has been implemented in the ATLAS software, ATHENA, and it is used for digital signal processing.

5.1 Introduction

The CSCs [1] play an important role in detecting muons in the forward region of the MS, covering the pseudorapidity region $2 < |\eta| < 2.7$. Due to the high counting rate characterizing the forward region, MDTs have been replaced by CSCs which can safely operate up to 1000 Hz/cm^2 (compared to the MDTs with a safe operation limit of 150 Hz/cm^2). The forward muons or else "standalone" muons, which fall outside ID's acceptance and have no track information, are of major importance in the multilepton physics analyses studied in this thesis. By analyzing $ZZ^{(*)} \rightarrow 4\mu$ Monte Carlo data, produced with PYTHIA [2] event generator, it has been proven that by extending the pseudorapidity coverage from η =2.5 to 2.7, one can increase the $ZZ^{(*)} \rightarrow 4\mu$ yield by ~9%. Figure 5.1 shows the event fraction of the $ZZ^{(*)} \rightarrow 4\mu$ process for different detector acceptances. All four muons must lie in the specified pseudodorapidity range $(-\eta, \eta)$. Therefore the implementation of "standalone" muons in the physics analyses implies the excelent performance of the detector with the best achievable resolution in

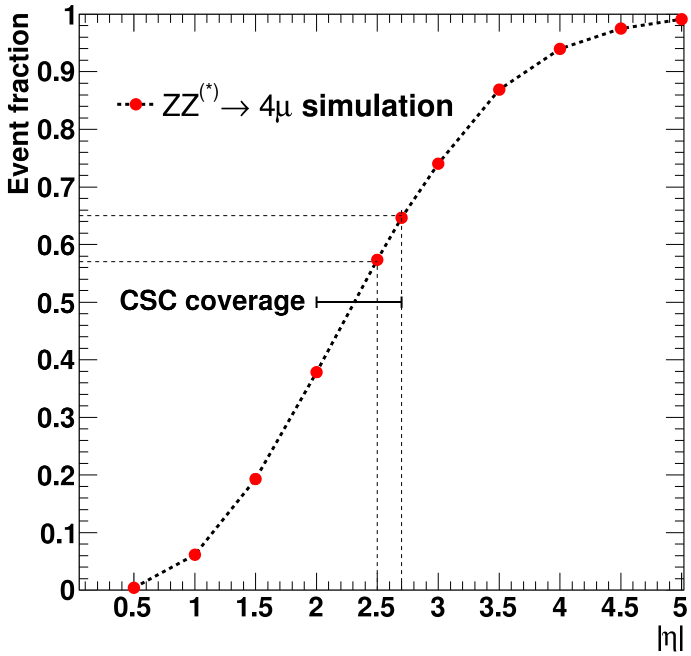

Figure 5.1: Event fraction of the $ZZ^{(*)} \rightarrow 4\mu$ process for different detector acceptances (0.5, 1.0, 1.5, 2.0, 2.5, 2.7, 3.0, 3.5, 4.0, 4.5, 5.0). All four muons must lie in the pseudorapidity region $(-\eta, \eta)$. The CSC coverage is indicated with the continues black line.

muons detection. The first part of the current chapter describes the CSCs while the second part introduces two new algorithms for the improvement of their operation.

5.2 Multiwire proportional chambers

The CSCs are multiwire proportional chambers (MWPC) [3; 4], consisting of a set of thin, parallel and equally spaced anode wires without separating walls, immersed in a Ar/CO_2:80/20 gas. The anode wires are symmetrically located between two cathode planes. A high voltage is applied on the anode wires, while the two cathodes are grounded. Each cathode is lithographically segmented, one with the strips parallel and the other with the strips perpendicular to the anode wires, thus providing us with two independent measurements. According to the direction of the toroidal magnetic field ($\overrightarrow{B} = B\widehat{\phi}$) and the radial direction of the anode wires, the cathode with the strips perpendicular to the anode wires provides the precision coordinate, η, while the

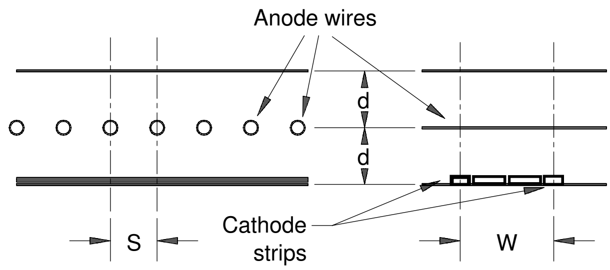

Figure 5.2: A schematic structure of a single CSC layer.

one with the strips parallel to the wires provides the second coordinate, ϕ. The above description corresponds to the schematic structure of a single layer illustrated in Figure 5.2. The anode wire pitch, s, is fixed at 2.54 mm and the cathode read out pitch, W, is 5.08 mm. The distance between the anode wires and the cathodes, d, is equal to the anode wire pitch.

The cathodes providing the precision coordinate consist of 192 strips, while the cathodes responsible for the ϕ measurement consist of 48 strips. The strips, orthogonal to the wires, are finer than the parallel ones, since a better resolution is needed in the direction of the magnetic field (bending direction). The corresponding resolution in the bending direction is 60 μm per CSC plane and 5 mm in the non-bending direction. The difference in scale results from the coarser segmentation of the cathode in the non-bending direction. A complete list with all the parameters and characteristics of the CSCs are summarized in Table 5.1 [6].

In addition to the high spatial resolution the CSCs can provide, there are also present other useful characteristics:

- Good two track resolution.
- The pairing of the measurements in the two coordinates resolves ambiguities if more than one tracks are present.
- Small drift time of electrons ($<$ 45 ns).
- Low sensitivity to neutrons due to the small gas volume and the absence of hydrogen in the gas mixture.

The operation principle of the CSCs is based on the charge multiplication. When a charged particle or photon passes through the gas chamber, it ionizes gas molecules.

Operating Voltage	1900 V	
Gas gain	6×10^4	
Gas mixture	Ar/CO_2 (80/20)	
Number of chambers	2×16	
Number of layers	4×32	
Inclination angle of the chambers	11.6^o	
Anode wire diameter	30 μm	
Anode wire pitch	2.5 mm	
Distance anode wires - cathode strips	2.5 mm	
Distance between the cathods	5 mm	
Distance between two possessed layers	25 mm	
Construction	Large	Small
Distance[a] from interaction point	7661 mm	7294 mm
Distance[a] from beam axis	1493.5 mm	1493.5 mm
Chamber length in r (mm)	1129.2	1176.9
Chamber width (mm)	610.1-1126.7	497.9-747.5
Number of wires per plane	402	250
Number of η strips per plane	574	574
η strip width (mm)	1.519	1.602
η strip gap (mm)	0.25	0.25
Number of η readout strips	192	192
η readout strip pitch	5.308	5.567
Number of ϕ strips	48	48
ϕ strip width (mm)	20.604	12.522
ϕ strip gap (mm)	0.4	0.4
ϕ readout strip pitch (mm)	21.004	12.922

[a] With respect to the center of the chamber.

Table 5.1: ATLAS CSC parameters - CSC operating values and technical characteristics. The values have been taken from [6].

As a consequence, the electrons released travel towards the anode wires. During their course they are accelerated by the strong electric field around the wire, ionizing more of the gas molecules. This results in a cascade of electrons deposited in the anode wires and the induced charge is measured in the cathode strips in four consecutive samples with 50 ns difference in order to have sufficient information for the pulse shape (see Section 5.4). A schematic view of the electric field as well as the isochrone lines is presented in Figure 5.3a[1], while the principle of operation is illustrated in Figure 5.3b[2].

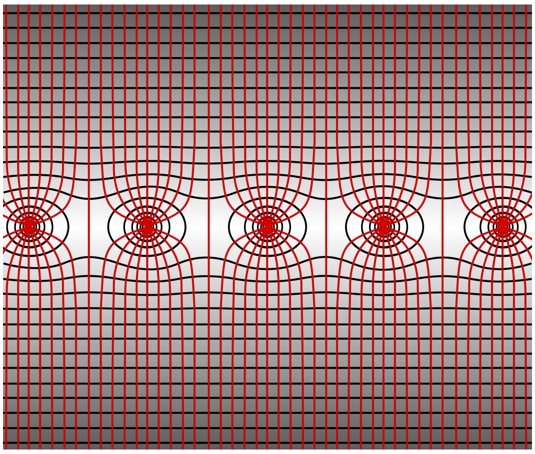

(a)

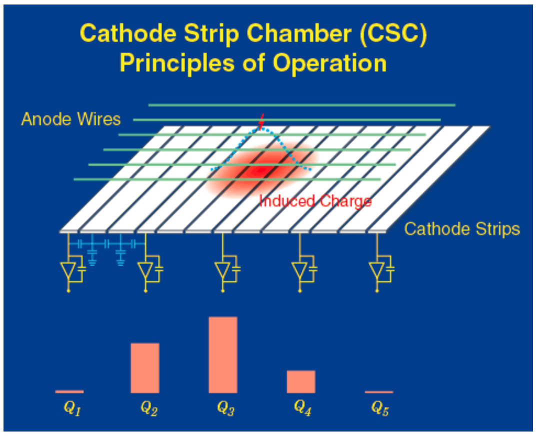

(b)

Figure 5.3: (a) Electric field of a multiwire proportional chamber - Isochronous lines (black) and electric field lines (red) of a multi-wire proportional chamber. (b) The particular cathode geometry is called two intermediate strips. With this geometry one can improve the position linearity using capacitive charge division.

The precision coordinate is obtained by a relative measurement of charges induced by the avalanche on adjacent cathode strips (see Figure 5.4), called clusters, by determining the center of gravity of the induced charge. The center of gravity (c.g.) is given by the equation:

$$x_{c.g.} = \frac{\sum_{i=1}^{N} x_i q_i}{\sum_{i=1}^{N} q_i} \tag{5.1}$$

[1]Image source: $http://en.wikipedia.org/wiki/Wire\_chamber$

[2]Image source: $http://www.inst.bnl.gov/programs/gasnobledet/hepnp/csc.shtml$

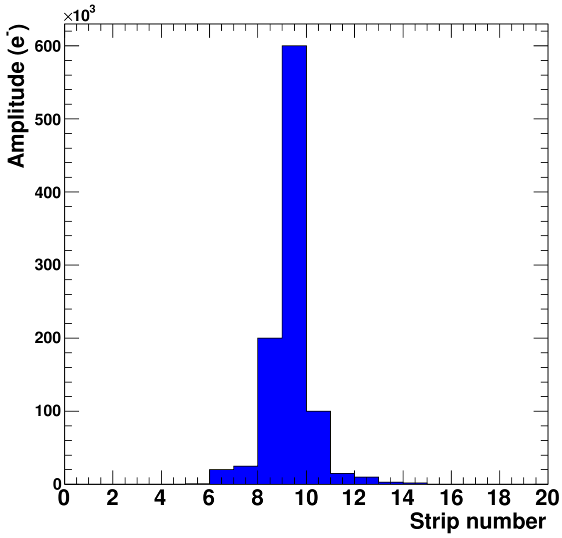

Figure 5.4: Example of a cluster formation in the precision cathode - The $x-$axis represents the active strips of the layer participating in the cluster formation.

where $x_i = iW$, W is the cathode readout pitch and q_i is the corresponding measured charge. If the charges are measured with an r.m.s error of σ then the uncertainty in $x_{c.g.}$ is

$$\delta x_{c.g.} = \frac{\sigma}{Q}\sqrt{2\sum_{i=1}^{N} x_i^2} \tag{5.2}$$

As a concequence, the resolution in the muon position, or else hit position, depends on the number of strips used. Monte Carlo studies have shown that the optimum number of strips lies between three and five strips. For less than three strips the resolution is getting worse due to insufficient information while the usage of more than five strips increases the resolution slowly because the electronic noise of more channels is added in quadrature.

Other effects degrading the spatial resolution of the CSCs are the inclined tracks, the Lorentz angle and $\delta-$electrons, all of which cause non-local charge depositions. In order to overcome the effect of the inclined tracks, the chambers have been tilted by an angle of 11.59^o, so that the tracks are normal to the plane of the chambers.

5.3 Layout of the CSC subdetector

The CSCs are positioned on the two innermost wheels, one in each end-cap. Each wheel is perpendicular to the beam axis and consists of eight large and eight small chambers, placed alternately in the $x-y$ plane. The chambers' distance from the beam axis is 1.5 m, while the distance of the wheel from the IP is 7.5 m. Figure 5.5 shows the hit position of muons from data as they have been detected from the CSCs. Figures 5.5a represent the local position of muons on the chambers, thus all hits are appeared on the same chamber. The histograms of Figures 5.5b show the geometry of the chambers after a rotation transformation going from the local to the global coordinates using the rotation:

$$\begin{pmatrix} x' \\ y' \end{pmatrix} = \begin{pmatrix} \cos\phi' & -\sin\phi' \\ \sin\phi' & \cos\phi' \end{pmatrix} \begin{pmatrix} x \\ y \end{pmatrix} \tag{5.3}$$

where x' and y' are the global coordinates, x and y are the local coordinates of the clusters and ϕ' is the angle between the radial center of the chamber and the $x-$ axis, equal to $n \cdot 22.5^o$ (where n is the chamber's number). The deep blue color represents the large chambers and the light blue the small ones.

Each chamber consists of four layers (see Figure 5.2) with which four pairs of $\eta - \phi$ measurements can be achieved. The combination of these measurements provides the track segment of each chamber [7].

5.3.1 Readout electronics

The CSC electronics are categorized as on-detector and off-detector electronics. The on-detector electronics, are used for charge amplification and signal shaping. The shaped pulses are sampled every 50 ns and the analog pulse height information is stored for the duration of the Level-1 trigger latency [10]. The selected pulse shape is bipolar, with peaking time 70 ns (see Figure 5.6b), which minimizes the effects of low frequency noise due to pile-up [11]. Upon receipt of a Level-1 trigger accept, four samples for each strip are digidized and transmitted to off-detector electronics through fiber-optic links [8].

The off-detector electronics consist of the Readout Drivers (RODs). Each ROD handles the data of two CSC chambers and is responsible to read out the detector,

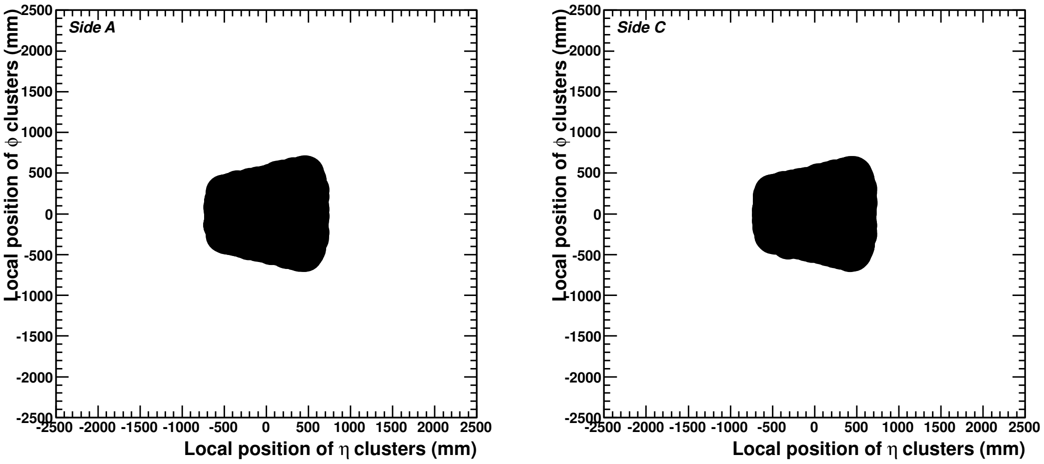

(a)

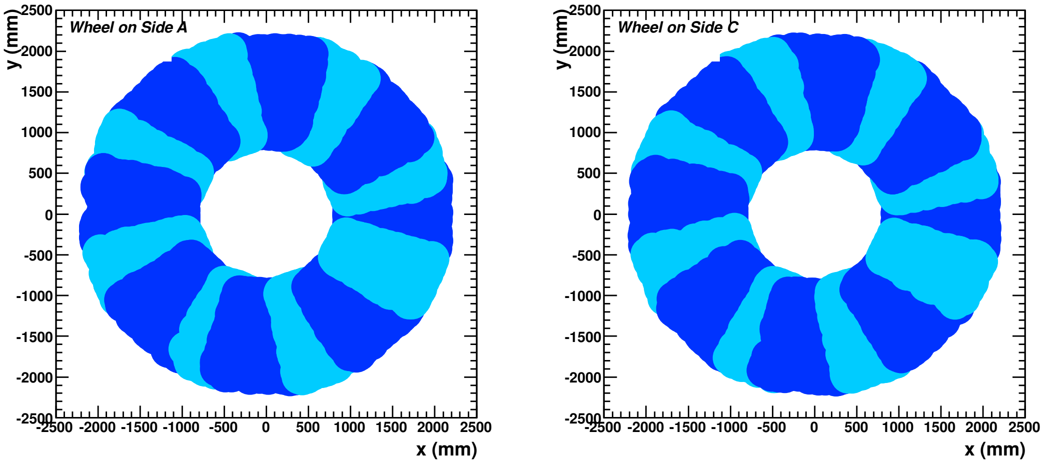

(b)

Figure 5.5: Hit position of data recorded from CSCs at (a) local and (b) global coordinates. The left and right histograms represent the chambers on Side A and Side C respectively. One can arrive at the plots below by applying a rotation transformation to the local coordinate of the clusters.

supress signals below a threshold cut, reject out-of-time signals, apply calibration constants and send data to the ATLAS TDAQ system [10; 12]. Specifically, the processing of the digital signal is as follows: As a first step, a fast algorithm rejects signals below threshold, while the channels (strips) above threshold and their nearest neighbors are flagged. In the second step, the processing is performed on the flagged channels in order to find the channel with the largest signal within each contiguous group of channels, called cluster. Once the channel is found the peaking time of the signal is calculated. The four time samples recorded from each strip provide information of the pulse shape. The three largest samples which are located on the positive lobe of the bipolar waveform are used to define a parabola. The peaking time is then determined from its maximum (see Figure 5.6a). Depending on whether the trigger arrived on (signals are marked as Phase 0) or mid-way (signals are marked as Phase 1) between the 50 ns sampling clock (see Figure 5.7), the second or third time sample is the largest (see Figure 5.8). This results in a phase ambiguity between the two clocks which was believen that can be resolved by subtracting 25 ns in the peaking time of the Phase 1 signals. Further studies on the calculation of the signal peaking times have shown a systematic shift of 10 ns in the peaking time distributions of Phase 1 clusters. Figure 5.9 shows the peaking time distributions after parabola fit. The shoulders presented in the case of data is a direct result of the three points fit.

The next sections presents the studies performed in this thesis in order to resolve the phase ambiguity between the two clocks.

5.4 Signal sampling

As it has been noted in the previous section, the sampling frequency is 20 MHz but the on-detector electronics can also be adapted to 40 MHz. Due to constraints from the trigger rate and the fiber-optic link bandwidth, a 20 MHz sampling frequency is preferred.

The bipolar pulse shape has been studied in reference [13] and can be described by the equation:

$$f(t) = \frac{A_p}{A_n}\left(1 - \frac{z}{n'+1}\right) z^n e^{-z} \tag{5.4}$$

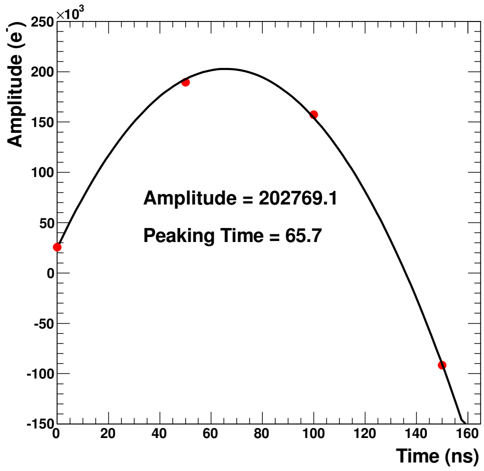

(a)

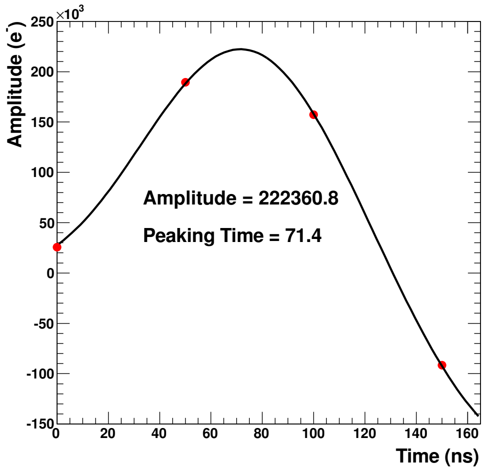

(b)

Figure 5.6: Example of a (a) parabola and (b) bipolar fit on the four samples. The parameters, amplitude and peaking time, as have been obtained from the fit are written on each graph. The pulse shape corresponds to the bipolar waveform.

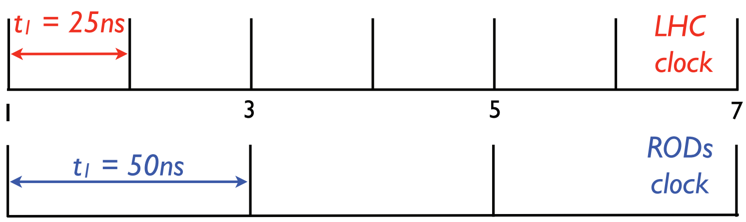

Figure 5.7: A time flow of the LHC and the RODs clock. The two clocks are synchronized only for the odd values (Phase 0 clusters). At the even values a 25 ns subtraction is needed and the clusters are marked as Phase 1 clusters.

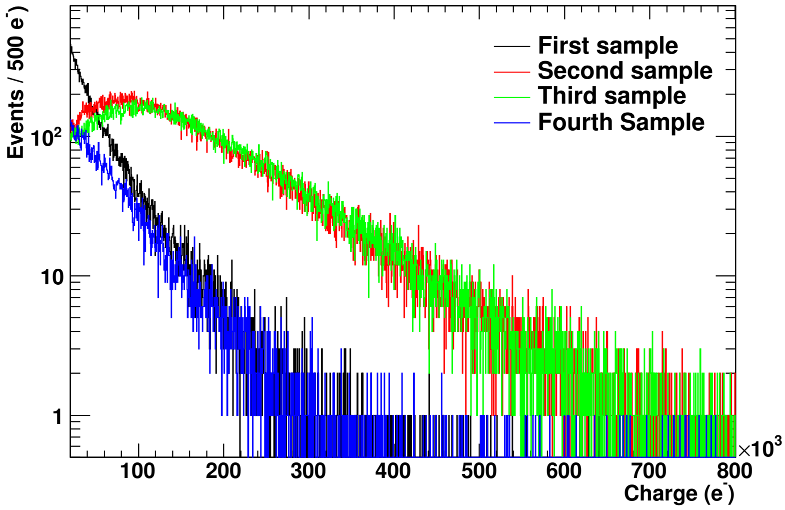

Figure 5.8: Charge distributions of the four consecutive samples.

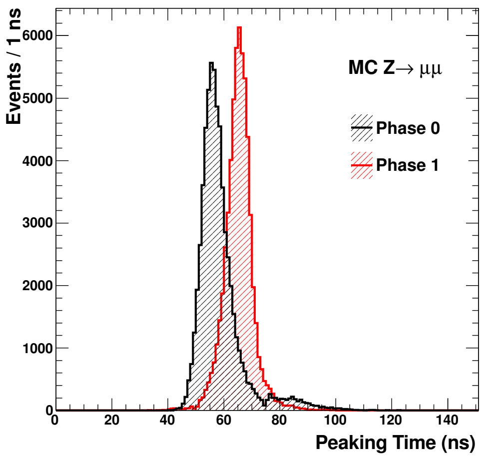

(a)

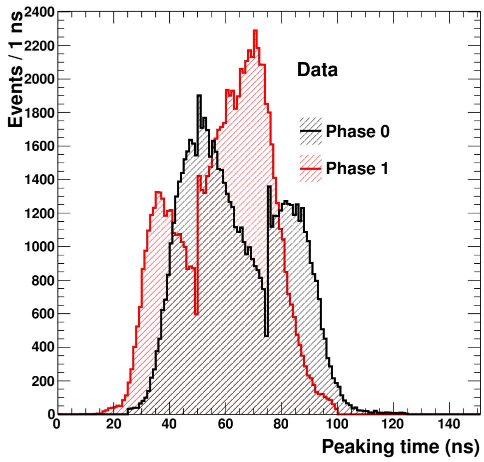

(b)

Figure 5.9: Peaking time distributions after a parabola fiton (a) MC $Z \to \mu\mu$ events and (b) data from run 153565. The Phase 1 distributions are after the 25 ns subtraction.

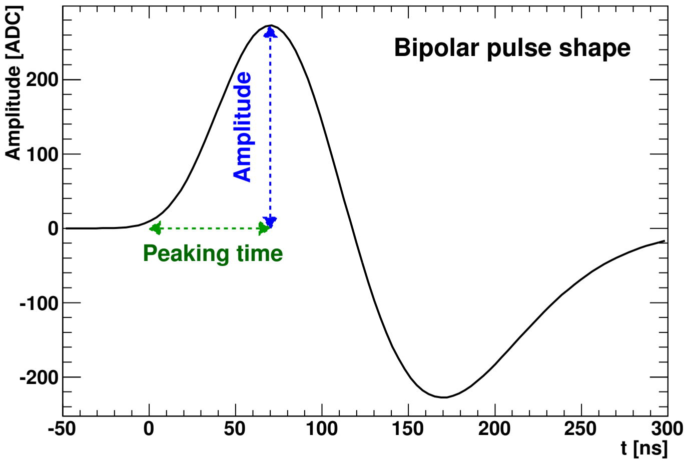

Figure 5.10: The bipolar pulse shape.

where $z = \frac{t-t_0}{t_w}$. For negative values of z the equation returns zero. The constant parameters $n = 12$ and $n' = 11.65$, have been determined empirically [13] and they are associated with the characteristics of the shaper. The other parameters are the pulse amplitude A_p, the pulse starting time t_0 and the width of the bipolar pulse t_w. A_n is the normalization constant equal to

$$A_n = f(z_{max}) = z_{max}^n \left(1 - \frac{z_{max}}{n' + 1}\right) e^{-z_{max}} \tag{5.5}$$

where the maximum of the pulse is observed at

$$z_{max} = \frac{1}{2}\left(n + n' + 2 - \sqrt{(n + n' + 2)^2 - 2n(n' + 1)}\right). \tag{5.6}$$

The peaking time is related with the pulse starting time via:

$$t_{max} = t_o + t_w z_{max} \tag{5.7}$$

The bipolar pulse and the parameters defining its shape is shown in Figure 5.10 .

The phase ambiguity described in Section 5.3.1 could be resolved by using a bipolar fit on the consecutive samples instead of parabola, as is shown in Figure 5.11. The width of the distributions is directly connected to the electrons' drift time. Due to CPU time limitations though, the direct usage of a bipolar fit on the four samples is not recommended.

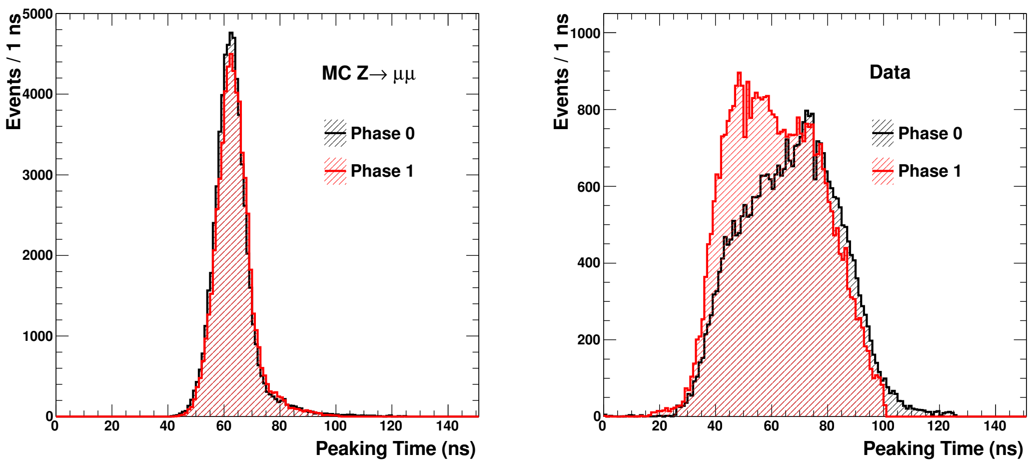

(a) (b)

Figure 5.11: Peaking time distributions after bioplar fit on (a) MC $Z \to \mu\mu$ events and (b) data from run 153565. The Phase 1 distributions are after the 25 ns subtraction.

A direct result of the distributions disagreement (see Figure 5.9) is a worse resolution in the calculation of the peaking times using the parabola fit. In addition, the small differences in the amplitude measurement between the parabola and the bipolar fit (see Figure 5.6) have as a consequence small shifts in the calculation of the hit position.

5.4.1 Time and position correction functions

Extensive studies have been carried out in order to build two correction functions which produce comparable results with the ones produced from the bipolar fit and also to satisfy the CPU time restrictions (1 μs). The two functions are based on the correlation of the bipolar and parabola fit peaking times and amplitudes.

The datasets used in this study are samples enriched in muons since in the analysis the signal are clusters formed by muons. The data correspond to a muon inclusive sample and have been recorded during 2010 (run 153565) and the MC sample are muons resulting from Z decays. The two samples are summarized in Table 5.2.

In order to reduce the background from neutrons and γ radiation contributing to the signal, clusters which do not form a track segment are rejected. This criterion has only be applied in the case of data, where 50% of the single clusters is a product of

Dataset - Run	Process	Generator	Events
105145	$Z \to \mu\mu$	PYTHIA	10000
153565	Inclusive muon sample	LHC	294508

Table 5.2: Samples used for the construction of the correction functions.

these processes [9]. In addition, the following quality cuts have been applied on both MC and data:

- Remove the cases where sample 1 or sample 4 had the highest charge (Q) value.
- Sample 2 and 3 must have charge values above threshold, Q $\geq$ 20000 or greater than 18 ADC counts[1].

5.4.2 Peaking time correction function

The correction function used to correct parabola's peaking times is shown in Figure 5.12. Specifically, this 2D histogram shows the correlation between bipolar's and parabola's peaking times. The blue curve refers to MC events and the red line to LHC data. Due to the exclusion of the cases where the first or the last sample had the highest charge values, peaking times $t < 25$ ns and $t > 125$ ns are represented with an empty space. In order to extend the correction function in these regions, a toy Monte Carlo has been developed based on the bipolar function described in Section 5.4. In specific, the toy MC has been built as follows: with a fix peaking time in the bipolar function, four random samples were generated in time intervals of 50 ns. The generated samples were then fitted with a parabola and a bipolar function for the calculation of the peaking times and the amplitude. This procedure has been repeated for peaking times from 0 to 150 ns with a step of 0.2 ns. The toy MC result is presented with the black curve in Figure 5.12. Comparing the three different samples, one can see the good agreement between the data and the results from the toy MC. The small divergence of the Monte Carlo sample is due to insufficient description of the detector's geometry by the MC. To conclude, the good agreement between data and toy MC calls on the usage of toy MC values for the correction of the parabola's fit results.

[1] One ADC count corresponds to 1100 electrons.

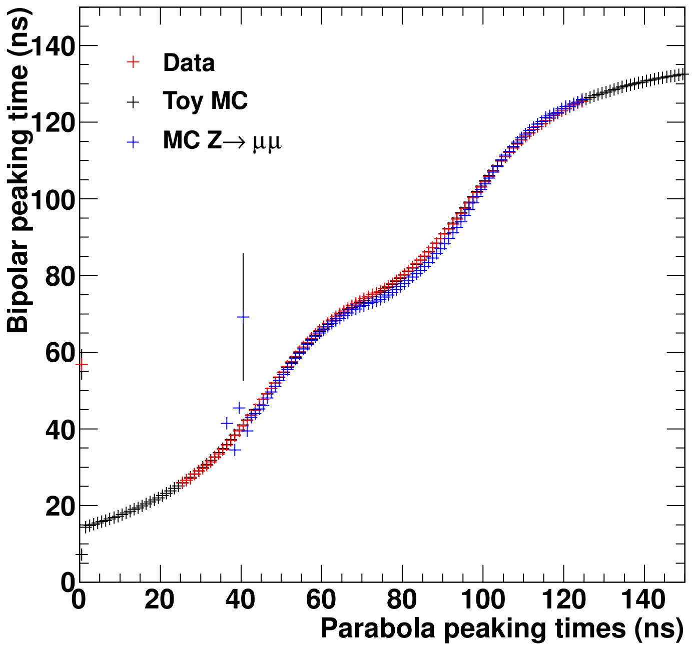

Figure 5.12: Bipolar vs Parabola peaking times.

Figure 5.13a shows the bipolar's fit peaking time versus the true bipolar's peaking time from toy MC. The true one is the peaking time given to the toy MC in order to produce four random samples. The first order polynomial fit in 5.13a validates the results of the toy MC. The stability histogram of Figure 5.13b shows how the fit peaking time fluctuates with respect to the true bipolar peaking time. The fluctuations are more intense at the borders ($t_{bipolar} < 20$ ns and $t_{bipolar} > 130$ ns) where a 5 ns difference is expected. For the rest of the time spectrum on average ∼2 ns difference is found. The results of the parabola peaking times and the corrected ones compared to bipolar fit's are compared in Figure 5.14, where the residuals are shown. A gaussian fit on the left distribution produces a relative error of 0.04%. The corrected peaking time distributions for MC and data are presented in Figures 5.15a and 5.15b respectively. The shape of the distributions is such due to the fact that they superimpose many detector optical links transmitting data from the on-detector to the off-detector electronics. As a consequence, each link can have a timing offset relative to the other links and this leads to the small shift between Phase 0 and Phase 1 distributions.

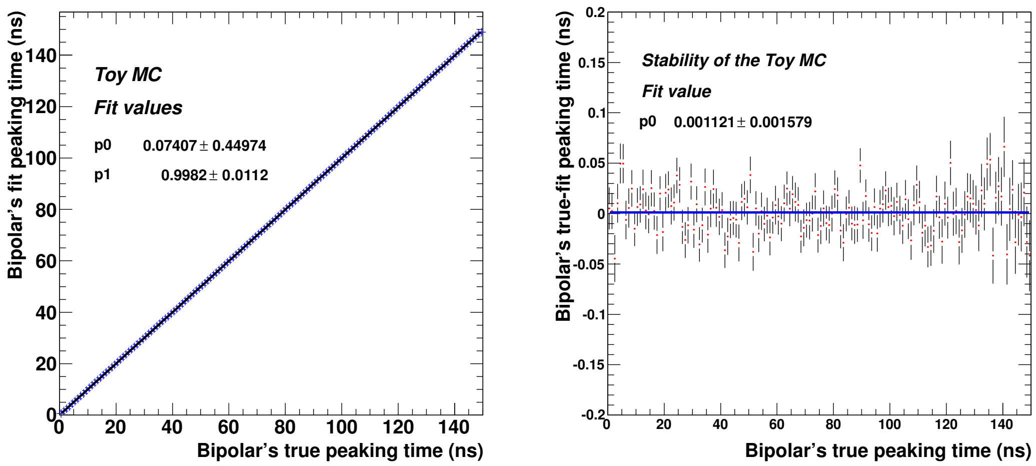

(a) (b)

Figure 5.13: (a) Results of the toy MC algorithm. The fit results validate the usage of the toy MC. (b) True minus fit bipolar's peaking times vs true bipolar's peaking times. A zero order polynomial fit is also shown on the plot. The largest divergencies from the straight line occures in the boundaries as expected.

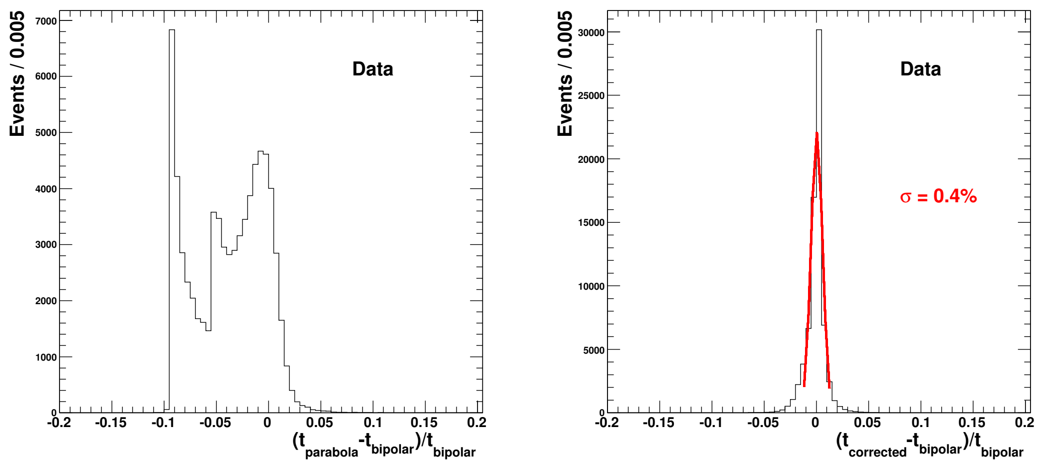

(a) (b)

Figure 5.14: Relative peaking time errors - (a)Residual of parabola fit results with respect to bipolar's fit results (b) Residual of the corrected peaking times with respect to bipolar's fit results. A gaussian fit is also shown with $\sigma = 0.4\%$.

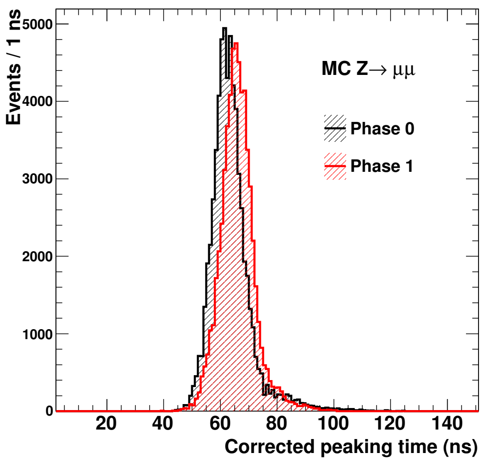

(a)

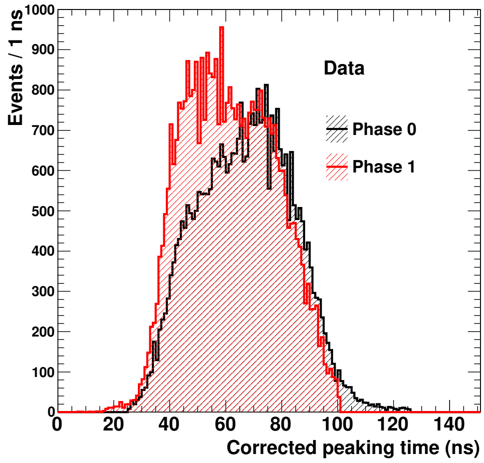

(b)

Figure 5.15: Corrected peaking time distributions for (a) MC $Z \rightarrow \mu\mu$ events and (b) data from run 153565.

5.4.3 Correction function of the position

The position of the clusters is directly connected with the cluster charge and can be improved by correcting the amplitude of the parabola's fit. Due to the dependence of the charge from the peaking time, a new correction function has been developed, by comparing the bipolar and parabola amplitude. The 2D plot in Figure 5.16 shows the correlation of the variables which have been selected to correct the position of clusters for five different ranges of amplitudes' values. The quantity of the y-axis, $(Amplitude_{Bipolar}\text{-}Amplitude_{Parabola})/Amplitude_{Bipolar}$, is the relative error whereas the x-axis represents the bipolar peaking time. As can be seen, the correlation of the two variables is independent of the amplitude's value, allowing the usage of a common function for all possible amplitudes' value. Figure 5.17 represents the position correction function and is the profile histogram of Figure 5.16. The black points represent the data and the red points refer to the results of the toy MC (see Subsection 5.4.2).

A comparison of the amplitude distributions which follow the Landau distribution are shown in Figures 5.18a and 5.18b. The first one refers to Phase 0 precision clusters and the second one to Phase 1 η clusters. The black line corresponds to the parabola

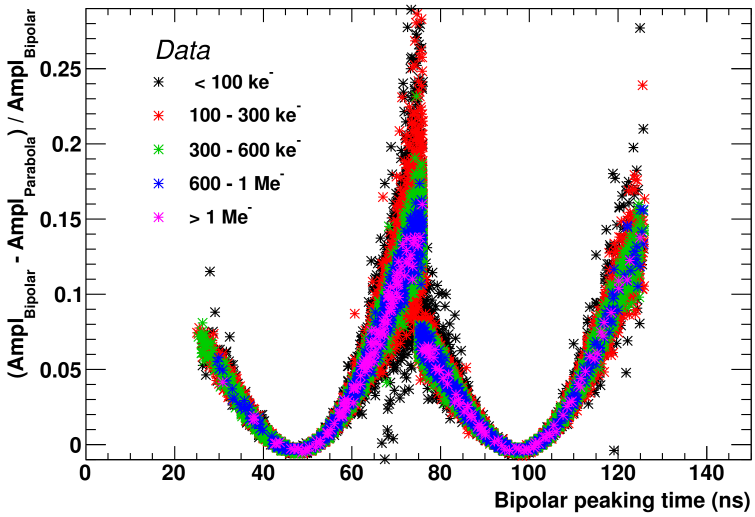

Figure 5.16: Correlation of the variables been selected to built the position correction function for different amplitude values.

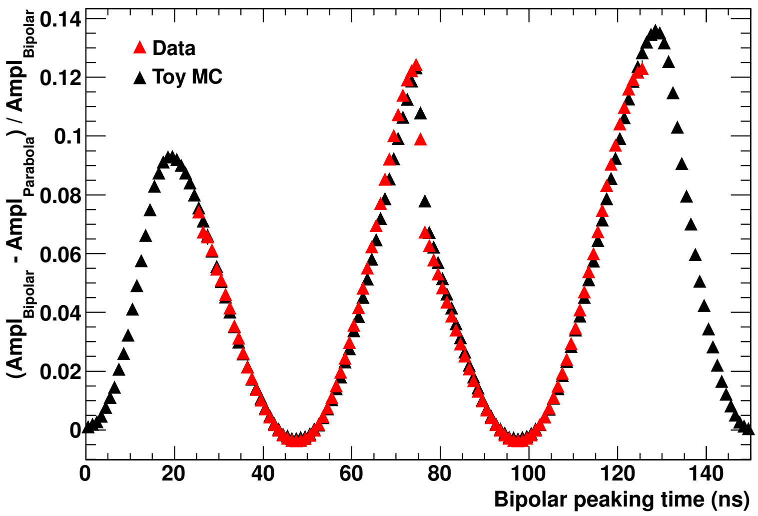

Figure 5.17: Position correction function.

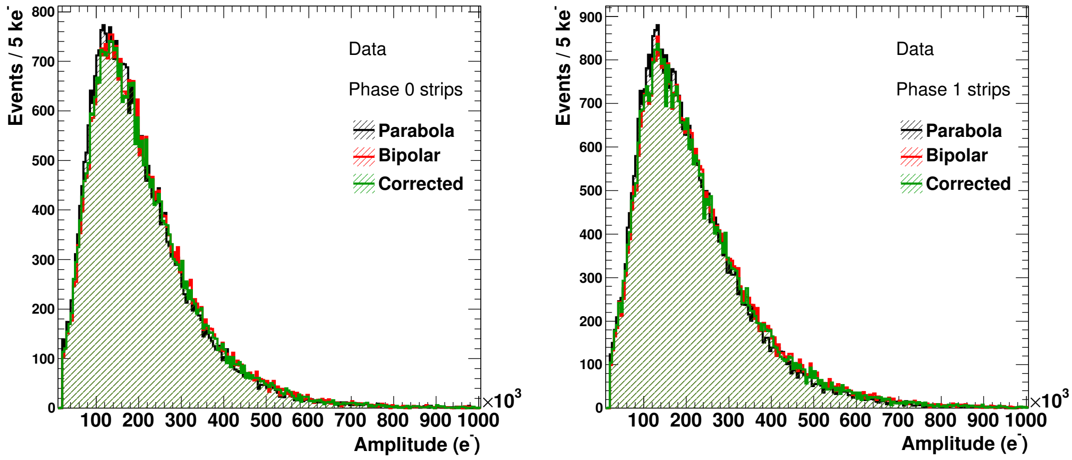

(a) (b)

Figure 5.18: Amplitude distributions for (a) Phase 0 and (b) Phase 1 signals. The black color refers to the parabola fit, red color to the bipolar fit and the green color to the correction.

fit, the red line to the bipolar amplitude and the green line is the corrected parabola. The resolution histogram in Figure 5.19a shows that by using the parabola fit for the amplitude extraction, the relative uncertainty with respect to the bipolar result can reach 20%, whereas by using the corrected values the gaussian fit of the distribution in Figure 5.19b produces 0.6% relative error.

5.5 Summary

The performance of the CSCs, in terms of position and peaking time resolution of the clusters formation have been studied using the first data delivered from LHC. Two correction functions have been constructed to improve the position and the peaking time of the clusters, with relative errors of 0.6% and 0.4% respectively. The resulting algorithms have been implemented to the ATLAS software and are used from the off-detector electronics for the selection of muon clusters.

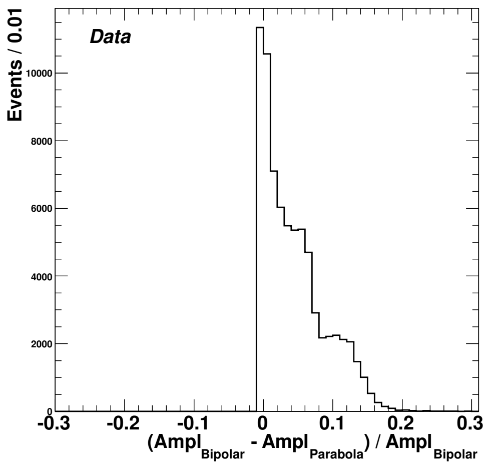

(a)

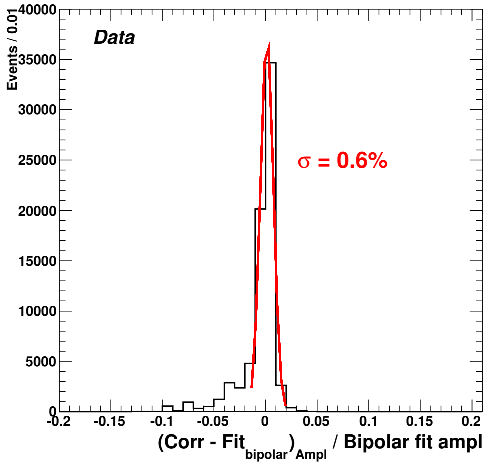

(b)

Figure 5.19: Relative amplitude errors of (a) the parabola and (b) the corrected amplitude values with respect to bipolar's fit amplitude. A gaussian fit on the relative amplitude error of the corrected value, produces a 0.6% systematic error.

Bibliography

[1] Atlas Collaboration,"Muon Spectrometer Technical Design Report", CERN/LHCC/97-22 (1997) 51

[2] T. Sjostrand, S. Mrenna and P. Skands, "Pythia 6.4 physics and manual", JHEP 0605 (2006) 026. 51

[3] G. Charpark, R. Bouclier, T. Bressani, J. Favier and C. Zupanic, "The use of multiwire proportional chambers to select and localize charged particles", Nucl. Instrum. Meth. 62 (1968) 262. 52

[4] E. Mathieson, "Induced charge distribution in proportional detectors" (1991). 52

[5] https://twiki.cern.ch/twiki/bin/viewauth/Atlas/CscReconstruction.

[6] J. Wotschack, "ATLAS Muon Chamber Construction Parameters for CSC, MDT and RPC chambers", ATL-MUON-PUB-2008-006. 53, 54

[7] E. Etzion, D. Primor, G. Mikenberg, N. Amram, H. Messer, "The use of cluster quality for track fitting in the CSC detector", Proceedings of 2006 IEEE NSS, San Diego, California, USA, November 2006, arXiv:physics/0612129v1 [physics.data-an]. 57

[8] S. Junnarkar, A. Kandasamy, P. O'Connor, "Advanced front end signal processing electronics for ATLAS CSC system: Status and post production performance", Prepared for the 11th Workshop on Electronics for LHC and Future Experiments (LECC 2005), Heidelberg, Germany, 12-16 September 2005. 57

[9] J. Dailing et all., "Performance and radiation tolerance of the ATLAS CSC On-Chamber Electronics", prepared for 6th Workshop on electronics for LHC experiments. Cracow, Poland, 11-15 Sep 2000. 64

[10] J. Dailing et al., "Off-detector electronics for a high-rate CSC detector", IEEE Trans. Nucl. Sci. 51 (2004) 461. 57, 59

[11] P. O'Connor et all, "Readout Electronics for a High-rate CSC Detector", Proceedings of the 5th Workshop on Electronics for LHC Experiments, Snowmass, Colorado, USA 20 - 24 September 1999. 57

[12] I. G. Eschrich, "Readout Electronics of the ATLAS Muon Cathode Strip Chambers", In press. 59

[13] K. Nikolopoulos, "Discovery Potential for the Standard Model Higgs $\rightarrow ZZ^{(*)} \rightarrow 4l$ and Contributions to Muon Detection in ATLAS", Ph.D Thesis (2010). 59, 62

..Data started flowing holding the key to the biggest mysteries of our universe...

Chapter 6

Testing the ATLAS detector with early data delivered from LHC using $Z/\gamma^* \rightarrow \ell\ell$ events

This chapter describes the methodology followed towards the first Z inclusive production cross section measurement at $\sqrt{s} = 7$ TeV, by analyzing the first proton-proton collisions of LHC [1; 2; 3]. A process which can be used as standard candle for these studies will follow in this thesis.

6.1 Introduction

In this chapter, the procedure followed to calculate a fiducial ($Z/\gamma^* \rightarrow ee$) and a total Z inclusive production cross section is explained step by step. The analysis skeleton built to detect $Z \rightarrow ee$ events is discussed and the systematic uncertainties entering the cross section calculation are presented. The data-driven technique utilized to estimate the QCD background and the systematic uncertainties in the background estimation are explained in detail. Finally, the results of the fiducial and the total cross section are shown.

6.2 Data and Monte Carlo samples

6.2.1 Collision data

The analysis is based on a data sample at $\sqrt{s} = 7$ TeV proton-proton collisions collected between April and June 2010. The data has been collected during stable beam operation and required all ATLAS sub-detectors operating in the range $(93 - 98\%)$. The selection of the good events was achieved through the usage of a Good Runs List [4] providing the good luminosity blocks of each run. All data are processed consistently in the May 2010 reprocessing campaign. Table 6.1 summarizes the data periods used in the analysis with their corresponding run numbers and integrated luminosities.

Data period	Run number range	Integrated luminosity (nb^{-1})
A	152166 - 153200	0.4
B	153565 - 155160	8.2
C	155228 - 156682	8.5
D	158045 - 159224	299.2
Total	152166 - 159224	316

Table 6.1: Data used in the Z inclusive studies - The samples' total integrated luminosity is 316 nb^{-1}.

6.2.2 Simulated Monte Carlo samples

The MC samples were generated with PYTHIA [5] and the ATLAS detector was simulated with GEANT4 [6]. The parton distribution functions (PDF) are modeled with MRST LO* [7]. Table 6.2 summarizes the MC samples used in the analysis with their corresponding number of events and cross sections. The quoted cross sections were used to compute the luminosity of each sample and then normalize the expected number of events of each data sample to the luminosity of the data. The cross section of the QCD multijet sample has been taken directly from PYTHIA, while the cross sections of the $Z \to ee/\tau\tau$ were taken from the FEWZ program [8] based on the NNLO calculations. Events with dileptons from Drell-Yan ($10 < M_{\ell\ell} < 60$ GeV) are not included in the PYTHIA samples. The uncertainties on the cross-sections arise from factorization and renormalization scale dependence, choice of PDF and the size of the correction from

NLO to NNLO. The total uncertainty is about 5% and is taken as an uncertainty on any event count predictions normalized using these cross-sections.

MCID	Process	Generator	Events	σ·BR [nb]
106046	$Z \to ee$	PYTHIA	$1 \cdot 10^6$	0.99±0.05 NNLO
106052	$Z \to \tau\tau$	PYTHIA	$2 \cdot 10^6$	0.99±0.05 NNLO
105200	$t\bar{t}$	MC@NLO	$1 \cdot 10^6$	0.16±0.01 NLO
105802	QCD	PYTHIA	$10 \cdot 10^6$	1.2×10^6 LO

Table 6.2: MC samples used in the $Z \to ee$ inclusive studies. The cross sections quoted are the ones used to estimate the expected number of events. The cross section for the QCD sample is directly from PYTHIA without correcting with the appropriate $k-$factor.

6.3 Electron Reconstruction and identification

6.3.1 Trigger requirement

Events were selected with the hardware-based L1 trigger (see Section 4.2.5). The L1 calorimeter trigger selects photons and electrons within $\eta < 2.5$ based on the energy deposition in the calorimeter. The trigger chain is called "L1_EM10". The selected events are triggered from an electron or a photon if the energy deposition of a $\Delta\eta \times \Delta\phi$ = 0.1×0.1 cluster is greater than 10 GeV.

6.3.2 Electron algorithm description

The ATLAS standard electron reconstruction and identification algorithm [10; 11; 12] is designed to provide electrons with various levels of background rejection optimized for high identification efficiencies for calorimeter transverse energy $E_T > 20$ GeV, over the full acceptance of the ID system. Electron reconstruction begins with a seed cluster of energy of $E_T > 2.5$ GeV, which are formed by a "sliding-window" algorithm. The window size is 3×5 in units of 0.025× 0.025 in $\eta \times \phi$ space, corresponding to the granularity of the second compartment of the EM calorimeter (see Section 4.2.2.1). A matching track, extrapolated to the middle EM calorimeter layer, is searched for in a broad window of $\Delta\eta \times \Delta\phi = 0.05 \times 0.1$ amongst all reconstructed tracks with $p_T > 0.5$ GeV. The closest-matched track to this layer's cluster barycenter is kept as that belonging to the electron candidate. The electron cluster is then rebuilt using

3×7 (5×5) longitudinal towers of cells in the barrel (endcaps). The cluster energy is determined [13] by summing the contributions from the estimated energy deposit in the material in front of the EM calorimeter, the measured energy deposit in the cluster, the estimated external energy deposit outside the cluster (lateral leakage) and the estimated energy deposit beyond the EM calorimeter (longitudinal leakage) [12]. The four-momentum of central electrons (η <2.5) is computed using information from both the final cluster and the track matched to the original seed cluster. The energy is given by the cluster energy. The η and ϕ directions are taken from the corresponding track parameters unless the track contains no silicon hits, in which case η is provided by the cluster's barycenter.

The baseline electron identification selections in the central region $|\eta| < 2.47$ are based on criteria using calorimeter shower parameters, track information and combined variables which provide good separation between isolated or non-isolated signal electrons, background electrons resulting from photon conversions and Dalitz decays (like $\pi^0 \to e^+ + e^- + \gamma$) and jets faking electrons. There are in total three sets of requirements: "Loose", "Medium" and "Tight" [14] and they have been optimized by the egamma ATLAS group [11]. Each set adds additional constraints to the previous requirements for stronger jet rejection at the expense of some identification efficiency loss. The information used from each set is:

- "Loose": this set refers to the basic selections and uses EM shower shape information from the second layer of the EM calorimeter and energy leakage into the hadronic calorimeters as discriminant variables. This set of requirements provides high and uniform identification efficiency but a low background rejection. In specific, the following variables are examined:
  - Lateral shower containment which is defined as the ratio of the energy in 3×7 cells over the energy in 7×7 cells;
  - Lateral shower width defined as $\sqrt{(\sum E_i \eta_i^2)/\sum E_i - ((\sum E_i \eta_i)/(\sum E_i))^2}$ where E_i is the energy and η_i is the pseudorapidity of cell i and the sum is calculated within a window of 3×5 cells;
  - Ratio of E_T in the first layer of the hadronic calorimeter to E_T of the EM cluster (used over the range $|\eta| < 0.8$ and $|\eta| > 1.37$);

  - Ratio of E_T in the hadronic calorimeter to E_T of the EM cluster (used over the range $|\eta| > 0.8$ and $|\eta| < 1.37$).

- "Medium": this set includes all the selections of the "loose" set and provides additional hadronic rejection by evaluating the energy deposit patterns in the first layer of the EM calorimeter, track quality variables and a tighter cluster-track matching variable. The selections are as follows:

  - Shower width, $\sqrt{(\sum E_i(i - i_{max})^2)/(\sum E_i)}$, where i runs ovel all strips in the first compartment of EM calorimeter in a window of $\Delta\eta \times \Delta\phi \approx 0.0625 \times 0.2$, corresponding typically to 20 strips in η and i_{max} is the index of the highest energy strip;
  - Ratio of the energy difference between the largest and second largest energy deposits in the cluster over the sum of these energies in the strip layer;
  - Number of hits in the pixel detector ($\geq$1);
  - Number of total hits in the pixel and SCT detectors ($\geq$7);
  - Transverse impact parameter ($|d_0|$ <5 mm);
  - $\Delta\eta$ between the cluster position in the middle layer and the extrapolated track ($|\Delta\eta < 0.01$);

- "Tight": This set of requirements further rejects charged hadrons and secondary electrons from conversions. It also includes E/p, particle identification using the TRT and discrimination against photon conversions via a b-layer hit requirement and information about reconstructed conversion vertices[15; 16];

  - $\Delta\phi$ between the cluster position in the middle layer and the extrapolated track ($|\Delta\phi| < 0.02$);
  - $\Delta\eta$ between the cluster position in the middle layer and the extrapolated track ($|\Delta\eta| < 0.005$);
  - Ratio of the cluster energy to the track momentum;
  - Tighter transverse impact parameter ($d_0 < 1$ mm);
  - Total number of hits in the TRT. The difference between the measured number of hits and the expected average number of hits is required to be within 15 hits.

- Ratio of the number of high-threshold hits to the total number of hits in the TRT. TRT runs with two thresholds, the low threshold corresponds to ordinary tracking hits, while the high threshold refers to transition radiation hits [15];
- Number of hits in the b-layer ($\geq$1);
- Veto electron candidates matched to reconstructed photon conversions. An explanation on how photon conversions are reconstructed is given in reference [15].

6.3.3 Problematic regions of the calorimenter

Electromagnetic clusters which are located in misbehaving regions of the detector are rejected. The tool has been developed by the egamma performance group and provides information of misbehaving regions by providing a two dimensional map ($\eta - \phi$) for each layer of the calorimeter. The maps were built from the on-line LAr calorimeter monitoring system and notify for:

- the regions affected by major high voltage problems;
- electronic front-end board card not providing output signal, due to a dead optical readout line.

6.4 Pile-up effects event reweighting

Starting from data period D, a significant fraction of events have additional soft interactions in the same bunch crossing as the hard scatter event, called *in-time pile-up*. The number of additional interactions follow a Poisson distribution with a mean determined from the beam parameters. Due to the fact that the mean value of the interactions per bunch crossing is not constant, but varies from bunch crossing to bunch crossing, the best estimator of the number of additional interactions in one event is the number of reconstructed primary vertices.

The MC samples described in Section 6.2.2 have been generated with a mean number of extra pile-up events of 2, while the average number of additional interactions in data is less than 2. In order to correct the MC samples from the pile-up effects, a re-weighting of the MC events depending on the number of primary vertices has been applied. The event weights used on the MC samples are listed in Table 6.3.

Number of primary vertices	MC event weight
1	3.88
2	1.06
3	0.34
4	0.12
5	0.05
6+	0.01

Table 6.3: MC event weights due to pile-up for the Z inclusive measuremet - Monte Carlo event weights for different number of reconstructed primary vertices.

6.5 Event Selection

The selection cuts applied for the detection of $Z/\gamma^* \rightarrow ee$ candidates is similar to the one used for the first Z observation [18]. The series of the cuts is presented in Table 6.4. The loose electron event selections correspond to the cuts which have been applied for the background estimation (see Section 6.8), while the tighter cuts have been used to select the Z candidate events.

In specific,

- Electrons must lie in $|\eta| < 2.47$ but the crack region[1] $1.37 < |\eta| < 1.52$ is excluded;
- All electrons must have $E_T > 20$ GeV and be reconstructed with the standard egamma algorithm described in Section 6.3.2;
- Both electrons must pass the "medium" identification requirements;
- Pair formation. Electrons of the pair are required to have opposite charge;
- The invariant mass of the candidate pairs must be in the mass range [66,116] GeV.

[1]The crack region is the transition from the barrel to the endcaps EM calorimeters (see Section 4.2.2.1) and it is used for maintenance of the solenoid magnet and the ID.

Criterion	Value
Primary vertex	$N_{vtx} \leq 1$ with $N_{tracks} \leq 3$
Trigger	L1_EM10
Loose electron event selection	
Electron selection	2 loose electrons
	$p_T > 20$ GeV, $\eta < 2.47$ but excluding $1.37 < \|\eta\|$ 1.52
Opposite charge	$c_1 \cdot c_2 < 0$
Invariant mass (M_{ee})	$66 < M_{ee} < 116$ GeV (consider all pairs of electrons)
Tighter electron event selection	
Final electron selection	2 medium electrons
Third electron veto	reject events with any additional medium electron(s)
Invariant mass (M_{ee})	$66 < M_{ee} < 116$ GeV

Table 6.4: Series of the selection cuts applied for the detection of $Z \to ee$ candidates.

6.6 The correction factor C_Z and the acceptance A_Z

The cross section is measured within a kinematic fiducial region given by the Equation 6.7. The fiducial volume is defined from the selection cuts:

- $E_T > 20$ GeV;
- $|\eta| < 2.47$ and $1.37 < |\eta| < 1.52$;
- 66 GeV $< M_{ee} <$ 116 GeV (where M_{ee} is the invariant mass of the two electrons).

The correction factor C_Z which appears in Equation 6.7 is calculated from the signal MC sample and represents the fraction of the weighted reconstructed signal events surviving the selection criteria of the analysis ($N_{MC\ rec}$) over the number of generated events passing the fiducial cuts ($N_{mc\ gen\ fiducial}$):

$$C_Z = \frac{N_{MC\ rec}}{N_{MC\ gen\ fiducial}} \tag{6.1}$$

In basic terms, it provides correction to the efficiency, energy resolution and QED radiation. The sources of uncertainties affecting the C_Z value result from uncertainties on the electron reconstruction efficiency and from material effects in the inner detector as well as from uncertainties on the electron energy scale and resolution. A summary of the systematic uncertainties is shown in Table 6.5 [3].

Source	$\delta C_Z/C_Z$ [%]
Trigger efficiency	< 0.2
Material effects, reconstruction and identification	8.8
Energy scale and resolution	1.9
Problematic regions in the calorimeter	2.7
Pile-up	0.2
Charge misidentifiaction	0.5
Final State Radiation modeling	0.3
Theoretical uncertainty (PDFs)	0.3
Total	9.4

Table 6.5: Breakdown of the systematic uncertainties contributing on C_Z. The decomposition has been made such that correlations between the various contributions are negligible.

To calculate the total cross section, given by the Equation 6.9, one must divide the fiducial cross section with the acceptance factor, A_Z, and the branching ratio of Z to decay in electron-positron pairs, $BR(Z \to ee) = 0.036$ [17]. A_Z is a pure MC quantity and is calculated from PYTHIA using the equation:

$$A_Z = \frac{N_{MC\ gen\ fiducial}}{N_{MC\ gen\ all}} \tag{6.2}$$

where $N_{MC\ gen\ all}$ is the number of generated events and $N_{MC\ gen\ fiducial}$ is the number of generated events after the fiducial cuts.

The systematic uncertainty on the acceptance is dominated by the limited knowledge of the proton PDFs and the modelling of the Z boson production at the LHC. The total uncertainty is calculated to be $\pm 3.8\%$ [3].

The computed values of A_Z and C_Z with their systematic errors are summarized in Table 6.6. The statistical uncertainties resulting from the MC samples are negligible.

$Z \to ee$	
A_Z	0.446 ± 0.018
C_Z	0.651 ± 0.061

Table 6.6: The A_Z and C_Z values and their systematic uncertainties.

6.7 Results

6.7.1 Candidates list

Table 6.7 lists the $Z/\gamma^* \rightarrow ee$ candidate events as well as the ones that fail the final invariant mass cut (shown in red color).

Data Period	Run number	Event number	Luminosity block	M_{ee}
B	154817	968871	18	88.81
	155112	112986956	558	87.11
	155160	17950341	333	91.10
C	155569	3028514	234	90.52
	155569	30063992	368	85.30
	155678	13584340	287	90.59
	155678	13304729	286	36.41
	155678	16270287	299	83.69
	155697	31407946	434	94.05
D	158045	1916920	118	84.56
	158116	4099621	127	93.10
	158116	18690615	246	89.32
	158116	16571301	227	93.46
	158299	11317786	411	87.72
	158392	5528736	233	106.46
	158392	5863564	235	85.85
	158392	12592579	292	83.56
	158545	3060495	242	89.21
	158548	8442314	153	91.61
	158548	14203149	187	74.30
	158582	9259901	96	78.75
	158582	13231807	120	85.65
	158582	14434569	126	89.82
	158582	13356393	120	91.56
	158582	44922321	312	77.03
	158582	48541867	334	71.03
	158632	1998176	161	89.51
	158801	25842368	296	92.00
	158801	9719944	204	89.39
	158975	15364408	173	93.70
	158975	8651494	136	85.89
	158975	41530390	332	92.32

Continued on next page

Table 6.7 – continued from previous page

Data Period	Run number	Event number	Luminosity block	M_{ee} (GeV)
	158975	21793243	209	93.88
	158975	30713414	255	98.14
	158975	23374251	218	90.19
	159041	11976617	176	92.55
	159041	10572857	167	105.66
	159041	12606284	179	96.13
	159041	13562051	184	96.03
	159041	36075685	308	68.94
	159041	43284559	344	60.64
	159086	63755995	494	86.10
	159086	13378192	191	83.63
	159086	72145469	540	80.94
	159086	43335033	379	87.43
	159086	43706234	381	2.77
	159086	43783954	382	62.93
	159086	34028709	322	90.89
	159086	2291231	120	89.66
	159086	15158080	202	85.46
	159086	15408477	204	59.39
	159086	65291118	502	42.14
	159086	13054270	189	95.92
	159086	42888841	376	91.26
	159086	24112824	261	85.61
	159086	21963805	247	61.91
	159113	13267323	317	90.20
	159113	42881541	481	88.16
	159113	49530723	516	82.12
	159113	7686188	287	90.08
	159113	4685338	270	90.31
	159113	29318983	407	87.22
	159179	12539738	314	84.48
	159179	4154168	237	90.15
	159179	12289901	312	85.95
	159202	6941331	234	91.20
	159203	3064472	36	85.15
	159203	3601844	42	91.58
	159203	6130908	71	84.71
	159224	3931588	254	91.67
	159224	4517702	259	94.33
	159224	19014851	403	94.07

Continued on next page

Table 6.7 – continued from previous page

Data Period	Run number	Event number	Luminosity block	M_{ee} (GeV)
	159224	20845268	427	86.55
	159224	26596822	496	86.25
	159224	28630240	519	82.48
	159224	37576306	622	16.68
	159224	38502686	632	85.33
	159224	44276181	696	87.53

Table 6.7: $Z/\gamma^* \to ee$ candidates list. The run number, event number, luminosity block and invariant mass of the dielectron candidates. The red color indicates the events failing the invariant mass cut.

6.7.2 Kinematic distributions

The invariant mass spectrum of the above candidates and the transverse momentum of Z, p_T^Z are shown in Figure 6.1.

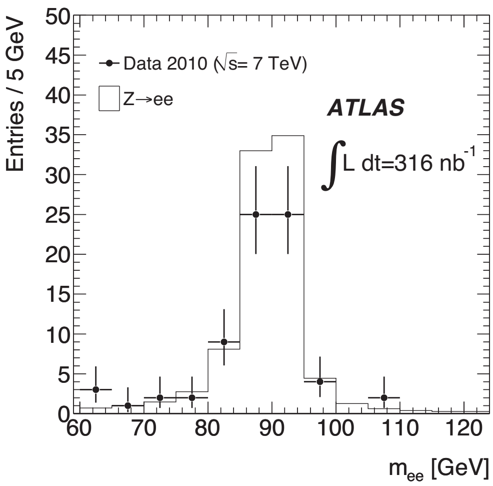

(a)

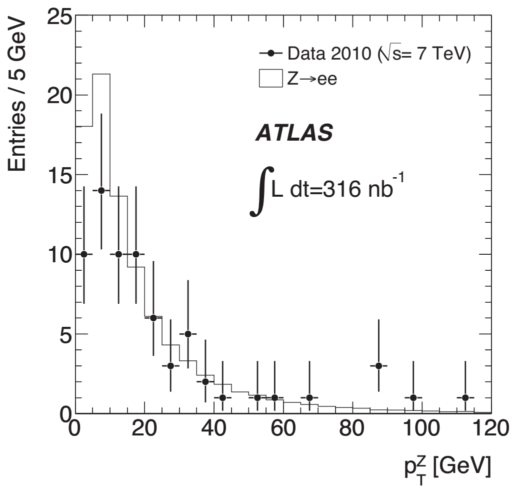

(b)

Figure 6.1: Kinematic distributions of the $Z/\gamma^* \to ee$ candiates at 316 nb^{-1} - (a) Invariant mass distribution and (b) transverse momentum distribution of the $Z \to ee$ candidates. The continuous line corresponds to the MC signal sample normalized to the luminosity of the data (L =316 nb^{-1})and the black points to the data at $\sqrt{s} = 7$ TeV.

6.8 Background Estimation in the $Z/\gamma^* \rightarrow ee$ inclusive channel

This section describes the two techniques used to estimate the QCD background contributing to the $Z/\gamma^* \rightarrow ee$ final state. The first technique uses the invariant mass distribution of the selected loose-loose electron pairs as a template to estimate the QCD contribution under the Z peak. In specific, the model consists of a Breit-Wigner convoluted with a Gaussian function for the signal and a second order polynomial fit for the background. The fitting range was in the mass window $50 < M_{ee} < 130$ GeV. The number of loose electron background candidate events within the mass window $66 < M_{ee} < 116$ GeV was estimated to be 48.5 $\pm$ 6.0 (stat). In order to correct the above number for medium-medium electron pairs, one must calculate the ratio of the medium electrons over the number of loose electrons with $p_T > 20$ GeV, reconstructed using the standard electron algorithm and within the η acceptance of the detector. The parameter is called"rejection factor, ϵ," and it is equal to:

$$\epsilon = \frac{N_{medium\ electrons}}{N_{loose\ electrons}} = 0.137 \pm 0.001(\text{stat}) \tag{6.3}$$

By applying this data-derived rejection factor to each electron in the "loose" pairs

$$N_{bkg}^{two\ medium\ electrons} = N_{two\ loose\ electrons} \times \epsilon \times \epsilon \tag{6.4}$$

a QCD background estimate totalling 0.91 $\pm$ 0.11 (stat) events in the opposite-charge distribution within the Z mass window was calculated.

The systematic uncertainty on the number of background events has been calculated by studying different electron identification definitions (e.g. two electrons before "loose" requirement, one "loose" one "medium" electron candidate) with their corresponding rejection factors. The fit stability was verified by changing the bin size of the invariant mass distribution and replacing the second-order polynomial function with a first-order one. The systematic uncertainty assigned to the number of backgournd events is 0.41. The final number of QCD background events at $\mathcal{L} = 316$ nb^{-1} with all its errors is:

$$N_{bkg} = 0.91 \pm 0.11(\text{stat}) \pm 0.41(\text{syst}) \tag{6.5}$$

The result of the above method has been cross checked using the Same Sign (SS) - Opposite Sign (OS) method and the difference observed in the background calculation (Equation 6.5) were taken into account as an extra systematic source on the background estimation. The SS-OS method was originally used for the estimation of the QCD background from a statistically smaller sample [1] and it is based on counting the events of loose OS and SS pairs which pass the invariant mass cut. Table 6.8 shows the numbers of loose-loose electron pairs as they have been measured from data (first row) and the MC QCD sample (second row).

	OS pass M_{ee}	SS pass M_{ee}
$N^{Data}_{loose-loose}$	39	35
$N^{MC\ QCD}_{loose-loose}$	29	31

Table 6.8: Number of opposite-sign and same-sign events with loose electron pairs which pass the invariant mass cut. The first row refers to data of integrated luminosity 316 nb^{-1} and the second row to the results of the QCD MC sample normalized to the luminosity of data.

By correcting these numbers with the rejection factor of Equation 6.3 as described above, the expected number of background events in the signal region is calculated to be 0.74 ± 0.12 (stat) in data and 0.67 ± 0.11 in the QCD MC sample. Taking into account that the largest contribution of the QCD background results from light flavor quarks where two jets are faking two electrons and assuming that the contribution of heavy flavor quarks decaying semi-leptonically is negligible, the two numbers can be cross checked from the number of events with same-sign pairs passing the invariant mass cut. Those numbers have been found to be 0.67 ± 0.11 (stat) and 0.71 ± 0.11 (stat) in the data and the MC sample respectively and they are in a good agreement with the ones in the opposite-sign category. Table 6.9 summarizes the expected background events of the two categories. The systematic uncertainty can be calculated by finding the difference of the opposite-sign and same-sign events. The final number of the expected background events is

$$N_{bkg} = 0.74 \pm 0.12(\text{stat}) \pm 0.07(\text{syst}) \tag{6.6}$$

The contributions from the $W \to e\nu$, $Z \to \tau\tau$ and $t\bar{t}$ processes have been taken from the corresponding MC samples and their values are 0.11, 0.06 and 0.10 events.

Estimated background	OS pass M_{ee}	SS pass M_{ee}
$N^{Data}_{medium-medium}$	0.74 ± 0.12	0.67 ± 0.11
$N^{MC\ QCD}_{medium-medium}$	0.67 ± 0.11	0.71 ± 0.11

Table 6.9: Comparison of expected number of background events in data and MC. The two numbers agree within error. A cross-check of the method can be done from the same-sign events where a similar number of events is expected. The first row refers to data of integrated luminosity 316 nb^{-1} and the second row to the results of the QCD MC sample normalized to the luminosity of data.

6.9 Cross section measurement

6.9.1 Fiducial cross section

The fiducial cross section can be calculated by subtracting the number of expected background events from the total observed events and then divide with the total correction factor C_Z and the integrated luminosity $\mathcal{L}$, like in equation:

$$\sigma^{fid}_{Z\to ee} = \frac{N^{obs} - N^{Bkg}}{C_Z \cdot \mathcal{L}} \tag{6.7}$$

The fiducial cross section is found to be:

$$\sigma^{fid}_{Z} \times BR(Z \to e^+e^-) = 0.33 \pm 0.04(\text{stat}) \pm 0.03(\text{syst}) \pm 0.04(\text{rmlumi})\text{nb} \tag{6.8}$$

6.9.2 Total cross section

The fiducial cross section can be easily turned into the total cross section by correcting with the acceptance factor A_Z as in the following equation:

$$\sigma^{fid}_{Z\to ee} = \frac{N^{obs} - N^{Bkg}}{C_Z \cdot A_Z \cdot \mathcal{L}} \tag{6.9}$$

The resulting total cross section times the braching ratio $BR(Z \to ee)$ of Z decaying in electron-positron is

$$\sigma^{tot}_{Z} \times BR(Z \to e^+e^-) = 0.75 \pm 0.09(stat) \pm 0.08(syst) \pm 0.08(lumi)\text{nb} \tag{6.10}$$

6.10 Summary

The first production cross section measurement of the Z inclusive channel at $\sqrt{s} = 7$ TeV has been established, analyzing the early data delivered from LHC and recorded from the ATLAS experiment in the period 11 April - 19 July 2010. In total, 70 $Z \to ee$ candidates have been observed while the expected background is 1.18 $\pm$ 0.11(stat) $\pm$ 0.41(syst). The total cross section times the branching ratio of the Z to decay in electron-positron pair has been found to be 0.75 $\pm$ 0.09(stat) $\pm$ 0.08(syst) $\pm$ 0.08(lumi) nb and agrees within error with the NNLO predictions of 0.99 $\pm$ 0.05 nb [8; 9].

Bibliography

[1] The ATLAS Collaboration,"Measurement of the $W \to \ell\nu$ production cross section and observation of $Z \to \ell\ell$ production in proton-proton collsions at $\sqrt{s} = 7$ TeV with the ATLAS detector", ATL-CONF-2010-051. 73, 86

[2] The ATLAS Collaboration,"Measurement of the $Z \to \ell\ell$ production cross section in proton-proton collsions at $\sqrt{s} = 7$ TeV with the ATLAS detector", ATL-CONF-2010-076. 73

[3] The ATLAS Collaboration,"Measurement of the $W \to \ell\nu$ and $Z/\gamma^* \to \ell\ell$ production cross sections in proton-proton collsions at $\sqrt{s} = 7$ TeV with the ATLAS detector", JHEP 1012 (2010) 060. 73, 80, 81

[4] J. Stelzer, A. Hoecker, "The Run Query Tool", ATLAS e-News, 23 February 2011. 74

[5] T. Sjostrand, S. Mrenna and P. Skands, "Pythia 6.4 physics and manual", JHEP 0605 (2006) 026. 74

[6] S. Agostinelli at al., "Geant4: A simulation toolkit", Nucl. Instrum. Meth., A506:250, 2003. 74

[7] A. Sherstnev and R. S. Thorne, "Parton Distributions for LO Generators", Eur. Phys. J., C55:553575, 2008. 74

[8] C. Anastasiou, L. J. Dixon, K. Melnikov and F. Petriello, "High precision QCD at hadron colliders: Electroweak gauge boson rapidity distributions at NNLO", Phys. Rev., D69:094008, 2004. 74, 88

[9] R. Hamberg, W. L. van Neerven, and T. Matsuura, "A complete calculation of the order a_s^2 correction to the Drell-Yan K factor", Nucl. Phys. B359 (1991) 343; Erratum-ibid. B644 (2002) 403. 88

[10] ATLAS Collaboration, "Electron and photon reconstruction and identification in atlas: expected performance at high energy and results at $sqrts = 900$ GeV", ATLAS-CONF-2010-005. 75

[11] ATLAS Collaboration, "Expected electron performance in the ATLAS experiment", ATL-PHYS-PUB-2011-006. 75, 76

[12] ATLAS Collaboration, "Electron performance measurements with the ATLAS detector using the 2010 LHC proton-proton collision data", Eur. Phys. J. C72 (2012) 1909. 75, 76

[13] ATLAS Collaboration, "Expected performance of the ATLAS experiment : detector, trigger and physics", CERN-OPEN-2008-20 , arXiv:0901.0512 [hep-ex]. 76

[14] ATLAS Collaboration, "Expected electron performance in the ATLAS experiment", ATL-PHYS-PUB-2011-006. 76

[15] ATLAS Collaboration, "Expected photon performance in the ATLAS experiment", ATL-PHYS-PUB-2011-007. 77, 78

[16] ATLAS Collaboration, "Reconstruction of Photon Conversions, in Expected Performance of the ATLAS Experiment: Detector, Trigger and Physics", pp. 112-140, CERN, Geneva, 2008. CERN-OPEN-2008-020, arXiv:0901.0512v4 [hep-ex]. 77

[17] K. Nakamura et al. (Particle Data Group) "Review of Particle Physics", J. Phys. G 37, 075021 (2010) . 81

[18] The ATLAS Collaboration,"Observation $W \to \ell\nu$ and $Z \to \ell\ell$ production in proton-proton collsions at $\sqrt{s} = 7$ TeV with the ATLAS detector", ATLAS-CONF-2010-044.
79

..Do not take Poisson statistics as a personal issue...

Chapter 7

Measurement of the ZZ production cross section at $\sqrt{s}$ =7 TeV with the ATLAS detector

This chapter is dedicated to the cross section measurement of the ZZ production channel at $\sqrt{s} = 7$ TeV using the ATLAS detector. Soon after the LHC started to operate at $\sqrt{s} = 7$ TeV, the $ZZ \rightarrow 4\ell$ analysis was transferred to the new center of mass energy. Some of the studies presented here are repeated from the previous chapter while others were required by the new energy regime.

7.1 Introduction

This chapter is the main subject of this thesis. A detailed explanation of the procedure followed to measure the fiducial and total production cross section of the ZZ channel is given. The event selection criteria of the analysis are described in depth and the data-driven technique utilized to estimate the background contribution in the $4e$, 4μ and $2e2\mu$ final states is discussed. Topics like systematic uncertainties affecting the cross section measurement, calculation of the reconstruction and acceptance factor and likelihood of features in observation are also addressed. A comparison of kinematic distributions between data and MC is shown for both $ZZ \rightarrow 4\ell$ and $Z \rightarrow 2\ell$ processes. Finally the statistical method used for the cross section extraction is presented.

7.2 Datasamples

7.2.1 Data 2011

This study uses a data sample of proton-proton collisions that was taken between April - June 2011 at a centre-of-mass energy of $\sqrt{s} = 7$ TeV at the LHC. The total integrated luminosity delivered up to that point was $\mathcal{L} = 1.25$ fb^{-1} (see Figure 3.2). Events are selected based on detector data-quality requirements which ensure the relevant sub-detectors are operational. The integrated luminosity as reported by the ATLAS luminosity calculation tool is 1.024 fb^{-1} corresponding to $\sim$ 82% of the total luminosity of ATLAS. The luminosity uncertainty for 2011 data is 3.7% [1]. According to the trigger object (electron, muon, jet, e.t.c) that fired the event, the data are separated to the corresponding physics streams. In the current analysis the electron and muon streams have been used. Events appearing in both streams were removed from the electron stream.

7.2.2 Monte Carlo samples

The ZZ production process and subsequent pure leptonic decays are modeled by PYTHIA [2] with MRST modified LO (LOmod) parton density function (PDF) set [3]. The PYTHIA simulation includes the interference terms between the Z and γ^* diagrams; the mass threshold for the Z/γ^* boson is set to 12 GeV. The produced sample also includes final states with τ leptons which can further decay to all the known final states. Although, filter is applied to the events at generator level, demanding at least 3 leptons (e or μ) with $p_T > 5$ GeV in $|\eta| < 10$. The filter mainly rejects τ events. The corresponding filter efficiency, ε_{filter}, is 62.35%. Table 7.1 lists the ZZ MC signal sample used in the analysis. The number of events, $k-$factor ($k = \frac{\sigma_{NLO}}{\sigma_{LO}}$), filter efficiency and cross section are also shown.

The detector responce is simulated [4] with a program based on GEANT4 [5].

MCID	Process	Generator	Events	k-factor	ε_{filter}	σ [pb]
109292	$ZZ \to \ell^+\ell^-\ell'^+\ell'^-$	PYTHIA	149969	1.41	0.6235	0.07494

Table 7.1: The ZZ signal production process, cross section and number of fully simulated MC events. The MC simulation filter demands at least 3 leptons (e or μ) with p_{T}>5 GeV and $|\eta| < 10$.

In order to have a well defined comparison between the data and MC simulations as well as to study the different background processes contributing to the signal, several MC samples have been used for data modeling. These include Z (Table C.1) and W (Table C.2) gauge bosons produced in association with jets and top events ($t\bar{t}$, Wt and single top, Table C.3). The MC@NLO [6] event generator has been used for the modeling of $t\bar{t}$ and single top events, whereas the ALPGEN [7] event generator has been employed for the Z and W inclusive samples. Events with dileptons from Drell-Yan ($10 < m < 40$ GeV) processes (Table C.1) are also modeled with ALPGEN. Events with heavy flavor dijets (Table C.3) are modeled with PYTHIAB [2]. The diboson processes WW and WZ are modeled with MC@NLO and the $W/Z+\gamma$ with MADGRAPH [8] (Table C.4).

The cross sections for the simulated processes, generator names, generator level filter efficiencies and total number of events are shown in Appendix C. Whenever LO event generators are used, the cross-sections are corrected by using k-factors to NLO or NNLO (if available) derived from matrix element calculations [10].

Additional inelastic pp events are included in the simulation, distributed so as to reproduce the number of collisions per bunch-crossing in the data.

7.3 Cross section definition

For any given physics channel, one can calculate a fiducial and a total cross section. The fiducial cross section is defined in a fiducial volume such that it corresponds to the experimental selection criteria and it is therefore free from any systematic errors that arise from extrapolating to regions of phase space which are not measured. In our case the $ZZ \to \ell\ell\ell'\ell'$ fiducial volume is defined from the selection cuts:

- $(Z/\gamma^*)(Z/\gamma^*) \to \ell^+\ell^-\ell^+\ell^-$, where $\ell = e, \mu$;
- Invariant mass of Z/γ^*: $66 < M_{Z/\gamma^*} < 116$ GeV;
- Transverse momentum of leptons: $p_T^\ell > 15$ GeV;
- Leptons must lie in pseudorapidity $\eta^\ell < 2.5$.

and it is given by the equation:

$$\sigma_{ZZ}^{fid} \times BR(ZZ \rightarrow \ell\ell\ell'\ell') = \frac{N_{\ell\ell\ell'\ell'}^{obs} - N_{\ell\ell\ell'\ell'}^{bkg}}{\mathcal{L} \times C_{ZZ\rightarrow\ell\ell\ell'\ell'}} \quad (7.1)$$

where $N_{\ell\ell\ell'\ell'}^{obs}$ and $N_{\ell\ell\ell'\ell'}^{bkg}$ denote the number of observed and background events respectively, $\mathcal{L}$ is the integrated luminosity, $BRZZ \rightarrow \ell\ell\ell'\ell'$ is the branching ratio for both Zs to decay leptonically and is equal to 0.0045 [11] and $C_{ZZ\rightarrow\ell\ell\ell'\ell'}$ is a correction function defined in Section 7.12.1.

The total cross section (Equation 7.2) can then be derived from the fiducial cross section by dividing with the acceptance factor, $A_{ZZ\rightarrow\ell\ell\ell'\ell'}$, which represents the efficiency of the fiducial cuts (see Section 7.12.2).

$$\sigma_{ZZ}^{tot} = \frac{N_{\ell\ell\ell'\ell'}^{obs} - N_{\ell\ell\ell'\ell'}^{bkg}}{\mathcal{L} \times BR(ZZ \rightarrow \ell\ell\ell'\ell') \times A_{ZZ\rightarrow\ell\ell\ell'\ell'} \times C_{ZZ\rightarrow\ell\ell\ell'\ell'}} \quad (7.2)$$

7.4 Signal Monte Carlo correction

The predicted number of signal events are obtained by correcting the predictions of Pythia with a $k-$factor to scale to the NLO cross section. The $k-$factor is calculated for the fiducial cross section (see Section 7.3) and is defined as the ratio of the MCFM [9] NLO cross section to the Pythia LO cross section. The average ratio is equal to 1.41. The $k-$factor is fairly independent of the ZZ mass for masses above ~200 GeV. The corresponding fiducial cross sections of the MCFM and Pythia as a function of the invariant mass of the ZZ system as well as their ratio is shown in Figure 7.1. It is worth mentioning that the $k-$factor of the total cross sections is different from the one of the fiducial cross sections and is calculated in reference [9].

7.5 Selection criteria in the $ZZ \rightarrow 4\ell$ process

The physics objects needed in the analysis for the reconstruction of ZZ events are electrons and muons. The candidate events must pass a series of requirements, based on event selection criteria, lepton preselection requirements and finally selection requirements of the ZZ system.

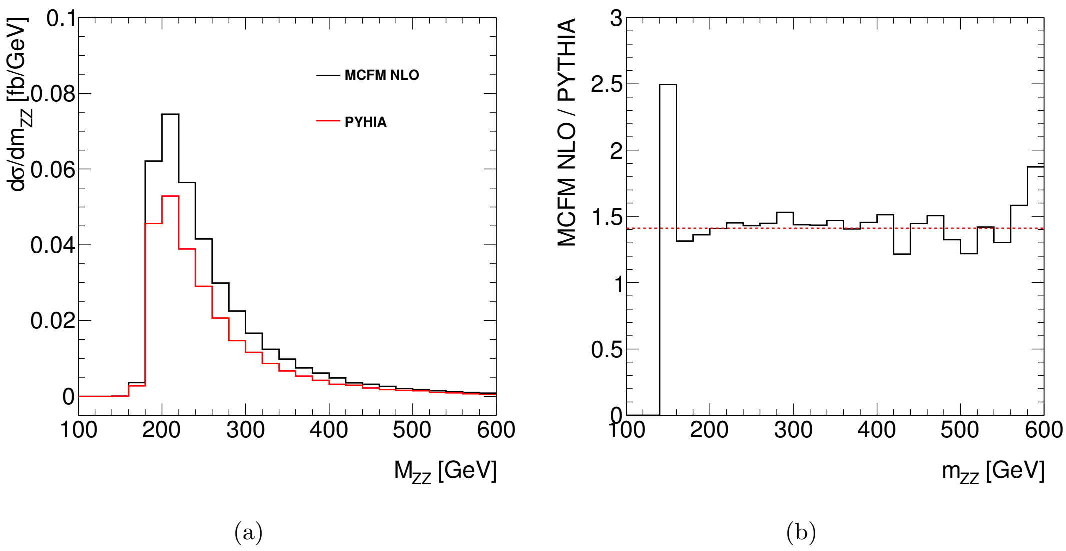

Figure 7.1: (a) Fiducial cross section for $ZZ \to ee\mu\mu$ as a function of the ZZ mass as calculated at LO by PYTHIA and at NLO by MCFM. (b) The resulting $k-$ factor (MCFM NLO / PYTHIA LO) is shown in the plot on the right.

7.5.1 Event selection

Good Runs List

Events are required to be recorded when the detector was fully operating.

Trigger requirement

The ZZ candidates with four-leptons in the final state are required to pass either the unprescaled single-electron or the unprescaled single-muon triggers. The former corresponds to an electron that fires the event. The specific electron must have $p_T >$ 20 GeV and also pass the medium identification requirements (see Section 6.3.2). The corresponding name of the trigger is "EF_e20_medium". The single muon trigger implies that the event has been triggered from a muon of $p_T >$ 18 GeV ("EF_mu18_MG") or from a central muon of $p_T >$ 40 GeV ("EF_mu40_MSonly_ barrel").

Number of tracks resulting from the primary vertex

The number of tracks resulting from the primary vertex should be ≥ 3 in order to avoid contributions from cosmic ray events.

7.5.2 Object preselection

Object reconstruction

Electrons must be reconstructed with the standard egamma algorithm described in Section 6.3.2. Muons must be combined or segment-tagged A.3.2. In addition, the inner detector tracks of muons must have a minimum number of hits in each silicon sub-detector: ≥1 hit in the pixel detector, ≥1 hit in the inner layer of the pixel detector if the pixel detector module at that location is operational, ≥6 hits in the SCT, and <2 missing hits on the track in pixel and SCT detectors. For $|\eta| < 1.9$, at least 6 TRT hits are required, and the number of TRT hits that are classified as “outliers” must be less than 90% of the total number of TRT hits on the track. The latter cut is also applied if $|\eta| \geq 1.9$ and at least 6 TRT hits are on the track. TRT outliers appear in two forms in the track reconstruction, as a straw tube with a signal but not crossed by the nearby track, or as a set of TRT measurements in the prolongation of a track which, however, failed to form a smooth trajectory together with the pixel and SCT measurements. This set of quality cuts is recommended from the muon performance group of ATLAS in order to supress fake tracks and discriminate against muons from hadron decays [13].

Identification requirements

Elecrons must pass “medium” identification (see Section 6.3.2) requirements and muons must pass “loose” track quality requirements [12].

Kinematis cuts

Electrons (muons) with $E_T(p_T) > 15$ GeV which lie in the pseudorapidity region of $|\eta| < 2.47$ for electrons and $|\eta| < 2.5$ for muons are selected. The analysis has been built for both Zs on shell, so a lower p_T or E_T cut would increase the background contamination without any gain in the signal yield. In order to have a precise measurement of electron’s E_T, their energy is taken from the cluster measurement while their direction (in η and ϕ coordinates) depends from the quality of the track. If the electron track has four or more silicon (SCT and Pixel) hits, the direction is taken from the track, otherwise all electron parameters are taken directly from the electromagnetic cluster.

Leptons from same primary vertex

To ensure that the lepton candidates come from the primary vertex, the $|z_0|$ (see Section 4.1) of the lepton track with respect to the primary vertex must be less than 10 mm

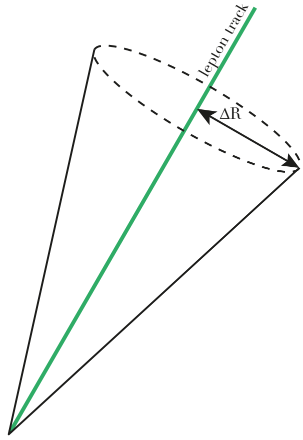

Figure 7.2: Cone opening around lepton's track to measure the track isolation.

and the d_0 significance (see Section 4.1) defined as d_0/σ_{d_0} is required to be less than 10.

Track isolation

The track isolation requirement is one of the most important cuts in the ZZ analysis, since the leptons from Z decays are expected to be energetic and highly isolated. The track isolation requirement, as all the other requirements, is applied to all leptons. It is defined as the ratio of the arithmetic p_T sum of tracks in a cone of radius ΔR (see Figure 7.2) divided by the leptons p_T:

$$Isolation = \frac{\sum_{i=1}^{n} p_T^i}{p_T^{electron}} < 0.15 \tag{7.3}$$

Figures 7.3 and 7.4 show the track isolation efficiencies of signal events (7.1) for three different cone sizes ($\Delta R = 0.2, 0.3, 0.4$) for the electron ($4e$) and muon channel (4μ) respectively. The efficiencies have been calculated with respect to the number of events passing the mass cut, since the track isolation is the last cut of object preselection. Due to lack of MC statistics, no event of the MC background samples passes any of these cuts.

As can be seen from figures 7.3 and 7.4, the smaller the cone size is, the higher efficiency can be achieved, because less tracks are included in the cone. Since no event of the MC background samples passes any track isolation cuts, a relaxed isolation cut

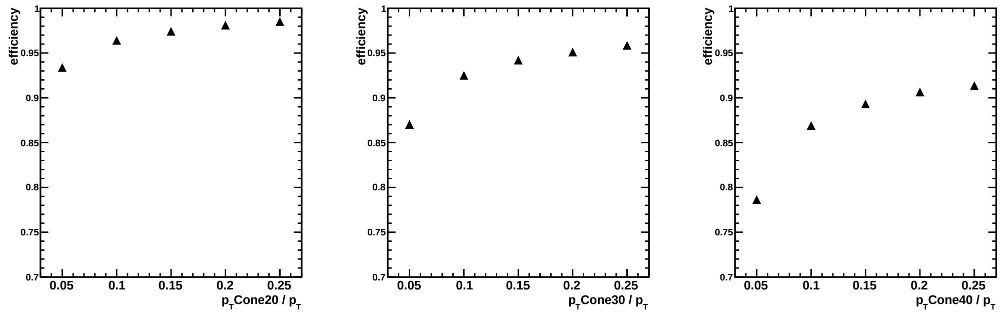

Figure 7.3: Electron track isolation efficiencies for three different cone sizes ΔR =0.2 (left), 0.3 (middle), 0.4 (right). Efficiency versus isolation parameter of 0.05, 0.1, 0.15, 0.20, 0.25.

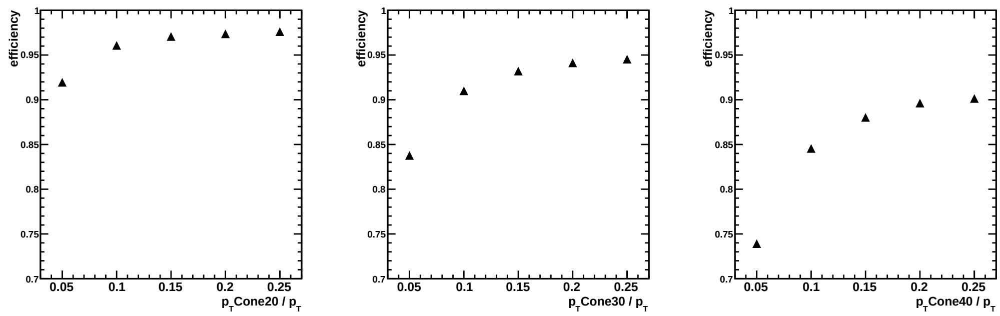

Figure 7.4: Muon track isolation efficiencies for three different cone sizes ΔR =0.2 (left), 0.3 (middle), 0.4 (right). Efficiency versus isolation parameter of 0.05, 0.1, 0.15, 0.20, 0.25.

has been chosen. The selected value is 0.15 for the smaller cone size. This value corresponds to $\sim 97\%$ efficiency for both electrons and muons.

7.5.3 Selection requirements on the ZZ system

The events containing four and only four leptons passing the preselection requirements are further examined.

Trigger object matching

In order to confirm that the event has been triggered from one of the selected leptons a trigger object matching is applied. The selected electrons (muons) with $E_T > 25$ GeV ($p_T > 20$ GeV) are examined if they match with trigger objects by applying a

ΔR matching cut <0.15 for electrons and 0.1 for muons. The muons are also required to be combined. The higher E_T cut for electrons compared to muons p_T is a result of the different plateau in the trigger efficiency. If none of these leptons is matched with a trigger object the event is rejected.

Resolving ambiguities in combinatorics

Following the trigger matching, the four leptons are used to form quadruplets consisting of two pairs of same-flavor and opposite-sign leptons. Since there are four leptons in the event, the maximum number of possible solutions (quadruplets) is two. In order to resolve the ambiguity in combinatorics, the quadruplet with the minimum distance from the Z pole is selected (see Equation 7.4). This method produces 2% mis-assignment.

$$\Delta M_{min} = |m_{\ell\ell}^{first} - m_Z| + |m_{\ell'\ell'}^{second} - m_Z| \tag{7.4}$$

The combinatorial problem becomes more complicated if more than four leptons are present in the event. Such scenarios could take place at the high luminosity environment of the LHC, where more inelastic scatterings are expected (pile-up). In such cases more sophisticated techniques could be applied, like extracting probabilities from Breit-Wigner distribution (see Appendix D), or maximizing a likelihood. Due to the presence of multiple solutions in the event the wrong one could be selected, leading to the loss of the signature of interest. Moreover, the wrong assignment of leptons to the Zs will lead to large systematic errors in any background estimation, like same-sign (SS) opposite-sign (OS) method, ABCD [14] method and every method based in the properties of the lepton pairs (like $p_T^{\ell\ell}$, $M_{\ell\ell}$). This thesis performed extensive studies in the mis-assignment of leptons to the Zs and the results can be found in Appendix D.

Mass cut

The selected quadruplet is then checked if it satisfies the mass cut, where both Zs are required to be in the mass range $66 < M_{\ell\ell} < 116$ GeV.

The full list of the selection criteria applied in the analysis is reported in Table A.2. A detailed comparison of the selections used in the $ZZ \to 4\ell$ analysis and the searches of a standard model Higgs boson decaying to four leptons, $H \to ZZ^* \to 4\ell$, is discussed in Appendix E [15].

Event Selection		
GRL	Good Run List	
Trigger	EF_e20_medium OR EF_mu18_MG OR EF_mu40_MSonly_barrel	
nTracks of primary vertex	≥ 3	
LAr Error	$= 0$	
Object Selection		
Cut	**Electrons**	**Muons**
Identification requirements	Medium	Loose
$\|\eta\|$	≤ 2.47	≤ 2.5
p_{T}	> 15 GeV	
z_0	< 10 mm	
d_0/σ_{d_0}	< 10	
$\sum p_T^i \ / \ p_T^{lepton}$	< 0.15	
Overlap Removal $e^- - \mu^-$	> 0.1	-
Overlap Removal $e^- - \mu^-$	> 0.1	-
Requirements for the ZZ system		
Number of leptons	4 and only 4 leptons	
Trigger matching $\Delta R = \sqrt{\Delta\eta^2 + \Delta\phi^2}$	$p_T > 25$ GeV $\Delta R < 0.15$	$p_T > 20$ GeV $\Delta R < 0.1$
Quadruplet formation	Minimize the quantity $\|m_{\ell\ell}^{first} - m_Z\| + \|m_{\ell'\ell'}^{second} - m_Z\|$	
Leading Z	Highest p_T pair satisfying $66 < m_{\ell\ell} < 116$ GeV	
Subleading Z	Remaining pair satisfying $66 < m_{\ell\ell} < 116$ GeV	

Table 7.2: Event selection, object preselection and post preselection cuts used for the detection of ZZ candidates.

7.6 Performance studies using single $Z \to ee/\mu\mu$ events

A direct comparison between data and MC has been performed by selecting single Z bosons according to the selection criteria of the $ZZ \to 4\ell$ analysis. Selected events must satisfy all the lepton selection requirements and must have two and only two candidate leptons lying in the mass region [66,116] GeV.

Specifically, once the events pass the trigger object matching, the pair formation comes next by requiring same flavor opposite sign pairs with an invariant mass within 25 GeV from the Z pole. "Pile-up reweighting" has been applied only to the MC samples using the official ATLAS tool. Reconstruction and identification efficiency scale factors are applied to both electrons and muons. Momentum smearing is applied to the leptons of the MC samples while to the data electrons energy rescaling has been applied. In order to have a realistic comparison between the data and MC, all available samples described in Sec 7.2 have been used, appropriately scaled to the data luminosity taking into account $k-$factors and filter efficiencies.

The distribution of the number of interactions per bunch crossing in the selected Z candidates is shown in Figure 7.5, and the invariant mass of the $Z \to \ell\ell$ (where $\ell = e, \mu$) candidate events is presented in Figure 7.6, where a comparison between data and the different MC samples is shown. The contribution of each MC sample (starting from the ZZ contribution and going upwards) is stacked to the next one. The lower panel of the plot is the ratio between data and MC. The yellow band indicates the total error:

$$\delta E_{tot} = \sqrt{(\delta E_{stat})^2 + (\delta E_{syst})^2}. \tag{7.5}$$

The systematic uncertainty has been calculated event by event and is the sum in quadrature of all the sources of systematic errors as they are not correlated. For the sources where there is a contribution from both leptons, the product of the two leptons is taken into account. This is given from the equation:

$$\delta E_{syst} = \pm \sqrt{(\prod_{i=1}^{2} \delta R_i)^2 + (\prod_{i=1}^{2} \delta I_i)^2 + (\delta T)^2 + (\delta \mathcal{L})^2} \tag{7.6}$$

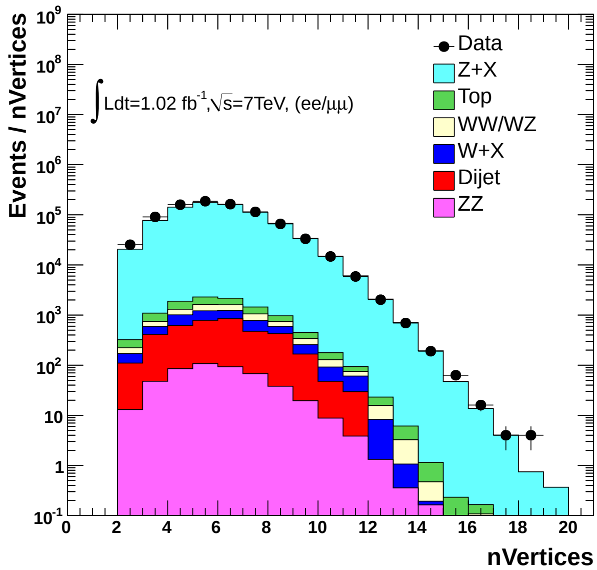

Figure 7.5: Distribution of the number of vertices per bunch crossing of the events passing the selection criteria of the ZZ analysis.

where $\prod_{i=1}^{2}$ accounts for both leptons, δR is the error of the reconstruction scale factors, δI symbolizes the error of the electron identification scale factors (this term is zero for the case of muons), δT is the cross section error given from theory equal to 5% and $\delta\mathcal{L}$ corresponds to the luminosity error 3.7%.

7.7 Background estimation

The main background processes in the detection of the $ZZ \rightarrow 4\ell$ analysis are $ZQ\bar{Q}$ ($Q = b, c$), $Zq\bar{q}$ (where $q = u, d, s$) and $t\bar{t}$. These processes have two prompt leptons and two QCD background leptons (from charged hadrons faking an electron or a muon or leptons from heavy flavor decays). The diboson channels WW and WZ containing two and three prompt leptons plus two and one fake leptons respectively, could also contribute to 4ℓ background contamination. Due to lack of statistics a MC based background estimate was not possible. A full data-driven background estimate method is developed for backgrounds which have one or two "fake" leptons (where "fake" lepton includes photon, pion, kaon, and heavy quark decays to real leptons as well as jets

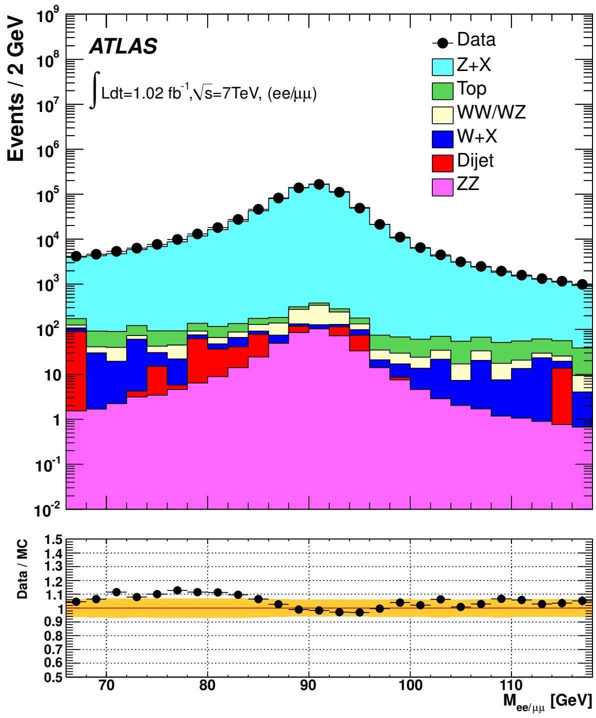

Figure 7.6: The invariant mass distributions of same-flavour opposite-sign lepton pairs selected using the $Z \to 4\ell$ criteria including the trigger requirement and compared to simulation after applying all corrections. The various background sources are shown in different colours. The ratio between data and MC is shown in the lower part of the histogram; the total uncertainty (statistical plus systematic) is indicated by the shaded band.

misidentified as leptons).

7.7.1 Methodology

ZZ signal events contain isolated, prompt leptons from vector-boson decay. Background events which contain three isolated prompt leptons from vector-boson decay can contain a fourth lepton from other sources, e.g. muons from in-flight decays of pions and kaons, heavy-flavor quark (b or c) decays, or jets with a leading pion misidentified as an electron. Leptons produced by a real W or Z may also include cases where the lepton derives from τ decay, and in $t\bar{t}$ events the lepton derive from the top decay to W.

While leptons from the decay of Z bosons are primarily isolated, leptons from the sources mentioned above tend to be spatially correlated with jets. While the majority of these leptons will fail the isolation requirement, the tails of the jet distributions may have electrons or muons which satisfy the isolation and identification requirements, and it is therefore important to estimate the background contribution due to these type of events. Since MC may not model the tails of jet fragmentation well and lacks sufficient statistics, data are used to extract estimates for this kind of background.

To estimate the background contribution of four-lepton events in which at least one lepton does not originate from a Z decay, a sample of events in the data adjacent to the signal region but dominated by events of this type is identified, by inverting some of the identification requirements. The background is then estimated by scaling this control sample by a measured "fake factor" FF (η and p_T dependent, treated as uncorrelated in the two variables), which is the ratio of the probability for a jet to satisfy the full lepton criteria to the probability to satisfy the lepton-like jet criteria.

7.7.1.1 Fake factor calculation for electron objects

The main source of "fake" electrons are mis-identified jets (soft jets) or electrons from heavy flavor decays. In order to calculate the fake factor, an object identification is applied by asking the electrons to fail either the "medium" identification or the isolation requirement. The definitions of the selected electrons and electron-like jets can be found in Table 7.3.

Selected electrons	**Electron-like jets**
Track isolation < 0.15 and MEDIUM	Track isolation > 0.15 or !MEDIUM

Table 7.3: Summary of requirements for selected electrons and electron-like jets.

For the extrapolation to the signal region one needs to know the rate at which jets pass or fail these requirements. The fake factor is defined as

$$FF_e = \frac{N^{data}_{selected\ electrons} - N^{MC\ W+Z}_{selected\ electrons}}{N^{data}_{electron-like\ jets} - N^{MC\ W+Z}_{electron-like\ jets}} \tag{7.7}$$

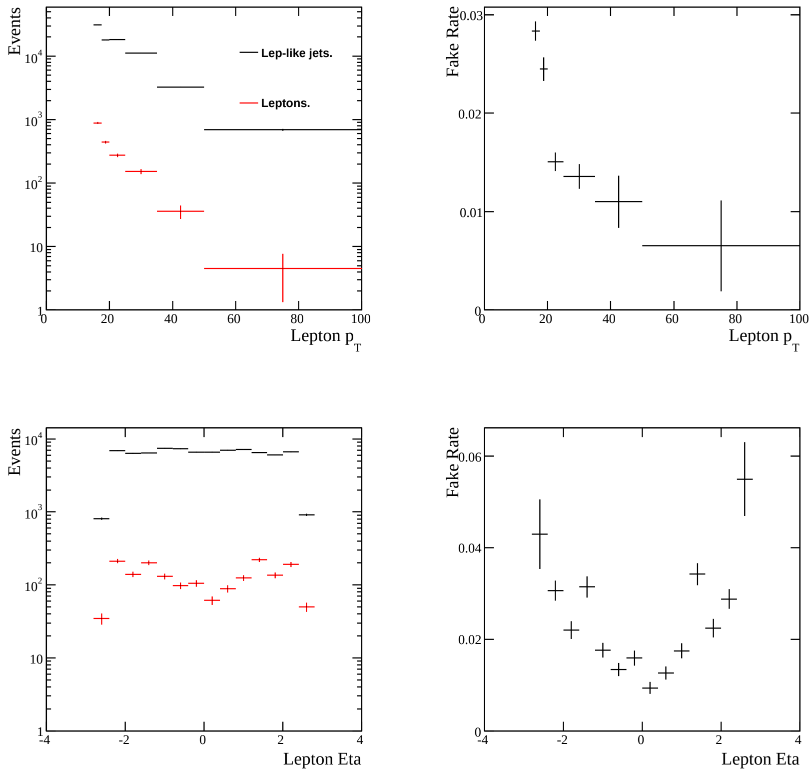

Figure 7.7: Electrons fake factor, FF_e. Left: Distribution of electron p_T and η for selected leptons and lepton-like jets; Right: Fake Rate ($\equiv FF$).

The calculation of this factor has been done in a sample dominated by jets by collecting all events surviving the photon trigger ("EF_g11_etcut"), which has no electron-specific identification requirements in order to avoid any biases due to real electron selection. To suppress the contribution from $W \to e\nu$ and $Z \to ee$, anti-W ($M_T < 60$ GeV if $N_e = 1$) and anti-Z ($M_{ee} < 60$ GeV if $N_e = 2$) cuts have been applied. The fake factor (FF_e) is then calculated by subtracting the remaining MC predicted W, Z contributions and forming the ratio as shown in Figure 7.7. The comparison with MC samples is shown in Figure 7.8.

Due to lack of statistics, the build-in of a two dimensional map was not possible. In order to resolve the statistics problem a parametrization of the FF_e is carried out in both electron p_T and η, directly using the histrograms and assuming no correlation

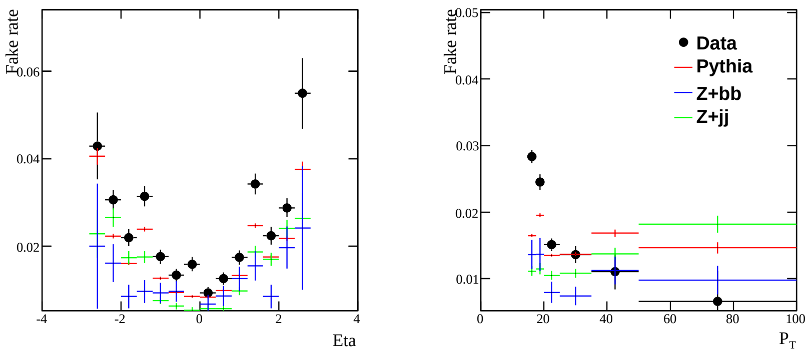

Figure 7.8: Comparison of the fake factor FF_e in data and MC samples; Left: η; Right: p_T

between the p_T and η dependence through equation:

$$FF(p_T, \eta) = \frac{FF(p_T) \times FF(\eta)}{< FF(p_T, \eta) >} \tag{7.8}$$

where $< FF(p_T, \eta) >$ is the average fake factor in the control samples. It is equivalent to $FF(< p_T >)$, where $< p_T >$ is the averaged p_T spectrum in the control sample and is dominated by the lowest p_T bin (15-20 GeV).

7.7.1.2 Fake factor calculation for muon objects

The sources of "fake" muons result from heavy flavor decays and π, K decays in flight. The fake factor (FR_μ) is calculated by selecting muons that fail the isolation requirement. The definitions of the selected muons and muon-like jets can be found in Table 7.4.

Selected muons	**Muon-like jets**
Track isolation < 0.15	Track isolation > 0.15

Table 7.4: Summary of requirements for selected muons and muon-like jets.

To extrapolate to the signal region one needs to know the rate at which jets pass or fail the track isolation requirement. The fake factor, as in the case of electrons, is

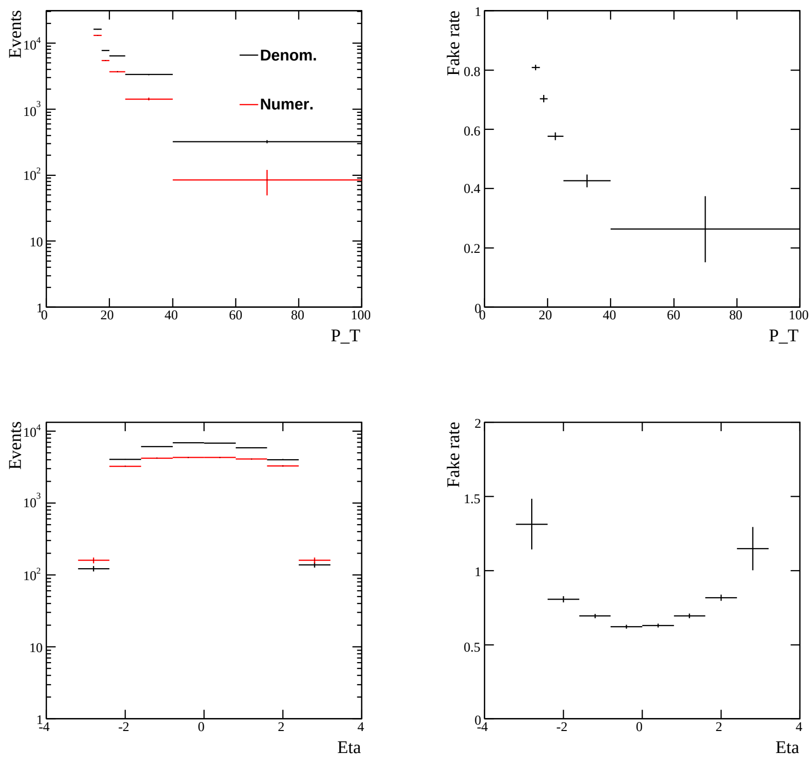

Figure 7.9: Muons fake factor, FF_μ. Left: Distributions of muons in p_T and η for selected leptons and lepton-like jets; Right: Fake Rate ($\equiv FF$).

defined by the equation:

$$FF_\mu = \frac{N^{data}_{selected\ muons} - N^{MC\ W+Z}_{selected\ muons}}{N^{data}_{muon-like\ jets} - N^{MC\ W+Z}_{muon-like\ jets}} \tag{7.9}$$

FF_μ is measured in a sample enriched in muons from heavy flavour by collecting events which survive the single muon trigger ("EF_mu13_MG") which has no isolation requirements. To suppress the contribution from $W \rightarrow \mu\nu$ and $Z \rightarrow \mu\mu$ events, an anti-W cut $M_T < 50$ GeV (if $N_\mu = 1$) and an anti-Z cut $M_{\mu\mu} < 50GeV$ (if $N_\mu = 2$) is applied. The FF_μ is then calculated by subtracting the remaining MC predicted W and Z contributions and forming the ratio, see Figure 7.9, with comparison to MC samples in Figure 7.10.

An average $< FF_\mu(p_T, n) >$ as in Equation 7.8 is also computed for the muons.

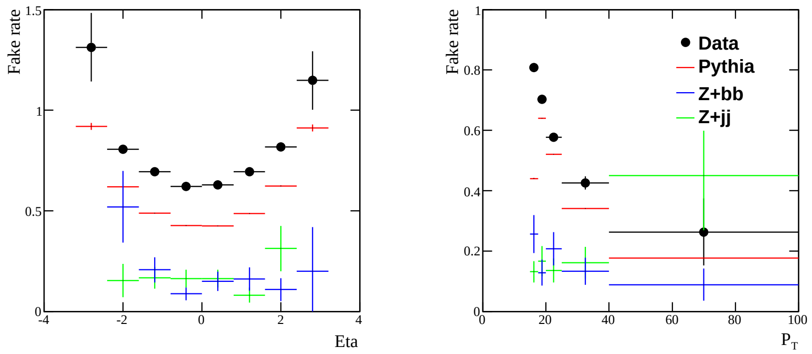

Figure 7.10: Comparison of the fake factor FF_{μ} in data and MC samples; Left: η; Right: p_T

7.7.2 Background calculation

The fake lepton background contribution to the signal region (four leptons) has contributions from events with two fake leptons F plus two true leptons T and events with one fake lepton plus three true leptons, while the contribution from events with more than two fake leptons is negligible:

$$N_{4l\ fake} = N_{TTFF} \times f \times f + N_{TTTF} \times f \tag{7.10}$$

where f is the fraction of fake leptons which are reconstructed as selected leptons). By denoting the selected leptons as L and the lepton-like jets as J, then the fake factor (FF) and the probability (f) of a fake lepton to be found as selected lepton are:

$$f = \frac{L}{L+J} \text{ and FF} = \frac{\text{L}}{\text{J}} \tag{7.11}$$

which when combined give:

$$FF = \frac{f}{1-f} \quad \text{and} \quad \text{f} = \frac{\text{FF}}{1+\text{FF}} \tag{7.12}$$

The number of events with two selected leptons and two lepton-like jets is given from the equation:

$$N_{LLJJ} = N_{TTFF} \times (1-f)^2 \tag{7.13}$$

where L stands for a lepton which was fake but reconstructed as good lepton. The number of events with three selected leptons and one lepton-like is given from equation:

$$N_{LLLJ} = N_{TTFF} \times 2.\, f.\, (1-f) + N_{TTTF} \times (1-f) \tag{7.14}$$

where the first term stands for the case where one of the two fake leptons is a lepton-like jet (the factor of 2 is due to combinatorics) while the second term refers to the case where there is only one fake lepton.

It can be proven that:

$$N_{4\ell\ fake} = N_{LLLJ} \times FF - N_{LLJJ} \times FF^2 \tag{7.15}$$

which is correct under the assumption that $L/(L+J) = 1.0$ for true leptons. This is nearly correct, but there is a small contribution from $ZZ \to 4\ell$ events which are reconstructed as $LLLJ$. By including this contribution the final equation takes the form:

$$N_{4\ell\ background} = N_{LLLJ} \times FF - N_{LLJJ} \times FF^2 - N_{ZZ\to 4\ell} \tag{7.16}$$

7.7.3 Statistical and systematic uncertainties in background estimation

As $LLJJ$ and $LLLJ$ events are found from the data, the statistical uncertainty is the statistical uncertainty in the FF calculation applied to these events. However, if one observes zero events, a 68% CL upper limit can be set on the expected contribution of < 1.29 events. In the case of $LLJJ$ for 4μ, the observed number of events is zero, which when scaled by FF^2 (evaluated at the p_T bin with the largest fake factor), gives a limit of < 0.83. While for the $2e2\mu$ channel the overall background is negative -0.013±0.029. In this case, a truncated Gaussian limit of <0.016 events is set. The largest difference in the fake factor distributions between data and simulation is taken as the systematic uncertainty. This results in an average systematic uncertainty of ~30% for each $p_T(\eta)$ bin except for the lowest p_T bin (15-20 GeV), for which the uncertainty is almost 100%.

Table 7.5 shows the estimated background values for each channel as well as the individual term contribution in the background calculation.

Component	$eeee$	$\mu\mu\mu\mu$	$ee\mu\mu$	$\ell\ell\ell\ell$
$(+)$ $N_{LLLJ} \times FF$	0.04 ± 0.02	0.27 ± 0.27	0.05 ± 0.02	0.36 ± 0.27
$(-)$ $N_{LLJJ} \times FF^2$	0.03 ± 0.002	$0.00^{+0.83}_{-0.00}$	0.03 ± 0.01	$0.06^{+0.83}_{-0.01}$
$(-)$ ZZ correction	0.003 ± 0.000	0.01 ± 0.003	0.02 ± 0.002	0.04 ± 0.004
Total	$0.01^{+0.03}_{-0.01}$(stat)	0.3 ± 0.3(stat)	< 0.01	0.3 ± 0.3(stat)
	$^{+0.05}_{-0.01}$(syst)	± 0.3(syst)	$^{+0.03}_{-0.01}$(syst)	$^{+0.4}_{-0.3}$(syst)

Table 7.5: Background estimation in the $ZZ \rightarrow 4\ell$ channel - Fake estimate in 1023 pb^{-1} of data for the three different signatures. The last column is the overall background estimate.

7.8 Systematic uncertainties in the cross section measurement

The systematic uncertainties in the cross section measurement result mainly from the electron and muon object reconstruction and identification. The unfolding of the uncertainties is described in subsections 7.8.1 and 7.8.2 for electrons and muons respectively.

7.8.1 Electron systematic uncertainties

The electron-related systematic uncertainties in the signal yield and efficiency originate from the reconstruction and identification efficiencies of electrons, track isolation and the track parameters d_0 significance and z_0 cuts. Their contributions are determined from MC by varying each systematic source within its associated uncertainty in each event. Since all electrons contribute to each source, the uncertainty per event is the result of the electrons' product ($\prod_{i=1}^{4} SF_i^{err}$ where the index i runs to all electrons and SF^{err} is the corresponding scale factor with its error). The systematic uncertainty assigned in each source is the fractional change in the final number of events passing the selection criteria. Table 7.6 shows the systematic uncertainties from each source.

The uncertainties of the reconstruction and identification efficiency scale factors (SF) have been provided by the egamma group [16] and they were calculated by using the T&P method on W and Z events [16].

- Reconstruction and Identification Efficiency: The differences observed in the reconstruction and identification efficiencies between the data and MC are resolved by weighting each event with scale factors applied to each electron ($\prod_{i=1}^{4} SF_i$). These scale factors are provided by the egamma group. The systematic uncertainties are then determined by varying the scale factors within their quoted uncertainties ($\pm 1\sigma$). The appropriate scale factors of each electron are extracted from a two dimensional map which is E_T and η dependent. The uncertainties of the η and E_T dependent scale factors are added in quadrature to obtain the combined electron identification uncertainty. Similar procedure is followed for the extraction of the reconstruction efficiency scale factors.

- Track isolation and track parameters: the single electron efficiency of the isolation, d_0 significance and z_0 cuts are estimated with T&P method on $Z \to ee$ events, where on the probe all electron selection criteria of this analysis were applied except the d_0 significance, z_0 and track isolation of which the efficiency need to be measured. The variation of the efficiency of each cut between data and MC is calculated, and a systematic is assigned in bins of p_T, taken to be the sum in quadrature of the variation of the data-MC scale factor from one, and the statistical uncertainties on the scale factor. The systematic uncertainty is determined to be in general around 0.1%. The systematic uncertainty of the event is evaluated by repeating the same procedure as it has been done for the determination of the identification systematic source.

- Energy Scale: The systematic uncertainties on the energy scale derived from the 2011 data, are used on the MC samples to obtain the associated uncertainty on the signal yield.

- Energy Smearing: Due to the fact that MC simulation does not reproduce the observed energy resolution in data, a smearing is applied to it. The systematic uncertainties associated with the smearing procedure are obtained from the official tool of ATLAS provided by the egamma performance group.

7.8.2 Muon systematic uncertainties

The systematic uncertainties coming from muon objects are similar to the electrons and are summarized in Table 7.7. In specific they are of three types:

Uncertainty per channel %	$eeee$	$ee\mu\mu$
Energy Scale	0.6	0.4
Energy Smearing	< 0.1	< 0.1
Reconstruction Efficiency	2.8	1.4
Identification Efficiency	6.0	2.8
Track Isolation	0.3	0.1
d_0/σ_{d_0}	0.5	0.2
z_0	0.2	0.1
Total	6.7	3.2

Table 7.6: Systematic uncertainties of the electron objects entering the ZZ analysis

- Reconstruction efficiency: event yields are computed while varying the reconstruction scale factors of each muon by $\pm 1\sigma$ per event. The values are given by the muon combined performance studies on 2011 data [17].

- Track isolation and track parameters: the single muon efficiency of the isolation, d_0 significance and z_0 cuts are estimated with Tag&Probe method on $Z \rightarrow \mu\mu$ events, where on the probe all muon selection criteria of this analysis were applied except the d_0 significance, z_0 and track isolation of which the efficiency need to be measured. The variation of the efficiency of each cut between data and MC is calculated, and a systematic is assigned in bins of p_T, taken to be the sum in quadrature of the variation of the data-MC scale factor from one and the statistical uncertainty on the scale factor. The systematic uncertainty is determined to be in general ~0.1%. The systematic uncertainty per event is the one resulting from the product of the SF of the four muons after varying them within their quoted uncertainties.

- p_T smearing: event yields are computed while varying the MC muon p_T, according to the uncertainty on muon p_T scale and resolution observed in data. This smearing uncertainty is estimated separately for the ID and MS tracks. As a conservative estimate the absolute value of the maximum variation between lower and higher p_T smearing is taken as the systematic uncertainty.

Uncertainty per channel (%)		$\mu\mu\mu\mu$	$ee\mu\mu$
Rec. efficiency		2.0	1.0
p_T smearing	ID	0.02	0.01
	MS	0.05	0.02
	combination	0.05	0.02
Muon isolation		0.1	0.1
d_0/σ_{d_0}		0.2	0.1
z_0		0.1	0.1
Total		2.0	1.0

Table 7.7: Systematic uncertainties of muons entering the ZZ analysis

7.8.3 Summary of systematic uncertainties

A complete summary of the acceptance systematic uncertainties which have been used in the cross section measurement is shown in Table 7.8. The trigger efficiency uncertainty is calculated using the trigger's working group recommendation by applying event by event scale factor. The lepton objects used for trigger efficiency scale factor calculation should satisfy medium identification criteria and p_T threshold at 25 GeV for the electron objects, whereas for muon objects the requirements are "tight" muons with $p_T > 20$ GeV. The systematics are evaluated by summing in quadrature the statistical uncertainty and the 1% systematic error of the efficiency.

7.9 Results

The events observed that fulfill the selection criteria of the ZZ analysis are twelve in total. The $4e$ and $2e2\mu$ final states have two events each and eight events have been observed in the 4μ channel. The MC signal expectation is 8.93 events and the corresponding background estimation is 0.26 events. The overall signal to background ratio is ~ 35. A complete list with all the candidates and some important characteristics of the events can be found in Table 7.9. A comparison between the observed and expected number of events is summarized in Table 7.10. Both statistical and systematic uncertainties are given for all three four-lepton channels. In Appendix F one can see the event displays for all the candidate events. The software used for the creation of the displays is Atlantis, release 09-16-01-08 [18].

Source %	$eeee$	$\mu\mu\mu\mu$	$ee\mu\mu$	combined
μ reconstruction efficiency	-	2.0	1.0	1.2
μ p_T smearing	-	0.1	< 0.1	< 0.1
μ trk isolation	-	0.1	0.1	0.1
μ d_0/σ_{d_0}	-	0.2	0.1	0.2
μ z_0	-	0.1	0.1	0.1
e reconstruction efficiency	2.8	-	1.4	1.2
e identification efficiency	6.0	-	2.8	2.4
e energy scale	0.6	-	0.4	0.3
e energy smearing	< 0.1			
e trk isolation	0.3	-	0.1	0.1
e d_0/σ_{d_0}	0.5	-	0.2	0.2
e z_0	0.2	-	0.1	0.1
trigger	< 0.1			
$ZZ \rightarrow \tau\tau\ell\ell$	0.3			
Total	6.7	2.0	3.3	3.0
PDF	1.3			
Parton shower model	1			
Luminosity	3.7			

Table 7.8: Summary of all relative efficiency uncertainties considered in the cross-section calculation. Sums in quadrature of all uncertainties and the weighted average of the three channels in a combined uncertainty are shown.

Signature	Run Number	Event Number	Luminosity block	$M_{ZZ\to 4l}$ [GeV]
$4e$	183216	75692579	371	270.1
$4e$	184022	20046902	320	245.2
4μ	183003	44433120	385	223.2
4μ	183426	47756740	317	459.9
4μ	183391	19834577	303	194.9
4μ	182284	91584073	745	286.7
4μ	182766	5404925	213	241.0
4μ	182486	33852510	282	208.0
4μ	184130	194694606	1304	183.1
4μ	183003	121099951	723	597.1
$2e2\mu$	182747	63217197	281	209.7
$2e2\mu$	183462	75344317	798	488.0

Table 7.9: List of ZZ candidates at $L = 1.02$ fb^{-1}.

Final State	$eeee$	$\mu\mu\mu\mu$	$ee\mu\mu$	combined
Observed	2	8	2	12
Signal	1.53±0.03± 0.10	3.03±0.04± 0.06	4.37±0.04± 0.14	8.93±0.06± 0.27
Background	$0.01^{+0.03}_{-0.01}$ $^{+0.05}_{-0.01}$	0.3±0.3±0.3	$<0.01^{+0.03}_{-0.01}$	$0.3 \pm 0.3^{+0.4}_{-0.3}$

Table 7.10: Summary of observed events and expected signal and background contributions in each of the four lepton and combined channels. The background predictions cover $Z+X$, $W+X$, top and other diboson process. The first error is statistical while the second is systematic. For each channel and each process, the fractional systematic uncertainties are calculated by combining different sources (Table 7.8) in quadrature and applying it to the central value to get the final systematic uncertainty. The systematics quoted on the signal and background yield do not include the uncertainty on the luminosity.

7.10 Kinematic distributions

Kinematic distributions of the diboson ZZ system are shown in Figure 7.11. The plot on the left represents the transverse momentum of the ZZ system and the plot on the right shows the invariant mass of the four leptons. Figure 7.12 shows the mass of the leading Z candidate versus the mass of the subleading Z candidate for data and predicted signal.

The observed correlation between the transverse momentum of the Z 's and the opening angle ΔR of the two leptons forming the pair, with MC expectations overlayed is shown in Figure 7.13. As expected, the two variables are strongly correlated, as more boosted the Zs are generated, the smaller the angle of the decaying leptons is. A direct comparison with the wrong combinations can be seen in the histogram on the right hand of Figure 7.13. Comparing the two histograms one can see that by taking the wrong combinations no correlation is observed and the distribution is flat. These variables can be used as discriminant variables for the correct assignment of leptons to the Zs as well as in studies for background estimation. In these studies due to lack of statistics no direct usage of this correletion is possible.

The invariant mass and the p_T^Z of the leading and subleading lepton pairs are shown in Figure 7.14. The η and p_T distributions of the individual leptons can be seen in Figure 7.15 while Figures 7.16 and 7.17 show the η and p_T distributions of the leptons, p_T ordered.

The shaded band of the above histograms indicates the total uncertainty, statistical plus systematic. The main sources contributing to the systematic uncertainties are the error from theory (5%), the luminosity error (3.7%) and the reconstruction and identification errors (see Table 7.8). The total uncertainty is the sum in quadrature of the above sources and is given by Equation 7.6.

Similar kinematic distributions are also provided for each channel separately in the Appendix G.

7.11 Signal significance

The ZZ significance estimation of the observed signal has been calculated using a simple probability based on the background-only hypothesis. The shape of the prior used for the background nuisance parameter was studied for two cases, with a truncated

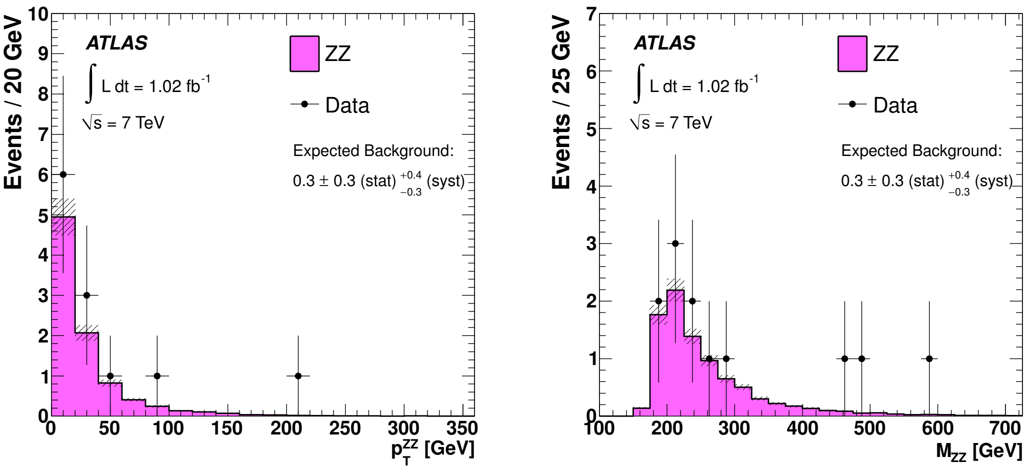

(a) (b)

Figure 7.11: (a) Transverse momentum p_{T}^{ZZ} and (b) invariant mass M_{ZZ} of the ZZ candidates. The points represent the observed data and the histograms show the signal prediction from simulation. The shaded band on each histogram shows the combined statistical and systematic uncertainty on the signal prediction. The predicted number of background events from the data-driven background estimate is indicated on each plot.

Gaussian and a Gamma distribution. The Gamma distribution is preferred, due to its ability to transit the background probability to zero at zero background yield instead of artificial truncation. The equation used for the probability extraction has the following form

$$Pr(N \geq N_{obs}; b, k_b, \theta_b) = \sum_{N=N_{obs}}^{\infty} \int_0^{\infty} P(N;x) Ga(x; k_b, \theta_b) \mathrm{d}x \tag{7.17}$$

where the Poisson function for the number of observed events N is

$$P(N;b) = \frac{b^N e^{-b}}{N!}, \tag{7.18}$$

the function for the background nuisance parameter is

$$Ga(x; k_b, \theta_b) = \frac{1}{\theta_b^{k_b} \Gamma(k_b)} x^{k_b - 1} e^{-x/\theta_b}, \tag{7.19}$$

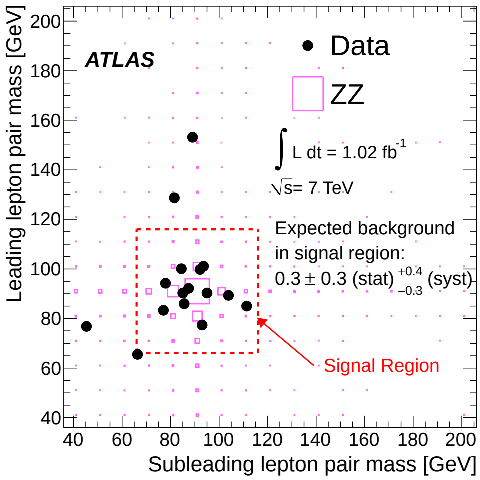

Figure 7.12: The mass of the leading Z candidate versus the mass of the subleading Z candidate. The events observed in the data are shown as solid points and the signal prediction from simulation as pink boxes. The red box indicates the signal region defined by the cuts on the Z masses.

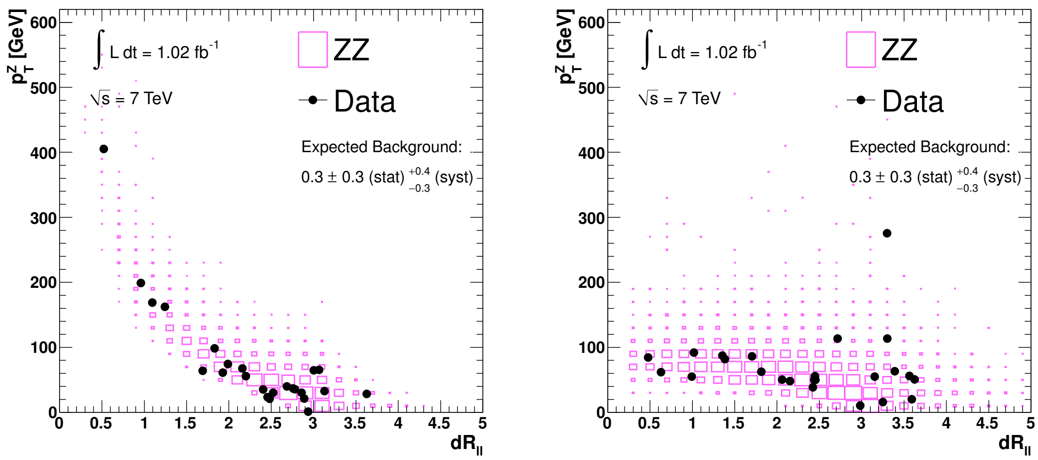

(a) (b)

Figure 7.13: Transverse momentum of the Z candidates versus the angle (ΔR) of the leptons forming the pair for (a) the correct combinations and (b) the wrong combinations.

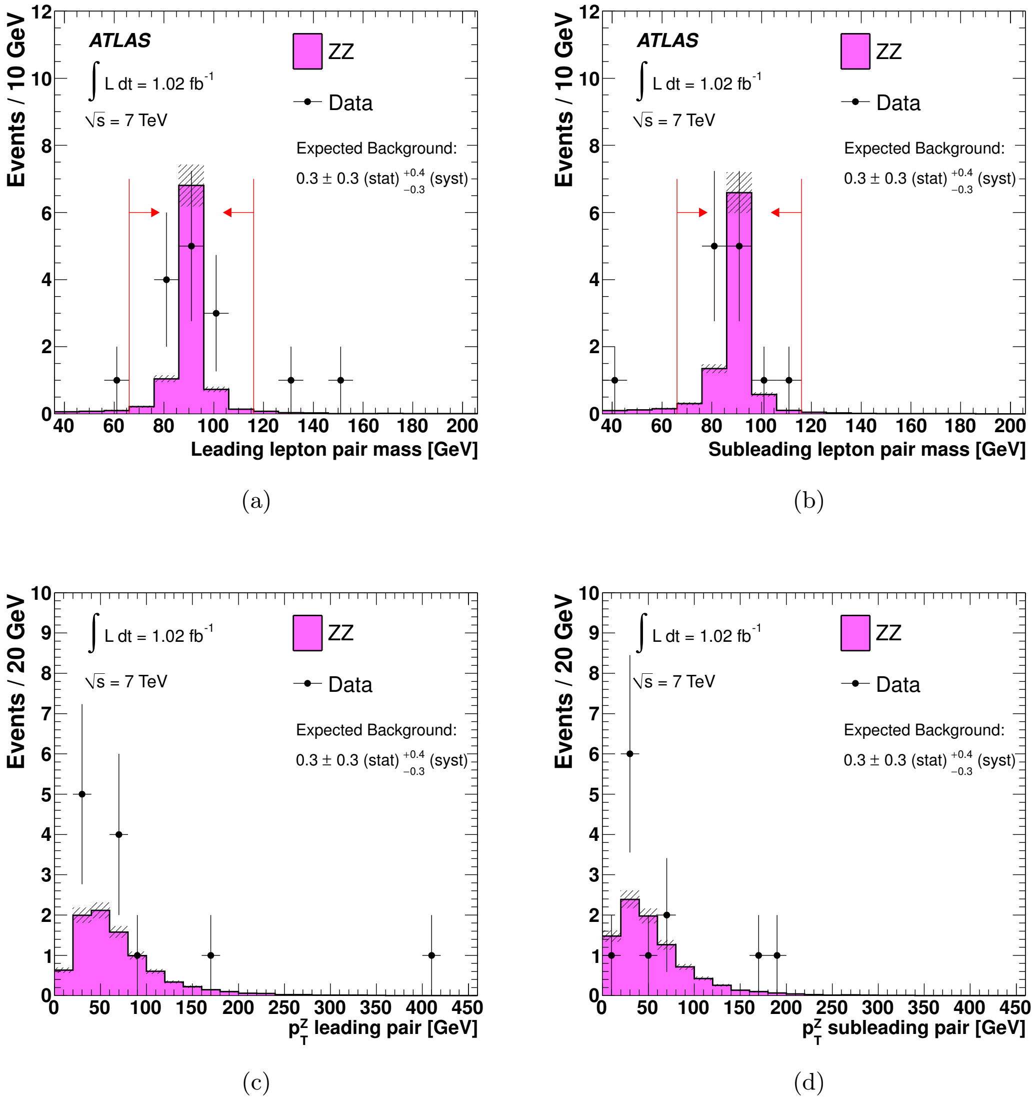

Figure 7.14: Kinematic distributions of leading and subleading pairs; Invariant mass of the (a) leading pair (b) subleading pair and transverse momentum p_T^Z of (c) leading pair and (d) subleading pair of the Z pairs. The points represent the observed data and the histograms show the signal prediction from simulation. The shaded band on each histogram shows the combined statistical and systematic uncertainty on the signal prediction. The predicted number of background events from the data-driven background estimate is indicated on each plot.

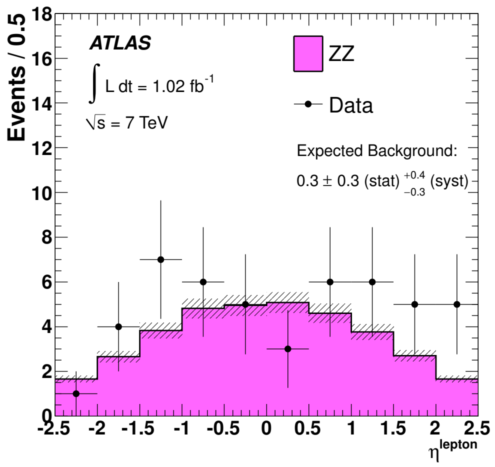

(a)

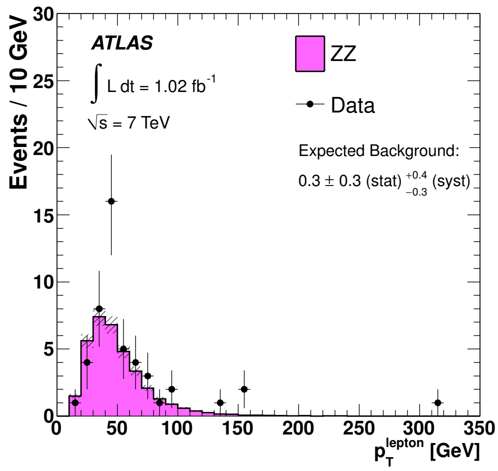

(b)

Figure 7.15: Kinematic distributions of the four lepton candidates; (a) η and (b) p_T of leptons. The points represent the observed data and the histograms show the signal prediction from simulation. The shaded band on each histogram shows the combined statistical and systematic uncertainty on the signal prediction. The predicted number of background events from the data-driven background estimate is indicated on each plot.

k_b and θ_b represent the shape and scale of the gamma function. The two variables are determined by using the estimated number of background events, $b^{+\sigma_b^H}_{-\sigma_b^L}$, so that the mode (the point of maximum probability) of the gamma function to be at the mean background estimate (b) and the variance to be the same as the variance of truncated Gaussian which has a mode equal to background estimate (b) and sigma equal to the uncertainty on the nominal background estimate. In order to include 68.3% of the area under a truncated Gaussian distribution, the interval $[0, b + \sigma_b^H]$ is considered. An iteration is done to determine the σ_b of the properly normalized Gaussian, and the variance of the truncated Gaussian distribution. A comparison of the two p.d.fs can be seen in Figure 7.18. Both priors share the same $mode = 0.26$ and $variance = 0.15$.

To take into account the possibility of background fluctuations alone explaining the observation, one billion pseudo-experiments were performed using the expected number of background events as the mean value of a Poisson distribution to produce "observed" events (N) for each pseudo-experiment. The background expectation is drawn from a

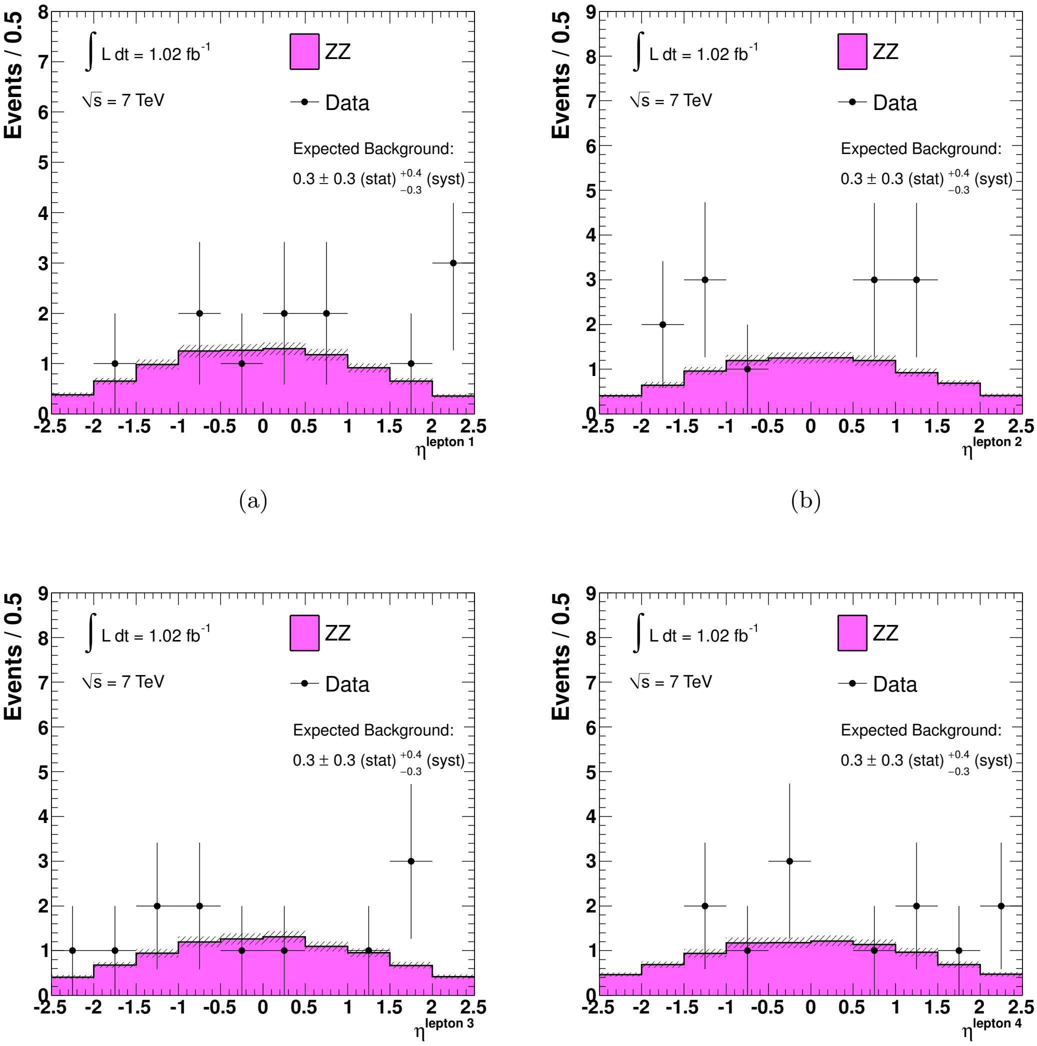

(a) (b) (c) (d)

Figure 7.16: Pseudorapidity η distributions of (a) leading (b) subleading (c) third and (d) fourth lepton. The points represent the observed data and the histograms show the signal prediction from simulation. The shaded band on each histogram shows the combined statistical and systematic uncertainty on the signal prediction. The predicted number of background events from the data-driven background estimate is indicated on each plot.

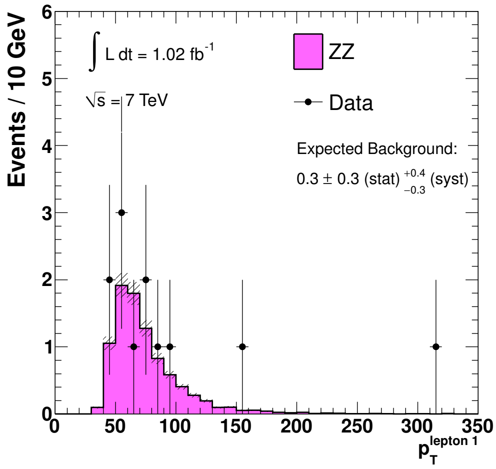

(a)

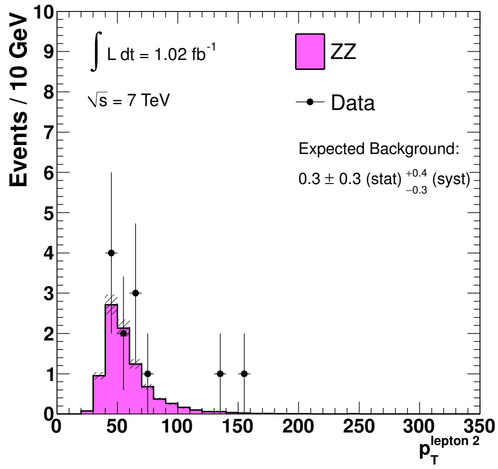

(b)

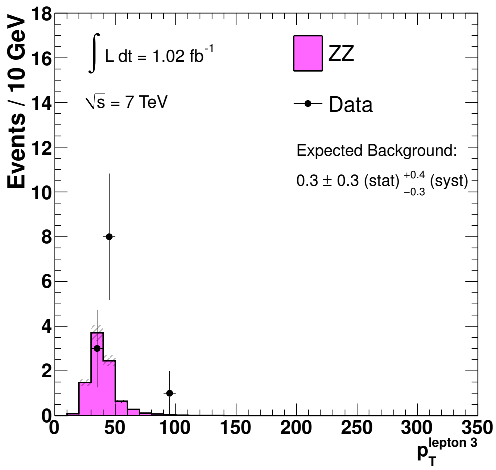

(c)

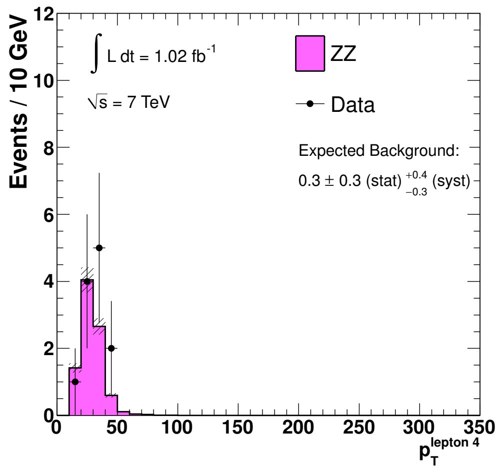

(d)

Figure 7.17: p_T distributions of (a) leading (b) subleading (c) third and (d) fourth lepton. The points represent the observed data and the histograms show the signal prediction from simulation. The shaded band on each histogram shows the combined statistical and systematic uncertainty on the signal prediction. The predicted number of background events from the data-driven background estimate is indicated on each plot.

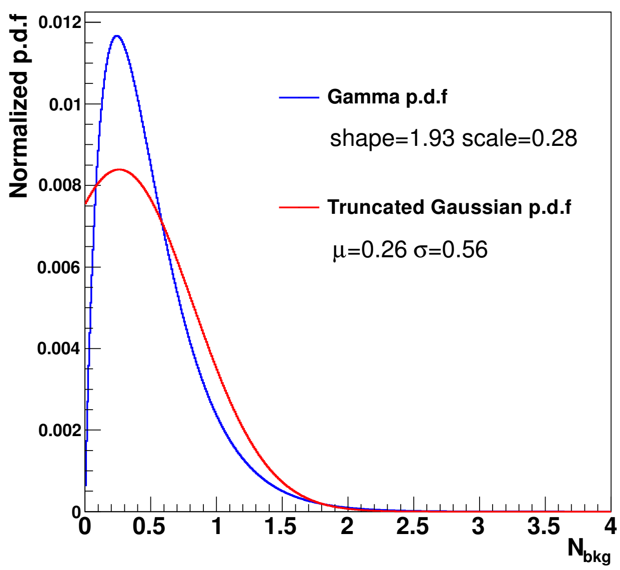

Figure 7.18: The background priors used for the $ZZ \to 4\ell$. Both Gamma and Truncated Gaussian p.d.f share the same mode =0.26 (nominal background estimate) and variance = 0.15 (nominal uncertainty estimate)

Gamma distribution with shape and scale equal to $k_b = 1.93$ and $\theta_b = 0.28$.

With twelve observed ZZ candidate events, the probability for the background to fluctuate up to the observed number of events in the absence of signal is 1.02×10^{-7}, corresponding to a significance[1] of 5.2 standard deviations for the signal observation.

As a cross-check, the following method is also used:

$$Pr(N \geq N_{obs}; b, \sigma_b^L, \sigma_b^H) = \sum_{N=N_{obs}}^{\infty} \int_0^{\infty} P(N; x) G(x; b, \sigma_b) \mathrm{d}x \tag{7.20}$$

where P is the Poisson distribution, as defined above, and G is a truncated Gaussian defined as:

[1]The probability or else $p-$value can be converted into a number of standard deviations σ of a Gaussian distribution, beyond which the one-sided tail area corresponds to $p-$value. Thus 5σ corresponds to a $p-$value of $3 \cdot 10^{-7}$.

$$G(x; b, \sigma_b) = \text{Norm} \times \exp\left[-\frac{1}{2}\left(\frac{x-b}{\sigma_b}\right)^2\right], \text{where}$$
$$\text{Norm} = \int_0^\infty \exp\left[-\frac{1}{2}\left(\frac{x-b}{\sigma_b}\right)^2\right] \mathrm{d}x \tag{7.21}$$

and x is restricted to be non-negative. The determination of the σ_b value is done by treating the interval $[0, b + \sigma_b^H]$ as covering 68.3 % of the area under the curve of the truncated Gaussian. This results in $\sigma_b = 0.56$.

For this construction, the p-value is 1.1×10^{-8}, corresponding to a significance of 5.6 standard deviations for the signal observation.

7.11.1 Likelihood of features in observation

There are two interesting features of possible concern in the observed signal. One is the number of observed events in the $\mu\mu\mu\mu$ channel. The other is the number of high four-lepton mass observed events. The likelihood of these features is determined from pseudoexperiments, under the signal plus background hypothesis:

$$Pr(N \geq N_{obs}; b, \sigma_b, s, \sigma_s) = \sum_{N=N_{obs}}^{\infty} \int_0^\infty \int_0^\infty P(N; x+y) Ga(x; k_b, \theta_b) G(y; s, \sigma_s) \mathrm{d}y \mathrm{d}x \tag{7.22}$$

where $s \pm \sigma_s$ represents the expected number of signal events and the other variables are defined as above.

In the $\mu\mu\mu\mu$ channel, the number of events observed are eight in total, where only $s = 3.03 \pm 0.07$ and $b = 0.26^{+0.27}_{-0.26}(\text{stat})\ ^{+0.35}_{-0.26}(\text{syst})$ events are expected. The probability of such an observation under the signal plus background hypothesis is 3.2 %.

To study the likelihood of observing the number of events counted in the high ZZ-mass region, an integration over the signal, background and data distributions is performed by taking various lower cut values of the mass ($M_{4\ell}$). The results are listed in Table 7.11.

$M_{4\ell}$ (GeV)	N	s	b	p-value (%)
350	3	0.84 ± 0.05	negl.	5.3
400	3	0.51 ± 0.03	negl.	1.6
450	3	0.32 ± 0.02	negl.	0.5

Table 7.11: Summary of significance studies - Summary of likelihood of observing N events with an expected signal (s) and background (b) with errors (stat.+lum.) for various lower cut values on $M(4\ell)$.

7.12 Cross section calculation

7.12.1 Definition of the reconstruction efficiency

The total cross section can be calculated by extrapolating the measurement within the detector acceptance. Due to the theoretical uncertainties on this extrapolation, one must first calculate the fiducial cross section without the full extrapolation and therefore with reduced uncertainties.

For the fiducial cross section calculation, a definition of a fiducial volume (see Section 7.3) and an efficiency correction term is necessary, in order to perform an extrapolation from the reconstructed level to the fiducial volume at generator level. In specific, the following quantity is defined:

$$C_{ZZ\to\ell\ell\ell'\ell'} = \epsilon_{trig} \times \epsilon_{event} \times \epsilon_{lep} \times \alpha_{reco} \tag{7.23}$$

where ϵ_{trig} is the trigger efficiency, ϵ_{event} is the efficiency of the event level cuts (like the primary vertex cut, etc.), $\epsilon_{lep} = \prod_{i=1}^{4} \epsilon_i^{lepton}$ is the product of the individual efficiencies for the four leptons to pass the lepton object selection cuts, and finally α_{reco} is the reconstruction to generator level fiducial volume correction which also includes smearing corrections and resolutions. In practice, C_{ZZ} can be calculated by applying the necessary MC wih respect to data corrections to the signal $ZZ \to \ell\ell\ell'\ell'$ (such as smearing, pileup re-weighting, reconstruction and identification scale factors, etc.) and then finding the ratio of the number of events which pass the reconstruction level cuts to the number of events which pass the fiducial volume cuts at generator level. Thus,

$$C_{ZZ\to\ell\ell\ell'\ell'} = \frac{N^{\text{MC Pass All Cuts}}_{\text{Reconstructed } ZZ\to\ell\ell\ell'\ell'} \times \text{SF}}{N^{\text{MC Fiducial Volume}}_{\text{Generated } ZZ\to\ell\ell\ell'\ell'}} \tag{7.24}$$

where the scale factor is understood to be applied on an event-by-event level. The scale factor (SF) is used to correct for discrepancies in trigger efficiency and reconstruction efficiency between data and MC, and is defined as

$$SF = \frac{\epsilon_{trig}^{data}}{\epsilon_{trig}^{MC}} \cdot \frac{\epsilon_{reco}^{data}}{\epsilon_{reco}^{MC}} \tag{7.25}$$

with $\epsilon_{reco} = \epsilon_{lep} \cdot \epsilon_{event}$.

This fiducial correction factor needs to be calculated for each $ZZ \to \ell\ell\ell'\ell'$ decay channel separately. It should be noted that this extrapolates from reconstructed level to truth fiducial level values within the given channel. Branching ratios and detector acceptance will be needed to combine channels and obtain a total cross-section.

The primary purpose of using the fiducial correction is to correct the reconstructed level cross-section to a truth level cross-section defined by a fiducial volume roughly corresponding to the volume of the detector. The reason for this procedure is that this correction will be less sensitive to purely theoretical uncertainties like PDF. The C_{ZZ} term provides the probability of reconstructing an event, given that all the objects in the event would have been in the detector and passed our selection level cuts.

Since the selection cuts for electrons and muons are different, the C_{ZZ} term corresponding to our selection cuts for each ZZ channel is also different. In order to calculate a combined fiducial cross section, one needs to first perform an additional extrapolation to a common fiducial volume (see Section 7.3) and then extract a combined cross section in the common volume.

It should be noted that for truth object selection, final state muons and "dressed" final state electrons have been used. A "dressed" final state electron has all photons within $\Delta R < 0.1$ added to the Lorentz vector of the electron. These photons can be a product of two different processes, final state radiation (FSR) [1] or Bremsstrahlung radiation [2].

The $ZZ \to \tau\tau ll$ with subsequent $\tau\tau \to \ell'\ell'$ contamination to the direct decay of $ZZ \to \ell\ell\ell'\ell'$ is negligible. This is due to the relatively tight Z mass requirement $66 < M_{ll} < 116$GeV. In the case of $Z \to \tau\tau \to ee$, only one candidate out of 7000 survived the selection criteria of the analysis.

[1] Final State Radiation (FSR) is a photon emmision during the decay of Zs to leptons.

[2] Bremsstrahlung radiation is an electromagnetic radiation produced by a charged particle when it interacts with matter.

7.12.2 Definition of the acceptance

As it has already been noted in the previous sections, the total cross section measurement can be achieved, by correcting the fiducial cross section to full phase space (see Equation 7.2). For this extraction one needs a correction factor, called acceptance, from truth level fiducial volume to the full phase space of truth. This correction is defined as A_{ZZ} and is calculated by the equation:

$$A_{ZZ\to\ell\ell\ell'\ell'} = \frac{N^{\text{MC Fiducial Volume}}_{\text{Generated } ZZ\to\ell\ell\ell'\ell'}}{N^{\text{MC All}}_{\text{Generated ZZ}\to\ell\ell\ell'\ell'}} \tag{7.26}$$

The acceptance efficiency is calculated from the MCFM [9; 19], using the MSTW2008 PDF [20] set and setting the renormalization and factorization scales as $\mu_R = \mu_F = \mu_Z$. The cross section for on-shell ZZ production according to the NLO calculations is 6.46 pb. Applying the fiducial cuts described above the cross section at NLO is 14.78 fb.

Note that this version of MCFM includes the gluon-gluon contribution to ZZ production, as well as the single-resonant diagrams (see Figure 7.19). The latter are not important for on-shell ZZ production, but the inclusion of the gluon-gluon (see Figure 2.4) contribution to the total NLO cross section is 6.3%; this fraction is slightly higher, 7.1%, with the fiducial cuts because the Z-bosons from gluon fusion are produced more centrally than those from the quark-antiquark process [21; 22].

The correction factor uncertainty from the fiducial to the total cross section is estimated by re-evaluating this factor using the CTEQ6.6 PDF [23; 24] set; the resulting uncertainty is 0.8%. The effect of changing the factorization and renormalization scales to $\mu_{\text{R}} = \mu_{\text{F}} = \sqrt{m_Z^2 + p_{\text{T}}(Z)^2}$ is 0.1%, and is thus much smaller than the PDF uncertainty. The uncertainty from CTEQ6.6 after testing 44 eigenvector sets [23; 24] for computation of the PDF uncertainty is 1.2%. The quadratic sum of the systematic uncertainty resulting from the comparison between MSTW2008 and CTEQ6.6 PDF and the systematic uncertainty due to variation of the CTEQ6.6 PDF produces a total systematic uncertainty of 1.3%.

The acceptance A_{ZZ}, is also affected dut to initial state radiation (ISR), final state radiation (FSR) and underlying event modeling. The evaluation of this systematic uncertainty has been done by calculating the A_{ZZ} with the MCFM and POWHEG BOX [25]. The relative difference is found to be at 1% and it is a consequence of the

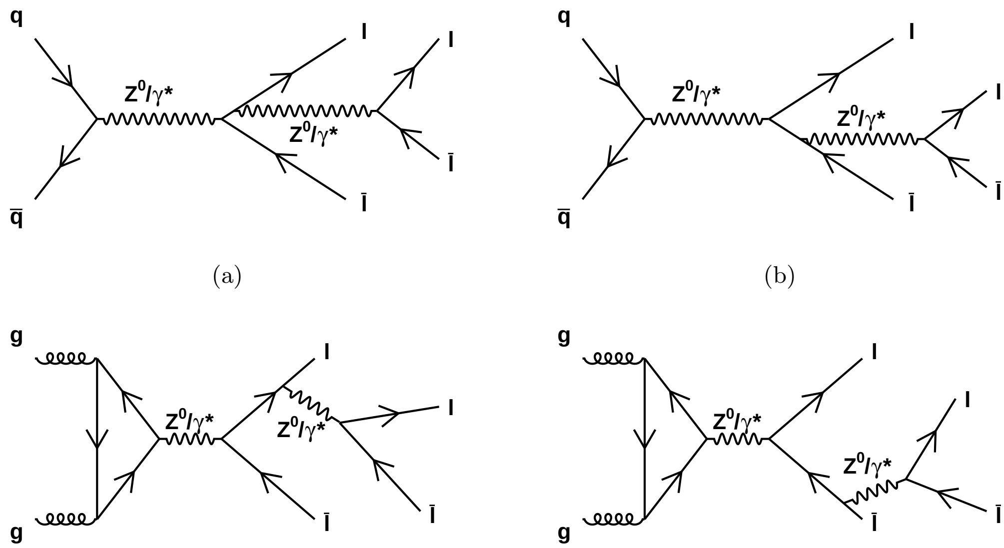

(a) (b) (c) (d)

Figure 7.19: Single resonant diagrams for (a)-(b) LO ($q\bar{q} \rightarrow (Z/\gamma^*)(Z/\gamma^*) \rightarrow \ell\ell'\ell'$) and (c)-(d) NLO $gg \rightarrow (Z/\gamma^*)(Z/\gamma^*) \rightarrow \ell\ell\ell'\ell'$ with the exchange of Z/γ^*.

effects due to generators, ISR, FSR, underlying event and PDF. By taking into account all the systematic sources affecting the A_{ZZ}, the total systematic uncertainty is 1.8%.

The reason for separating the total acceptance this way is that the theoretical uncertainties will primarily affect $A_{ZZ\rightarrow\ell\ell\ell'\ell'}$ and only lead to small uncertainties on $C_{ZZ\rightarrow\ell\ell\ell'\ell'}$.

7.12.3 Reconstruction and Acceptance Values

Using the definitions for the $C_{ZZ\rightarrow\ell\ell\ell'\ell'}$ and $A_{ZZ\rightarrow\ell\ell\ell'\ell'}$ respectively, one can calculate these values by using the signal MC sample. The exact numbers per channel can be found in Table 7.12.

Table 7.13 shows a comparison of fiducial reconstruction efficiency C_{ZZ} between Pythia and MC@NLO generators. This comparison accounts for the different kinematic distributions between LO and NLO processes, different parton shower models, underlying events and PDF. As can be seen the relative difference is less than 0.5%.

	eeee	$\mu\mu\mu\mu$	$ee\mu\mu$	combined
C_{ZZ}	0.414±0.005± 0.028	0.808±0.004± 0.016	0.570±0.004± 0.019	0.591±0.003± 0.018
A_{ZZ}	0.507±0.009	0.507±0.009	0.507±0.009	0.507±0.009

Table 7.12: Correction factor and acceptance corrections per channel. For C_{ZZ} the first uncertainty is statistical and the second systematic. For A_{ZZ} the uncertainty is due to PDF and parton shower uncertainties.

	eeee	$\mu\mu\mu\mu$	$ee\mu\mu$	combined
PYTHIA	0.414±0.005	0.808±0.004	0.570±0.004	0.591±0.003
MC@NLO	0.412±0.002	0.806±0.001	0.577±0.002	0.594±0.002

Table 7.13: Comparison of the correction factor C_{ZZ}, between PYTHIA and MC@NLO. Only statistical uncertainty is included in the table.

7.12.4 Cross section measurement

A minimum log-likelihood approach has been used to calculate the combined ($4e + 4\mu + 2e2\mu$) cross section. This approach takes into account the Poisson statistics of our samples as well as the systematic uncertainties. The measurement of the cross-section is carried out by merging the three channels and then maximizing the profile likelihood function L with respect to the cross section σ.

Two different background priors (Gamma and Truncated Gaussian, see Section 7.11) have been tested as a bakground nuisance parameters.

7.12.4.1 Fiducial cross section measurement

The profile likelihood function for the fiducial cross section is the product of a Poisson probability distribution (P), a Gamma distribution function (Γ) for the background parameter and a Gaussian distribution function (G) for the remaining nuisance parameters (C_{ZZ}, $\mathcal{L}$).

$$L(\sigma, C_{ZZ}, b, \mathcal{L}; \Delta_b, \Delta_{C_{ZZ}}, \Delta_{\mathcal{L}}, N) = P(\sigma, C'_{ZZ}, b'; N)G(C'_{ZZ}; C_{ZZ}, \Delta_{C_{ZZ}})\Gamma(b'; b, \Delta_b) \\ G(\mathcal{L}'; \mathcal{L}, \Delta_{\mathcal{L}}) \tag{7.27}$$

The Poisson function for the number of observed events N is

$$P(\sigma, C_{ZZ}, b; N) = \frac{e^{-(s(\sigma,C_{ZZ})+b)}\,(s(\sigma, C_{ZZ}) + b)^N}{N!}, \tag{7.28}$$

where the number of signal events is a function of the cross section and other quantities such as the integrated luminosity, the correction factor C_{ZZ} and the background estimation. The number of signal events for the fiducial cross section is given by the equation:

$$s(\sigma_{\text{fiducial}}, C_{ZZ}) = \sigma_{\text{fiducial}}\mathcal{L}C_{ZZ}4 \tag{7.29}$$

where the factor of four accounts for the four different final states $(4e, 4\mu, 2e2\mu, 2\mu2e)$.

The $-\ln L$ is minimized for computational convenience rather than maximize L. The corresponding likelihood minimization can be seen in Figure 7.20, where the figure on the left corresponds to a Gamma p.d.f prior for the background and the figure on the right refers to a truncated Gaussian p.d.f prior for background.

Two types of uncertainties, statistical and systematic, are associated with the cross section measurement. The result without any variation in systematic uncertainties in the fit represents the statistical uncertainty. By including the individual systematic uncertainties and minimizing each time the $-\ln L$ one can calculate the systematic uncertainty in the cross section for each source. The steps are as follows:

1. Find the result of the fit without variation in any systematic uncertainty. The minimum value of the fit corresponds to the central value of the cross section while the value of $-\ln L = 0.05$ represents the 95% C.L. error of the minimized value;

2. Repeat the above procedure by considering also the gaussian variation of one of the systematic sources which affect the result;

3. The systematic uncertainty can then be calculated from the equation: $\sigma_{syst} = \sqrt{\sigma_{gauss}^2 - \sigma_{stat}^2}$.

The statistical uncertainty and the individual systematic uncertainties to the cross section measurement can be found in Table 7.14. The cross section uncertainty is larger in the negative side due to a large tail in the background prior. The Gamma distribution uncertainty is roughly half of the Gaussian due to a relatively narrower distribution around the peak (mode) of the distributions. Table 7.15 summarizes the fiducial cross section results.

Source	Relative Uncertainties %	
Statistiacl Uncer.	+32	-27
A_{ZZ}	+2.0	-1.2
C_{ZZ}	+3.8	-2.4
Luminosity	+4.7	-2.8
Gaussian Bkg	+4.6	-5.0
Gamma Dist Bkg	+2.1	-2.5

Table 7.14: Summary of the relative uncertainties of the cross-section measurement.

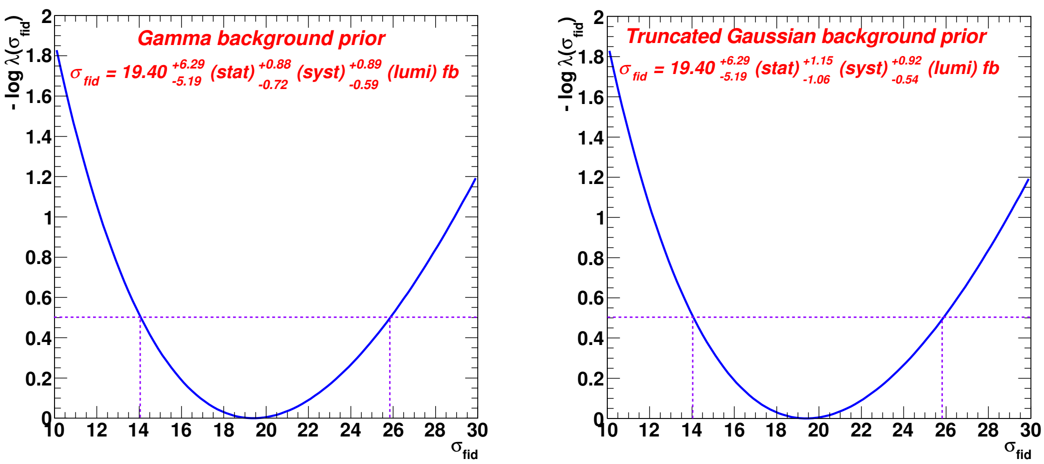

(a) (b)

Figure 7.20: Fiducial cross-section profile likelihood for (a) Gamma background prior and (b) truncated Gaussian background prior. The dashed lines show the 95% C.L.

7.12.5 Total cross section measurement

For the calculation of the total cross section, one must append the term $G(A'_{ZZ}; A_{ZZ}, \Delta_{A_{ZZ}})$ to the likelihood to account for the uncertainty on the detector acceptance A_{ZZ}. The

Background Prior	Fiducial cross-section $[fb]$
Gamma	$19.4^{+6.29}_{-5.19}(stat.)^{+0.88}_{-0.72}(syst.)^{+0.89}_{-0.59}(lumi)$
Truncated Gaussian	$19.4^{+6.29}_{-5.19}(stat.)^{+1.15}_{-1.06}(syst.)^{+0.92}_{-0.54}(lumi)$

Table 7.15: Fiducial cross section measurements using Gamma p.d.f background prior as well as a Truncated Gaussian p.d.f background prior. The systematic uncertainties are also shown in the table. The Gamma p.d.f is the default for the final result.

L is then taking the form

$$L(\sigma, C_{ZZ}, A_{zz}, b; \Delta_b, \Delta_{C_{ZZ}}, \Delta_{A_{ZZ}}, N) = P(\sigma, C'_{ZZ}, A'_{ZZ}, b'; N)G(C'_{ZZ}; C_{ZZ}, \Delta_{C_{ZZ}}) \\ G(A'_{ZZ}; A_{ZZ}, \Delta_{A_{ZZ}})\Gamma(b'; b, \Delta_b) \tag{7.30}$$

where the signal events are now given by the following equation

$$s(\sigma_{\text{total}}, C_{ZZ}) = \sigma_{\text{total}}\mathcal{L}C_{ZZ}A_{ZZ}4BR(ZZ \to \ell\ell\ell'\ell') \tag{7.31}$$

The A_{ZZ} term accounts for the total volume of the measurement, as well as the $k-$ factors for the NLO effects. The official results of the ZZ paper [26] published November 2011 are based on the Gamma distribution function. The total cross section for each background prior is presented in Table 7.16, while the minimization of the likelihood is shown in Figure 7.21.

For sake of comparison and completeness, results of the total ZZ cross section, after analyzing the full 2011 statistics corresponding to $\mathcal{L} = 4.7$ fb^{-1} of data, are shown in Table 7.17. This measurement confirms the results of the statistically smaller sample with the first 1 fb^{-1}. The result in also consistent with the NLO Standard Model total cross section for this process of $6.5^{+0.3}_{-0.2}$ pb. A direct comparison of the fiducial cross sections is not possible because the fiducial volume has been changed. A detail description of the analysis on the full 2011 statistics can be found in reference [27].

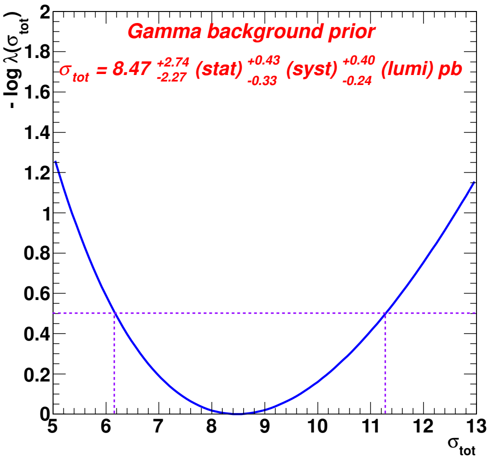

(a)

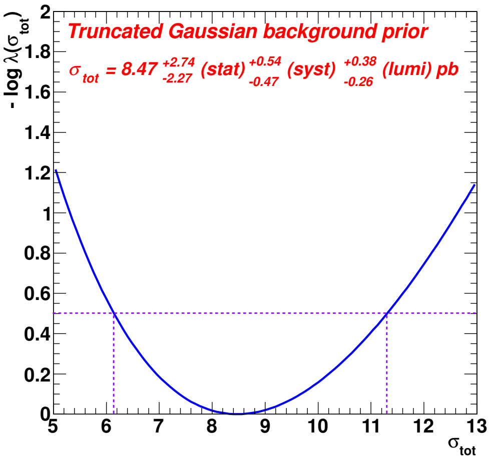

(b)

Figure 7.21: Total cross-section profile likelihood at $\mathcal{L} = 1.02$ fb^{-1} with (a) Gamma background prior and (b) truncated Gaussian background prior. The dashed lines show the 95% C.L.

Background Prior	Total cross-section [pb]
Gamma	$8.47^{+2.74}_{-2.27}(rmstat)^{+0.43}_{-0.33}(\text{syst})^{+0.40}_{-0.24}(\text{lumi})$
Truncated Gaussian	$8.47^{+2.74}_{-2.27}(rmstat)^{+0.54}_{-0.47}(\text{syst})^{+0.38}_{-0.26}(\text{lumi})$

Table 7.16: Total ZZ cross-section measurements corresponding to $\mathcal{L} = 1.02$ fb^{-1} using Gamma p.d.f bakground prior as well as a Truncated Gaussian p.d.f background prior. The systematic uncertainties are also shown in the table. The Gamma p.d.f is the default for the final result.

Background Prior	Total cross-section [pb]
Gamma	$7.24^{+1.08}_{-0.92}(rmstat)^{+0.38}_{-0.32}$(syst) $\pm$ 0.3(lumi)
Truncated Gaussian	$7.24^{+1.08}_{-0.92}$(stat)$^{+0.44}_{-0.40}$(syst) $\pm$ 0.3(lumi)

Table 7.17: Total ZZ cross-section measurements corresponding to $\mathcal{L} = 4.7$ fb^{-1} using Gamma p.d.f bakground prior as well as a Truncated Gaussian p.d.f background prior. The systematic uncertainties are also shown in the table. The Gamma p.d.f is the default for the final result.

7.13 Summary

A measurement of the ZZ production cross section with the ATLAS detector at $\sqrt{s} =$ 7 TeV has been performed using electrons and muons in the final state. In a dataset with an integrated luminosity of $\sim$ 1 fb^{-1} a total of twelve candidates are observed with a background expectation of 0.3 $\pm$ 0.3(stat) $^{+0.4}_{-0.3}$(syst), corresponding to a signal significance of 5.2σ. The Standard Model expectation for the number of signal events is 8.9 $\pm$ 0.1(stat) $\pm$ 0.3(syst). The fiducial and total cross sections were determined to be

$$\begin{aligned}\sigma^{\text{fid}}_{ZZ\to\ell^+\ell^-\ell^+\ell^-} &= 19.4^{+6.3}_{-5.2}\ (\text{stat})^{+0.9}_{-0.7}\ (\text{syst})\ ^{+0.9}_{-0.6}\ (\text{lumi})\ \text{fb} \\ \sigma^{\text{tot}}_{ZZ} &= 8.5^{+2.7}_{-2.3}\ (\text{stat})\ ^{+0.4}_{-0.3}\ (\text{syst})\ \pm 0.3\ (\text{lumi})\ \text{pb.}\end{aligned}$$

The result agrees within error with the analysis performed on the full 2011 sample corresponding to $\mathcal{L} = 4.7$ fb^{-1} of data. The total cross section has been found to be:

$$\sigma^{\text{tot}}_{ZZ} = 7.2^{+1.1}_{-0.9}\ (\text{stat})\ ^{+0.4}_{-0.3}\ (\text{syst})\ \pm 0.3\ (\text{lumi})\ \text{pb.}$$

Both cross section measurements are statistically consistent with the SM total cross section equal to $6.5^{+0.3}_{-0.2}$ pb which is calculated with MC@NLO [28] MC generator with parton density function set CTEQ6.6.

Bibliography

[1] ATLAS Collaboration, "Updated Luminosity Determination in pp Collisions at $\sqrt{s}$ =7 TeV using the ATLAS Detector", ATLAS-CONF-2011-011. 92

[2] T. Sjostrand et al., "High-energy physics event generation with PYTHIA 6.1", Comput.Phys.Commun.135:238-259, 2001. 92, 93

[3] A. Sherstnev, R.S. Thorne, "Parton Distributions for LO Generators", Eur.Phys.J.C55:553-575, 2008. 92

[4] The ATLAS Collaboration, "The ATLAS Simulation Infrastructure", Eur.Phys.J.C70:823-874, 2010. 92

[5] S. Angostinelli et all., "GEANT4a simulation toolkit", Nucl. Instrum. Meth. A 506, 250 (2003). 92

[6] S. Frixione, F. Stoeckli, P. Torrielli, B. R. Webber, C. D. White, "The MC@NLO 4.0 Event Generator", arXiv:1010.0819v1 [hep-ph]. 93

[7] M.L. Mangano, M. Moretti, F. Piccinini, R. Pittau, A.D. Polosa, "Alpgen, a generator for hard multiparton processes in hadronic collisions", JHEP 0307 (2003) 001. 93

[8] J. Alwall et all., "MadGraph/MadEvent v4: The New Web Generation", HEP0709:028, 2007. 93

[9] J. Campbell, K. Ellis, and C. Williams, "Vector Boson Pair Production at the LHC", JHEP 1107:018,2011. 94, 127

[10] J. Butterworth et all., “Single Boson and Diboson Production Cross Sections in pp Collisions at $\sqrt{s}$=7 TeV”, Tech. Rep. ATL-COM-PHYS-2010-695, CERN, Geneva, Aug, 2010. 93

[11] K. Nakamura et al. (Particle Data Group), “Review of Particle Physics”, J. Phys. G 37, 075021 (2010). 94

[12] R. Nicolaidou et all., “Muon identification procedure for the ATLAS detector at the LHC using Muonboy reconstruction package and tests of its performance using cosmic rays and single beam data”, J. Phys.Conf. Ser. 219 032052, 2010. 96

[13] ATLAS MCP Group, “https://twiki.cern.ch/twiki/bin/view/AtlasProtected/MCP AnalysisGuidelinesEPS”, 2011. 96

[14] G. Kasieczka, “Early SUSY Searches at the CMS Experiment at CERN”, PhD Thesis, 2009 99

[15] ATLAS Collaboration, “Search for a Standard Model Higgs boson in the decay channel $H \to ZZ^* \to 4\ell$ with the ATLAS detector”, ATLAS-CONF-2011-131, 2011. 99

[16] ATLAS Collaboation, “Electron performance measurements with the ATLAS detector using the 2010 LHC proton-proton collision data”, Eur. Phys. J. C72 (2012) 1909. 110

[17] ATLAS Collaboration, “Muon reconstruction efficiency in reprocessed 2010 LHC proton-proton collision data recorded with the ATLAS detector”, ATLAS-CONF-2011-063. 112

[18] http://www.hep.ucl.ac.uk/atlas/atlantis/?q=documentation. 113, 204

[19] J. M. Campbell, R. K. Ellis,“MCFM for the Tevatron and the LHC”, Nucl.Phys.Proc.Suppl.205-206:10-15, 2010. 127

[20] A.D. Martin, W.J. Stirling, R.S. Thorne, G. Watt, “Parton distributions for the LHC”, Eur.Phys.J.C63:189-285,2009. 127

[21] E. W. N. Glover and J. J. V. der Bij, “Z-boson pair production via gluon fusion”, Nuclear Physics B 321, 561 (1989). 127

[22] C. Zecher, T. Matsuura, and J. J. van der Bij, "Leptonic Signals from off-shell Z Boson Pairs at Hadron Colliders", Z.Phys. C64 (1994) 219-226. 127

[23] P. M. Nadolsky et al., "Implications of CTEQ global analysis for collider observables", Phys. Rev. D78 (2008) 013004. 127

[24] http://hep.pa.msu.edu/cteq/public/cteq6.html. 127

[25] T. Melia, P. Nason, R. Rontsch, and G. Zanderighi, "W^+W^-, WZ and ZZ production in the POWHEG BOX", arXiv:1107.5051v3 [hep-ph]. 127

[26] ATLAS Collaboration, "Measurement of the ZZ production cross section and limits on anomalous neutral gauge couplings in proton-proton collisions at $\sqrt{s} = 7$ TeV with the ATLAS detector", Phys.Rev.Lett. 108 (2012) 041804. 132

[27] ATLAS Collaboration, "Measurement of the total ZZ production cross section in the four-lepton channel using 4.7 fb^{-1} of ATLAS data", ATLAS-CONF-2012-026. 132

[28] S. Frixione and B. R. Webber, "Matching NLO QCD computations and parton shower simulations", JHEP 06 (2002) 029, arXiv:hep-ph/0204244. 134

..Higgs particle, the joker in particle physics...

Chapter 8

Searches for new physics with 4 charged leptons in the final state

This chapter describes the work for the Randal-Sundrum Graviton (RS Graviton) and doubly charged Higgs ($H^{\pm\pm}H^{\mp\mp}$) searches. The selection criteria used in the analysis are based on the ones used for the ZZ production cross section measurement described in detail in the previous chapter. Limits in their production cross section have been extracted after analyzing 1 fb^{-1} of data.

8.1 Introduction

This chapter discusses the methodology followed for the searches of new physics with four leptons in the final state. The two searches are $H^{\pm\pm}H^{\mp\mp} \rightarrow \ell^{\pm}\ell^{\pm}\ell^{\mp}\ell^{\mp}$ and $G \rightarrow ZZ \rightarrow \ell^{+}\ell^{-}\ell^{+}\ell^{-}$ where $\ell = e, \mu$. The $H^{\pm\pm}H^{\mp\mp}$ corresponds to a non-ZZ search since the final states must not contain an opposite-sign same-flavor pairs with invariant mass 66< $M_{\ell\ell}$ <116 GeV, while in the searches for a Graviton the final states must include two opposite-sign same-flavor pairs, each one lying in the mass region 66< $M_{\ell\ell}$ <116 GeV (ZZ resonance search). The principle of the data-driven background technique utilized to estimate the background in the two searches is the same as in the ZZ analysis but the control regions used to extrapolate the background to signal region are different. The method used for the extraction of limits and the results are also presented.

8.2 Datasamples and event reconstruction

The data sample used for the two searches correspond to proton-proton collisions that were taken between February and July 2011 at $\sqrt{s} = 7$ TeV at the LHC and it is the same as in $ZZ \to 4\ell$ analysis (see Section 7.2). These analyses also use the same trigger and object reconstruction and identification algorithms 7.5.1 as in the previous chapter.

In addition to the MC samples described in Section 7.2.2, the following MC samples have also been used. The RS G^* signal events are generated via gluon-gluon fusion (see Figure 2.6) with PYTHIA [3] using MRST LO* [4] parton distribution functions for $m_{G^*} = 350$ and 500 - 1500 GeV in steps 250 GeV steps. All samples assume the dimensionless coupling parameter $k/\bar{M}_{P\ell} = 0.1$. The doubly charged Higgs bosons are generated using MADGRAPH [2] showered and hadronized in PYTHIA [3]. All the samples are simulated with the full ATLAS detector simulation [5; 6].

The BR of the $H^{\pm\pm}$ can be 100% to one lepton flavor (e, μ, τ) or 100% to $e\mu$ or equally decaying to all lepton flavors [1]. As a benchmark scenario the branching fractions have been selected to be equal between all lepton flavors, also including the lepton flavor violation cases.

- 1/9 $H^{\pm\pm} \to e^{\pm}e^{\pm}$
- 1/9 $H^{\pm\pm} \to \mu^{\pm}\mu^{\pm}$
- 1/9 $H^{\pm\pm} \to \tau^{\pm}\tau^{\pm}$
- 2/9 $H^{\pm\pm} \to e^{\pm}\mu^{\pm}$
- 2/9 $H^{\pm\pm} \to e^{\pm}\tau^{\pm}$
- 2/9 $H^{\pm\pm} \to \mu^{\pm}\tau^{\pm}$

where the factor of 2 in the last three channels is due to the combinatorics.

8.3 Event selection

The selection criteria used in the analyses have been discussed in great detail in Section 7.5, so the discussion here is concentrated in the differences between the two analysis.

- Events must contain $\geq$4 leptons.

Process	Generator	Events	M_H [GeV]	$\sigma_{singlet}$ [pb]	$\sigma_{doublet}$[pb]	$\sigma_{triplet}$[pb]
$H^{\pm\pm}H^{\mp\mp}$	MadGraph	90000	100	0.15	0.17	0.40
$H^{\pm\pm}H^{\mp\mp}$	MadGraph	80973	150	0.033	0.039	0.089
$H^{\pm\pm}H^{\mp\mp}$	MadGraph	90000	200	0.10	0.012	0.027
$H^{\pm\pm}H^{\mp\mp}$	MadGraph	90000	300	0.0017	0.0021	0.0045

Table 8.1: MC samples used in the four charged lepton searches. Depending on the model, the doubly-charged Higgs can be a member of a singlet, doublet or triplet symmetry group [1]; doublet or triplet models are sometimes classified as Right- or Left-handed production [7], respectively.

- Events are sorted into the following categories depending on the combinations of pairs that can be formed (where $\ell, \ell' = e, \mu$):
  - two OS-SF pairs: $\ell^{\pm}\ell^{\mp}\ell'^{\pm}\ell'^{\mp}$;
  - one OS-SF pair: $\ell^{\pm}\ell^{\mp}\ell'\ell'$ (where $\ell'\ell'$ is either SS or OF);
  - no OS-SF pairs, $\geq$1 OS-OF: $\ell^{\pm}\ell'^{\mp}\ell^{*}\ell^{*}$ (where $\ell^{*}\ell^{*}$ is SS or OF);
  - four SS leptons with any flavors: $\ell^{\pm}\ell^{\pm}\ell^{\pm}\ell^{\pm}$;

The above categorization helps to separate ZZ candidate events from the events dominated by fake leptons (see Section 7.7) . In the channels with two OS-SF pairs or four SS leptons, ambiguities are resolved by choosing the solution (quadruplet) that results in the smaller value of $|m_{\ell\ell}^{first} - m_Z| + |m_{\ell'\ell'}^{second} - m_Z|$, as with the $ZZ \to 4\ell$ analysis. In all categories, a primary pair is considered to be the one closest to the Z pole.

8.4 Background estimation

The primary source giving four leptons in the final state is the ZZ production, which has been simulated with Pythia generator, as in the case of the $ZZ \to 4\ell$ analysis 7.2.2. The background contribution due to three true leptons plus one fake lepton or two true leptons and two fake objects is expected to be small and has been calculated according to the methodology described in Section 7.7.

In the cases, where the control regions from which the background estimate is extrapolated ($LLLJ$, $LLJJ$) contain zero events, a 68% C.L upper limit on the mean

Process	$4e$	4μ	$2e2\mu$
ZZ MC	$1.25 \pm 0.08 \pm 0.06$	$2.49 \pm 0.14 \pm 0.14$	$3.54 \pm 0.15 \pm 0.11$
Fake	$0.01^{+0.02}_{-0.01}{}^{+0.02}_{-0.01}$	$0.25^{+0.88}_{-0.25} \pm 0.20$	$0.00^{+1.03}_{-0.00}{}^{+0.75}_{-0.00}$
Total	$1.26 \pm 0.08 \pm 0.06$	$2.74^{+0.89}_{-0.30} \pm 0.25$	$3.54^{+1.04}_{-0.15}{}^{+0.76}_{-0.11}$
Data	2	6	1

Table 8.2: Observed events and expected background contributions (ZZ and fake lepton) inside the ZZ control region in $\mathcal{L} = 1.02$ fb^{-1}, for events with two OS-SF pairs lying in the mass region $M_{\ell\ell}\epsilon$ [66,116] GeV while the invariant mass of the four lepton system must be $M_{4\ell} < 300$ GeV. The first quoted uncertainty is statistical and the second systematic.

of a Poisson of zero events has been set. This corresponds to N $= 0.00^{+1.29}_{-0.00}$ events. The background is then calculated by multiplying the lepton fake factor "FF" in the lowest p_T bin - containing the largest "FF" (for example FR=0.8) - with the value $0.00^{+1.29}_{-0.00}$ ($0.00^{+1.29}_{-0.00} \times 0.8 = 0.00^{+1.03}_{-0.00}$). When multiple categories are combined, this technique is applied to the combined category, rather than adding the individual categories in quadrature. The systematic error in such cases is evaluated using the fake factor uncertainty in the lowest p_T bin (see Section 7.7.3).

8.5 Background validation

The modeling of the ZZ and non-ZZ SM backgrounds is verified by using two data subsamples. The validation of the ZZ background has been done in sample containing two OS and SF pairs both within the mass window $66 < M_{\ell\ell} < 116$ GeV. To be orthogonal with the signal region for the graviton search, the invariant mass of the ZZ system is required to be $M_{ZZ} < 300$ GeV. These selections result to an "almost pure" sample of ZZ events because there is a small contribution from background sources discussed in Section 7.7. A comparison between the SM ZZ expectation and the observation in the ZZ control region shows agreement within limited statistics and Poisson fluctuations (see Table 8.2), indicating satisfactory modeling of ZZ production.

Requiring fewer than two OS-SF pairs inside the ZZ mass window ($66 < M_{\ell\ell} < 116$ GeV for both pairs and $M_{4\ell} < 300$ GeV) rejects almost all of the SM ZZ production, so this sample can be used to validate the fake lepton background estimate. This region is still orthogonal to the non-ZZ and $G \to ZZ$ signal regions. The results can be found in

Process	$e^+e^-\ell^*\ell^*$	$\mu^+\mu^-\ell^*\ell^*$	$e^\pm\mu^\mp\ell^*\ell^*$	$\ell^\pm\ell^\pm\ell^\pm\ell^\pm$
ZZ MC	$0.07 \pm 0.01 \pm 0.01$	$0.08 \pm 0.01 \pm 0.01$	$0.00 \pm 0.00 \pm 0.00$	$0.00 \pm 0.00 \pm 0.00$
Fakes	$0.00^{+1.03}_{-0.00}{}^{+0.75}_{-0.00}$	$0.00^{+1.03}_{-0.00}{}^{+0.75}_{-0.00}$	$0.00^{+1.03}_{-0.00}{}^{+0.75}_{-0.00}$	$0.00^{+1.03}_{-0.00}{}^{+0.75}_{-0.00}$
Total	$0.07^{+1.03}_{-0.01}{}^{+0.75}_{-0.01}$	$0.08^{+1.03}_{-0.01}{}^{+0.75}_{-0.01}$	$0.00^{+1.03}_{-0.00}{}^{+0.75}_{-0.00}$	$0.00^{+1.03}_{-0.00}{}^{+0.75}_{-0.00}$
Data	0	0	0	0

Table 8.3: Observed and expected background contributions inside the fake lepton control region for $\mathcal{L} = 1.02$ fb^{-1}, for events with fewer than two OS SF pairs. Both pairs are required to have $M_{\ell\ell}$ in the region [66,116] GeV. Pairs labelled as $\ell^*\ell^*$ are either OF or SS. Both pairs are required to lie in the mass region $M_{\ell\ell}\epsilon$ [66,116] GeV and the invariant mass of the four lepton system must be $M_{4\ell} < 300$ GeV. The first quoted uncertainty is statistical and the second systematic.

Table 8.3 and shows a reasonable agreement between expectation from the fake lepton model and observation.

8.6 Statistical Interpretation

A single bin counting experiment has been used in order to set a 95% CL upper limit for new physics processes. The log-likelihood ratio (Q) test [8] is utilized as a test statistic to discriminate signal-like outcomes from background-like outcomes. Essentially, Q is the ratio of probability density functions for a given experimental observation (N_{obs}) for two alteranative hypotheses. The first hypothesis, called test-hypothesis, corresponds to the presence of signal (S) plus background (B) events for the description of the observation while the second one is called null-hypothesis and attempts to explain the data in the absence of signal events (or else only with the expected background).

The Q is a function of the expected signal events S and it is given by the equation:

$$Q(S) = \frac{L(N_{obs}|B+S)}{L(N_{obs}|B)} = \frac{P(N_{obs}|S+B)}{P(N_{obs}|B)} = (1+\frac{S}{B})^{N_{obs}}e^{-S} \tag{8.1}$$

The log-likelihood ratio (-ln Q), is then taking the form:

$$-\ln Q(S) = S - N_{obs}\ln(1+\frac{S}{B}) \tag{8.2}$$

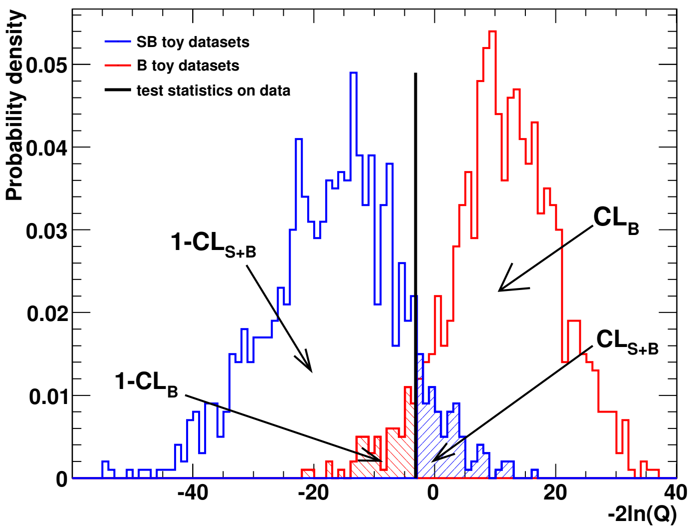

Figure 8.1: Example of a Log-Likelihood Ratio. The signal plus background corresponds to the blue color while the background only hypothesis is represented by the red color. The black line shows the test statistic result on the observed events. The arrows indicate the regions corresponding to the variables $CL_B, 1 - CL_B, CL_{S+B}, 1 - CL_{S+B}$.

which shows that the likelihood ratio test is based on counting weighted events with all events having the same weight ($\ln(1 + S/B)$), since the examination is based on a single channel counting experiment [9].

An example of a log-likelihood ratio test is shown in Figure 8.1. As it has already been noted, in order to quantify the agreement between data and signal plus background hypothesis (blue-line) or background only hypothesis (red-line), one has to generate (using pseudoexperiments) the expected probability distributions of the test statistic in the two hypothesis (for example: $N_{data} = N_S + N_B$ and $N_{data} = N_B$) as shown in Figure 8.1. The black line is the result of the test statistic on data (observed events). The arrows indicate the regions corresponding to the confidence of CL_{S+B}, $1-CL_{S+B}$, CL_B and $1 - CL_B$.

The confidence level for excluding the possibility of signal presence (graviton or doubly charged Higgs) plus background hypothesis is:

$$CL_{S+B} = P_{S+B}(-\ln Q \geq -\ln Q_{obs}) = \int_{-\ln Q_{obs}}^{\infty} \frac{dP_{S+B}}{d\ln Q} d\ln Q \tag{8.3}$$

where $dP_{S+B}/d\ln Q$ is the probability distribution function of the test statistic for the test-hypothesis.

The confidence level for the background only hypothesis is calculated from the integral:

$$CL_B = P_B(-\ln Q \geq -\ln Q_{obs}) = \int_{-\ln Q_{obs}}^{\infty} \frac{dP_B}{d\ln Q} d\ln Q \tag{8.4}$$

with $dP_B/d\ln Q$ being the probability density for the null-hypothesis. CL_B expresses the probability to get a result less compatible with the B only hypothesis than with the observed one (discovery potential). The confidence level 1-CL_B measures the confidence for the background hypothesis, also called $p-$value.

The confidence level 1-CL_{S+B} can also be used to provide exclusion limits (Frequentist method [10]), but it is not recommended because if there is downward fluctuation of the background and the signal is absent in observation, the exclusion limits would be so strong that even zero signal events would be excluded at confidence levels higher than 95% [9; 11]. In order to be conservative with the limits on gravitons and doubly charged Higgs bosons, the Modified Frequentist confidence level CL_S [11] is preferred for the limit extraction. The CL_S is calculated by the ratio of Equations 8.3 and 8.4:

$$CL_S = \frac{CL_{S+B}}{CL_B} \tag{8.5}$$

and provides protection against a downward fluctuation of the observed data by producing more conservative limits than $1 - CL_{S+B}$ in the regions where the experiment has no sensitivity to the production of new particles. The observed upper limit at 95% CL can then be extracted from the integration of the $\ln Q$ distributions from $-\ln Q_{obs}$ to infinity. Exclusion can be done only if the ratio between the two integrals is less than 0.05 ($CL_S < 0.05$). So, the 95% CL limit is defined as the value of S for which:

$$CL_S = \frac{P(-\ln Q \geq -\ln Q_{obs}|S+B)}{P(-\ln Q \geq -\ln Q_{obs}|B)} = 0.05 \tag{8.6}$$

The upper limit on signal events S_{up}, can be calculated by varying the expected signal S so the CL_S value is equal to 0.05 (95% CL). The exclusion at 95% CL means that the probability to observe more events than seen in the data with the test-hypothesis normalized to the probability of the null-hypothesis is less than 5%. Any model giving $S > S_{up}$ is excluded with 95% CL, while for $S < S_{up}$ no exclusion is possible. It is worth mentioning the special case where the observed number of events is equal to zero ($N_{obs} = 0$). In that case the CL_S can be calculated analytically. It can be proved that

$$CL_S = \frac{e^{-(S+B)}}{e^{-B}} = e^{-S} \Rightarrow S = -\ln(CL_S) \tag{8.7}$$

By setting the $CL_S = 0.05$ one can find:

$$S_{up} = -\ell n(0.05) \approx 3 \tag{8.8}$$

As can be seen, the exclusion limit cannot be stronger than 3 events in the CL_S method, regardless of the expected background.

8.6.1 Pseudoexperiment generation for doubly charged Higgs bosons and RS Graviton

The prescription used for the pseudo-experiment generation is based on the following sequence:

- Draw a random number μ_{fake} from the fake leptons background p.d.f, which is defined by a bifurcated Gaussian truncated at zero, since the expected background cannot be negative. For non-ZZ search the Bifurcated Gauss is defined as Bif.Gauss(μ = 0.61, σ_{left} = 0.61, σ_{right} = 1.55) and for the G searches Bif. Gauss(μ = 0.02, σ_{left} = 0.02, σ_{right} = 1.27). The σ_{left} and σ_{right} values are calculated as the quadratic sum of the statistical and systematic errors;

- Draw a random number μ_{ZZ} from the ZZ background p.d.f which is described by a Gaussian. For non-ZZ search it is defined as G($\mu = 0.1$, $\sigma = 0.014$) and for G searches is G($\mu = 1.85$, $\sigma = 0.14$);

- Draw a random number from a Poisson distribution whose mean is the addition of the random numbers picked from the fake and ZZ background sources P($\mu = r_{fake} + r_{ZZ}$).

Figure 8.2 and 8.3 shows the models used in pseudoexperiments generation based in the SM hypothesis for non-ZZ and G search respectively.

The performance of the analysis is described by the median expected upper limits at 95% CL and the 68% and 95% errors at these values. This value is based on the

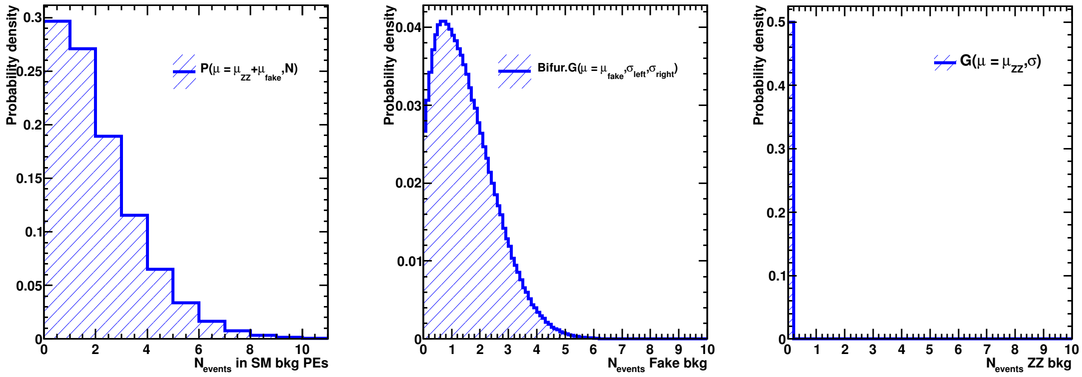

Figure 8.2: Distributions of the pseudo-experiments in the non-ZZ search. Left: Poisson distribution of the number of events in background only pseudoexperiments; Middle: Bifurcated Gauss for the fake background; Right: Gauss for the ZZ background.

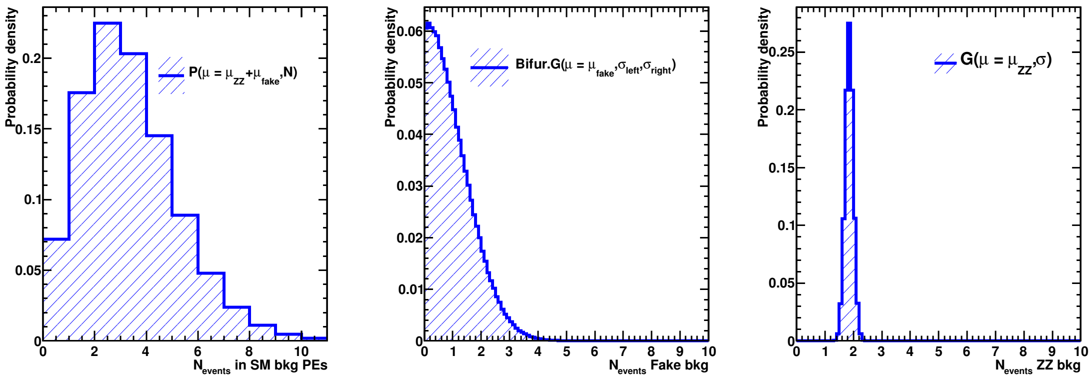

Figure 8.3: Distributions of the pseudo-experiments in the $G \to ZZ$ search. Left: Poisson distribution of the number of events in background only pseudoexperiments; Middle: Bifurcated Gauss for the fake background; Right: Gauss for the ZZ background.

background only hypothesis and is calculated by replacing $\ln Q_{obs}$ with $\ln Q_B$. This requires once again to generate pseudoexperiments according to the null-hypothesis and for each value of the test statistic $\ln Q_B$ a new S_{up}^{exp} is calculated. This procedure leads to a distribution of expected signal upper limits at 95% CL. The resulting distribution is then used for the following measures:

- *median*: The median of a distribution with a continuous random variable is defined as the value m such that the probability is at least 50% that a randomly chosen point on the function will be $\leq m$ and the probability is at least 50% that a randomly chosen point on the function will be $\geq m$;
- $\pm 1\sigma$: The range of pseudoexperiments which contain 68% of the pseudoexperiments (21% and 79% quantiles);
- $\pm 2\sigma$: The range of pseudoexperiments which contain 95% of the pseudoexperiments (2.5% and 97.5% quantiles).

8.7 Limit extraction for new physics beyond the ZZ channel

8.7.1 Searches for Doubly charged Higgs

One can search for processes beyond the SM ZZ channel by examining four lepton events where the first dilepton pair is not an OS SF pair with its invariant mass lying in the region $M_{\ell\ell}$ ϵ [66,116] GeV. The total number of expected and observed events after the Z veto is shown in Table 8.4. In total $0.7^{+1.3}_{-0.6}$(stat.) $^{+0.9}_{-0.5}$(syst.) background events are expected from SM processes while no events are observed.

Process	Total	$e^+e^-e^+e^-$	$\mu^+\mu^-\mu^+\mu^-$	$e^+e^-\mu^+\mu^-$	$\mu^+\mu^-e^+e^-$
ZZ	$0.10 \pm 0.01 \pm 0.01$	$0.02 \pm 0.00 \pm 0.00$	$0.03 \pm 0.01 \pm 0.00$	$0.01 \pm 0.00 \pm 0.00$	$0.01 \pm 0.00 \pm 0.01$
Fakes	$0.61^{+1.25}_{-0.61}{}^{+0.91}_{-0.51}$	$0.01 \pm 0.01 \pm 0.01$	$0.00^{+1.03}_{-0.00}{}^{+0.75}_{-0.00}$	$0.00^{+1.03}_{-0.00}{}^{+0.75}_{-0.00}$	$0.00^{+0.01}_{-0.00}{}^{+0.01}_{-0.00}$
Total Bkg	$0.71^{+1.25}_{-0.61}{}^{+0.91}_{-0.51}$	$0.02 \pm 0.01 \pm 0.01$	$0.03^{+1.03}_{-0.01}{}^{+0.75}_{-0.00}$	$0.01^{+1.03}_{-0.01}{}^{+0.75}_{-0.00}$	$0.01 \pm 0.01 \pm 0.01$
$H^{\pm\pm}_{200}$	$1.27 \pm 0.04 \pm 0.03$	$0.05 \pm 0.01 \pm 0.01$	$0.09 \pm 0.01 \pm 0.01$	$0.13 \pm 0.01 \pm 0.01$	$0.16 \pm 0.01 \pm 0.01$
Data	0	0	0	0	0

Process	$e^+e^-\ell\ell$	$\mu^+\mu^-\ell\ell$	$e^\pm e^\mp\ell\ell$	4 same-sign
ZZ	$0.01 \pm 0.00 \pm 0.00$	$0.01 \pm 0.00 \pm 0.00$	$0.00 \pm 0.00 \pm 0.00$	$0.01 \pm 0.01 \pm 0.00$
Fakes	$0.61^{+0.69}_{-0.61} \pm 0.51$	$0.01^{+1.03}_{-0.01}{}^{+0.75}_{-0.00}$	$0.00^{+1.03}_{-0.00}{}^{+0.75}_{-0.00}$	$0.00^{+1.03}_{-0.00}{}^{+0.75}_{-0.00}$
Total Bkg	$0.61^{+0.69}_{-0.61} \pm 0.51$	$0.02^{+1.03}_{-0.02}{}^{+0.75}_{-0.00}$	$0.00^{+1.03}_{-0.00}{}^{+0.75}_{-0.00}$	$0.01^{+1.03}_{-0.01}{}^{+0.75}_{-0.00}$
$H^{\pm\pm}_{200}$	$0.30 \pm 0.02 \pm 0.02$	$0.37 \pm 0.02 \pm 0.02$	$0.18 \pm 0.01 \pm 0.01$	$0.00 \pm 0.00 \pm 0.00$
Data	0	0	0	0

Table 8.4: Observed and expected background events in $\mathcal{L} = 1.02$ fb^{-1}, after final selection for the non-ZZ search, which requires that the first dilepton pair is not an opposite-sign same-flavor pair with invariant mass $M_{\ell\ell}\epsilon$ [66,116] GeV. Pairs labeled as $\ell\ell$ are either opposite-flavor or same-sign; Also shown for comparison is the expected $H^{\pm\pm}$ yield for a singlet model with $M_{H^{\pm\pm}} = 200$ GeV ($\sigma = 10$ fb). The first quoted uncertainty is statistical; the second systematic.

$M_{H^{\pm\pm}}$ [GeV]	Fiducial Acceptance [%]	non-ZZ selection efficiency [%]
100	7	62
150	12	66
200	16	67
300	22	67

Table 8.5: Acceptance and selection efficiencies in the non-ZZ seaches. The relative statistical and systematic uncertainties on the selection efficiency have been calculated to be 1% and 5% respectively.

Figure 8.4 shows the mass of the first dilepton pair of events passing the selection criteria of the analysis.

8.7.2 Limits on doubly charged Higgs production

As described in Section 8.6, the method used for the limit extraction is the CL_S with a single bin counting experiment, accounting for systematic uncertainties on the background estimate, signal acceptance and luminosity. The observation of zero events leads to an upper limit on the number of events from new physics sources of $N_{4\ell} < 3.0$ events at 95% C.L. The median expected upper limit on the number of events from new phenomena sources is $N_{4\ell} < 4.1$ events at 95% C.L.

These results can be translated into a limit on the production cross section for new physics processes by defining a fiducial region at parton level, containing events with four charged leptons (e or μ) each with $p_T > 15$ GeV and lying in $\eta < 2.5$. These events must not contain OS SF pairs with invariant mass ($M_{\ell\ell}$) in the region [66,116] GeV. The efficiency of the non-ZZ search, within this fiducial region, is calculated for a benchmark model production of doubly-charged Higgs bosons. The most important source of systematic uncertainty is the lepton reconstruction efficiency. Table 8.5 summarizes the fiducial acceptance and selection efficiencies in the non-ZZ searches for four different $H^{\pm\pm}$ mass values (100, 150, 200 and 300 GeV). The relative statistical and systematic uncertainties on the selection efficiency inside the fiducial region are 1% and 5% respectively. The small variation in the efficiency values between the low mass and high mass Higgs results from the fact that the higher mass events are more central.

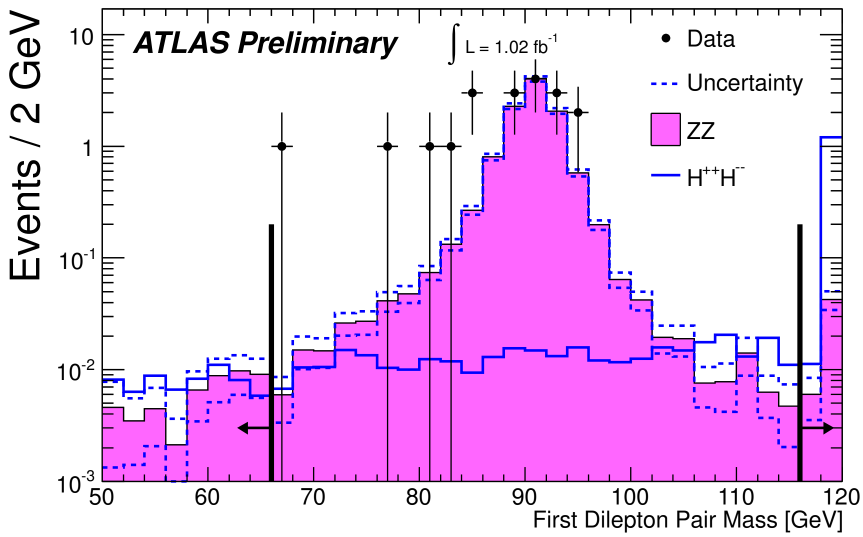

Figure 8.4: Distribution of the first dilepton pair mass for all categories. The fake lepton background is not shown. A hypothetical $H^{++}H^{--}$ distribution is overlaid using the singlet model (blue line), with $M_{H^{\pm\pm}} = 200$ GeV. Events inside the window $M_{\ell\ell}$ ϵ [66,116] GeV indicated by the vertical black lines serve as a control region; the non-ZZ search region rejects opposite-sign same-flavor events in this window. Overflow events are shown in the highest mass bin.

The limit on the number of events $N_{4\ell} < 3$ can be converted into limits on the production cross section of doubly charged Higgs bosons by using the equation:

$$\sigma_{4\ell\ fid} < \frac{N_{4\ell}}{\varepsilon_{non-ZZ} \times \mathcal{L}} = \frac{3.0}{0.62 \times 1.02\text{fb}^{-1}} = 4.7\text{fb} \tag{8.9}$$

where ε_{non-ZZ} is the smallest measured efficiency from Table 8.5 and $\mathcal{L}$ is the integrated luminosity.

This limit can then be extrapolated on the total doubly-charged Higgs bosons production cross section by dividing the result of Equation 8.9 with the fiducial acceptance (Table 8.5) for each Higgs mass. Figure 8.5 shows the behavior of the exclusion curve on the total production cross section of doubly charged Higgses as a function of the Higgs masses. The black points represent the observed limit and the red points the expected ones. The green and yellow zones show the $\pm$ 1,2 σ regions from pseudoexperiments drawn from the SM hypothesis. The dashed lines correspond to the theoretical pre-

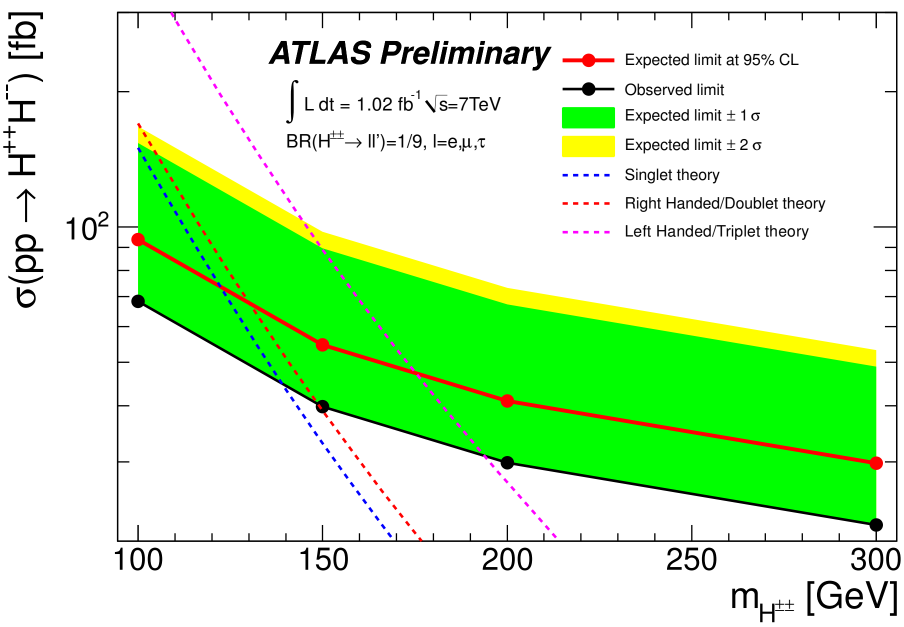

Figure 8.5: Observed 95% C.L. limits on $H^{++}H^{--}$ production, using the four lepton fiducial cross section upper limit, and the fraction of the produced events which fall into the fiducial region. The median expected result and $\pm 1, 2\sigma$ regions from pseudo experiments drawn from the SM hypothesis are shown; the observed limit corresponds to $N_{obs} = 0$, which lies on the -1σ and -2σ lines. Three theoretical predictions are also drawn, which depend on whether the doubly-charged Higgs is a member of a singlet, doublet or triplet symmetry group.

dictions which depend on whether the doubly charged Higgs is a member of a singlet, doublet or triplet of $SU(2)_L$.

8.7.3 Graviton searches

In this subsection a discussion on the searches for an RS graviton decaying to ZZ in the full leptonic channel is described ($G \to ZZ \to 4\ell$). The selection criteria applied to the data are the same as in the case of the ZZ production cross section measurement except from the fact that, in that case the signal region starts for $M_{ZZ} > 300$ GeV. Figure 8.6 shows the invariant mass of the 4ℓ candidates in the full mass ($M_{4\ell}$) range. The expected signal yield for different graviton masses, the expected background and the number of observed events for $M_{ZZ} > 300$ GeV are summarized on Table 8.6. In total, $1.87^{+1.04}_{-0.11}{}^{+0.75}_{-0.09}$ background events are expected from SM processes.

8.7.4 Limits on Gravitons

As in the case of the doubly charged Higgs production, limits have been set using the CLs method with a single bin counting experiment, accounting for systematic uncertainties on the background estimate and signal acceptance. The median expected upper limit on the number of events from a new source is $N_{ZZ} < 5.7$ events at 95% C.L. The observation of three events leads to an upper limit of $N_{ZZ} < 5.7$ events at 95% C.L.

In these studies, the fiducial region at parton level is defined by four charged leptons ($\ell = e, \mu$) each with $p_T > 15$ GeV and $|\eta| < 2.5$ which form two OS SF pairs with their invariant mass ($M_{\ell\ell}, M_{\ell'\ell'}$) lying in the mass region [66, 116] GeV. In addition the invariant mass of the 4ℓ system must be greater than $M_{4\ell}$ >300 GeV. Table 8.7 shows the fiducial acceptance and selection efficiencies for different hypothetical graviton masses. According to the definition of the fiducial region described above, the efficiency of the $G \to ZZ$ selection is almost independent of the graviton mass for the RS graviton benchmark model. By using the following equation, one can calculate the limit on the fiducial cross section:

$$\sigma_{ZZ}^{fid} < \frac{N_{ZZ}}{\varepsilon_{ZZ} \times BF(ZZ \to 4\ell) \times \mathcal{L}} = \frac{5.7}{0.61 \times 0.010 \times 1.02rmfb^{-1}} = 0.92 \text{ pb} \quad (8.10)$$

The above value can then be easily extrapolated to the total phase space ($\sigma(pp \to G) \times BF(G \to ZZ)$) by dividing with the acceptance of each graviton mass. Figure 8.7 shows the observed and expected upper limits on the graviton searches.

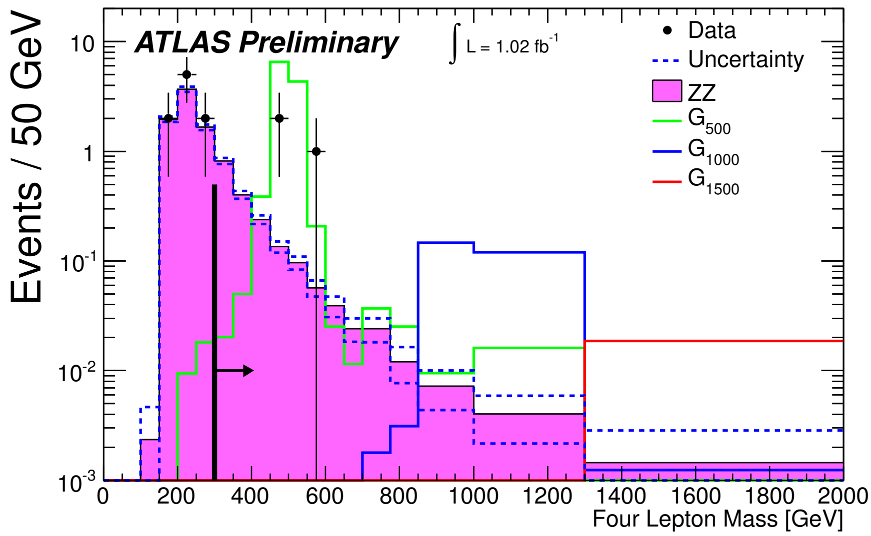

Figure 8.6: Invariant mass distribution of the 4ℓ before applying the mass cut $M_{4\ell} > 300$ GeV. Three different mass distributions (0.5, 1.0 and 1.5 TeV) of gravitons are overlaid. The blue dashed line shows the variation of the SM ZZ background ($\pm 1\sigma$) according to the leptons' systematic uncertainties.

Process	Total
ZZ	$1.85 \pm 0.11 \pm 0.09$
Fakes	$0.02^{+1.03+0.75}_{-0.01-0.02}$
Total Bkg	$1.87^{+1.04\ +0.75}_{-0.11\ -0.09}$
Data	3
G (350 GeV)	$71\pm3\pm4$
G (500 GeV)	$12\pm0.5\pm0.6$
G (750 GeV)	$1.50\pm0.08\pm0.07$
G (1000 GeV)	$0.27\pm0.02\pm0.01$
G (1250 GeV)	$0.066\pm0.004\pm0.003$
G (1500 GeV)	$0.019\pm0.001\pm0.001$

Process	$e^+e^-e^+e^-$	$\mu^+\mu^-\mu^+\mu^-$	$e^+e^-\mu^+\mu^-$	$\mu^+\mu^-e^+e^-$
ZZ	$0.32 \pm 0.03 \pm 0.01$	$0.63 \pm 0.04 \pm 0.03$	$0.53 \pm 0.04 \pm 0.03$	$0.37 \pm 0.03 \pm 0.02$
Fakes	$0.00^{+0.04\ \ 0.03}_{-0.00\ -0.00}$	$0.00^{+1.03\ +0.75}_{-0.00\ -0.00}$	$0.00^{+1.03+0.75}_{-0.01-0.00}$	$0.02 \pm 0.02 \pm 0.02$
Total Bkg	$0.32^{+0.05+0.03}_{-0.03-0.01}$	$0.63^{+1.03\ +0.75}_{-0.04\ -0.03}$	$0.54^{+1.03\ +0.75}_{-0.04\ -0.03}$	$0.39\pm0.04\pm0.03$
Data	0	2	1	0
G (350 GeV)	$12\pm1\pm1$	$23\pm2\pm1$	$20\pm2\pm1$	$16\pm1\pm1$
G (500 GeV)	$2.1\pm0.2\pm0.1$	$4.0\pm0.3\pm0.2$	$3.2\pm0.2\pm0.2$	$2.3\pm0.2\pm0.1$
G (750 GeV)	$0.30\pm0.02\pm0.01$	$0.46\pm0.03\pm0.01$	$0.43\pm0.03\pm0.01$	$0.26\pm0.02\pm0.01$
G (1000 GeV)	$0.6\pm0.05\pm0.05$	$0.85\pm0.06\pm0.05$	$0.86\pm0.06\pm0.06$	$0.43\pm0.04\pm0.05$
G (1250 GeV)	$0.013\pm0.001\pm0.001$	$0.020\pm0.001\pm0.001$	$0.024\pm0.002\pm0.001$	$0.009\pm0.001\pm0.001$
G (1500 GeV)	$0.0041\pm0.0003\pm0.0002$	$0.0056\pm0.0004\pm0.0002$	$0.0070\pm0.0005\pm0.0003$	$0.0026\pm0.0002\pm0.0002$

Table 8.6: Expected backgrounds and observed events in $\mathcal{L} = 1.02$ fb^{-1}, after final selection for the graviton search $M_{4\ell} > 300$GeV. Also shown are expected yields for $G \rightarrow ZZ$ samples for a coupling of $k/M_{pl} = 0.1$. The first quoted uncertainty is statistical and the second systematic.

M_G [GeV]	Fiducial Acceptance [%]	Selection efficiency [%]
350	27	61
500	28	63
750	31	66
1000	32	66
1250	33	67
1500	35	66

Table 8.7: Acceptance and selection efficiencies for different hypothetical graviton masses. The lowest selection efficiency (61%) is used to set limits on all mass points.

8.8 Conclusions

The first exclusion limits on doubly charged Higgses and RS Graviton production at $\sqrt{s} = 7$ TeV using 1fb^{-1} of data have been established. For doubly charged Higgs, we expect $0.7^{+1.3}_{-0.6}$(stat.)$^{+0.9}_{-0.5}$(syst.) events and observe zero. This leads us to set fiducial cross section limit on four lepton production at 4.7 fb. For a RS Graviton, the expected events from SM processes are $1.9^{+1.0}_{-0.1}$(stat.)$^{+0.8}_{-0.1}$(syst.) and the observation is 3. With a coupling of $k/\bar{M}_{pl} = 0.1$, the observed limit on graviton production is 0.92 pb and the lower limit of the Graviton mass is $M_G > 575$ GeV.

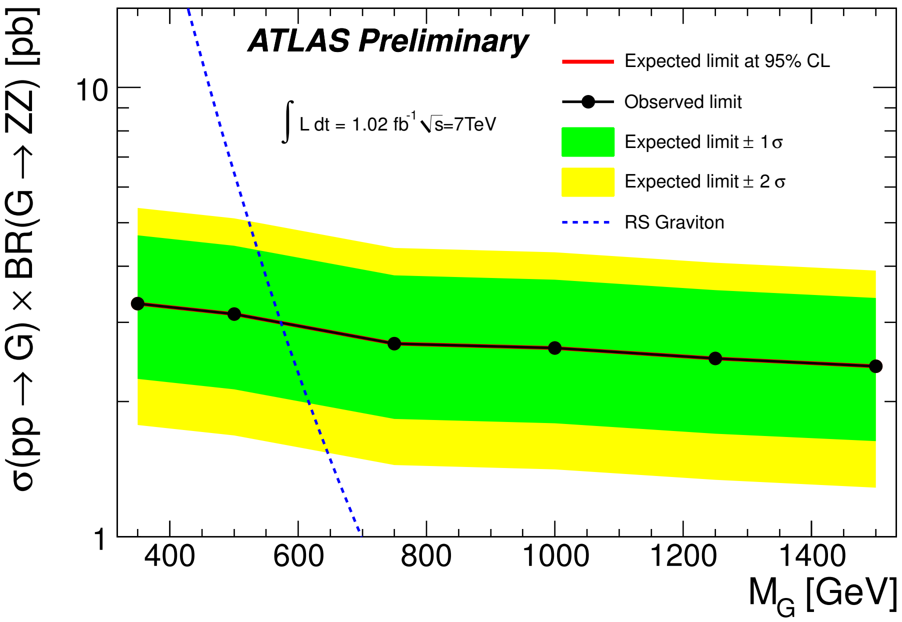

Figure 8.7: Expected and observed 95% C.L. limits for $G \rightarrow ZZ$ using the ZZ fiducial cross section upper limit and the fiducial acceptance. The median expected result and the $\pm 1\sigma$ and $\pm 2\sigma$ from pseudoexperiments drawn from the SM hypothesis are shown; the observed limit corresponds to $N_{obs} = 3$. The leading-order theoretical prediction is also shown.

Bibliography

[1] V. Rentala, W. Shepherd and S. Su, "A Simplified Model Approach to Same-sign Dilepton Resonances", Phys. Rev. D85 (2011) 35004. 139, 140

[2] J. Alwall, M. Herquet, F. Maltoni, O. Mattelaer and T. Stelzer,"MadGraph 5 : Going Beyond", arXiv:1106.0522v1 [hep-ph]. 139

[3] T. Sjostrand et al., "High-energy physics event generation with PYTHIA 6.1", Comput.Phys.Commun.135:238-259, 2001. 139

[4] A. Sherstnev, R. S. Thorne, "Parton Distributions for LO Generators", Eur.Phys.J.C55:553-575, 2008. 139

[5] S. Agostinelli et al., "Geant4 - a simulation toolkit", Nucl. Instrum. Meth. A 506, 250 (2003). 139

[6] ATLAS Collaboration, "The ATLAS Simulation Infrastructure", Eur.Phys.J.C70:823-874, 2010. 139

[7] T. Rizzo, "Doubly charged Higgs bosons and lepton-number-violating processes", Phys. Rev. D25 (1982) 1355. 140

[8] F. James, "Statistical methods in experimental particle physics", 2nd edition North-Holland Publishing (2006). 142

[9] A. L. Read, "Modified frequentist analysis if search results", Workshop on Confidence Limits, CERN Yellow Report 2000-05, p81. 143, 144

[10] L. Lyons, "Open statistical issues in particle physics", Annals of Applied Statistics 2008, Vol. 2, No. 3, 887-915. 144

[11] T. Junk, "Confidence Level Computation for Combining Searches with Small Statistics",Nucl. Instrum. Meth. A 434 (1999) 435. 144

Chapter 9

Summary and conclusions

This thesis presented a wide range of particle physics aspects including detector related issues, production cross section measurements of Standard Model processes and searches for new physics, by analyzing the data of proton-proton collisions at $\sqrt{s} = 7$ TeV recorded by the ATLAS detector during 2011.

One important component of the ATLAS detector is the Muon Spectrometer, responsible for muon identification and measurement of their position and momenta. The CSC, is one of the four sub-detection systems of the Muon Spectrometer employed to cover the forward region of ATLAS, a region characterized by high counting rates. Studies carried out in this thesis have shown that the CSCs play an important role in physics processes involving multiple muons in the final state, in particular to the $ZZ \to 4\mu$ channel, where a significant fraction of events has at least one muon falling outside the Inner Detector's acceptance and has a track in the Muon Spectrometer. In order to reduce background contribution due to high track activity, the position of muons should be known with high accuracy. This thesis presented a detailed study for improvement of the hit position and peaking time resolution of the CSCs with 0.6% and 0.4% relative errors respectively. The resulting $C++$ algorithms have been implemented in the ATLAS software and are used from the off-detector electronics of CSCs for the selection of single clusters.

This thesis has also contributed to the first Z inclusive cross section measurement at $\sqrt{s} = 7$ TeV, by analyzing the very early data recorded by the ATLAS detector. The $Z \to \ell\ell$ cross section measurement is used as a standard candle for detector performance assessment as well as for tuning of theoretical predictions at the new energy regime. The cross sections have been found to be:

$$\sigma^{\rm fid}_{Z\to ee} = 0.33 \pm 0.04({\rm stat}) \pm 0.03\ ({\rm syst})\ \pm 0.04\ ({\rm lumi})\ {\rm nb}$$
$$\sigma^{\rm tot}_{Z} = 0.75 \pm 0.09\ ({\rm stat})\ \pm 0.08\ ({\rm syst})\ \pm 0.08\ ({\rm lumi})\ {\rm nb}.$$

and are in agreement with the SM NNLO predictions of 0.96±0.05 nb.

The Z inclusive measurement and the analysis of the first data delivered from LHC mediate to reach the main goal of this thesis which was the ZZ production cross section measurement. This is a physics channel of major importance beacuse the good understanding of the $ZZ \to 4\ell$ process can reveal the Standard Model Higgs boson through the decaying channel $H \to ZZ \to 4\ell$, since it constitutes the irreducible background process in the Higgs searches. This thesis studied the $ZZ \to 4\ell$ process and completed the analysis for 1 fb^{-1}. The fiducial and total cross section were determined to be:

$$\sigma^{\rm fid}_{ZZ\to\ell^+\ell^-\ell^+\ell^-} = 19.4^{+6.3}_{-5.2}\ ({\rm stat})^{+0.9}_{-0.7}\ ({\rm syst})\ ^{+0.9}_{-0.6}\ ({\rm lumi})\ {\rm fb}$$
$$\sigma^{\rm tot}_{ZZ} = 8.5^{+2.7}_{-2.3}\ ({\rm stat})\ ^{+0.4}_{-0.3}\ ({\rm syst})\ \pm 0.3\ ({\rm lumi})\ {\rm pb}.$$

and are statistically consistent with the SM NLO total cross section of $6.5^{+0.3}_{-0.2}$ pb.

Based on the selection criteria of the ZZ analysis at $\sqrt{s} = 7$ TeV, the studies were further extended in order to search for doubly charged Higgses as well as for a Randal-Sundrum Graviton, processes which share the same final states with $ZZ \to 4\ell$. In the former, an upper limit on the fiducial cross section of four lepton production has been set at 4.7 fb and in the graviton case, an upper limit on the production cross section of ZZ pairs from high mass sources was established, within the fiducial region, at 0.92 pb. The observed and expected 95% C.L. lower limit on the mass of the graviton is $M_G > 575$ GeV.

Several contributions of the present thesis were of major importance for the analysis that followed on ZZ with the full statistics of 2011, where some of them could be utilized in the 2012 data analysis, where higher statistics will be available. For example, the forward muons at $\eta > 2.5$ were included in the analysis of the full 2011 dataset by increasing the statistics by 6%. Finally, issues like ambiguities in combinatorial same-flavor four-lepton events during pair formations could be reliably resolved using suggestions of the current thesis.

..Simulation is an asset for scientists to recreate nature's behavior...

Appendix A

Monte Carlo studies of the $ZZ^* \rightarrow 4\ell$ production at $\sqrt{s} = 10$ TeV

This chapter describes the analysis for the detection of $ZZ \rightarrow 4\ell$ candidates at $\sqrt{s} = 10$ TeV using fully simulated MC events. This analysis has been performed along the plans of ATLAS for Computing System Commissioning (CSC).

A.1 Introduction

The current chapter studies the observation potential of $ZZ^{(*)}$ diboson production through the four lepton final states at $\sqrt{s} = 10$ TeV of proton-proton collisions. The reconstruction and identification effieciencies of leptons are discussed and the kinematic distributions of the 4ℓ system are shown. The results from different selection criteria applied to the analysis are compared and the expected number of signal and background events at 1 fb^{-1} is also shown.

A.2 Datasamples

The MC samples used in these studies correspond to the MC08 production campaign. LO generators have been used for all the processes except $t\bar{t}$ where a NLO generator has been employed. A full list of the samples is presented in Table A.1.

MCID	Process	Generator	Events	ϵ_{filter}	σ [pb]
109292	$ZZ \rightarrow \ell^+\ell^-\ell'^+\ell'^-$	PYTHIA	195723	1	0.103
106050	$Z \rightarrow ee$ inclusive	PYTHIA	4982718	0.96	1143.96
106051	$Z \rightarrow \mu\mu$ inclusive	PYTHIA	5000000	0.96	1143.96
109400	Z$eebb$Np0	ALPGEN/JIMMY	100000	0.003	12.22
109401	Z$eebb$Np1	ALPGEN/JIMMY	50000	0.0104	4.947
109405	Z$\mu\mu bb$Np0	ALPGEN/JIMMY	100000	0.0049	12.28
109406	Z$\mu\mu bb$Np1	ALPGEN/JIMMY	50000	0.0123	4.924
109341	$t\bar{t}$	MC@NLO	98280	0.0109	373.6

Table A.1: List of MC samples used for the studies at $\sqrt{s}$ = 10 TeV -

A.3 Object reconstruction

A.3.1 Electrons

The electron objects used in the analysis have been reconstructed with the standard egamma algorithm described in Section 6.3.2.

A.3.2 Muons

The ATLAS muon identification and reconstruction algorithms take advantage of multiple sub-detector technologies which provide complementary approaches and cover pseudorapidities up to 2.7 [3].

- **"standalone"**: The stand-alone muon reconstruction is based entirely on muon-spectrometer information, independently of whether or not the muon-spectrometer track is also reconstructed in the inner detector. The muon reconstruction is initiated locally in a muon chamber by a search for straight line track segments in the bending plane. Hits in the precision chambers are used and the segment candidates are required to point to the centre of ATLAS. When available, the hit coordinate ϕ in the non-bending plane measured by the trigger detectors is associated to the segment. Two or more track segments in different muon stations are combined to form a muon track candidate using three-dimensional tracking in the magnetic field. The track parameters (p_T, η, ϕ, transverse and longitudinal distances of closest approach to the primary vertex) obtained from the muon spectrometer track fit are extrapolated to the interaction point taking into account both multiple scattering and energy loss in the calorimeters. For the latter, the reconstruction utilises either a parameterisation or actual measurements of calorimeter energy losses, together with a parameterisation of energy loss in the inert material. The average muon energy loss in the calorimeters is 3 GeV. The stand-alone muon reconstruction algorithms use the least-squares formalism to fit tracks in the muon spectrometer, with most material effects directly integrated into the χ^2 function.

- "combined": The combined muon reconstruction associates a stand-alone muon-spectrometer track to an inner-detector track. The association is performed using a χ^2-test, defined from the difference between the respective track parameters weighted by their combined covariance matrices. The parameters are evaluated at the point of closest approach to the beam axis. The combined track parameters are derived either from a statistical combination of the two tracks or from a refit of the full track. To validate the results presented in this paper, these two independent reconstruction chains were exercised and good agreement was observed. The results presented here are based on the statistical combination of muon-spectrometer and inner-detector measurement.

- "Segment tagged (ST) muon": In contrast to the above approaches the reconstruction of ST muon is based in an inner detector track. A track in the ID is identified as a muon if the track extrapolated to the MS is associated with straight track segments in the precision muon chambers.

A.4 Selection Criteria

The selection criteria of the analysis have been built to account for three final states, $4e, 4\mu$ and $2e2\mu$ and the optimization has been done by considering high p_T and isolated leptons.

The analysis starts with the preselection cuts of electrons and muons. The selected electrons must be reconstructed with the standard electron finding algorithm described in Section 6.3.2. Their p_T threshold is at 6 GeV and they must lie in the pseudorapidity region $|\eta| < 2.5$. The muon objects must be combined or standalone reconstructed with the respective algorithms explained in the previous Section.The p_T cut used is the same as for electrons and the η cut extends up to 2.7 for the inclusion of muons reconstructed in the region $2.5 < |\eta| < 2.7$. All track fits as well as the matching of the associated MS and ID tracks should have χ^2/ndf[1] < 15.

In the first stage, the selected leptons are used to create same flavor opposite charge pairs and in the second stage, the created pairs are used for the quadruplet formation. All the leptons of the candidate quadruplets must be separated, so a cut on the angle ($\Delta R > 0.2$) among them is applied. In addition, each pair of the quadruplet is required to have at least one lepton with $p_T > 20$ GeV. In the case of the $4e$ ($2e2\mu$) signature, three different sets of identification requirements have been examined:

- four "loose" electrons (two "loose" electrons);
- the two hardest electrons with the highest p_T are required to be "loose" and the sub-leading leptons must be "medium" (the hardest must be "loose" and the sub-leading"medium");
- four "medium" electrons (two "medium" electrons).

In the case of the 4μ and $2e2\mu$ signature, all the muons must be isolated around a cone of radius $\Delta R = 0.4$ by requiring the p_T sum inside that cone to be smaller than 20% of the candidate's muon transverse momentum.

An additional cut on the number of the candidate quadruplets has been applied, in order to reduce the background contribution from $Zq\bar{q}$ processes, where two energetic leptons result from Z decays accompanied by leptons in heavy quark jets, typically jets from b and c quarks or leptons in light quark jets or jets misidentification. Studies have shown than the leptons from the $Zq\bar{q}$ processes have small opening angles with respect to each other, allowing so to the formation of only one possible solution (quadruplet). The other solution is rejected due to the $\Delta R > 0.2$ cut. On the contrary, leptons resulting from dibosons have large opening angles and form two quadrupltets. The cut on quadruplets is strongly correlated with the mass cut, the final cut of the analysis, where the primary lepton pair is required to be on-mass-shell lying in the mass region $70 < M_{\ell\ell} <$110 GeV and the other one to be off-mass-shell, $M_{\ell'\ell'} > 20$ GeV.

[1] "ndf" is the number of degrees of freedom

Electrons	Muons
Standard electrons $p_T > 6$ GeV, $\lvert\eta\rvert < 2.5$	Combined Track or Standalone Track for $\lvert\eta\rvert > 2.5$ χ^2/DoF < 15 on match $p_T > 6$ GeV, $\lvert\eta\rvert < 2.7$
Event Selection	
Create same flavor opposite charge pairs with $\Delta R > 0.2$	
At least one lepton in each pair with $p_T > 20$ GeV	
Loose ID requirements to all electrons Medium ID to softers	$IsoCone40 = \frac{\sum_{i=1}^{n} p_T^i}{p_T^{muon}} < 0.2$
Number of candidate quadruplets per event > 1	
$70 < M_{Z_1} < 110$ GeV, $M_{Z_2} > 20$ GeV	

Table A.2: $ZZ \to 4\ell$ selection criteria at $\sqrt{s} = 10$ TeV - Selection criteria used for the detection of ZZ candidates at $\sqrt{s} = 10$ TeV.

A.5 Trigger requirement

In order to find the most suitable trigger for the analysis, single lepton and dilepton trigger chains have been applied as the final cut of the analysis. All triggers applied are illustrated in Table A.3. The "L1, L2, EF" represent the level of the trigger (see Section 4.2.5), "EM, *e*, *mu*" refer to the kind of the trigger object where "EM" stands for electromagnetic cluster, "*e*" for electrons and "*mu*" for muons. The numbers declare the p_T cut of the corresponding trigger object which means that the event is triggered if the trigger object has p_T greater than this value. The letter "i" means that the trigger object must be isolated and "loose, medium, tight" correspond to the identification requirements applied to the trigger object (see Section 6.3.2).

The efficiencies shown in Table A.3 represent the fraction of events that pass the specific chain. As can be seen, the efficiency of all the trigger chains is greater than 99% except tight di-electron trigger and di-muon trigger with a p_T cut at 20 GeV, where the efficiency drops to 95% and 91% respectively. The single lepton trigger chains L1_EM18 - L2_e20_loose - EF_e20_loose and L1_MU20 - L2_mu20 - EF_mu20, which are closer to the analysis, have also been used to match the trigger object with the leptons one which passed the selection criteria of the analysis. This is done in order to calculate the single electron and muon trigger efficiencies which have been found to be 94% and 92% for electron and muon respectively.

A.6 Tag and probe method

The Tag and Probe method is a data-driven method used for the calculation of the reconstruction and idetification efficiencies of leptons. The principle of operation is based on the kinematic and dynamic correlation of the leptons resulting from Z decays. The "tag" lepton is detected by using the full detector information applying tight criteria. Then, by taking advantage of the Z mass constraint a list of "probe" objects is selected in order to calulcate the reconstruction and identification efficiencies [1; 2].

A.6.1 Reconstruction and identification efficiencies of electrons

For the case of the electron objects the cuts corresponding to the "tag" electron make use of the ID and the electromagnetic calorimeter. Specifically, they must be reconstructed with the standard electron algorithm and they must fulfill the tight identification criteria described in Section 6.3.2. Their p_T should be greater than 25 GeV and they must lie in the pseudorapidity region $|\eta| < 2.5$. Finally, the event must pass a certain trigger requirement and the tag electron must be the one which fired the trigger. For that reason a $\Delta R = \sqrt{\Delta\eta^2 + \Delta\phi^2} < 0.2$ matching is applied between the tag and the triggered object.

The "probe" electron collection are electromagnetic clusters which are selected by utilizing the invariant mass correlation of the probe with the "tag" electron. The series of the cuts for both the tag electron and the probe object are illustrated in Table A.4 [5].

The reconstruction efficiencies are then calculated from the ratio of the number of clusters which correspond to reconstructed electrons to the number of selected clusters as shown in the following equation:

$$\varepsilon_i = \frac{N^i_{reco\ electrons}}{N^i_{selected\ probes}} \qquad i = 1,\ 2,\ ...,\ nbins \tag{A.1}$$

where ε_i stands for the efficiency calculation in each bin of p_T, η and ϕ.

In order to compare the T&P efficiency results with the efficiency computed using MC-truth information, the electromagnetic clusters with $p_T > 20$ GeV and $|\eta| < 2.5$

L1	L2	EF	Events pass (%)
Single electron trigger chains			
EM13	e15_medium	e15_medium	99.95
EM13I	e15i_medium	e15i_medium	99.90
EM18	e20_loose	e20_loose	99.97
EM18I	e20i_loose	e20i_loose	99.92
Di-electron trigger chains			
2EM7	2e12_tight	2e12_tight	94.47
2EM13	2e15_medium	2e15_medium	99.82
2EM18	2e20_loose	2e20_loose	99.39
Single muon trigger chains			
MU11	mu15	mu15	99.69
MU11	mu15i_loose	mu15i_loose	99.55
MU20	mu20	mu20	99.55
MU20	mu20i_loose	mu20i_loose	99.42
Di-muon trigger chians			
2MU10	2mu10	2mu10	99.08
2MU20	2mu20	2mu20	91.57

Table A.3: Efficiencies of various trigger chains for $ZZ^* \to 4\ell analysis$.. The first column corresponds to L1, second column to L2 and third column to EF (see Section 4.2.5). The last column shows the percentage of events passing the full trigger chain. The "loose, medium and tight" shows the kind of identification requirements applied to the trigger objects and the "i" denotes if an isolation cut has been applied to the trigger object. The number in front of the letters "e" and "mu" shows the p_T cut of each trigger.

Tag selection criteria		**Probe selection criteria**	
Cut	Value	Cut	Value
Author	1 or 3	Probe type	e/m cluster
$\|\eta\|$	< 2.5	$\|\eta\|$	< 2.5
p_T	> 20 GeV	$\Delta\phi = \phi_{tag} - \phi_{probe}$	$> \pi/2$
ID requirement	Tight	ΔM	< 30 GeV
Trigger L1	L1_EM18		
Trigger L2	L2_e20_loose		
Trigger EF	EF_e20_loose		

Table A.4: Series of selection criteria applied on the "tag" and the "probe" electrons. The $\Delta\phi$ and ΔM cuts of the probe electron are with respect to the "tag" electron.

were first matched to generated "true" electrons, after which we obtain the number of fully reconstructed electrons. The ratio

$$\varepsilon_i^{MC} = \frac{N_{reco\ electrons}}{N_{cluster\ truth\ matched}} \qquad i = 1,\ 2,\ ...,\ nbins \tag{A.2}$$

provides the electron reconstruction efficiency with respect to the electron cluster identification.

For the MC based results the $ZZ \to 4e$ fully simulated samples were used as a clean and enriched electron sample with similar properties to the $Z \to ee$. The same comparison was repeated using MC-truth information of the $Z \to ee$ fully simulated samples. The relative differences (calculated from Equation A.3) in both cases $Z \to ee$ & $ZZ \to 4e$ are in excellent agreement $< 1\%$.

$$RD = \frac{1}{N_{bins}} \sum_{i=1}^{n} \frac{|TP_i - MC_i|}{MC_i} \tag{A.3}$$

where TP are the Tag&Probe results and MC correspond to the MC-truth efficiencies.

Figure A.1 shows the results of both methods. In red color the Tag&Probe method's results and in black color the MC-truth efficiencies.

Following the same logic, one can calculate the "loose", "medium" and "tight" (see Section 6.3.2) identification efficiencies of electrons as a function of electrons p_T, η and ϕ, as shown in equation A.4. In this case the denominator of the ratio corresponds to

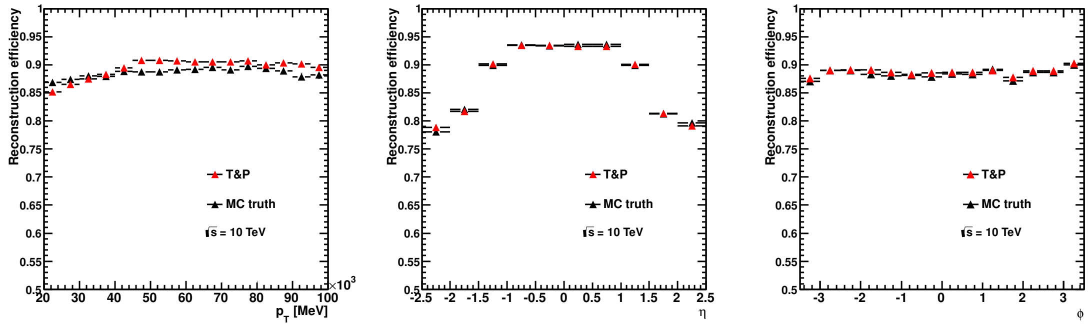

Figure A.1: Electron reconstruction efficiencies versus p_T (left), η (middle) and ϕ (right) at $\sqrt{s}$ = 10 TeV.

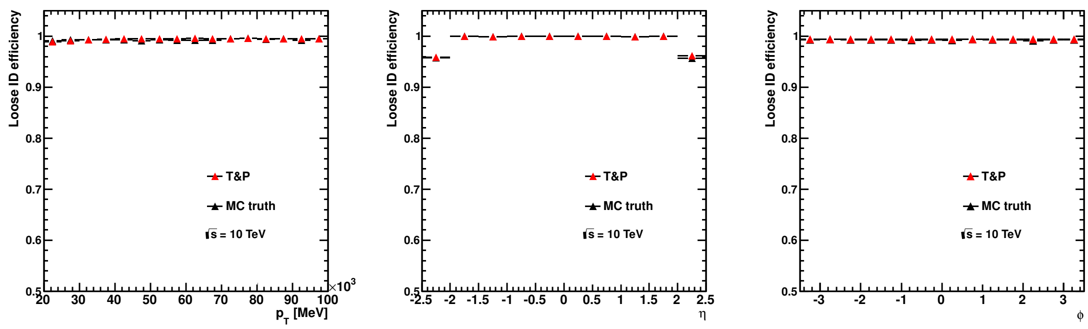

Figure A.2: Loose electron identification efficiencies versus p_T (left), η (middle) and ϕ (right) at $\sqrt{s}$ = 10 TeV.

the reconstructed electrons matched with probes and the numerator is the number of electrons passing the specific identification requirement.

$$\varepsilon_i = \frac{N^i_{el\ identified}}{N^i_{el\ reco}} \qquad i = 1,\ 2,\ ...,\ nbins \tag{A.4}$$

Figures A.2, A.3, A.4 show the different identification efficiencies as a function of p_T, η and phi. As can be seen from the plots, there is a good agreement between the two methods and this is also confirmed from the relative differences which are of the order $< 1\%$.

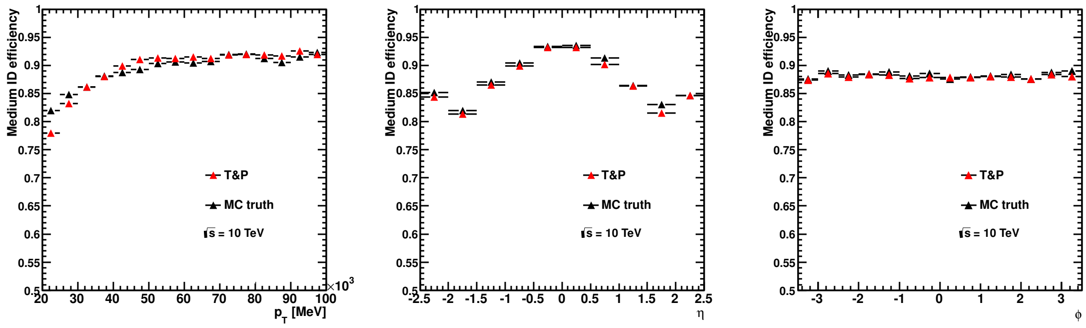

Figure A.3: Medium electron identification efficiencies versus p_T (left), η (middle) and ϕ (right) at $\sqrt{s}$ = 10 TeV.

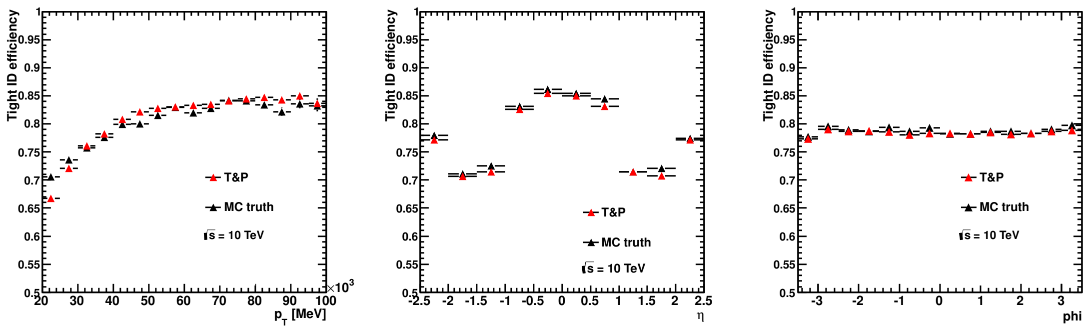

Figure A.4: Tight electron identification efficiencies versus p_T (left), η (middle) and ϕ (right) at $\sqrt{s}$ = 10 TeV.

Tag selection criteria		**Probe selection criteria**	
Cut	Value	Cut	Value
Type	Combined muon	Probe type	ID track
Trigger requirement	EF_mu20	p_T	> 5GeV
p_T	> 20 GeV	η	< 2.4
$\|\eta\|$	< 2.5	d_0	< 1.0 mm
Track isolation	< 4.5 GeV	Track isolation	< 1.6 GeV
d_0	< 1.0 mm	$\Delta z_0 = z_0^{tag} - z_0^{probe}$	$< 0.5\ mm$
		$\Delta\phi = \phi^{tag} - \phi^{probe}$	$> \pi/2$
		$\Delta M = \|M_{system} - M_Z\|$	< 12 GeV

Table A.5: Series of selection criteria applied on the “tag” and the “probe” muons. The $\Delta\phi$ and ΔM cuts of the probe muon are with respect to the “tag” one

A.6.2 Reconstruction efficiencies of muons

A similar procedure can be followed for the case of muons [6]. The tag muons are required to be combined muons and also to be the ones that fired the trigger. This can be achieved with a ΔR matching between the tag muon and the triggered object. The trigger chain used in the current analysis is the EF_mu20 and the value of the trigger object matching was $\Delta R < 0.02$. The p_T cut on the tag is determined from the trigger requirement and in that case was greater than 20 GeV. Since the tag is required to be combined, it must lie in the pseudorapidity region $\eta < 2.5$. In addition, the tag is required to originate from the primary interaction vertex. For that reason a cut on the transverse impact parameter, d_0, is applied. Finally, it must be track isolated. In that case, the track isolation is defined as the sum of the transverse momenta of the ID tracks in a cone of radius $\Delta R < 0.3$ around the tag muon.

Once the tag muon is selected, the probe selection starts by checking the inner detector track collection for tracks with opposite charge, $p_T > 5$ GeV and $|\eta| < 2.5$. In order to reduce the combinatorial problem, the probe is required to come from the same primary vertex as the tag muon by applying a longitudinal (z_0) and transverse impact parameter cut. Also it must be track isolated. Finally, a cut on the difference of their azimuthal angle ($\Delta\phi$) [6] as well as on the invariant mass of the system is applied.

A complete list of the series of the cuts for the tag muons and the probes can be seen in Table A.5.

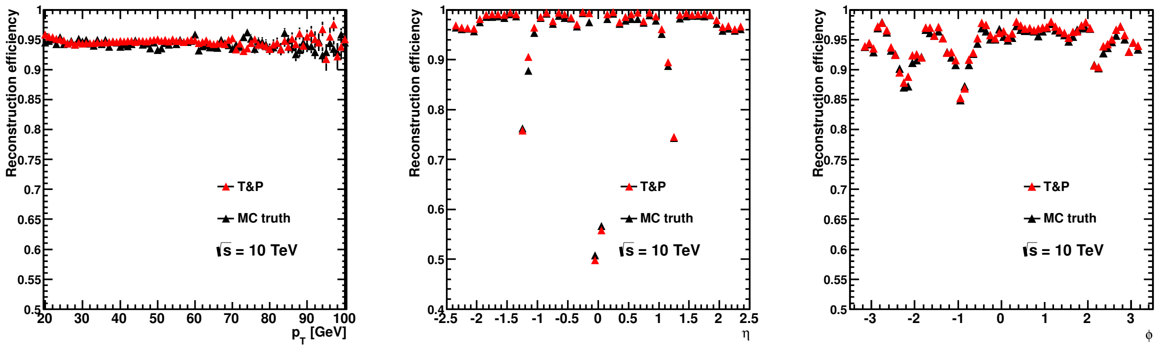

Figure A.5: Muon reconstruction efficiencies versus p_T (left), η (middle) and ϕ (right) at $\sqrt{s}$ = 10 TeV.

The reconstruction efficieny of the MS can then be calculated from Equation A.5. The numerator corresponds to the selected tracks which have been matched ($\Delta R <$ 0.005) with a reconstructed combined muon and the denominator is the number of the total probes. In order to have a deeper understanding of how the efficiency behaves, it has been calculated as a function of p_T, η and ϕ.

$$\varepsilon_i = \frac{N^i_{muon\ reco}}{N^i_{selected\ probes}} \qquad i = 1,\ 2,\ ...,\ nbins \tag{A.5}$$

To understand the systematics of the method, a comparison was made of the efficiency results of the T&P method with the efficiency using MC-truth information. The ratio between the fully reconstructed combined muons and the "true" muons from the MC, matched to an ID track ($\Delta R < 0.005$) was computed.

Figure A.5 compares the results of the two methods. The red points correspond to the T&P method and the black points refer to MC-truth efficiencies. The excellent agreement is also validated from the relative differences which are $< 1\%$.

A.7 Background

A detailed explanation of the background processes that contribute to the $ZZ \to 4\ell$ analysis and the data-driven technique developed to estimate the background for the cross section exraction at $\sqrt{s}$ = 7 TeV is described in Section 7.7. For the sake of completeness, a short description of the background processes that contribute in the $ZZ \to 4\ell$ analysis follows:

- $Z + Jets$: Production of a Z boson in association with two jets. The main source of background in the electron channel is the contamination of light jets faking an electron. This source can be eliminated by applying tight electron identification requirements. In the muon channel the main background is the $Zb\bar{b}$ process where B mesons decay semileptonically to muons.

- $t\bar{t}$: Another source of background in the $ZZ \to 4\ell$ channel is the production of $t\bar{t} \to WWb\bar{b}$. The leptons resulting from W decays can mimic the leptons from Z decays, since they are high p_T and isolated leptons. In combination with the leptons from the semi-leptonic decays of the $b-$ quarks they can lead to 4ℓ final states. The production of $t\bar{t}$ will be dominant in the LHC due to its large cross section, but this cross section becomes smaller when one multiplies it with the corresponding branching franctions of the W and b to decay leptonically. As a consequence a very small number is expected to contribute to the background.

- WZ: The WZ diboson production could also contribute as a background in the analysis but due to its small cross section, it can be considered as a secondary source, at least for the first few inverse femtobarns.

A.8 Results

The number of events surviving the selection criteria of the analysis, for the signal and the background processes $Z + Jets$, $Zb\bar{b}$ and $\bar{t}t$ are summarized in Table A.6. For the signatures involving electrons $4e$ ($2e2\mu$), three different electron identification requirements have been examined. The first case corresponds to four "loose" electrons (two loose electrons), the second one corresponds to two (one) "loose" electrons and the two (one) sub-leading electrons are required to be "medium" and in the last case the four electrons are required to fulfill the "medium" requirements.

As can be seen, the best option is the requirement of 4 "medium" electrons, in order to get rid of the $Z + Jets$ background. The four "loose" and two "loose" - two "medium" cases produce similar results for the signal. The small fraction of events which are rejected in the four "medium" case is mostly a contribution of ZZ^* events with an invariant mass of the $Z^* < 70$ GeV. The 4μ final state provides a very clean signature with negligible background contribution. The absence of $Z + Jets \to 4\mu$

and $t\bar{t} \rightarrow 4\mu$ processes is due to a lack of MC statistics, but still their contribution to the background is expected to be very small. The $2e2\mu$ signature has the most events because the branching ratio is double.

The expected numbers of signal events for the three different cases, starting from the loose criteria and moving to the tighter ones are 10.66 ± 0.08, 10.30 ± 0.10 and 8.96 ± 0.11. The corresponding numbers for the total background are 94.08 ± 5.68, 17.86 ± 2.86 and 0.31 ± 0.28.

Expected number of events at $\sqrt{s}$ = 10 TeV			
	Identification requirement		
Process	**4 Loose**	**2 Loose 2 Medium**	**4 Medium**
$ZZ^* \rightarrow 4e$	2.29 ± 0.02	2.13 ± 0.03	1.54 ± 0.03
$ZZ^* \rightarrow 4\mu$	3.19 ± 0.03		
$ZZ^* \rightarrow 2e2\mu$	5.18 ± 0.03	4.98 ± 0.04	4.23 ± 0.05
Total signal	10.66 ± 0.08	10.30 ± 0.10	8.96 ± 0.11
$Z + Jets \rightarrow 4e$	43.30 ± 2.64	5.93 ± 1.14	-
$Z + Jets \rightarrow 2e2\mu$	48.79 ± 2.94	11.21 ± 1.57	0.22 ± 0.22
$Zb\bar{b} \rightarrow 4e$	0.23 ± 0.02	0.09 ± 0.01	0.02 ± 0.01
$Zb\bar{b} \rightarrow 4\mu$	0.004 ± 0.003		
$Zb\bar{b} \rightarrow 2e2\mu$	0.27 ± 0.02	0.13 ± 0.02	0.03 ± 0.01
$t\bar{t} \rightarrow 4e$	0.87 ± 0.03	0.25 ± 0.01	-
$t\bar{t} \rightarrow 2e2\mu$	0.62 ± 0.03	0.25 ± 0.01	0.04 ± 0.04
Total background	94.08 ± 5.68	17.86 ± 2.86	0.31 ± 0.28

Table A.6: Numbers of events surviving the selection criteria of the analysis for the signal and the different background processes. All the numbers are normalized at $\mathcal{L}$ = 1 fb^{-1}. The uncertainties provided for each number correspond to the statistical error.

Figures A.6 and A.7 refer to the $4e$ final state with the two loose-two medium requirement. The first one shows the invariant mass distributions of the first (Z_1) and second (Z_2) pair and the other one shows the invariant mass of the $4e$ system. Similar distributions for the $2e2\mu$ channel are illustrated in Figures A.10 and A.11. These plots show how the signal is dominated from the $Z + Jets$ background due to the inability of the "loose" identification requirements to reject jets faking electrons. The $t\bar{t}$ and $Zb\bar{b}$ contributions are significant in the low mass region. The invariant mass distributions

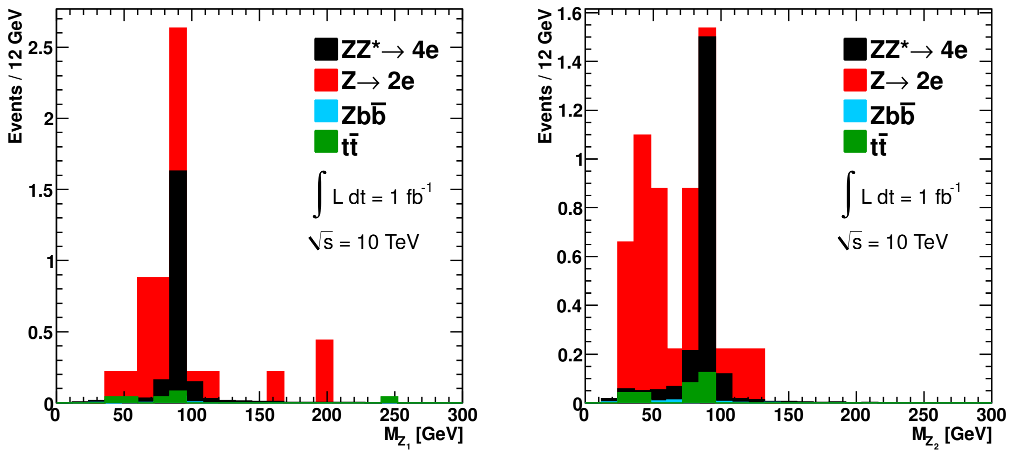

Figure A.6: Invariant mass distributions of Z_1 (left) and Z_2 (right) of the $4e$ channel at $\sqrt{s}$ = 10 TeV.

of the 4μ final state are presented in Figures A.8 and A.9. As it can be observed, this signature is almost background free, with a small contribution of the $Zb\bar{b}$ process.

A.9 Summary

A study of the diboson production channel $ZZ^* \to 4\ell$ (where $\ell = e, \mu$) has been presented at $\sqrt{s}$ = 10 TeV using fully simulated MC events. Trigger studies have shown high efficiencies (>99%) for both single lepton and di-lepton trigger chains. Different electron identification requirements have been tested and the best significance ($N_{signal}/\sqrt{N_{background}}$) can be achieved by requiring four medium electrons. The expected number of signal events at $L = 1$ fb^{-1} is 8.96 ± 0.11 and the estimated number of background events (based on MC) is 0.31 ± 0.28. The application of the Tag&Probe method has shown that a 2% systematic uncertainty on the lepton reconstruction and identification efficiencies is expected.

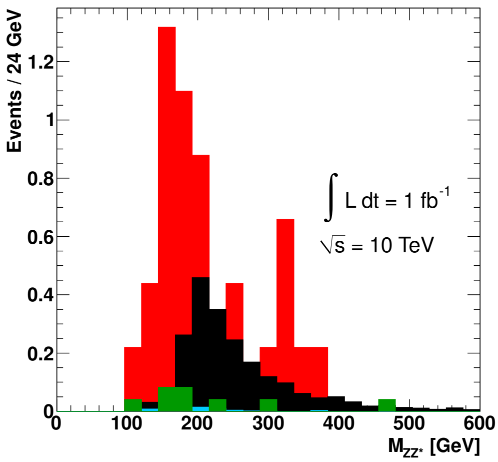

Figure A.7: Invariant mass distributions of the 4e system at $\sqrt{s} = 10$ TeV.

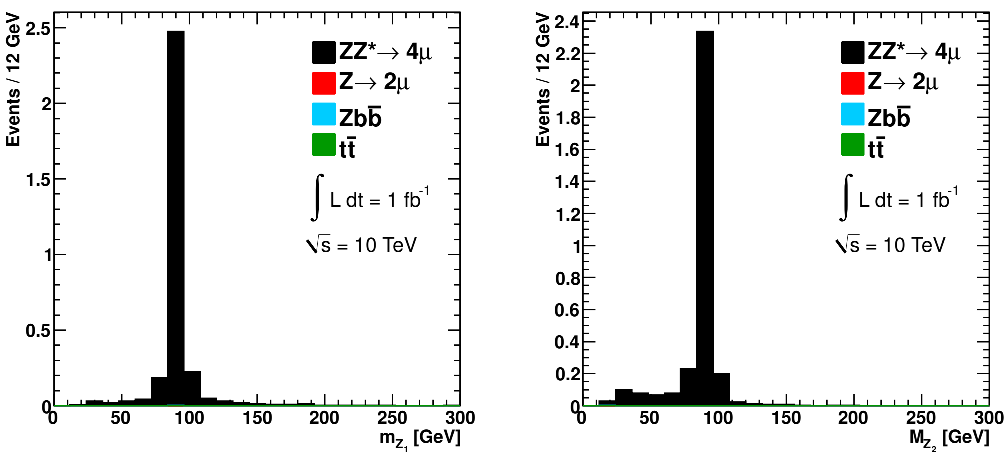

Figure A.8: Invariant mass distributions of Z_1 (left) and Z_2 (right) of the 4μ channel at $\sqrt{s} = 10$ TeV.

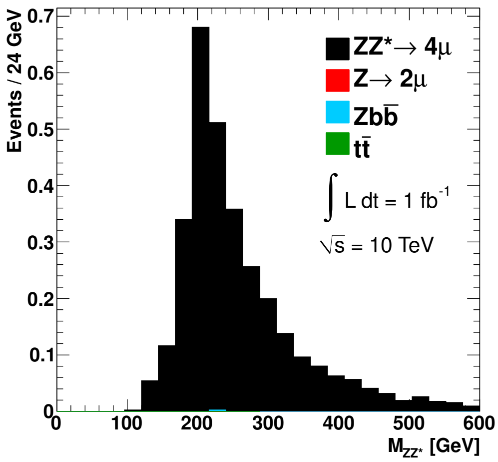

Figure A.9: Invariant mass distributions of the 4μ system at $\sqrt{s}$ = 10 TeV.

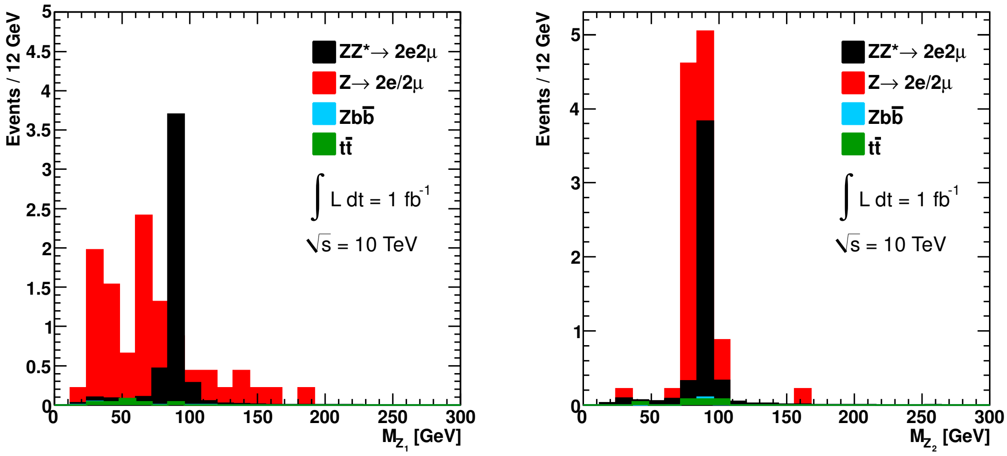

Figure A.10: Invariant mass distributions of Z_1 (left) and Z_2 (right) of the $2e2\mu$ channel at $\sqrt{s}$ = 10 TeV.

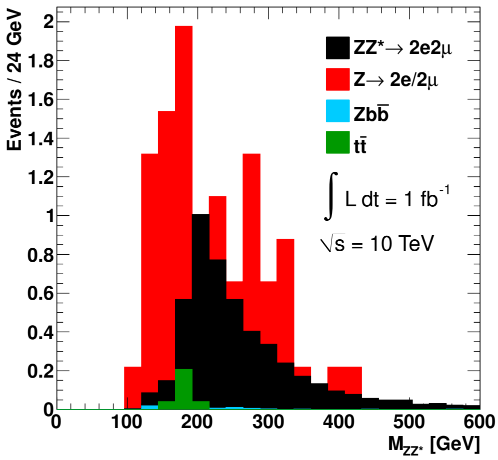

Figure A.11: Invariant mass distributions of the $2e2\mu$ system at $\sqrt{s} = 10$ TeV.

Bibliography

[1] ATLAS Collaboation, “Electron performance measurements with the ATLAS detector using the 2010 LHC proton-proton collision data”, Eur. Phys. J. C72 (2012) 1909. 167

[2] ATLAS Collaboration, “Muon reconstruction efficiency in reprocessed 2010 LHC proton-proton collision data recorded with the ATLAS detector”, ATLAS-CONF-2011-063. 167

[3] The ATLAS Collaboration, “Expected performance of the ATLAS experiment: detector, trigger and physics”, CERN-OPEN-2008-020, arXiv:0901.0512 [hep-ex]. 163

[4] T.Dai, H. Liu, B. Mansoulie, J. Purdham, J. Qian, J. Strandberg, R. Thun, “Production cross sections of standard model processes in pp collisions at $\sqrt{s} = 10$ TeV and their dependences on QCD scales”, ATLAS NOTE, ATL-COM-PHYS-2009-242.

[5] O. Arnaez, “Electron Reconstruction and Identification with the ATLAS Detector”, AIP Conf.Proc. 1200 (2010) 693-696. 167

[6] S. Borroni, “Study of the $pp \to Z \to \mu^+\mu^-$ Process at ATLAS: Detector Performance and First Cross-Section Measurement at 7 TeV”, PhD thesis, 2010.
172

Appendix B

Historical retrospective of Particle Physics

The most powerful building blocks and discoveries in the particle physics are summarized below.

- 1895. The electron is discovered by J. J. Thomson after experimenting in the Cavedish Laboratory at Cambridge University;
- 1896. The X rays are discovered by the German physicist W. C. Roentgen;
- 1899. Ernest Rutherford discovers the α-particles and in 1907 he proves, with Thomas Royds, that these particles are helium (He) ions;
- 1910. Rutherford successfully proposes an atom model which describes the mass of the atom as mostly concentrated in a small area centrally located and with a positive charge, the so called nucleus, whereas negatively charged electrons move in circular orbits around the nucleus;
- 1932. James Chadwick discovers the neutron;
- 1932. The positron is discovered by Carl D. Anderson;
- 1937. J. C. Street and E. C. Stevenson discover the existence of muon in a cloud chamber;
- 1947 - 1961. A series of particles - mesons and baryons - are discovered;

- 1960. Sheldon Glashow unifies the electromagnetic and weak interactions into one interaction, the electroweak interaction;
- 1963. Gell-Mann Murray and George Zweig independently assume the existence of up, down and strange quarks;
- 1965. O. W. Greenberg, M. Y. Han, and Yoichiro Nambu introduce the color charge as a property of the quarks;
- 1967. Steven Weinberg and Abdus Salam separately incorporate the Higgs mechanism into Glashow's electroweak theory. Their model predicts the existence of a neutral, weakly interacting boson as well as an additional massive boson called the Higgs boson.
- 1968. Experiments at the Stanford Linear Accelerator Center (SLAC) provide evidence of quarks;
- 1970. The GIM mechanism is introduced by the Sheldon Glashow, John Iliopoulos, and Luciano Maiani;
- 1973. Harald Fritzsch and Murray Gell-Mann propose the quantum field theory of strong interactions, Quantum Chromodynamics (QCD);
- 1973. David Politzer, David Gross, and Frank Wilczek discover the asymptotic freedom of the strong interactions;
- 1974 A fourth quark is discovered, the charm quark. Two different experiments, one in the SLAC and the other at the Brookhaven National Laboratory (BNL) discovered the $J\psi$ meson consisting of a charm and an anticharm quark;
- 1975. Martin Lewis Perl and his colleagues discover the τ lepton;
- 1977. A fifth quark, the bottom or beauty quark is discovered by a team of physicists, led by Leon M. Lederman at Fermilab. In specific the Υ meson has been detected which is a bound state of the bottom quark and its antiquark.
- 1979. Evidence for gluon radiation from quarks in the DESY laboratory in Hamburg.

- 1983. Experiments at CERN led by Carlo Rubbia and Simon van der Meer using the Super Proton Synchotron accelerator discover the W and Z bosons.

- 1989. Experiments at CERN and SLAC measure the lifetime of the Z boson and they show that the number of light neutrino types is 3.

- 1995. The top quark is discovered by the CDF and D0 experiments at Fermilab.

- 2000. After eleven years, the Large Electron Positron (LEP) accelerator at CERN ceases to operate.

- 2003. The experiments at LEP, ALEPH, DELPHI, L3 and OPAL publish their combined results for the SM Higgs boson, putting a lower bound in its mass at 114.4 GeV/c^2 at the 95% confidence level (CL).

- 2006. The CDF experiment at Tevatron makes the first measurement of B_s oscillations, and observes two types of Σ baryon.

- 2007. The CDF and DØ experiments at Tevatron reported direct observation of the "Cascade B" (Ξ_b^- baryon).

- 2010. The LHC starts to operate succesully at $\sqrt{s} = 7$ TeV.

- 2010. The ATLAS experiment at CERN observes a centrality-dependent dijet asymmetry in $Pb - Pb$ collisions which may point to an interpretation in terms of strong jet energy loss in a hot, dense medium.

- 2011. The CDF collaboration announces the discovery of a possible new particle after a new non-Higgs particle appeared in their data. However, an independent analysis from the DØ collaboration did not observe anything.

- 2011. The TEVATRON stops operation on 30 September after 28 years of successful running.

- 2012. The CDF and DØ experiments exclude a SM Higgs boson in the mass range 156 to 177 GeV.

- 2012. The ATLAS experiment at CERN excludes a wide range of Higgs masses at 95% CL between 110.0 GeV and 117.5 GeV, 118.5 GeV and 122.5 GeV, and 129 GeV to 539 GeV, leaving a small window in the mass range 122.5 GeV to 129 GeV where an excess of events is observed around $m_H \sim 126$ GeV.
- 2012. The CMS experiment at CERN excludes a SM Higgs boson in the mass range 127 to 600 GeV at 95% CL with a most probable value of a Higgs mass at 124 GeV.

Appendix C

Monte Carlo samples

C.1 Monte Carlo samples used in the $ZZ \to 4\ell$ production cross section measurement

MCID	Process	Generator	Events	k-factor	ϵ_{filter}	σ[pb]
107650	ZeeNp0	ALPGEN/JIMMY	6612265	1.25	1.0	668.3
107651	ZeeNp1	ALPGEN/JIMMY	1333745	1.25	1.0	134.4
107652	ZeeNp2	ALPGEN/JIMMY	404873	1.25	1.0	40.5
107653	ZeeNp3	ALPGEN/JIMMY	109942	1.25	1.0	11.2
107654	ZeeNp4	ALPGEN/JIMMY	29992	1.25	1.0	2.9
107655	ZeeNp5	ALPGEN/JIMMY	8992	1.25	1.00	0.8
107660	$Z\mu\mu$Np0	ALPGEN/JIMMY	6619010	1.25	1.0	668.7
107661	$Z\mu\mu$Np1	ALPGEN/JIMMY	1334723	1.25	1.0	134.1
107662	$Z\mu\mu$Np2	ALPGEN/JIMMY	403886	1.25	1.0	40.3
107663	$Z\mu\mu$Np3	ALPGEN/JIMMY	109954	1.25	1.0	11.2
107664	$Z\mu\mu$Np4	ALPGEN/JIMMY	29978	1.25	1.0	2.8
107665	$Z\mu\mu$Np5	ALPGEN/JIMMY	9993	1.25	1.0	0.8
107670	$Z\tau\tau$Np0	ALPGEN/JIMMY	6608784	1.25	1.0	668.4
107671	$Z\tau\tau$Np1	ALPGEN/JIMMY	1327672	1.25	1.0	134.8
107672	$Z\tau\tau$Np2	ALPGEN/JIMMY	403864	1.25	1.0	40.4
107673	$Z\tau\tau$Np3	ALPGEN/JIMMY	109947	1.25	1.0	11.3
107674	$Z\tau\tau$Np4	ALPGEN/JIMMY	29977	1.25	1.0	2.8
107675	$Z\tau\tau$Np5	ALPGEN/JIMMY	9999	1.25	1.0	0.8
109300	$Zeebb$Np0	ALPGEN/JIMMY	149971	1.25	1.0	6.6
109301	$Zeebb$Np1	ALPGEN/JIMMY	99977	1.25	1.0	2.5
109302	$Zeebb$Np2	ALPGEN/JIMMY	38985	1.25	1.0	0.9
109303	$Zeebb$Np3	ALPGEN/JIMMY	9990	1.25	1.0	0.4
109305	$Z\mu\mu$bbNp0	ALPGEN/JIMMY	149971	1.25	1.0	6.6
						Continued on next page

Table C.1 – continued from previous page

MCID	Process	Generator	Events	k-factor	ϵ_{filter}	σ[pb]
109306	$Z\mu\mu$bbNp1	ALPGEN/JIMMY	109962	1.25	1.0	2.5
109307	$Z\mu\mu$bbNp2	ALPGEN/JIMMY	39980	1.25	1.0	0.9
109308	$Z\mu\mu$bbNp3	ALPGEN/JIMMY	9994	1.25	1.0	0.4
109380	$Zeebb$Np0 3ℓ	ALPGEN/JIMMY	199948	1.25	0.09	6.6
109381	$Zeebb$Np1 3ℓ	ALPGEN/JIMMY	99975	1.25	0.14	2.5
109382	$Zeebb$Np2 3ℓ	ALPGEN/JIMMY	39986	1.25	0.16	0.9
109383	$Zeebb$Np3 3ℓ	ALPGEN/JIMMY	19987	1.25	0.19	0.4
109385	$Z\mu\mu bb$Np0 3ℓ	ALPGEN/JIMMY	199948	1.25	0.09	6.6
109386	$Z\mu\mu bb$Np1 3ℓ	ALPGEN/JIMMY	99975	1.25	0.14	2.5
109387	$Z\mu\mu bb$Np2 3ℓ	ALPGEN/JIMMY	39982	1.25	0.16	0.9
109388	$Z\mu\mu bb$Np3 3ℓ	ALPGEN/JIMMY	19988	1.25	0.2	0.4
116250	ZeeNp0 M10to40	ALPGEN/JIMMY	999859	1.22	1.0	3055.2
116251	ZeeNp1 M10to40	ALPGEN/JIMMY	299940	1.22	1.0	84.9
116252	ZeeNp2 M10to40	ALPGEN/JIMMY	499880	1.22	1.0	41.4
116253	ZeeNp3 M10to40	ALPGEN/JIMMY	149940	1.22	1.0	8.4
116254	ZeeNp4 M10to40	ALPGEN/JIMMY	39973	1.22	1.0	1.9
116255	ZeeNp5 M10to40	ALPGEN/JIMMY	9995	1.22	1.0	0.5
116260	$Z\mu\mu$Np0 M10to40	ALPGEN/JIMMY	999869	1.22	1.0	3054.9
116261	$Z\mu\mu$Np1 M10to40	ALPGEN/JIMMY	299890	1.22	1.0	84.9
116262	$Z\mu\mu$Np2 M10to40	ALPGEN/JIMMY	499864	1.22	1.0	41.5
116263	$Z\mu\mu$Np3 M10to40	ALPGEN/JIMMY	149939	1.22	1.0	8.4
116264	$Z\mu\mu$Np4 M10to40	ALPGEN/JIMMY	39988	1.22	1.0	1.9
116265	$Z\mu\mu$Np5 M10to40	ALPGEN/JIMMY	9996	1.22	1.0	0.5
116270	$Z\tau\tau$Np0 M10to40	ALPGEN/JIMMY	959877	1.22	1.0	3055.1
116271	$Z\tau\tau$Np1 M10to40	ALPGEN/JIMMY	296945	1.22	1.0	84.9
116272	$Z\tau\tau$Np2 M10to40	ALPGEN/JIMMY	498804	1.22	1.0	41.5
116273	$Z\tau\tau$Np3 M10to40	ALPGEN/JIMMY	149953	1.22	1.0	8.4
116274	$Z\tau\tau$Np4 M10to40	ALPGEN/JIMMY	39980	1.22	1.0	1.9
116275	$Z\tau\tau$Np5 M10to40	ALPGEN/JIMMY	9995	1.22	1.0	0.5

Table C.1: MC samples used to model Z+X, including Z+jets and Drell-Yan samples. The corresponding cross-sections, generator names, generator level filter efficiencies, k-factor and total numbers of events are shown in this table. NpX (X=0...5) in the process name refers to the number of additional partons in the final state.

MCID	Process	Generator	Events	k-factor	ϵ_{filter}	σ[pb]
107680	$We\nu$Np0	ALPGEN	2072731	1.2	1.0	6921.6
107681	$We\nu$Np1	ALPGEN	632500	1.2	1.0	1304.3

Continued on next page

Table C.2 – continued from previous page

MCID	Process	Generator	Events	k-factor	ϵ_{filter}	σ[pb]
107682	$We\nu$Np2	ALPGEN	3768265	1.2	1.0	378.3
107683	$We\nu$Np3	ALPGEN	1009641	1.2	1.0	101.4
107684	$We\nu$Np4	ALPGEN	249869	1.2	1.0	25.9
107685	$We\nu$Np5	ALPGEN	69953	1.2	1.0	7.0
107690	$W\mu\nu$Np0	ALPGEN	3467000	1.2	1.0	6919.6
107691	$W\mu\nu$Np1	ALPGEN	642000	1.2	1.0	1304.2
107692	$W\mu\nu$Np2	ALPGEN	3768893	1.2	1.0	377.8
107693	$W\mu\nu$Np3	ALPGEN	1009589	1.2	1.0	101.88
107694	$W\mu\nu$Np4	ALPGEN	254879	1.2	1.0	25.8
107695	$W\mu\nu$Np5	ALPGEN	69958	1.2	1.0	6.9
107700	$W\tau\nu$Np0	ALPGEN	3259564	1.2	1.0	6918.6
107701	$W\tau\nu$Np1	ALPGEN	2496467	1.2	1.0	1303.2
107702	$W\tau\nu$Np2	ALPGEN	3764804	1.2	1.0	378.2
107703	$W\tau\nu$Np3	ALPGEN	1008514	1.2	1.0	101.5
107704	$W\tau\nu$Np4	ALPGEN	248864	1.2	1.0	25.6
107705	$W\tau\nu$Np5	ALPGEN	64950	1.2	1.0	7.0

Table C.2: MC samples used to model W inclusive processes. The corresponding cross-sections, generator names, generator level filter efficiencies and total numbers of events are shown in this table. NpX (X=0. . . 5) in the process name refers to the number of additional partons in the final state.

MCID	Process	Generator	Events	k-factor	ϵ_{filter}	σ[pb]
106001	γW^{+}(e)	PYTHIA,MG	49998	1.75	1.0	28.00
106002	$\gamma W^{+}(\mu)$	PYTHIA,MG	49995	1.75	1.0	28.00
106003	$\gamma W^{+}(\tau)$	PYTHIA,MG	46996	1.75	1.0	25.40
108288	γW^{-}(e)	PYTHIA,MG	49995	1.83	1.0	18.53
108289	$\gamma W^{-}(\mu)$	PYTHIA,MG	49996	1.83	1.0	18.62
108290	$\gamma W^{-}(\tau)$	PYTHIA,MG	49996	1.83	1.0	16.80
108323	$\gamma Z(ee)$	PYTHIA,MG	49997	1.41	1.0	9.63
108324	$\gamma(Z\mu\mu)$	PYTHIA,MG	49995	1.41	1.0	9.63
108325	$\gamma(Z\tau\tau)$	PYTHIA,MG	49997	1.41	0.15	9.41
105941	$W^{+}Z \to \ell\nu\ell\ell$	MC@NLO	24995	1.0	1.0	0.16
105971	$W^{-}Z \to \ell\nu\ell\ell$	MC@NLO	99972	1.0	1.0	0.09
106024	$W^{+}Z \to \tau\nu\ell\ell$	MC@NLO	24994	1.0	1.0	0.08
106027	$W^{-}Z \to \tau\nu\ell\ell$	MC@NLO	24997	1.0	1.0	0.04
105940	$W^{+}Z \to \ell\nu qq$	MC@NLO	24989	1.0	1.0	1.69

Continued on next page

Table C.4 – continued from previous page

MCID	Process	Generator	Events	k-factor	ϵ_{filter}	σ[pb]
105970	$W^{-}Z \rightarrow \ell\nu qq$	MC@NLO	24993	1.0	1.0	0.91
105942	$W^{+}Z \rightarrow qq\ell\ell$	MC@NLO	24992	1.0	1.0	0.50
105972	$W^{-}Z \rightarrow qq\ell\ell$	MC@NLO	99968	1.0	1.0	0.27
106025	$W^{+}Z \rightarrow \ell\nu\tau\tau$	MC@NLO	24992	1.0	1.0	0.08
106028	$W^{-}Z \rightarrow \ell\nu\tau\tau$	MC@NLO	24993	1.0	1.0	0.04
106026	$W^{+}Z \rightarrow \tau\nu\tau\tau$	MC@NLO	24990	1.0	1.0	0.04
106029	$W^{-}Z \rightarrow \tau\nu\tau\tau$	MC@NLO	24941	1.0	1.0	0.02
113190	$W^{+}Z \rightarrow qq\tau\tau$	MC@NLO	24987	1.0	1.0	0.25
113191	$W^{-}Z \rightarrow qq\tau\tau$	MC@NLO	24989	1.0	1.0	0.14
105921	$qq \rightarrow W^{+}W^{-} \rightarrow ee\nu\nu$	MC@NLO	149972	1.0	1.0	0.50
105921	$qq \rightarrow W^{+}W^{-} \rightarrow ee\nu\nu$	MC@NLO	49988	1.0	1.0	0.50
105922	$qq \rightarrow W^{+}W^{-} \rightarrow e\mu\nu\nu$	MC@NLO	49987	1.0	1.0	0.50
105922	$qq \rightarrow W^{+}W^{-} \rightarrow e\mu\nu\nu$	MC@NLO	149973	1.0	1.0	0.50
105923	$qq \rightarrow W^{+}W^{-} \rightarrow e\tau\nu\nu$	MC@NLO	198943	1.0	1.0	0.50
105924	$qq \rightarrow W^{+}W^{-} \rightarrow \mu\mu\nu\nu$	MC@NLO	149964	1.0	1.0	0.50
105924	$qq \rightarrow W^{+}W^{-} \rightarrow \mu\mu\nu\nu$	MC@NLO	49992	1.0	1.0	0.50
105925	$qq \rightarrow W^{+}W^{-} \rightarrow \mu e\nu\nu$	MC@NLO	49990	1.0	1.0	0.50
105925	$qq \rightarrow W^{+}W^{-} \rightarrow \mu e\nu\nu$	MC@NLO	149971	1.0	1.0	0.50
105926	$qq \rightarrow W^{+}W^{-} \rightarrow \mu\tau\nu\nu$	MC@NLO	198957	1.0	1.0	0.50
105927	$qq \rightarrow W^{+}W^{-} \rightarrow \tau\tau\nu\nu$	MC@NLO	198952	1.0	1.0	0.50
105928	$qq \rightarrow W^{+}W^{-} \rightarrow \tau e\nu\nu$	MC@NLO	198962	1.0	1.0	0.50
105929	$qq \rightarrow W^{+}W^{-} \rightarrow \tau\mu\nu\nu$	MC@NLO	198954	1.0	1.0	0.50
106011	$gg \rightarrow W^{+}W^{-} \rightarrow ee\nu\nu$	gg2ww	9998	1.0	0.99	0.01
106012	$gg \rightarrow W^{+}W^{-} \rightarrow e\mu\nu\nu$	gg2ww	9999	1.0	0.99	0.01
106013	$gg \rightarrow W^{+}W^{-} \rightarrow e\tau\nu\nu$	gg2ww	9997	1.0	0.92	0.01
106014	$gg \rightarrow W^{+}W^{-} \rightarrow \mu\mu\nu\nu$	gg2ww	9998	1.0	0.99	0.01
106015	$gg \rightarrow W^{+}W^{-} \rightarrow \mu e\nu\nu$	gg2ww	9998	1.0	0.99	0.01
106016	$gg \rightarrow W^{+}W^{-} \rightarrow \mu\tau\nu\nu$	gg2ww	9997	1.0	0.93	0.01
106017	$gg \rightarrow W^{+}W^{-} \rightarrow \tau\tau\nu\nu$	gg2ww	9998	1.0	0.33	0.01
106018	$gg \rightarrow W^{+}W^{-} \rightarrow \tau e\nu\nu$	gg2ww	9997	1.0	0.92	0.01
106019	$gg \rightarrow W^{+}W^{-} \rightarrow \tau\mu\nu\nu$	gg2ww	9998	1.0	0.93	0.01

Table C.4: MC samples used to model diboson processes, including WW, $W\gamma$ and $Z\gamma$. The corresponding cross-sections, generator names, generator level filter efficiencies and total numbers of events are shown in the table.

MCID	Process	Generator	Events	k-factor	$\epsilon_{\rm filter}$	σ [pb]
105200	$t\bar{t}$	MC@NLO	999332	1.0	0.56	164.6
108340	t-channel$\rightarrow e$	MC@NLO	9996	1.0	1.0	7.2
108341	t-channel$\rightarrow \mu$	MC@NLO	9994	1.0	1.0	7.2
108342	t-channel$\rightarrow \tau$	MC@NLO	9995	1.0	1.0	7.1
108343	s-channel$\rightarrow e$	MC@NLO	9992	1.0	1.0	0.5
108344	s-channel$\rightarrow \mu$	MC@NLO	9991	1.0	1.0	0.5
108345	s-channel$\rightarrow \tau$	MC@NLO	9997	1.0	1.0	0.5
108346	Wt	MC@NLO	59960	1.0	1.0	13.1
105757	*bbcc* μ10μ10X	PythiaB	297118	1.0	0.9	2727.0
105758	*bbcc* μ10e10X	PythiaB	796391	1.0	0.9	3963.0
105759	*bbcc* $e10e10X$	PythiaB	290326	1.0	10^{-3}	3068.0

Table C.3: Top quark and dijet MC samples - MC samples used to model top (including $t\bar{t}$ and single top) and dijet backgrounds. The corresponding cross-sections, generator names, generator level filter efficiencies and total numbers of events are shown in the table. (Only in the 105759 sample the filter cuts have been applied, thus the small filter efficiency).

Appendix D

Mis-assignment studies in the $ZZ \to 4\ell$ channel

Consider the simple case where after the application of all the selection criteria of the analysis there are four same flavor leptons, two positively and two negatively charged ones ($\ell_1^+\ell_2^-\ell_3^+\ell_4^-$) which result from ZZ decays. With these 4 leptons one can form two possible solutions:

- $\ell_1^+\ell_2^-\ell_3^+\ell_4^-$
- $\ell_1^+\ell_4^-\ell_3^+\ell_2^-$

In these cases one must be careful in the final selection since the wrong assignment of leptons to the Z pair can lead to crucial systematic errors in the background estimation as well as to introduce bias in the invariant mass distribution of the pairs. In order to eliminate the systematic errors due to wrong assignment of leptons to the Zs the following methods have been tested:

- Method 1: Select the pair closest to the Z pole;
  It is the most common method used so far. The resulting mis-assignment percentage is $\sim 6\%$ and $\sim 17\%$ for the ZZ and ZZ^* cases respectively. The invariant mass of the correct and wrong combinations of the $4e$ and 4μ cases are shown in the figures D.1 and D.2 respectively. The upper histograms show the correct combination of leptons while the other two histograms show the wrong combination. From these distributions one can see the resulting bias in the wrong combinations (solution 2) of the first and second pair around the Z pole.

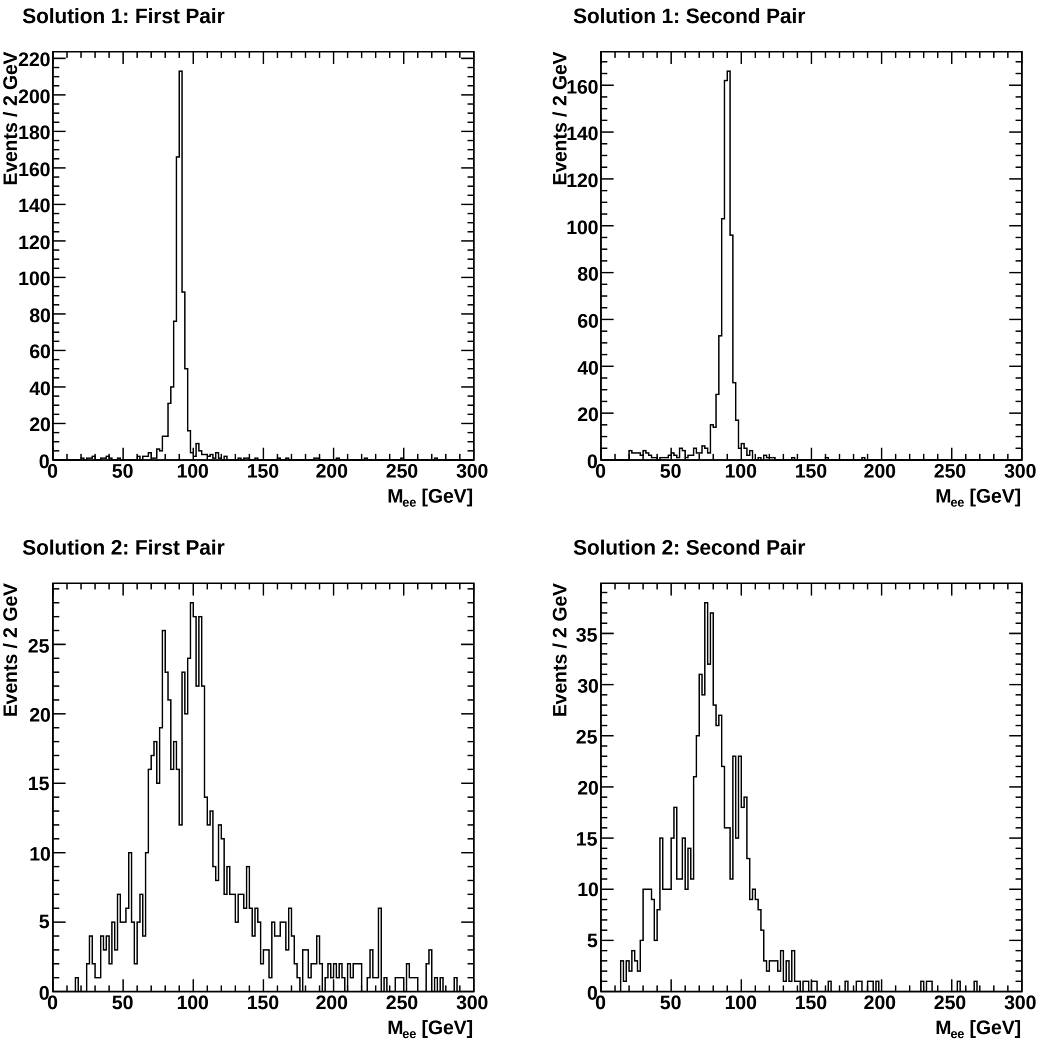

Figure D.1: Mis-assignment Method 1 $ZZ \to 4e$ - Invariant mass distributions of the four pairs. The upper plots refer to the first solution (by selecting the ones which are closest to the Z pole) and the histograms below to the second solution (remaining pairs).

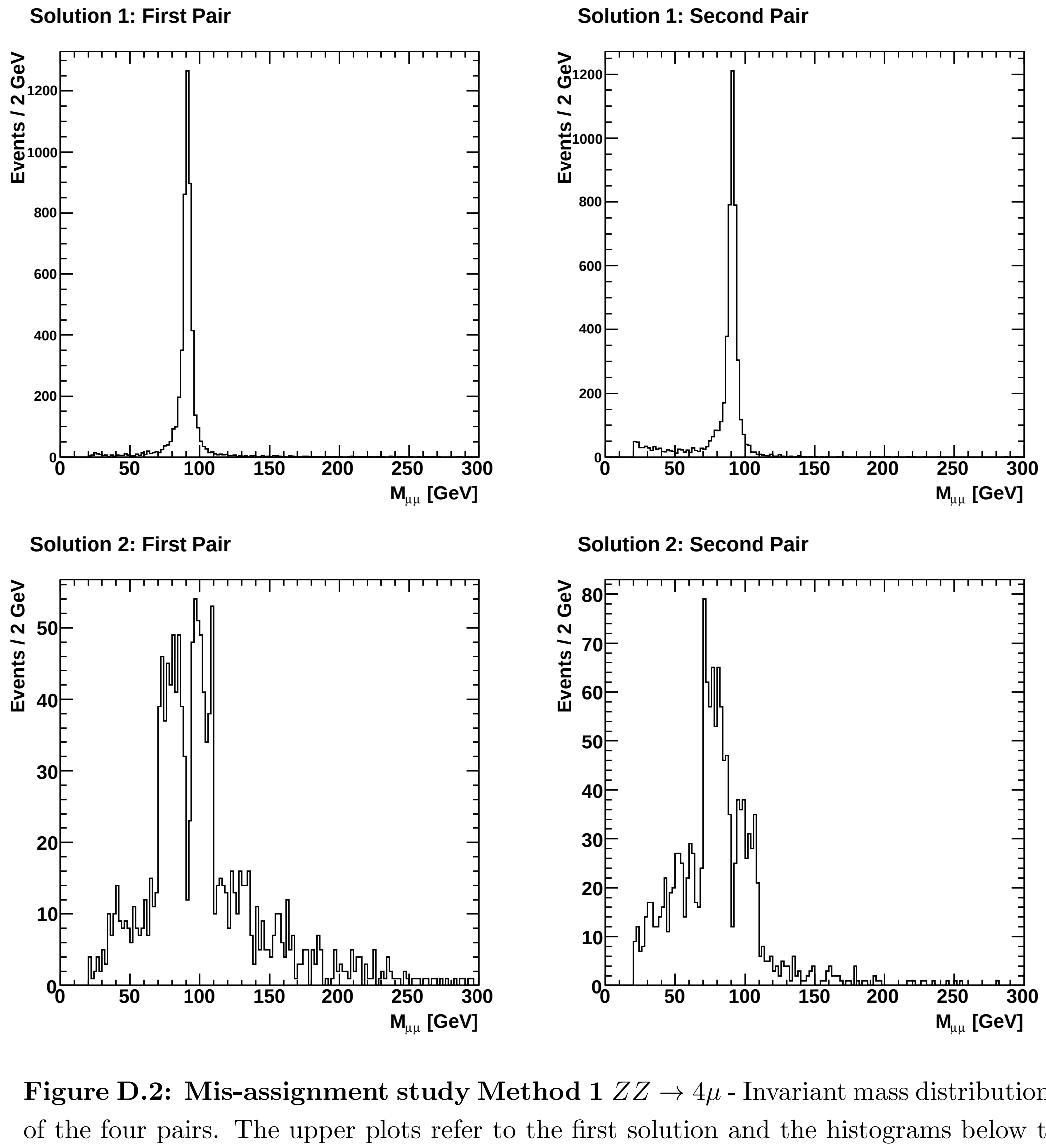

Figure D.2: Mis-assignment study Method 1 $ZZ \to 4\mu$ - Invariant mass distributions of the four pairs. The upper plots refer to the first solution and the histograms below to the second solution.

- Random selection of the final solution;

  The resulting mis-assignment percentage is $\sim 23\%$ and $\sim 31\%$ for ZZ and ZZ^* respectively. Figures D.3 and D.4 show the invariant mass distributions for the correct and wrong combinations for the two different signatures $4e$ and 4μ.

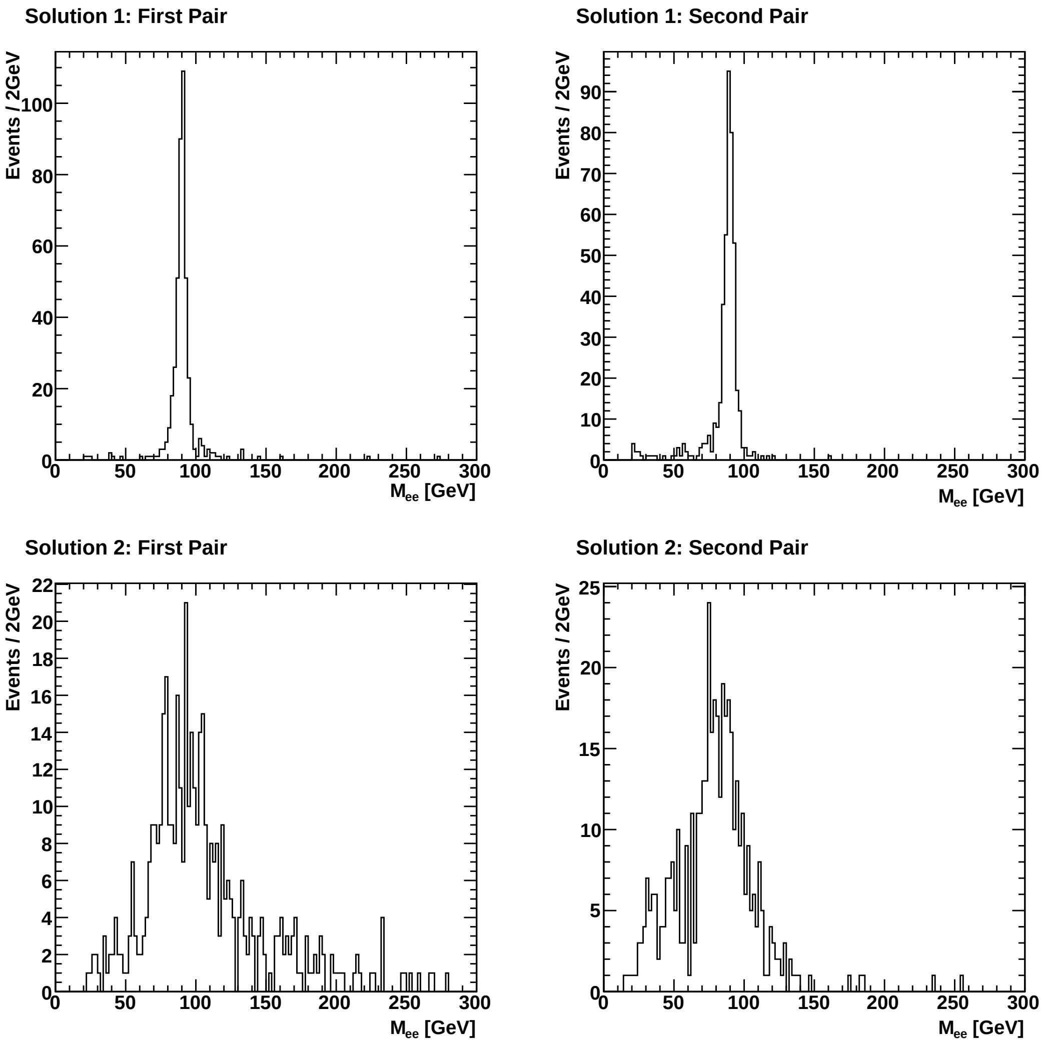

Figure D.3: Mis-assignment study $ZZ \rightarrow 4e$, Method 2 - Invariant mass distributions of the four pairs. Random Selection. The upper plots refer to the first solution and the histograms below to the second solution.

- Extract probabilities from Breit-Wigner parton distribution function (PDF) for the pairs lying in the mass region $66 < M_{ll} < 116$ GeV.

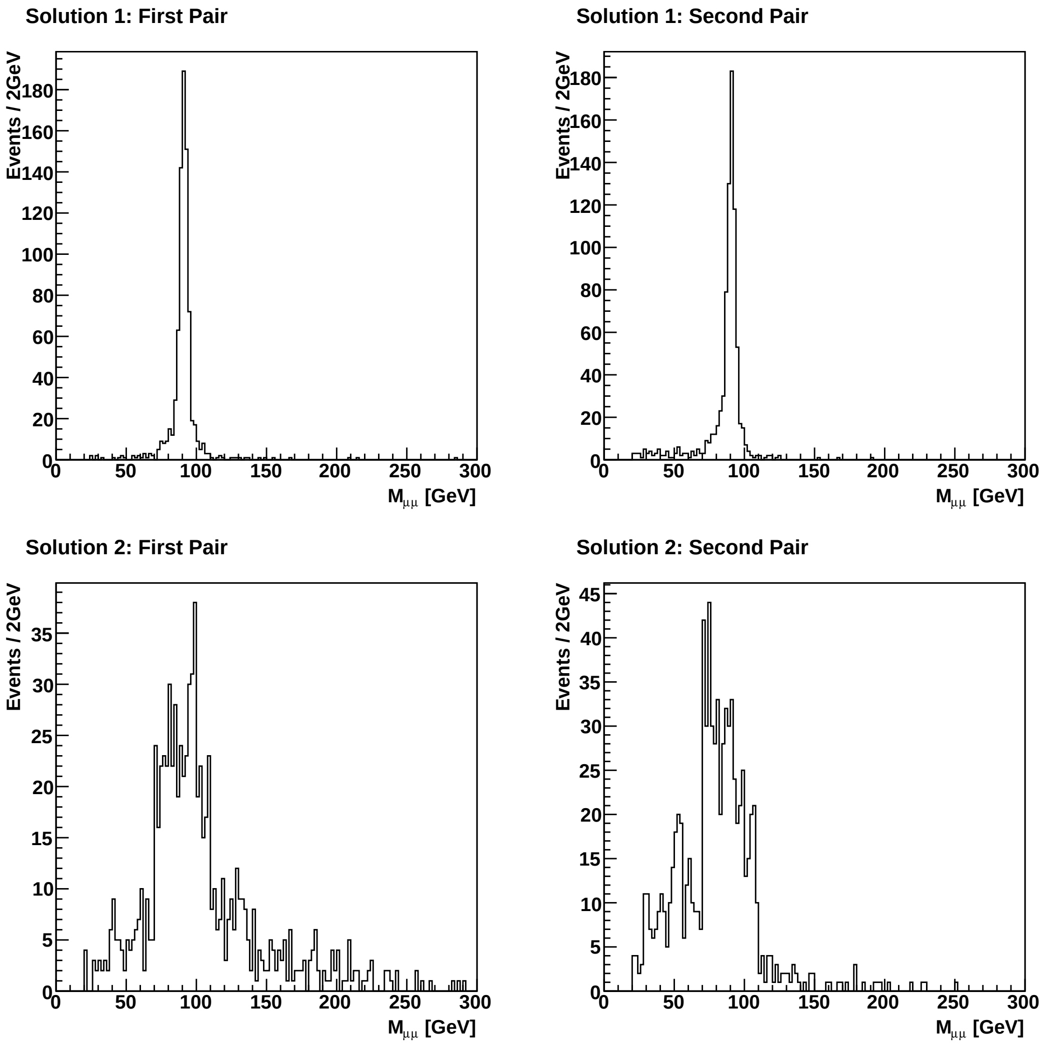

Figure D.4: Mis-assignment study $ZZ \to 4\mu$, Method 2 - Invariant mass distributions of the four pairs. The upper plots refer to the first solution and the histograms below to the second solution.

- For two Zs on shell the combination with the highest product probability is chosen;
  - For one Z on shell the combination which includes the closest pair to the Z pole is selected;
  - If both solutions are present in the event then the one with two Zs on-shell is kept.

  The mis-assignment probability of this method is $\sim 2\%$ for both Zs on shell and and $\sim 16\%$ if one Z is off-shell. Similar invariant mass distributions with the previous methods can be found in figures D.5 and D.6. As can be seen from the figures with the probability method one can avoid the bias in the invariant mass distributions.

- Select the combination with the lower value of the sum of $|M_{\ell^+\ell^-} - M_Z|$.

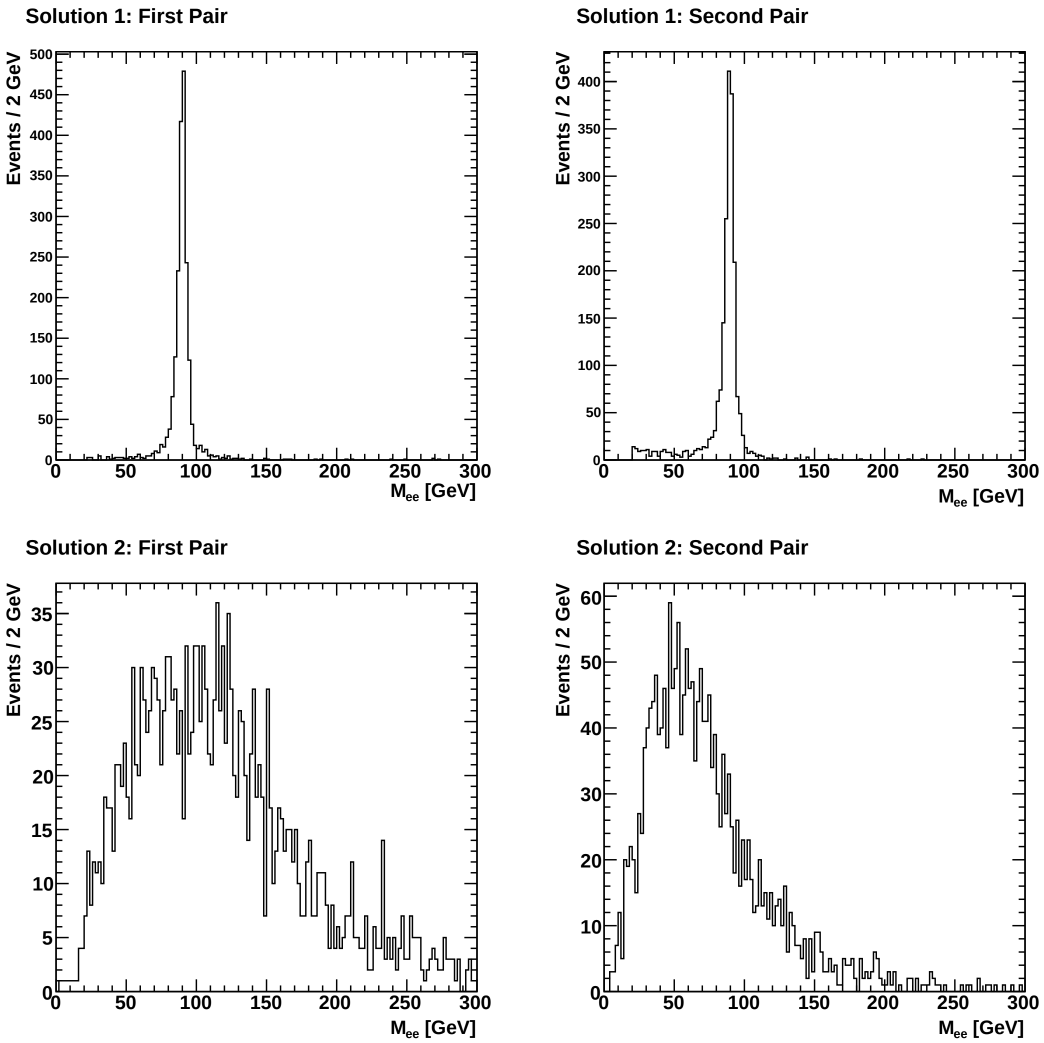

Figure D.5: Mis-assignment study $ZZ \to 4e$, Method 4 - Invariant mass distributions of the four pairs. Probabilities (BW) but without mass cut. The upper plots refer to the first solution and the histograms below to the second solution.

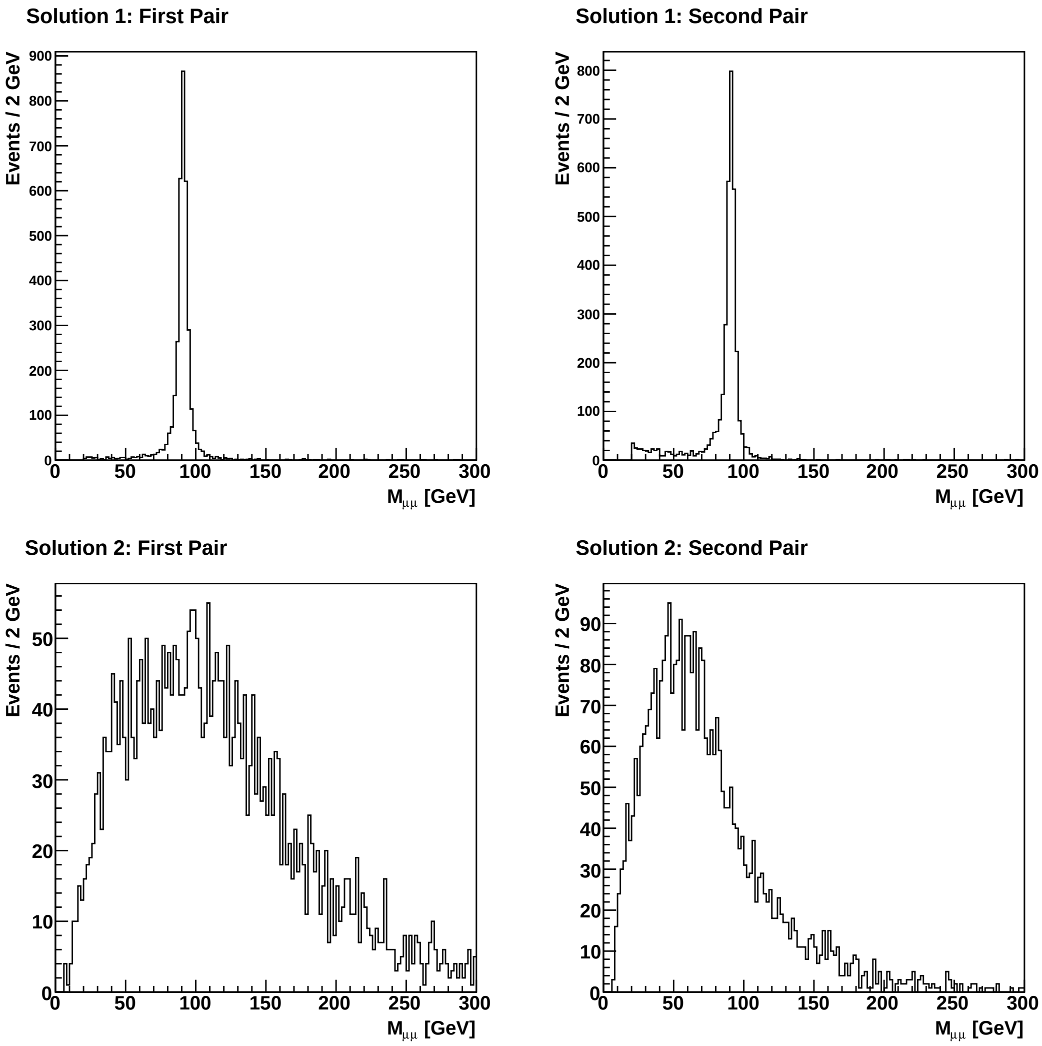

Figure D.6: Mis-assignment study $ZZ \to 4e$, Method 4 - Invariant mass distributions of the four pairs. Probabilities (BW) but without mass cut. The upper plots refer to the first solution and the histograms below to the second solution.

Appendix E

Comparison between the selection criteria used in the $ZZ \to 4\ell$ analysis and the searches for $H \to ZZ^* \to 4\ell$

Table E.1 lists the event selection requirements used by the $ZZ \to 4\ell$ analysis (Section 7.5), and the searches for a Standard Model Higgs boson done by the Higgs working group[1] for the same final states: $e^+e^-e^+e^-$, $\mu^+\mu^-\mu^+\mu^-$, $e^+e^-\mu^+\mu^-$ and $\mu^+\mu^-e^+e^-$.

Requirement	$ZZ \to 4\ell$	$H \to ZZ^{(*)} \to 4\ell$
Event selection:		
1. Good Run Lists	Same GRL for all channels	Separate GRLs for each channel
2. Event cleaning	LAr noise warning flag not set	same
3. Vertex	vertex with >= 3 tracks	same
4. Trigger	μ: EF_mu18_MG or EF_mu40_MSonly;	
	e: EF_e20_medium	same
Object Selection:		
5. μ: type	"loose" STACO muons	"loose" STACO muons ("author=6 or 7")
		Continued on next page

[1] ATLAS-CONF-2011-131

Table E.1 – continued from previous page		
Requirement	$ZZ \to 4\ell$	$H \to ZZ^{(*)} \to 4\ell$
		or, TightMuons for MUID muons
6. μ: cosmic removal	no requirement	only keep muons with $\|d_0\| < 1$ mm
7. μ: p_T and η	$p_T > 15$ GeV, $\|\eta\| < 2.5$	$p_T > 7$ GeV, $\|\eta\| < 2.5$
8. μ: ID hits	as in Sec.7.5.1	same
9. μ: z_0	$z_0 < 10$ mm	same
10. μ: d_0	$d_0/\sigma(d_0) < 10$	if μ is among the 2 lowest p_T leptons and $M(4\ell) < 190$ GeV: ask $d_0/\sigma(d_0) < 3.5$
11. μ: track iso	$\Sigma p_T(\Delta R < 0.2) < 15\%$	same
12. μ: calo iso	not applied	calo iso $(\Delta R < 0.2) < 30\%$
13. e: type	"medium" electrons, author=1 or 3	same
14. e: quality	(OQ AND 1444==0)	same
15. e: E_T and η	$E_T > 15$ GeV, $\|\eta\| < 2.47$	$E_T > 7$ GeV, $\|\eta\| < 2.47$
		But, exclude electrons with $E_T < 15$ GeV in crack region $(1.37 < \|\eta_{Cluster}\| < 1.52)$
16. e: z_0	$z_0 < 10$ mm	same
17. e: d_0	$d_0/\sigma(d_0) < 10$	if e is among the 2 lowest p_T leptons and $M(4\ell) < 190$ GeV: ask $d_0/\sigma(d_0) < 6$
18. e: track iso	$\Sigma p_T(\Delta R < 0.2) < 15\%$	same
19. e: calo iso	not applied	calo iso $(\Delta R < 0.2) < 30\%$
20. e: overlap removal	a) remove e if $\Delta R < 0.1$ from μ;	a) remove e if same ID track as μ
	b) remove lowest E_T e	a) same condition, but instead of ΔR
	if $\Delta R < 0.1$ from another e	use "same ID track"
<u>4ℓ selection</u>:		
21. Trigger matching	at least 1 lepton with $p_T > 20$ GeV (μ)	e or μ: no matching, just
		Continued on next page

Table E.1 – continued from previous page

Requirement	$ZZ \to 4\ell$	$H \to ZZ^{(*)} \to 4\ell$
	or $E_T > 25$ GeV (e),	ask for 2 ℓ's with $p_T >$ 20 GeV
	matched ($\Delta R < 0.1$) to trigger object	
22. Lepton topology	no requirement	$\Delta R > 0.1$ from each other lepton in event (check this after e overlap removal)
23. Number of leptons	exactly 4 leptons	4 or more leptons
24. Quadruplet formation	exactly 2 pairs of:	≥ 2 pairs of OS SF leptons;
	Opposite Sign (OS),	a) If > 4 leptons, choose 1 quadruple
	Same Flavour (SF) leptons	as explained in "lepton pairing"
		b) For 2e2μ, 2μ2e : $M_{ee} \geq 15$ GeV and $M_{\mu\mu} \geq 15$ GeV
25. Lepton Pairing	pairing with minimum	1^{st} pair ($\ell_1\ell_2$): has the min$\lvert M_{12} - M_Z\rvert$;
	$\Sigma(\lvert M_{12} - M_Z\rvert + \lvert M_{34} - M_Z\rvert)$	2^{nd} pair ($\ell_3\ell_4$): has highest $p_T(\ell_3\ell_4)$ among remaining pairs
26. Dilepton kinematics	both Zs on-shell:	one Z on-shell, other can be Z^*:
	$\lvert M_{\ell\ell} - M_Z\rvert < 25$ GeV	$\lvert M_{\ell_1\ell_2} - M_Z\rvert < 15$ GeV ; $\lvert M_{\ell_3\ell_4}\rvert < 115$ GeV

Table E.1: Comparison of selection requirements between SM $ZZ \to 4\ell$ and $H \to ZZ^{(*)} \to 4\ell$ analyses.

In general, the selection criteria of the $ZZ \to 4\ell$ analysis are more uniform across the four final states. The kinematic cuts of the leptons are also relatively high, since the analysis has been built for two Zs on-shell. Compared to the Higgs analysis which requires only one of the Z's to be on-shell, the kinematic cuts has been relaxed for two of the leptons, down to 7 GeV. Going through the items in Table E.1 a comprehensive explanation for each choice follows:

1. In order to have uniformity with the other SM EW analyses (WW, WZ) a common GRL has been used with the other groups. The disadvantage of this GRL results from the fact that it covers all the physics objects (electrons, muons, jets etc.) and gives 1.024 fb^{-1} everywhere, while the Higgs group uses explicit GRLs for each object (electrons and muons) and depending on the final state they use different GRLs. This increases the luminosotity from 1.04 to 1.21 fb^{-1}, depending on the channel.

2-5. Same in both analyses.

6. Redundant cut in the $ZZ \to 4\ell$ analysis, since all muons are required to be consistent with the primary vertex by applying a d_0 significance cut to all leptons (see items 10).

7. The Higgs group allows the second Z to be off-shell, so it needs lower p_T leptons than in the $ZZ \to 4\ell$ analysis where both Zs are required to be on-shell.

8-9. Standard selections recommented from the Muon Performance Group.

10. For a uniform approach for all leptons, like the rest of the SM EW groups. For the muons this is a quite loose cut. This loose cut (< 10) guarantees to stay away from mis-modeled regions close to zero.

11. This track isolation requirement preserved $\sim 97\%$ of the ZZ signal, while rejecting all bkg events. Used by Higgs group as well. Opening the cone was rejecting signal. The cut value is close to the efficiency plateau for this requirement (see Section **??**).

12. Calorimetric isolation requirement only harm an already clean ZZ signal, so no calorimetric isolation has been applied in the $ZZ \to 4\ell$ analysis.

13-14. Same in both analyses.

15. Same comment as for muons above for the kinematic cuts. Concerning the use of the electrons in the transition regions: there are scale factors for $E_T > 15$ GeV electrons everywhere. In addition, the performance studies (on the Z inclusive samples) done for the $ZZ \to 4\ell$ analysis show that there is no any evidence for the crack electrons deteriorating the data to MC comparisons.

16. Same in both analyses.

17. A uniform approach to all leptons has been decided, like in rest of SM EW groups. The cut is loose for the muons, but rejects some electrons which radiate

Bremsstrahlung radiation[1]. In fact, this cut rejects one $2e2\mu$ candidate in the $ZZ \to 4\ell$ analysis, which is preserved by the Higgs group's selection.

18-19. Same discussion as in items 11 and 12, above. For the calorimetric isolation of electrons, it is worth to note that by applying a cut similar to the one used by the other SM EW groups, defined as the E_T sum in a cone of radius $\Delta R = 0.2$ to be smaller that 4 GeV, would reject $\sim 20\%$ of $ZZ \to 4e$ signal events. According to these results the decision was to do not apply any calorimetric isolation.

20. Suggestion of implementing the search for a nearby related "lepton" is different in the two groups, but otherwise this is a standard requirement.

21. In the $ZZ \to 4\ell$ analysis an explicit trigger matching of one of the four candidate leptons to facilitate the trigger efficiency estimates is done. The higher E_T threshold for the electrons guarantees that electrons is on the efficiency plateau.

22. Such a cut on the lepton separation is not applied in the $ZZ \to 4\ell$ analysis, in accordance with rest of SM EW groups. A study on this has shown that this cut makes no difference in any case.

23-24. Having 4 leptons fixes the quadruple and avoids the cases of combinatorics. Although, only a very small fraction of signal events ($\sim 1\%$) contains more than four leptons.

25. The method used from the ZZ analysis D for the pairing minimizes the biases in the dilepton mass distributions and also reduces the mis-assignment to $\sim 1.5\%$, compared to $\sim 6\%$ of the algorithm used by the Higgs analysis.

26. In the ZZ analysis both Zs are required to be on-shell, so a wider mass cut around the Z mass is afforded compared to the Higgs group (± 25 GeV for ZZ vs. ± 15 GeV in the Higgs analysis).

Table E.2 summarizes the event yields of the two analyses: expected (from $ZZ^{(*)}$ signal and background) and observed events. The Higgs group selection for ZZ^* production yields about 60% more events than the ZZ selections (an expected yield of 14.17 events vs. 8.93 events). Keep in mind that part of this increase comes from the use of an integrated luminosity of up to 20% higher for the Higgs analysis, depending on the 4ℓ channel.

[1]The bremsstrahlung radiation is electromagnetic radiation produced by a charged particle when it interacts with matter (atomic nucleus).

Final State	$eeee$	$\mu\mu\mu\mu$	$ee\mu\mu$
Observed:			
ZZ	2	8	2
$H \to ZZ^{(*)}$	2	10	6
expected ZZ:			
ZZ	1.53±0.03± 0.10	3.03±0.04±0.06	4.37±0.04± 0.14
$H \to ZZ^{(*)}$	2.43±0.41	5.34±0.71	6.40±0.81
expected Bkg:			
ZZ	$0.01^{+0.03}_{-0.01}$(stat) $^{+0.05}_{-0.01}$(syst)	0.3±0.3(stat)±0.3(syst)	$<0.01^{+0.03}_{-0.01}$(stat)
$H \to ZZ^{(*)}$	0.19±0.06	0.04±0.01	0.23±0.07

Table E.2: Comparison of selection requirements between SM $ZZ \to 4\ell$ and $H \to ZZ^{(*)} \to 4\ell$ analyses. Summary of observed events and expected signal ($ZZ^{(*)}$) and background contributions in the four lepton channels.

Appendix F

Event Displays of the $ZZ \to 4l$ candidates

Figures F.1, F.2, F.3, F.4, F.5, F.6, F.7, F.8, F.9, F.10, F.11, F.12 display all the events considered in the $ZZ \to 4l$ analysis: $ZZ \to e^+e^-e^+e^-$, $ZZ \to \mu^+\mu^-\mu^+\mu^-$ and $ZZ \to e^+e^-\mu^+\mu^-$.

In the top right part of each figure the identifier of each event (Run Number and Event Number) is shown. In the top left part the transverse view of the detector $(X - Y)$ is shown, where only the central detector systems ('barrel' part) are shown. Moving away from the collision point at the centre, a particle can go through the inner detector tracker, the electromagnetic calorimeter (shown as the light-green ring), the hadronic calorimeter (brick red ring) and the muon system (in blue) which surrounds everything.

Energy depositions in the endcap calorimeters do not show up in this view. The energy/momentum of the lepton is indicated as a bar starting from the outer radius of the hadronic calorimeter and going outwards; the height of the bar is proportional to the energy/momentum of the lepton. In the bottom part, we show the $\rho - Z$ projection, where all main detector systems are visible (barrel and end-cap regions).

In each plot, the lepton pairings are indicated with a colour code: each Z candidate is formed by the leptons with the same colour (red and green). All the event displays have been produced with Atlantis software release 09-16-01-08 [18].

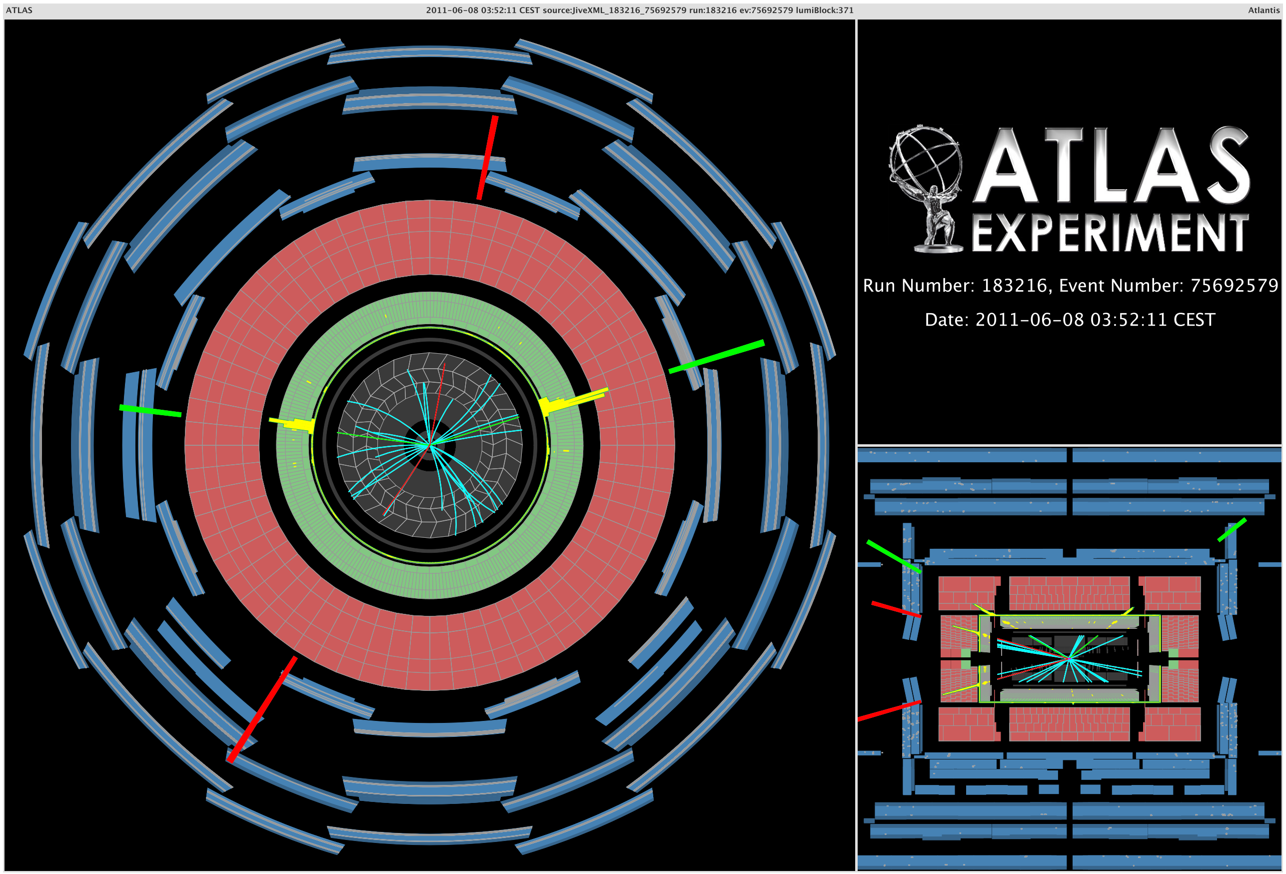

Figure F.1: Event display of the $ZZ \to eeee$ candidate event (RunNumber 183216, Event Number 75692579). One Z candidate has a mass of 85.0 GeVand a p_T of 26.9 GeV; it is formed by two electrons (in red) with p_T, η, ϕ of 55.5 GeV, -1.96, -2.14 rad and 33.7 GeV, -1.97, 1.37 rad, respectively. The other Z candidate has a mass of 111.3 GeVand a p_T of 22.7 GeV; it is formed by two electrons (in green) with $[_T$, η, ϕ of 42.0 GeV, -1.31, 0.30 rad and 23.4 GeV, 1.05, 3.02 rad, respectively. The four lepton system has a mass of 270.1 GeVand a p_T of 6.4 GeV. Inner detector tracks with a transverse momentum p_T larger than 1 GeVare displayed as blue helices.

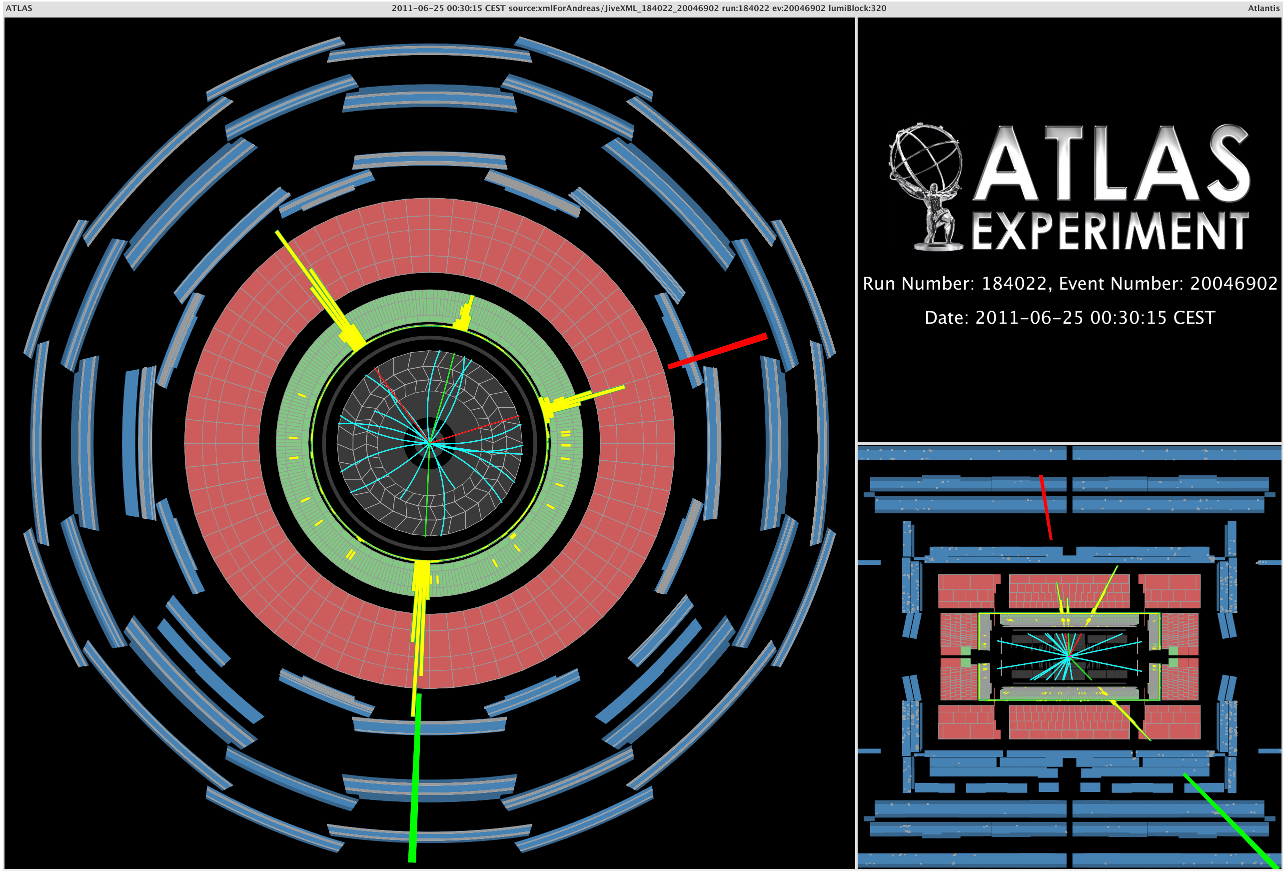

Figure F.2: Event display of the $ZZ \to eeee$ candidate event (RunNumber 184022, Event Number 20046902). One Z candidate has a mass of 99.8 GeVand a p_T of 72.5 GeV; it is formed by two electrons (in red) with p_T, η, ϕ of 43.8 GeV, -0.16, 0.31 rad and 73.2 GeV, 0.52, 2.20 rad, respectively. The other Z candidate has a mass of 92.1 GeVand a p_T of 71.0 GeV; it is formed by two electrons (in green) with p_T, η, ϕ of 90.0 GeV, 0.87, -1.61 rad and 19.7 GeV, -0.02, 1.29 rad, respectively. The four lepton system has a mass of 245.2 GeVand a p_T of 1.5 GeV. Inner detector tracks with a transverse momentum p_T larger than 1 GeVare displayed as blue helices.

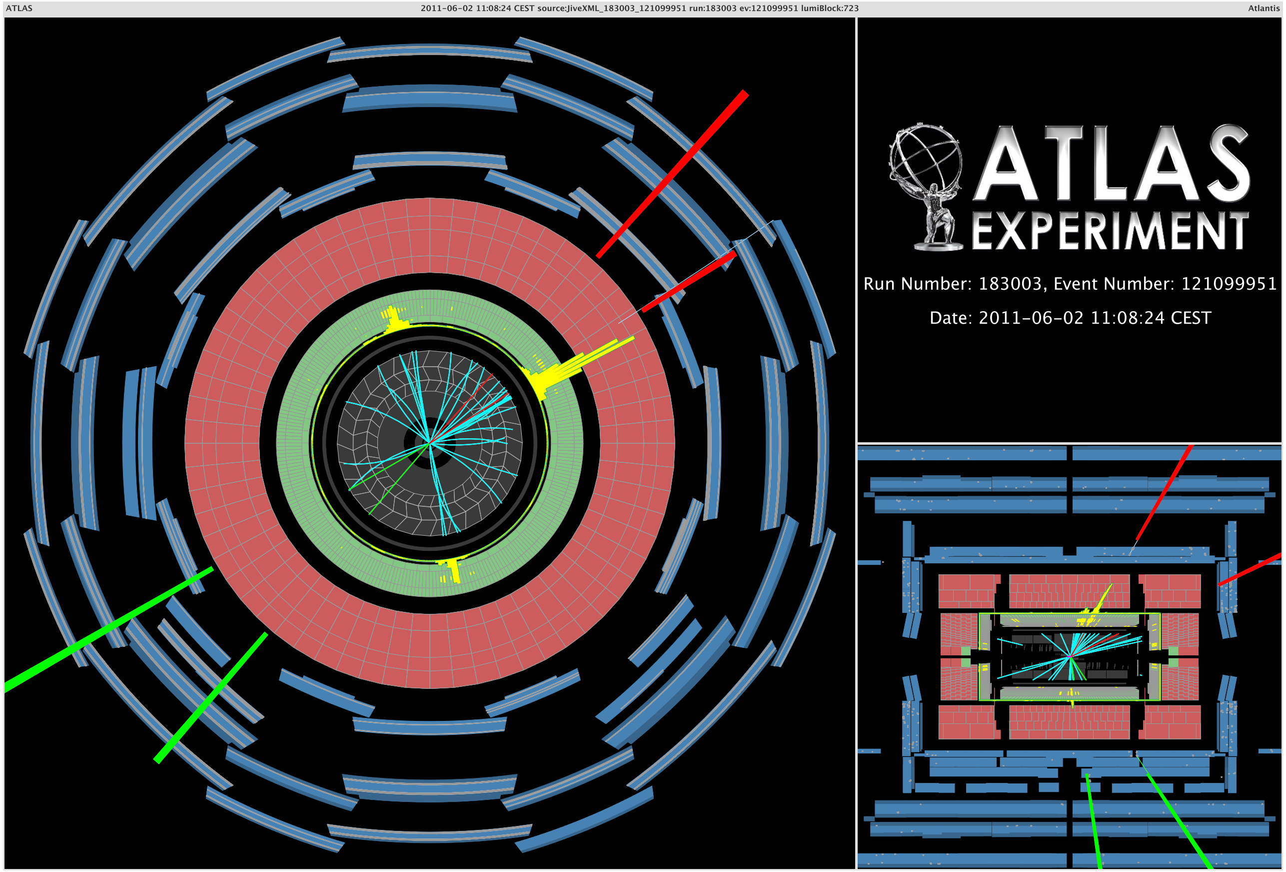

Figure F.3: Event display of a $ZZ \to \mu\mu\mu\mu$ candidate event (Run Number 183003, Event Number 121099951). One Z candidate has a mass of 84.4 GeVand a p_T of 196.0 GeV, and it is formed by two muons (in red) with p_T, η, ϕ of 150.2 GeV, 0.55, 0.84 rad and 47.1 GeV, 1.48, 0.56 rad, respectively. The other Z candidate has a mass of 100.1 GeVand a p_T of 403.4 GeVand it is formed by two muons (in green) with p_T, η, ϕ of 317.0 GeV, 0.63, -2.62 rad and 90.4 GeV, 0.14, -2.28 rad, respectively. The four lepton system has a mass of 597.1 GeVand a p_T of 213.2 GeV. Inner detector tracks with a transverse momentum p_T larger than 1 GeV are displayed as blue helices.

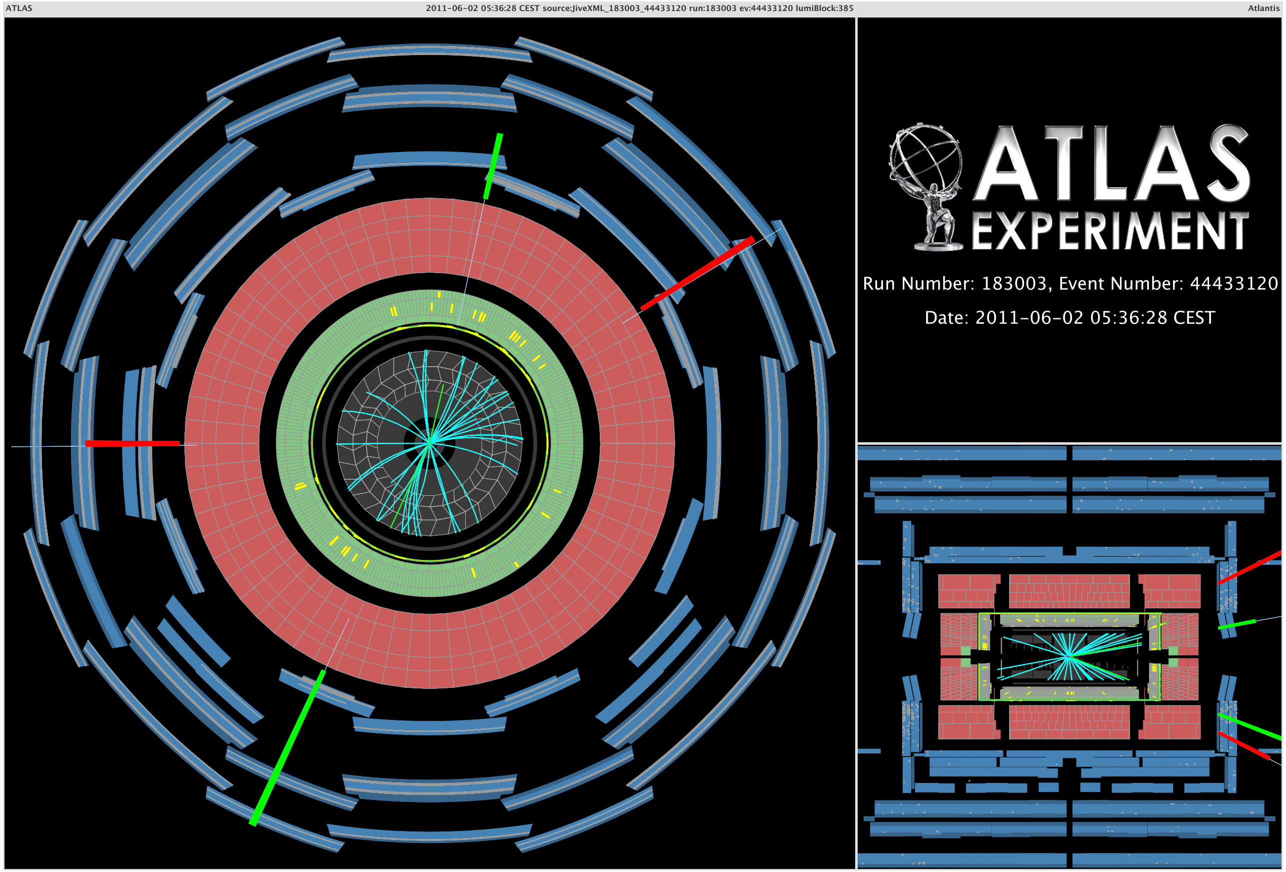

Figure F.4: Event display of a $ZZ \to \mu\mu\mu\mu$ candidate event (Run Number 183003, Event Number 44433120). One Z candidate has a mass of 101.1 GeVand a p_T of 66.9 GeV, and it is formed by two muons (in green) with p_T, η, ϕ of 25.3 GeV, 2.35, 1.34 rad and 91.4 GeV, 1.68, -2.01 rad, respectively. The other Z candidate has a mass of 93.5 GeVand a p_T of 35.7 GeVand it is formed by two muons (in red) with p_T, η, ϕ of 61.7 GeV, 1.46, 0.56 rad and 38.4 GeV, 1.43, -3.14 rad, respectively. The four lepton system has a mass of 223.2 GeVand a p_T of 31.7 GeV. Inner detector tracks with a transverse momentum p_T larger than 1 GeV are displayed as blue helices.

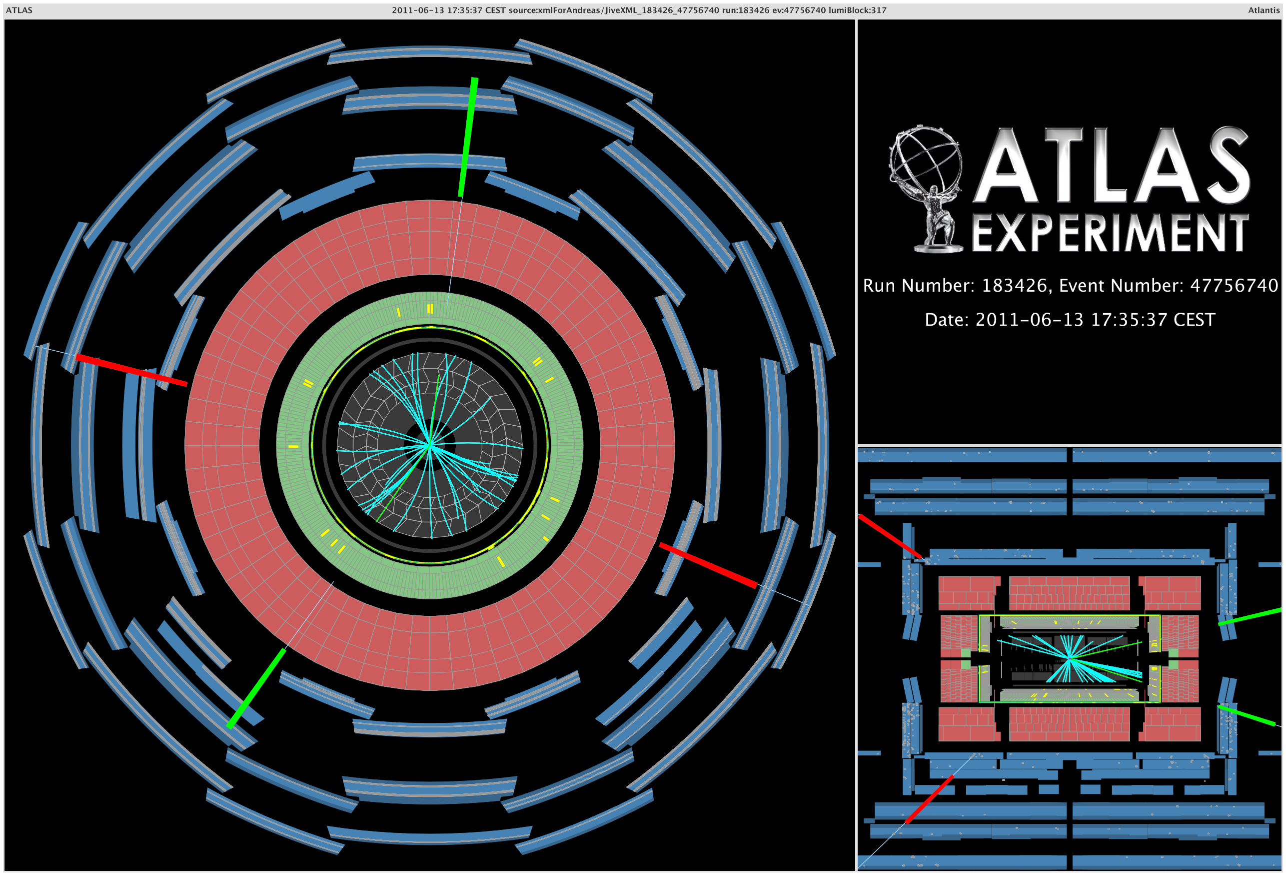

Figure F.5: Event display of a $ZZ \rightarrow \mu\mu\mu\mu$ candidate event (Run Number 183426, Event Number 47756740). One Z candidate has a mass of 90.3 GeVand a p_T of 26.4 GeV, and it is formed by two muons (in green) with p_T, η, ϕ of 53.3 GeV, 2.17, 1.45 rad and 39.7 GeV, 1.86, -2.19 rad, respectively. The other Z candidate has a mass of 95.0 GeVand a p_T of 9.2 GeVand it is formed by two muons (in red) with p_T, η, ϕ of 49.8 GeV, -1.18, 2.90 rad and 44.5 GeV, -0.88, -0.41 rad, respectively. The four lepton system has a mass of 459.8 GeVand a p_T of 28.3 GeV. Inner detector tracks with a transverse momentum p_T larger than 1 GeV are displayed as blue helices.

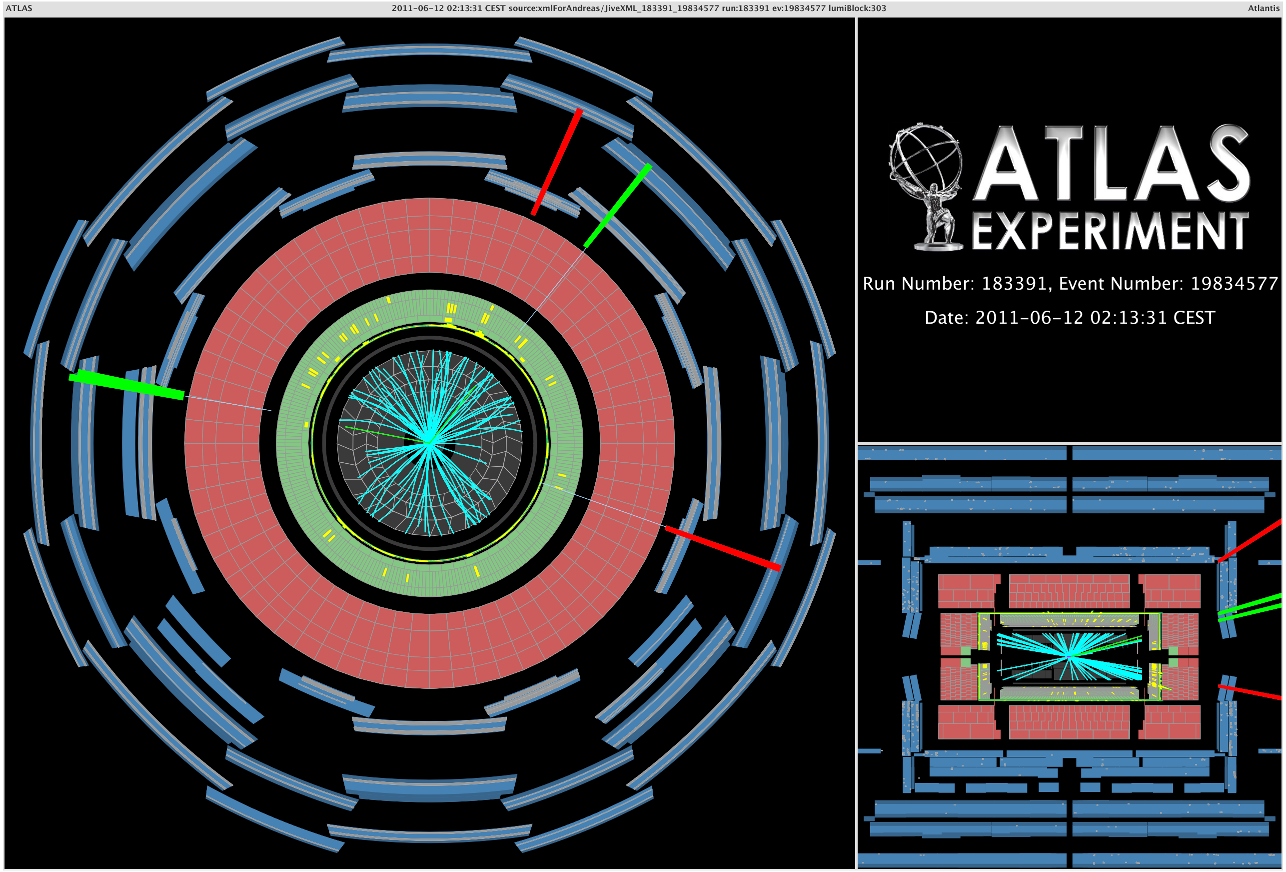

Figure F.6: Event display of a $ZZ \rightarrow \mu\mu\mu\mu$ candidate event (Run Number 183391, Event Number 19834577). One Z candidate has a mass of 94.3 GeVand a p_T of 77.7 GeV, and it is formed by two muons (in red) with p_T, η, ϕ of 51.0 GeV, 1.23, 1.15 rad and 54.7 GeV, 2.34, -0.34 rad, respectively. The other Z candidate has a mass of 77.9 GeVand a p_T of 47.5 GeVand it is formed by two muons (in green) with p_T, η, ϕ of 44.3 GeV, 2.12, 0.90 rad and 46.5 GeV, 1.95, 2.94 rad, respectively. The four lepton system has a mass of 194.9 GeVand a p_T of 90.2 GeV. Inner detector tracks with a transverse momentum p_T larger than 1 GeV are displayed as blue helices.

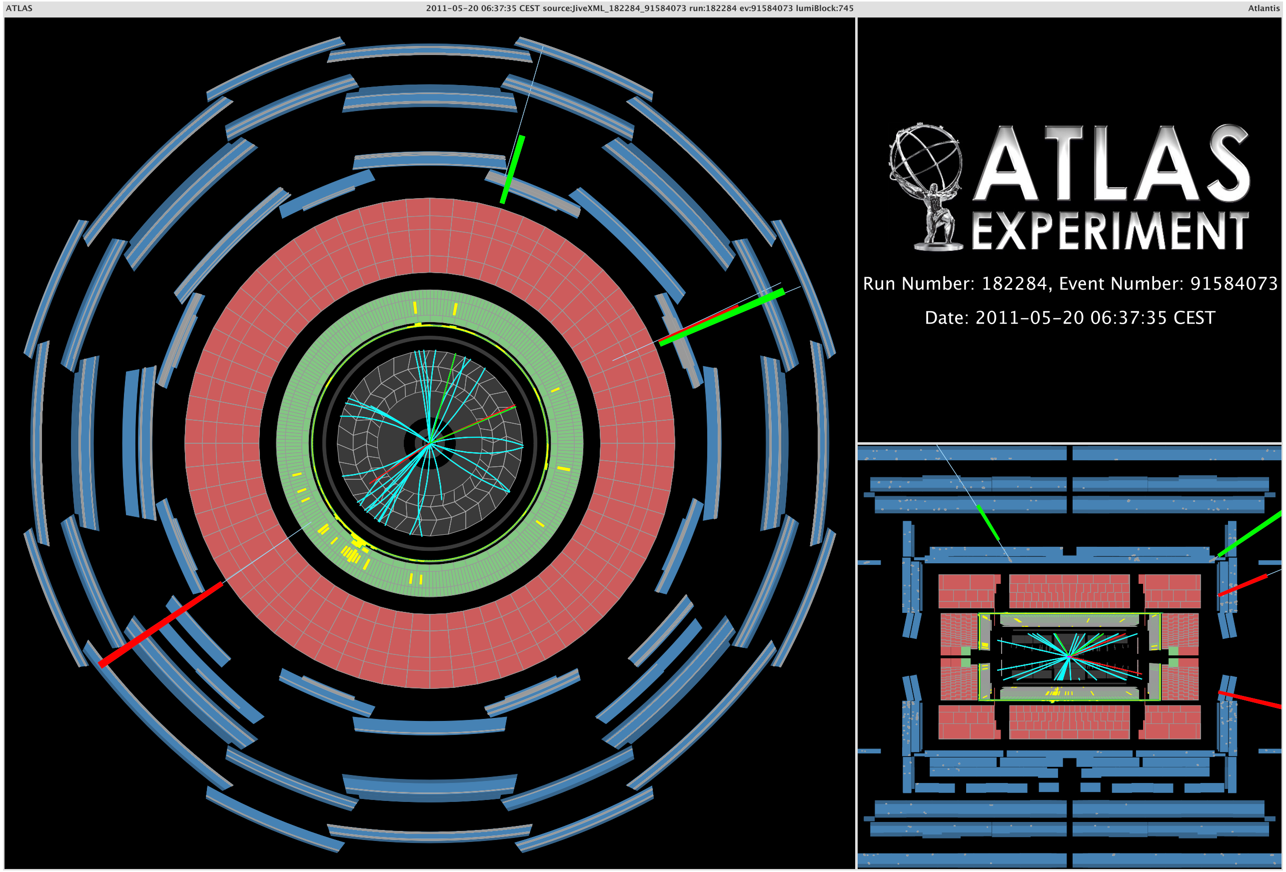

Figure F.7: Event display of a $ZZ \to \mu\mu\mu\mu$ candidate event (Run Number 182284, Event Number 91584073). One Z candidate has a mass of 89.3 GeVand a p_T of 83.3 GeV, and it is formed by two muons (in green) with p_T, η, ϕ of 63.4 GeV, 1.18, 0.41 rad and 26.9 GeV, -0.58, 1.28 rad, respectively. The other Z candidate has a mass of 103.8 GeVand a p_T of 38.4 GeVand it is formed by two muons (in red) with p_T, η, ϕ of 72.4 GeV, 2.15, -2.55 rad and 35.0 GeV, 1.62, 0.41 rad, respectively. The four lepton system has a mass of 286.7 GeVand a p_T of 45.3 GeV. Inner detector tracks with a transverse momentum p_T larger than 1 GeV are displayed as blue helices.

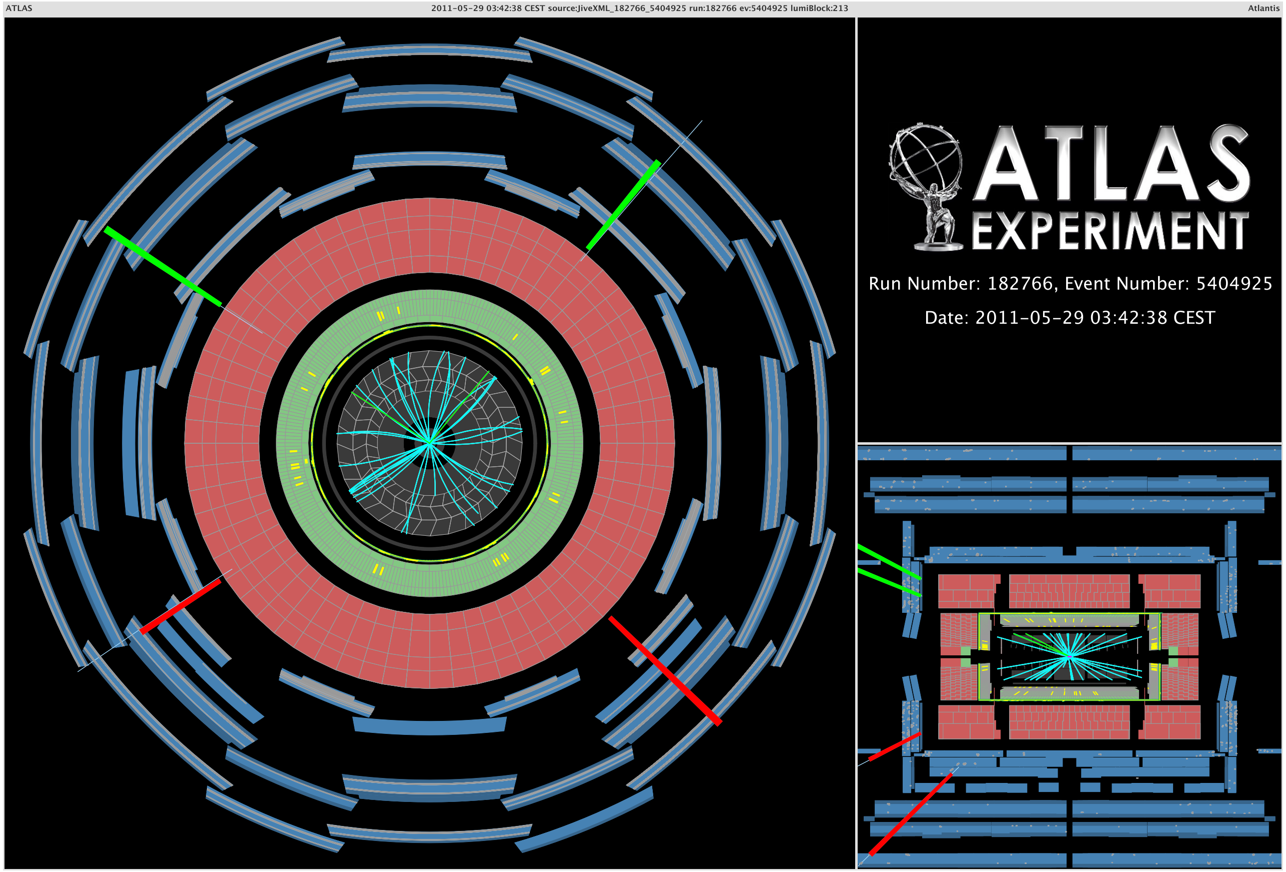

Figure F.8: Event display of a $ZZ \rightarrow \mu\mu\mu\mu$ candidate event (Run Number 182766, Event Number 5404925). One Z candidate has a mass of 90.3 GeVand a p_T of 78.1 GeV, and it is formed by two muons (in red) with p_T, η, ϕ of 38.7 GeV, -1.42, -2.56 rad and 76.9 GeV, -0.89, -0.77 rad, respectively. The other Z candidate has a mass of 85.0 GeVand a p_T of 77.9 GeVand it is formed by two muons (in green) with p_T, η, ϕ of 49.0 GeV, -1.40, 0.89 rad and 65.6 GeV, -1.63, 2.56 rad, respectively. The four lepton system has a mass of 241.0 GeVand a p_T of 1.0 GeV. Inner detector tracks with a transverse momentum p_T larger than 1 GeV are displayed as blue helices.

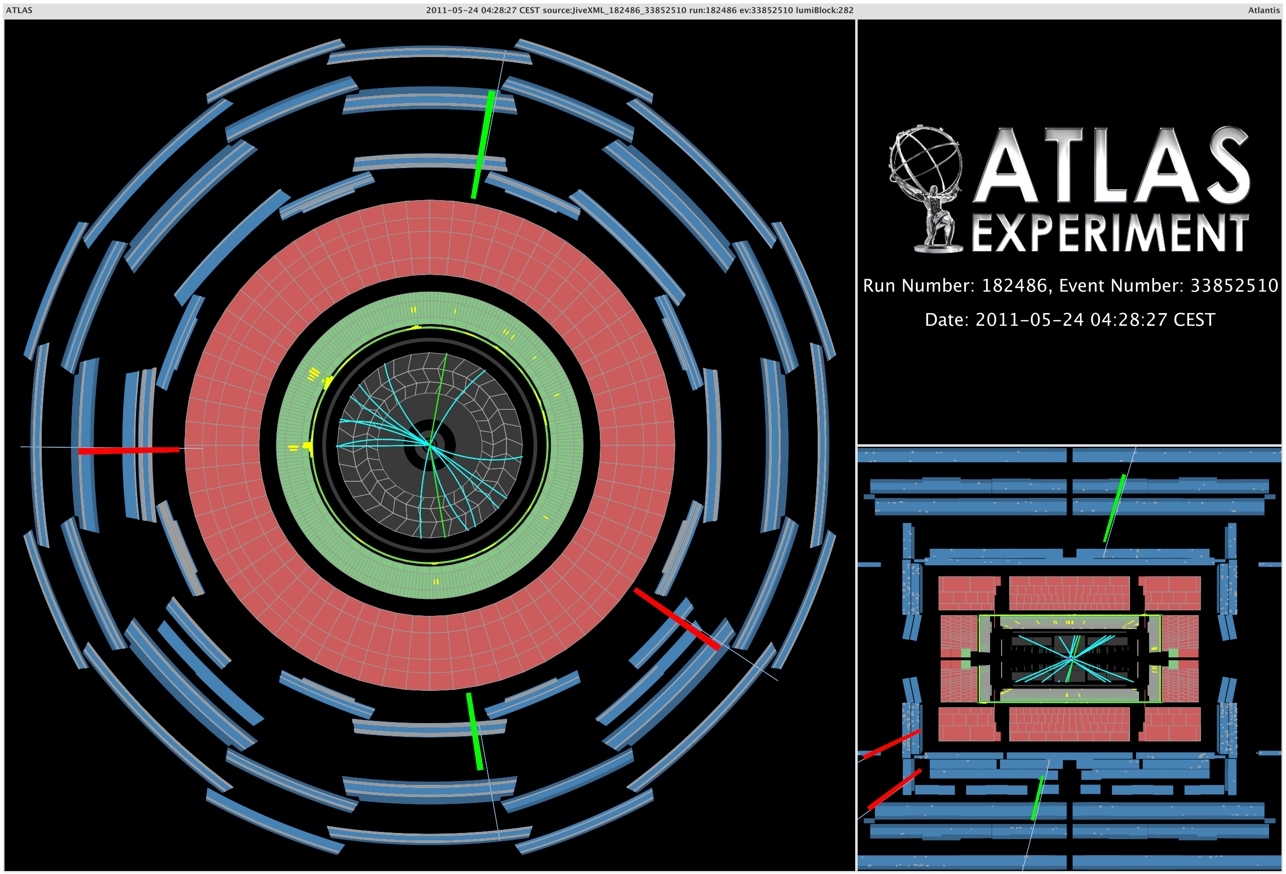

Figure F.9: Event display of a $ZZ \rightarrow \mu\mu\mu\mu$ candidate event (Run Number 182486, Event Number 33852510). One Z candidate has a mass of 83.3 GeVand a p_T of 26.6 GeV, and it is formed by two muons (in red) with p_T, η, ϕ of 42.3 GeV, -1.48, -3.12 rad and 43.6 GeV, -1.10, -0.61 rad, respectively. The other Z candidate has a mass of 77.1 GeVand a p_T of 20.7 GeVand it is formed by two muons (in green) with p_T, η, ϕ of 46.9 GeV, 0.29, 1.40 rad and 30.4 GeV, -0.23, -1.42 rad, respectively. The four lepton system has a mass of 208.0 GeVand a p_T of 11.4 GeV. Inner detector tracks with a transverse momentum p_T larger than 1 GeV are displayed as blue helices.

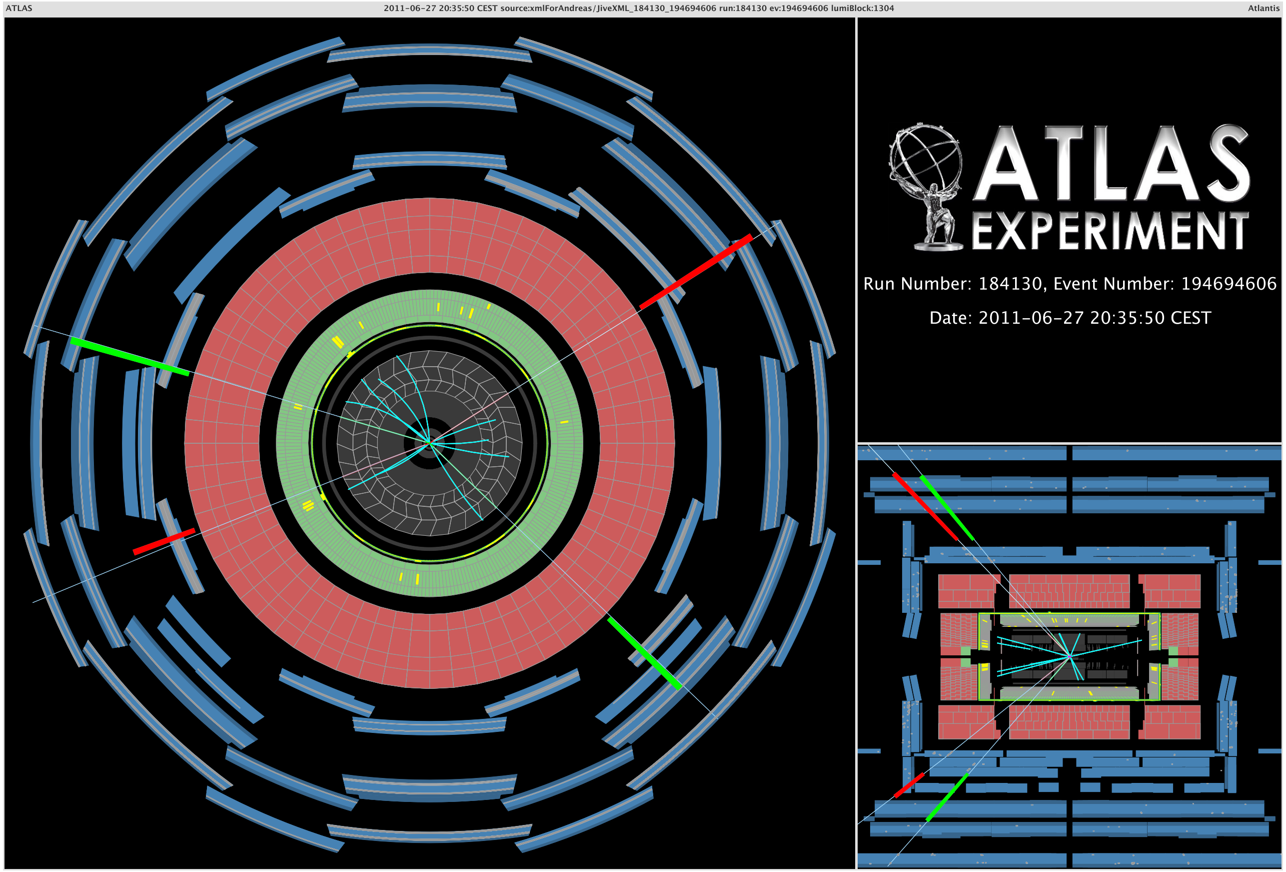

Figure F.10: Event display of a $ZZ \to \mu\mu\mu\mu$ candidate event (Run Number 184130, Event Number 194694606). One Z candidate has a mass of 77.4 GeVand a p_T of 38.1 GeV, and it is formed by two muons (in red) with p_T, η, ϕ of 61.5 GeV, -0.85, 0.57 rad and 24.4 GeV, -1.05, -2.79 rad, respectively. The other Z candidate has a mass of 93.0 GeVand a p_T of 27.1 GeVand it is formed by two muons (in green) with p_T, η, ϕ of 55.2 GeV, -0.75, 2.86 rad and 41.6 GeV, -0.79, -0.77 rad, respectively. The four lepton system has a mass of 183.1 GeVand a p_T of 12.3 GeV. Inner detector tracks with a transverse momentum p_T larger than 1 GeV are displayed as blue helices.

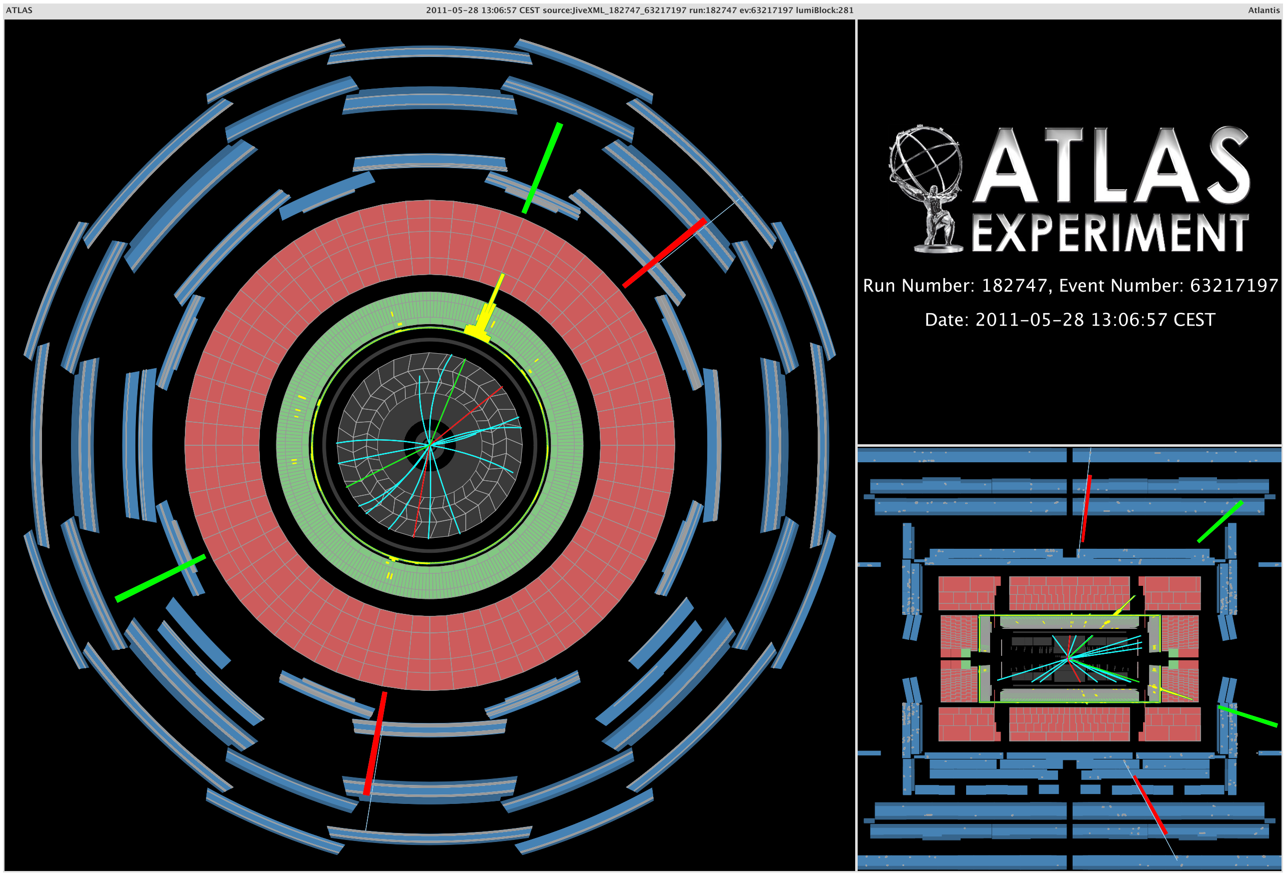

Figure F.11: Event display of a $ZZ \rightarrow \mu\mu\mu\mu$ candidate event (Run Number 182747, Event Number 63217197). One Z candidate has a mass of 85.9 GeVand a p_T of 30.8 GeV, and it is formed by two muons (in red) with p_T, η, ϕ of 44.9 GeV, 0.11, 0.69 rad and 44.5 GeV, 0.53, -1.75 rad, respectively. The other Z candidate has a mass of 85.5 GeVand a p_T of 29.3 GeVand it is formed by two electrons (in green) with p_T, η, ϕ of 39.6 GeV, 0.95, 1.19 rad and 42.3 GeV, 1.85, -2.69 rad, respectively. The four lepton system has a mass of 209.7 GeVand a p_T of 4.6 GeV. Inner detector tracks with a transverse momentum p_T larger than 1 GeV are displayed as blue helices.

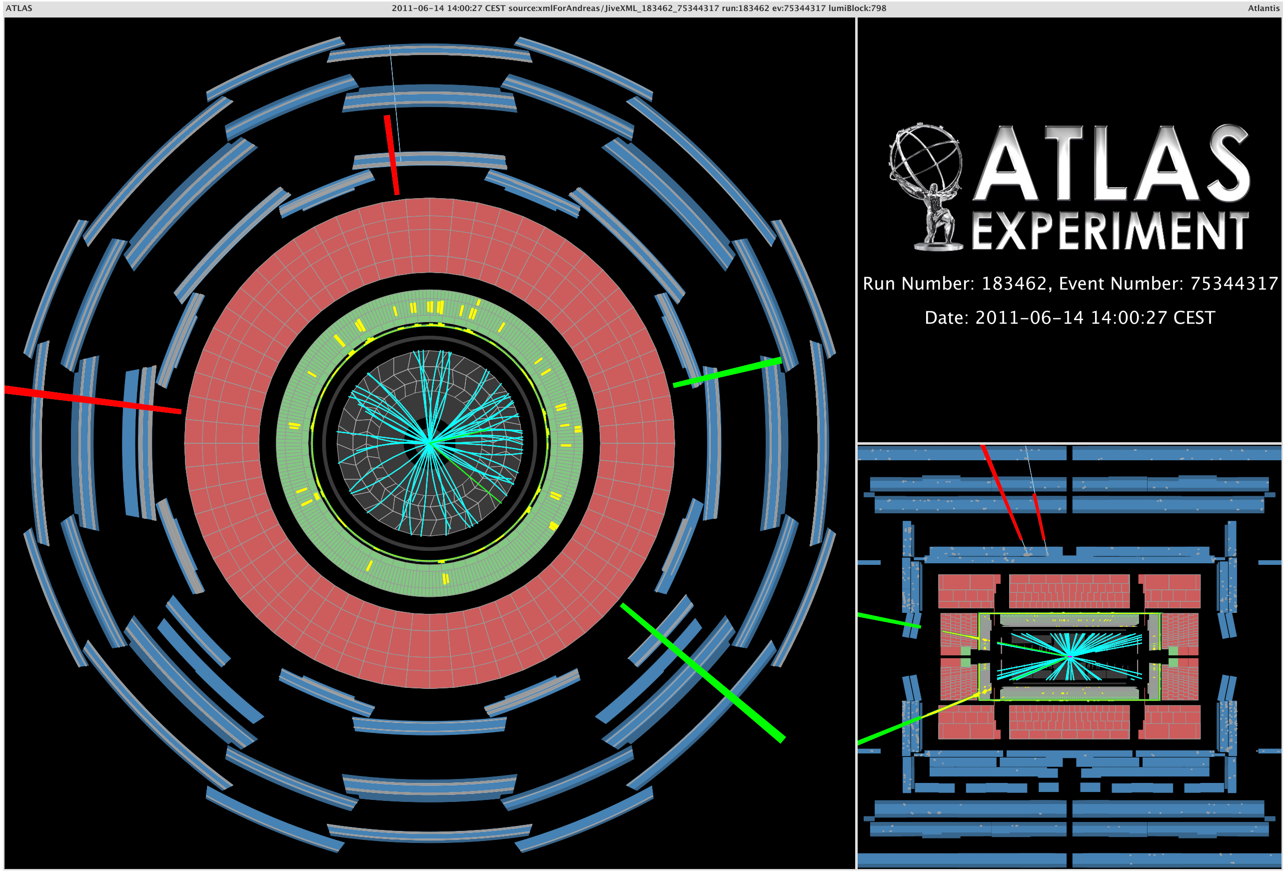

Figure F.12: Event display of a $ZZ \rightarrow ee\mu\mu$ candidate event (Run Number 183462, Event Number 75344317). One Z candidate has a mass of 92.2 GeVand a p_T of 169.9 GeV, and it is formed by two electrons (in green) with p_T, η, ϕ of 48.1 GeV, -2.31, 0.23 rad and 136.7 GeV, -1.63, -0.70 rad, respectively. The other Z candidate has a mass of 87.4 GeVand a p_T of 169.8 GeVand it is formed by two muons (in red) with p_T, η, ϕ of 31.4 GeV, -0.22, 1.70 rad and 159.1 GeV, -0.40, 3.02 rad, respectively. The four lepton system has a mass of 488.0 GeVand a p_T of 27.7 GeV. Inner detector tracks with a transverse momentum p_T larger than 1 GeV are displayed as blue helices.

Appendix G

Kinematic distributions of the $ZZ \to 4l$ candidates

G.1 Kinematic Distributions of the $ZZ \to 4e$ channel

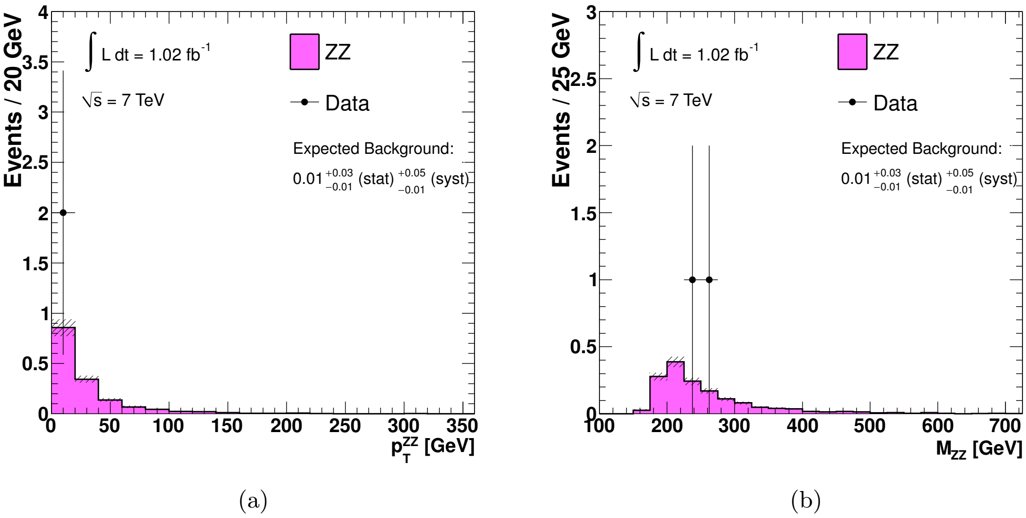

Figure G.1: (a) Transverse momentum p_{T}^{ZZ} and (b) invariant mass M_{ZZ} of the $ZZ \to 4e$ candidates. The points represent the observed data and the histograms show the signal prediction from simulation. The shaded band on each histogram shows the combined statistical and systematic uncertainty on the signal prediction. The predicted number of background events from the data-driven background estimate is indicated on the plot.

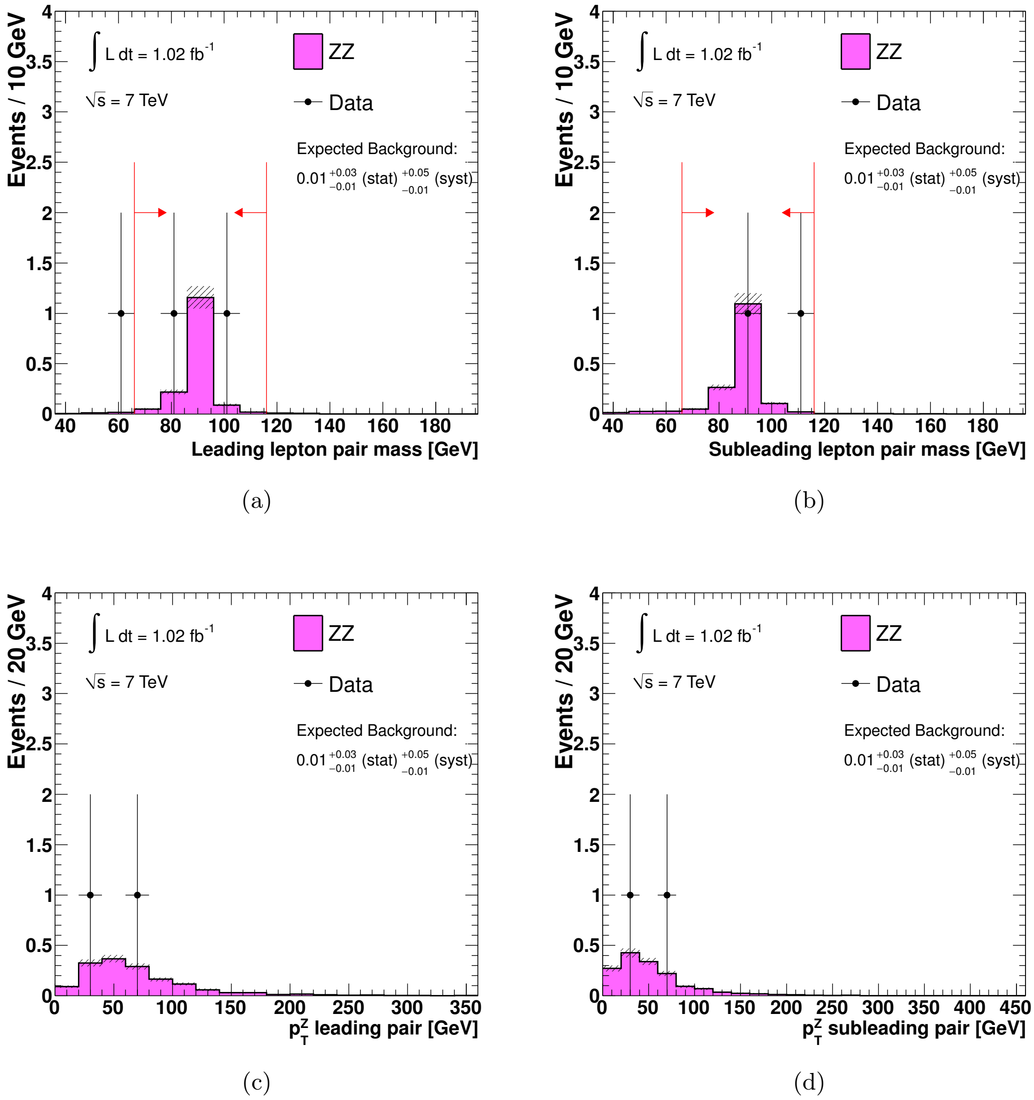

Figure G.2: Invariant mass of (a) leading pair (b) subleading pair and transverse momentum p_T^Z of (c) leading pair and (d) subleading pair of the ee pairs. The points represent the observed data and the histograms show the signal prediction from simulation. The shaded band on each histogram shows the combined statistical and systematic uncertainty on the signal prediction. The predicted number of background events from the data-driven background estimate is indicated on the plot.

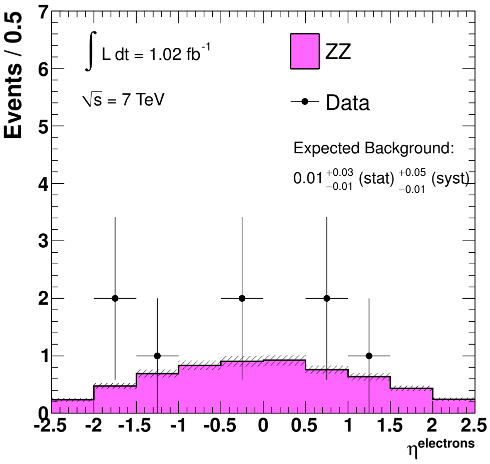

(a)

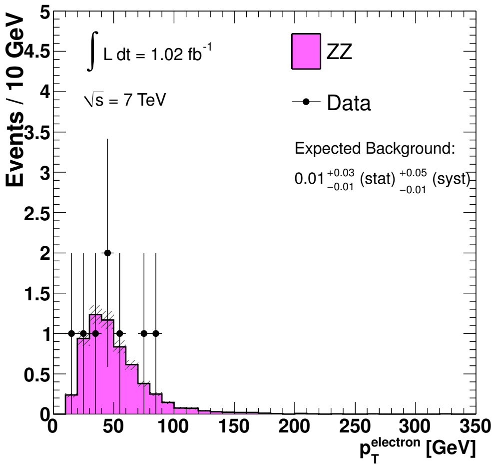

(b)

Figure G.3: (a) η and (b) p_T of the final electrons. The points represent the observed data and the histograms show the signal prediction from simulation. The shaded band on each histogram shows the combined statistical and systematic uncertainty on the signal prediction. The predicted number of background events from the data-driven background estimate is indicated on the plot.

G.2 Kinematic Distributions of the $ZZ \to 4\mu$ channel

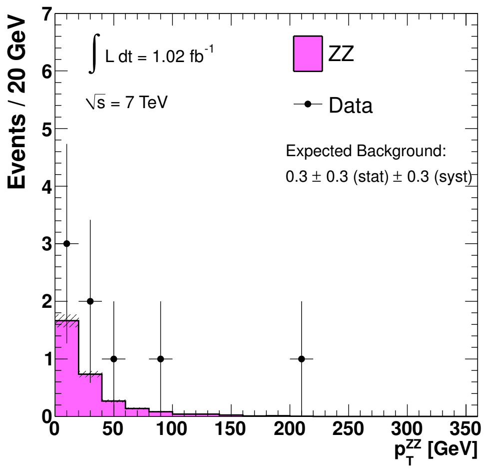

(a)

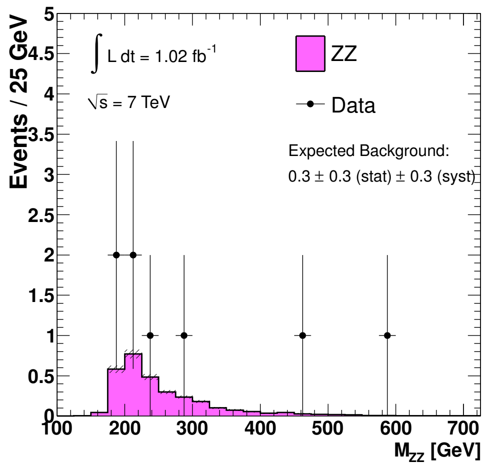

(b)

Figure G.4: (a) Transverse momentum p_{T}^{ZZ} and (b) invariant mass M_{ZZ} of the $ZZ \to 4\mu$ candidates. The points represent the observed data and the histograms show the signal prediction from simulation. The shaded band on each histogram shows the combined statistical and systematic uncertainty on the signal prediction. The predicted number of background events from the data-driven background estimate is indicated on the plot.

G.3 Kinematic Distributions of the $ZZ \to 2e2\mu$ channel

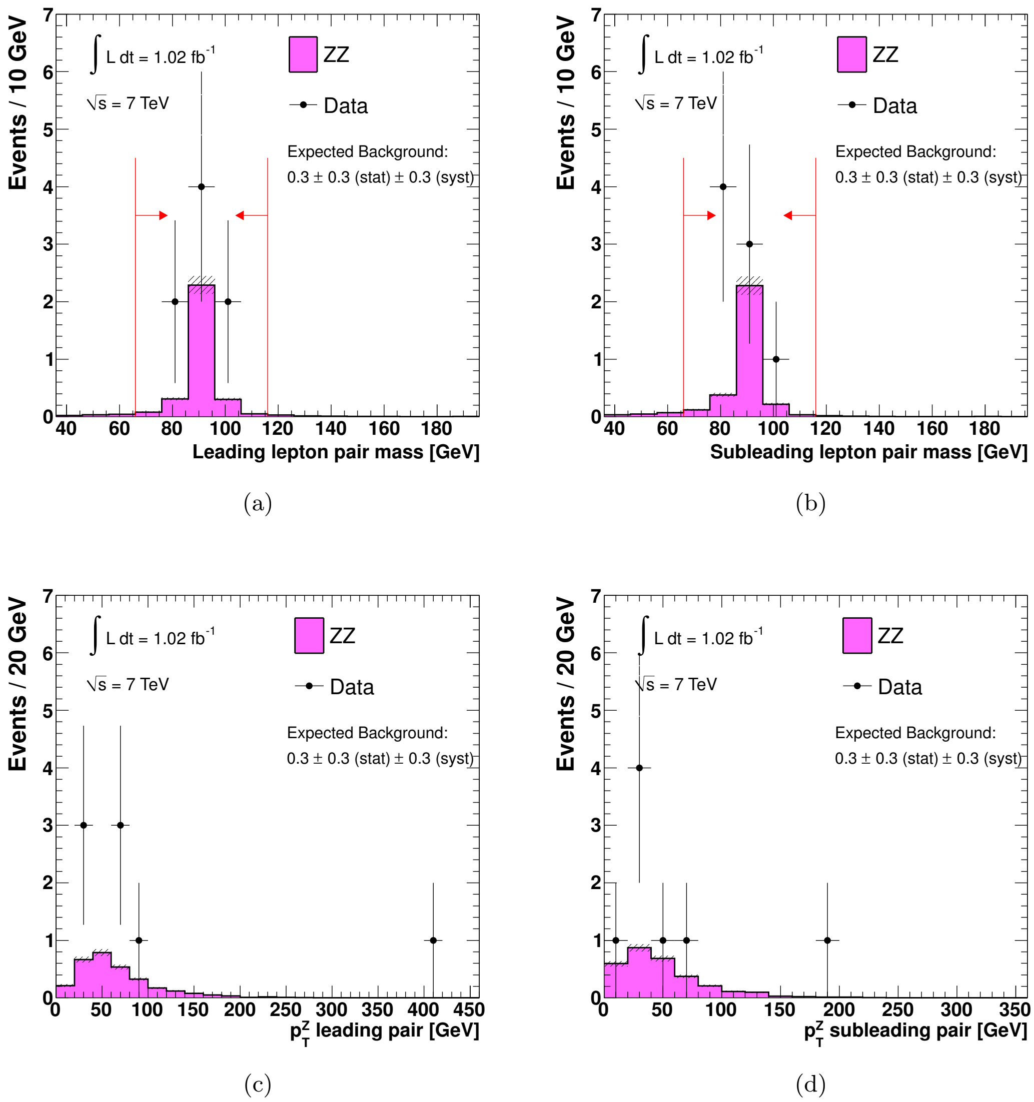

Figure G.5: Invariant mass of (a) leading pair (b) subleading pair and transverse momentum p_T^Z of (c) leading pair and (d) subleading pair of the $\mu\mu$ pairs. The points represent the observed data and the histograms show the signal prediction from simulation. The shaded band on each histogram shows the combined statistical and systematic uncertainty on the signal prediction. The predicted number of background events from the data-driven background estimate is indicated on the plot.

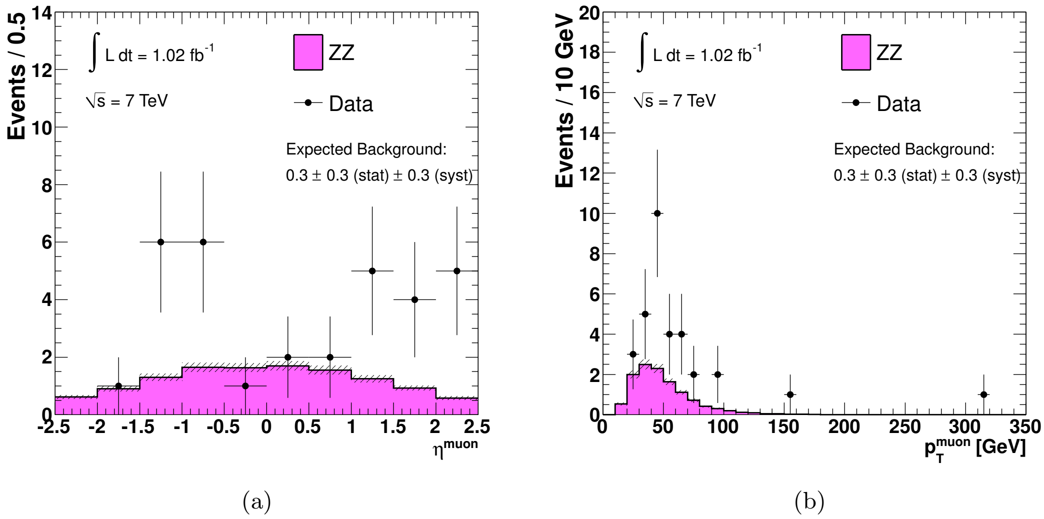

Figure G.6: (a) η and (b) p_T of the final muons. The points represent the observed data and the histograms show the signal prediction from simulation. The shaded band on each histogram shows the combined statistical and systematic uncertainty on the signal prediction. The predicted number of background events from the data-driven background estimate is indicated on the plot.

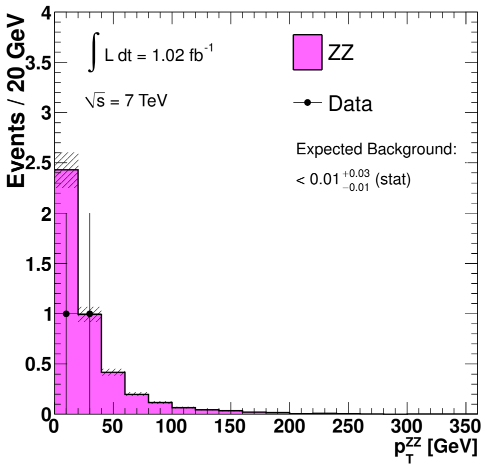

(a)

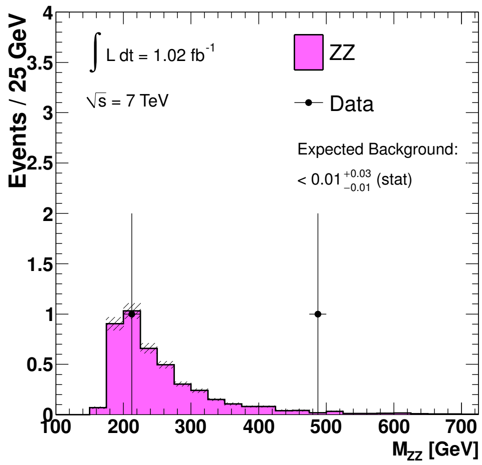

(b)

Figure G.7: (a) Transverse momentum p_{T}^{ZZ} and (b) invariant mass M_{ZZ} of the $ZZ \to 2e2\mu$ candidates. The points represent the observed data and the histograms show the signal prediction from simulation. The shaded band on each histogram shows the combined statistical and systematic uncertainty on the signal prediction. The predicted number of background events from the data-driven background estimate is indicated on the plot.

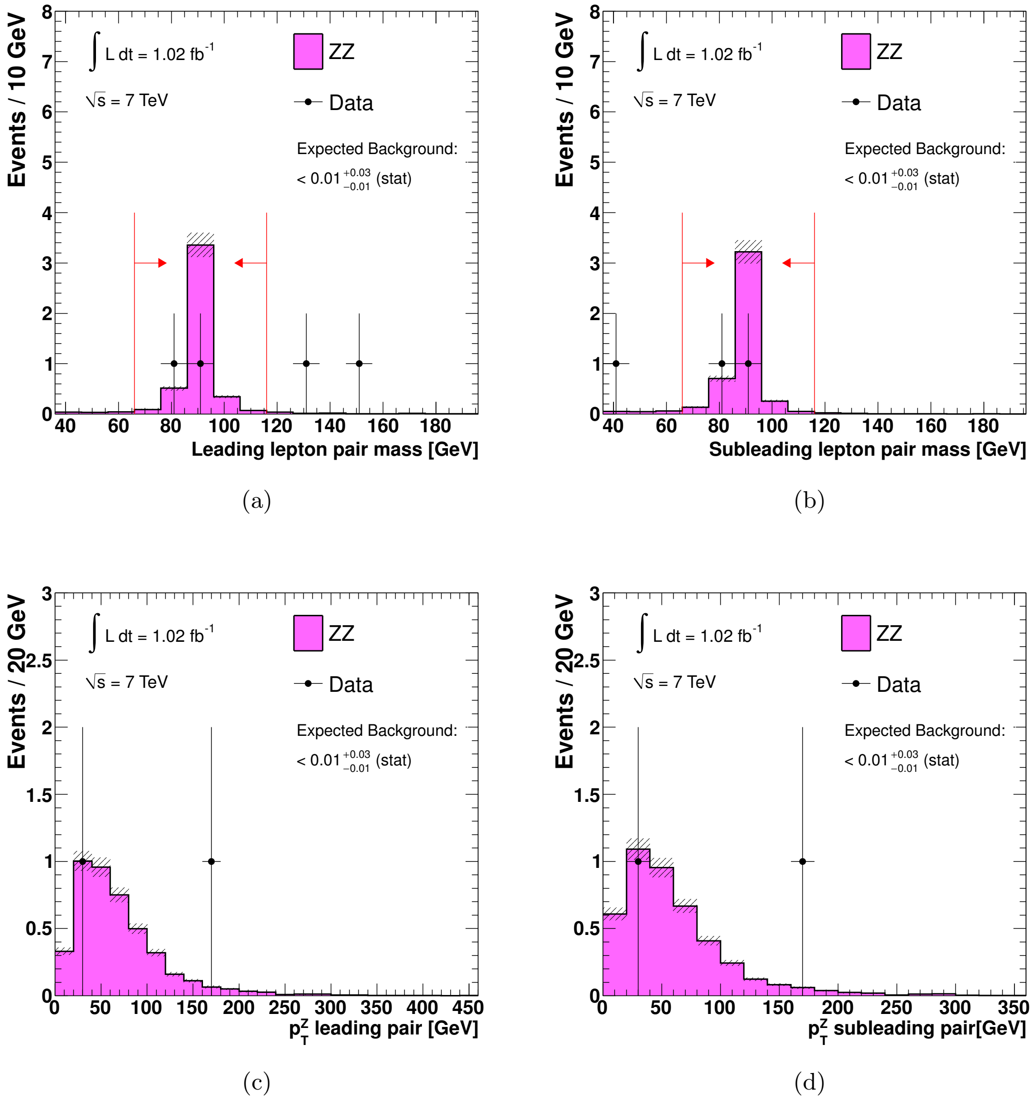

Figure G.8: Invariant mass of (a) leading pair (b) subleading pair and transverse momentum p_T^Z of (c) leading pair and (d) subleading pair of the ll pairs. The points represent the observed data and the histograms show the signal prediction from simulation. The shaded band on each histogram shows the combined statistical and systematic uncertainty on the signal prediction. The predicted number of background events from the data-driven background estimate is indicated on the plot.

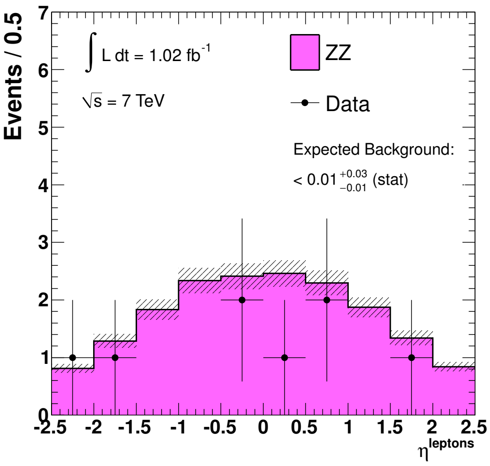

(a)

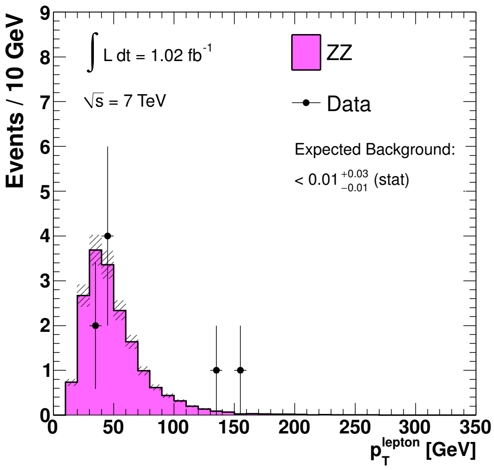

(b)

Figure G.9: (a) η and (b) p_T of the final $2e2\mu$ single leptons. The points represent the observed data and the histograms show the signal prediction from simulation. The shaded band on each histogram shows the combined statistical and systematic uncertainty on the signal prediction. The predicted number of background events from the data-driven background estimate is indicated on the plot.

Declaration

I herewith declare that I have produced this paper without the prohibited assistance of third parties and without making use of aids other than those specified; notions taken over directly or indirectly from other sources have been identified as such. This paper has not previously been presented in identical or similar form to any other Greek or foreign examination board.

The thesis work was conducted from 2008 to 2012 under the supervision of Prof. Chara Petridou at Aristotle University of Thessaloniki.

Andreas Petridis